Woodhead Publishing Series in Civil and Structural Engineering: Number 57

Acoustic Emission (AE) and Related Non-destructive Evaluation (NDE) Techniques in the Fracture Mechanics of Concrete

Fundamentals and Applications

Edited by

Masayasu Ohtsu

AMSTERDAM • BOSTON • CAMBRIDGE • HEIDELBERG
LONDON • NEW YORK • OXFORD • PARIS • SAN DIEGO
SAN FRANCISCO • SINGAPORE • SYDNEY • TOKYO
Woodhead Publishing is an imprint of Elsevier

List of contributors

F. Accornero Department of Structural, Geotechnical and Building Engineering, Politecnico di Torino, Torino, Italy

D.G. Aggelis Vrije Universiteit Brussel, Pleinlaan, Brussels, Belgium

L. Calabrese University of Messina, Messina, Italy

A. Carpinteri Department of Structural, Geotechnical and Building Engineering, Politecnico di Torino, Torino, Italy

A. Deraemaeker Université Libre de Bruxelles (ULB), Brussels, Belgium

C. Dumoulin Université Libre de Bruxelles (ULB), Brussels, Belgium

M. ElBatanouny University of South Carolina, Columbia, SC, USA

F. Grondin UNAM Université, École Centrale de Nantes, Nantes, France

K. Izuno Ritsumeikan University, Kusatsu, Shiga, Japan

G. Karaiskos Université Libre de Bruxelles (ULB), Brussels, Belgium

Y. Kawasaki Ritsumeikan University, Kusatsu, Shiga, Japan

G. Lacidogna Department of Structural, Geotechnical and Building Engineering, Politecnico di Torino, Torino, Italy

L. Linzer University of the Witwatersrand, Johannesburg, South Africa

A. Loukili UNAM Université, École Centrale de Nantes, Nantes, France

A. Manuello Department of Structural, Geotechnical and Building Engineering, Politecnico di Torino, Torino, Italy

T.E. Matikas University of Ioannina, Ioannina, Greece

L. Mhamdi University of Delaware, Newark, DE, USA

A.C. Mpalaskas University of Ioannina, Ioannina, Greece

G. Niccolini Department of Structural, Geotechnical and Building Engineering, Politecnico di Torino, Torino, Italy

K. Ohno Tokyo Metropolitan University, Hachioji-shi, Tokyo, Japan

T. Okamoto Ritsumeikan University, Kusatsu, Shiga, Japan

H. Oshita Chuo University, Tokyo, Japan

K. Otsuka Tohoku Gakuin University, Tagajo, Miyagi, Japan

E. Proverbio University of Messina, Messina, Italy

B.K. Raghu Prasad Indian Institute of Science, Bangalore, India

J. Saliba UNAM Université, École Centrale de Nantes, Nantes, France; Université de Bordeaux, Bordeaux, France

T. Schumacher University of Delaware, Newark, DE, USA

R.K. Singh Bhabha Atomic Research Centre, Mumbai, India

T. Suzuki Niigata University, Niigata, Japan

M. Takeda Tohoku Gakuin University, Tagajo, Miyagi, Japan

R. Vidya Sagar Indian Institute of Science, Bangalore, India

P. Ziehl University of South Carolina, Columbia, SC, USA

Introduction

M. Ohtsu
Kumamoto University, Kumamoto, Japan

1 Introduction

In the following chapters, we deal mostly with acoustic emission (AE) techniques. Consequently, fundamentals of AE measurement are briefly stated in relation with failure and fracture mechanics of concrete. Due to crack nucleation, AE phenomena such as elastic wave generation and propagation are observed. In order to detect AE waves, fundamentals for the measurement are summarized. Theoretically, the measuring system is formulated by applying the linear system theory. As a result, the frequency response of the system is a key issue for the measurement. Recently, the standardizations of AE tests in concrete are in progress. Thus, three recommendations by RILEM are presented.

2 Acoustic emission and fracture mechanics

Fracture in a material takes place with the release of stored strain energy, which is consumed by nucleating new external surfaces (cracks) and emitting elastic waves. The latter phenomenon is defined as acoustic emission (AE). The elastic waves propagate inside a material and are detected by an AE sensor as shown in Figure 1.

Concrete materials can be observed in the various scales from atomic structure to large-scale buildings. At the micro scale, the individual cement grains and are the complex pore structure are visible. Upon increasing the meso-scale to 10^{-3} m, individual sand and aggregate particles can be distinguished. At this scale, nucleation of micro-cracks can be identified and detected as AE phenomena. At the macro-scale, these cracks coalesce macroscopically, resulting in final failure. In the case, AE events are actively observed.

For theoretical treatment of AE, elastic waves due to cracking in a homogeneous medium are normally taken into account. Although concrete materials are not homogeneous but inhomogeneous and heterogeneous, elastodynamic theories are applicable. This is because material properties in elastodynamics are fundamentally dependent on the characteristic dimensions of materials. The dynamic heterogeneity is closely dependent on the relation between these and wavelengths of propagating waves. According to the theory of wave scattering, in the case that the wavelengths are even longer than the sizes of heterogeneous inclusions, the effect of heterogeneity

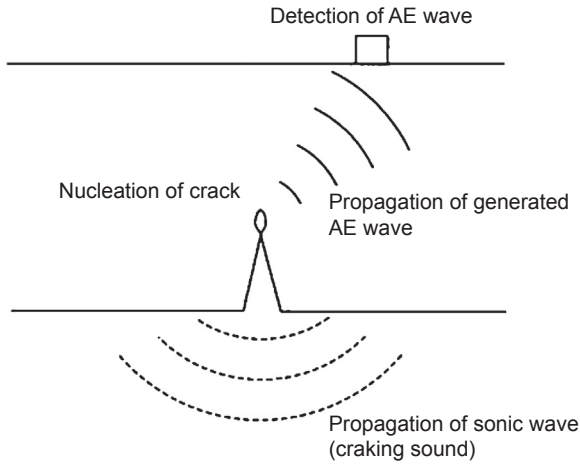

Figure 1 Detection of acoustic emission waves.

is inconsequent. In the case of AE waves in concrete, the velocities of elastic waves are over 1000 m/s. Thus, the use of frequency range up to some 100 kHz corresponds to the case where the wavelengths are longer than several centimeters. It results in the fact that concrete consisting of normal aggregate (with around 10 mm diameter) is reasonably referred to as homogeneous.

In fracture mechanics, cracks can nucleate in three distinct modes, namely tensile opening (mode I), in-plane shear (mode II) and out-of-plane shear (mode III). According to a three-dimensional (3D) lattice analysis at the meso-scale (Lilliu & van Mier, 2003), it is demonstrated that mode I plays a key role for crack extension. In addition, it is confirmed that AE technique is useful to detect prepeak mode I cracking in concrete (van Mier, 2007). So, opening cracks are to be detected as micro-cracks prior to reaching final failure. Concerning crack modes, a theoretical analysis of AE waves can provide kinematic information on mechanisms at the meso-scale. To this end, the moment tensor analysis (Ohtsu, Okamoto, & Yuyama, 1998) is applicable to classify various crack types and to determine three-dimensionally crack orientations, along with crack locations.

At the macro-scale, crack propagation due to expansive pressure was previously analyzed on the basis of linear elastic fracture mechanics and a repair strategy was investigated (Ohtsu & Yoshimura, 1998). From further investigation (Ohtsu & Yoshimura, 1997), it is found that the spalling crack normally extends in the case that the concrete cover thickness is comparable to the size of coarse aggregate and thus the surface crack is arrested by the aggregate, which is stronger or stiffer than mortar matrix. It is confirmed that these cracking behaviors are readily detected by AE measurement.

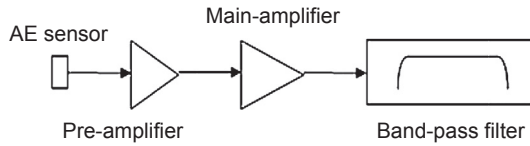

Figure 2 Acoustic emission measuring system.

3 Fundamentals of acoustic emission (AE) measurement

For AE measurement, care is needed because detection of AE signals is affected by environmental vibrations from a string wind, passersby, and a truck passing on a nearby street. Many of these problems have been eliminated with development of instrumentation systems. In updated devices, the frequency range of the measurement is normally set above that of audio or environmental noises, which are substantially minimized by grounding. Owing to advances of measuring systems, the use of a band-pass filter effectively eliminates background noises and allows meaningful tests under usual laboratory environments.

Although recent AE devices are fully digitized, detection systems are basically of analog type as shown in Figure 2. AE waves are detected by AE sensor, which converts dynamic vibrations at the surface of a material into electrical signals. Because AE signals are weak, they are normally amplified by two amplifiers of a preamplifier and a main amplifier. The signal-to-noise ratio of the devices shall be low, and the amplifiers often provide more than 1000 times gain. Lately, it is set to normally 100 times or so.

In concrete materials, the band width from several kilohertz to several 100 kHz or 1 MHz is recommended in the measurement. The frequency range of the waves could cover the inaudible range over the audible range (acoustic or lower than 20 kHz). The sonic waves higher than the audible range are defined as ultrasonic waves. Rigorously speaking, AE waves are neither ultrasonic nor acoustic. Sonic or acoustic waves are waves in air, consisting of only volumetric waves (P wave). In contrast, AE waves are elastic waves of solid in the ultrasonic range.

4 System response

AE signals are detected, as dynamic motions at the surface of a material, and are converted into electric signals by the sensor. The electrical signals are amplified and filtered. Mathematically, the system response is formulated by the linear system as,

$$g(t) = f(t) * w(t) \tag{1}$$

This implies that the sensor response $g(t)$ is obtained from the convolution (*) of the source $f(t)$ with the impulse response of the system $w(t)$. Introducing the Fourier transform,

$$G(f) = F(f)W(f) \tag{2}$$

Here $G(f)$, $F(f)$, and $W(f)$ are Fourier transforms of $g(t)$, $f(t)$, and $w(t)$, respectively.

The signals measured using AE sensors are of small magnitude compared to other methods. As a result, AE signals obtained by the sensors are very weak and have to be so amplified as to be detected and recorded. All of these influences can be assigned by different transfer functions. As a result, AE signal $a(t)$ recorded in the system are mathematically represented as,

$$a(t) = w_f(t) * w_a(t) * w(t) * f(t) \tag{3}$$

where $w_f(t)$ and $w_a(t)$ are transfer functions of the filter and the amplifiers. For characterizing AE sources theoretically, it is so important to know the weights of these functions as to eliminate their influences. In usual cases, the transfer functions of both the filter $w_f(t)$ and the amplifier $w_a(t)$ are known to be fairly flat or almost constant in the frequency domain. Eventually, it is found that the frequency response or the transfer function $w(t)$ or $W(f)$ of AE sensor significantly affects the frequency contents of AE signals.

5 Standardization of AE measurement

RILEM Technical Committee 212-ACD: Acoustic Emission (AE) and Related Nondestructive Evaluation (NDE) Techniques for Crack Detection and Damage Evaluation in Concrete was set up in 2004, and established three recommendations as follows:

5.1 Recommendation for AE measurement (Ohtsu, 2010a)

For crack detection and damage evaluation, AE phenomena are to be observed under in-service conditions. This implies that AE measurement could be conducted not only in a laboratory, but also *in situ*. Taking into account the fact, a measurement method is standardized for detecting AE signals in concrete and concrete structures.

From the definition, transient elastic waves are generated by the release of energy in concrete. These waves due to crack nucleation are referred to as AE waves, which propagate inside a material and are detected by an AE sensor as illustrated in Figure 1. AE signals are detected by AE sensor, which can convert elastic motions into electrical signals. A resonance-type AE sensor is widely employed, because it is most sensitive around the resonant frequency. It is known that a broad-band sensor has approximately

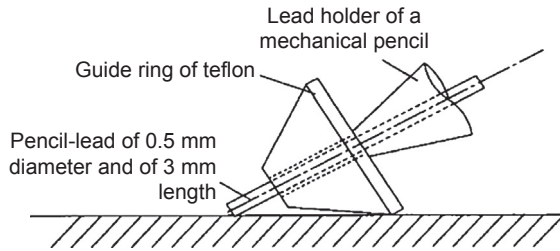

Figure 3 Acoustic emission standard source by pencil-lead (2H) break.

flat response in the target range, but is less sensitive than the resonance-type. So far, resonance-type AE sensors have been mostly applied in the frequency range of 50–250 kHz in concrete.

Sensitivity calibrations of AE sensors, as well as measuring systems, are usually performed by employing the standard source. A simulated AE source due to pencil-lead break has been defined by ASTM, ASNT, and EWGAE as listed in the references. The standard source is illustrated in Figure 3, where a guide ring is recommended to be employed. The pencil-lead break is known as Hsu–Nielsen source in AE technology (Hsu & Breckenridge, 1981; Nielsen, 1977). Sensitivity of AE channels in the system is to be checked routinely by employing the standard source. Variation within the channels shall be less than 3% in the voltage.

The gain of the amplifier is given in dB (decibels), which means the ratio of the output voltage V_o to the input voltage V_i as,

$$dB = 20 \log_{10}(V_o/V_i) \tag{4}$$

A total gain of pre- and main-amplifiers employed in concrete is 40–60 dB. The frequency range is to be determined prior to the measurement, taking into account the performance of AE sensors and systems. Selection of the frequency range is closely related to elimination of noises. In concrete, a band-pass filter between around 10 kHz and several 100 kHz up to 1 MHz is recommended.

One waveform is to be counted as one AE hit, while the cycles over the threshold level are named as AE ringdown counts (or simply "counts"). Here, the threshold is a preset voltage level, which has to be exceeded before one AE signal is detected and processed. The threshold level applied in AE measurement is usually 30–50 dB in concrete.

5.2 *Recommendation for damage qualification by AE (Ohtsu, 2010b)*

Reinforced concrete structures in service could deteriorate due to heavy traffic loads and fatigue. In order to assess the damage levels of the structures by AE, one criterion based on the Kaiser effect (Grosse and Ohtsu, 2007) is proposed. The damages of such

reinforced concrete beams in service as bridges, docks, and buildings are qualified, by simply applying cyclic loading and monitoring AE activity.

Due to damage evolution in reinforced concrete structures, AE events are often observed under in-service conditions. For signal analysis, one AE parameter of AE count or AE hit is to be detected and processed. In advance to *in situ* AE measurement, the noise levels need to be estimated. Then, counteract against external noises, wind, rain, sunshine, and so forth is usually conducted to decrease the noise level as low as possible.

In the case that the noises have similar frequency contents, amplitudes to AE signals or sources of the noises are unknown, characteristics of the noises are quantitatively estimated prior to the measurement, and separation of AE signals from the noises can be achieved. For this purpose, the use of filters is applicable after determining the proper frequency range for the measurement. Normally, to eliminate mechanical noises due to vibrations, traffics, and so forth, a high-pass filter over several kilohertz is useful. Elimination of electrical noises is made by a low-pass filter over several 100 kHz. AE activity is evaluated from the number of AE counts or hits. The onset of AE activity is identified at the time when more than 10 counts over the threshold are continuously observed under loading.

To quantify the Kaiser effect in AE monitoring, the Felicity ratio (F-ratio) was proposed (Fowler, 1986):

F-ratio = the load level of the onset of AE activity/the previous load level at maximum.

Provided that the Kaiser effect is present, the F-ratio should be equal to 1.0. It was reported that this ratio became lower than 1.0 due to the damage repeated in the reinforced concrete beams. In principle, the concrete structures undamaged are statically stable with high redundancy. Because the Kaiser effect is closely associated with structural stability, the F-ratio could become larger than 1.0 in a very sound structure. Along with damage accumulation, the ratio decreases lower than 1.0, due to AE generation even at lower loading levels than before. Thus, the ratio is a good indication of the damage accumulation and structural instability. Further, AE activity during unloading is another indication of structural integrity. In the case that the structure is statically stable, AE activity is seldom observed in the unloading process.

In the present recommendation, the ratios to estimate the Kaiser effect are defined, as follows:

1. Ratio of load at the onset of AE activity to previous load:

load ratio = load at the onset of AE activity in the subsequent loading/the previous maximum load.

2. Ratio of cumulative AE activity during the unloading process to that of the last maximum loading cycle:

calm ratio = the number of cumulative AE activity under unloading/total AE activity during the whole cycle.

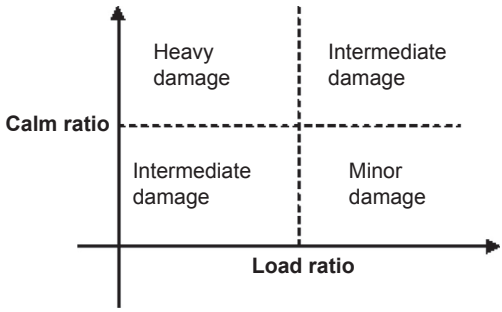

Figure 4 Qualification of the damages by the two ratios.

In the practice, the damage assessment is proposed to classify the damage levels as prescribed in Figure 4. The classification shall be applied to AE activity under loading such as incremental, cyclic, and repeated. The particular values to classify the damages of the calm ratio and the load ratio shall be properly determined in advance to the establishment of the criterion, based on experimental data obtained at the site or in a laboratory. For example, 0.9 of the load ratio and 0.05 of the calm ratio were suggested for the classification in laboratory tests of 3-m-span reinforced concrete beams (Ohtsu, Uchida, Okamoto, & Yuyama, 2002). For concrete bridge beams, 0.3–0.45 of the load ratio and 0.6 of the calm ratio were applied (Colombo, Forde, Main, Halliday, & Shigeishi, 2005; Colombo, Forde, Main, & Shigeishi, 2005). Recently, for shorter beams less than 1 m, 0.4–0.5 of the load ratio and 1.0 of the calm ratio were applied (Liu & Ziehl, 2009).

5.3 *Recommendation for crack classification by AE (Ohtsu, 2010c)*

For *in situ* inspection, estimation of active cracks is of significant importance. Due to damage evolution in reinforced concrete structures, AE events are observed under in-service conditions. Generally speaking, nucleation of shear cracks follows tensile cracks on an existing failure surface. Accordingly, for an early warning of crack nucleation, the classification of active cracks is in great demand. In this recommendation, a classification criterion for micro-cracks in concrete is proposed on the basis of the measurement of AE parameters.

AE signals due to cracking are detected properly for the duration of the measurement. In order to detect and locate active cracks, load application is necessary but does not cause critical damages in a target structure. In advance to the test, the attenuation properties of the target are to be estimated, by employing the standard source or the equivalent.

From AE parameters of the rise time and the peak amplitude in Figure 5, the RA value is defined as,

$$\text{RA} = \text{the rise time}/\text{the peak amplitude} \tag{5}$$

shall be calculated.

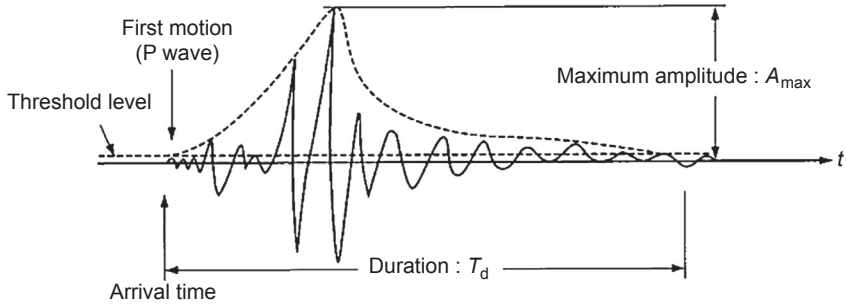

Figure 5 Acoustic emission waveform parameters.

The averaged frequency F_a of each waveform shall be calculated from,

$$\text{Average frequency } (F_a) = \text{AE ringdown counts}/\text{the duration time} \tag{6}$$

where the duration time is given in Figure 5, and the ringdown counts correspond to the number of threshold crossings within the duration time.

By applying these parameters, classification of cracks into tensile cracks and other-type cracks including shear cracks is performed as shown in Figure 6, where RA values and average frequencies plotted shall be calculated from the moving average of more

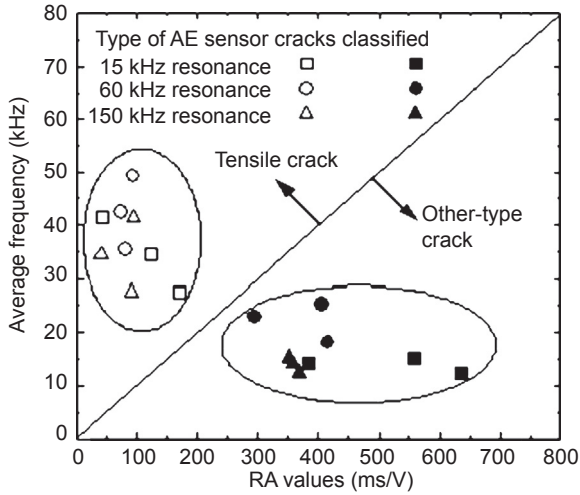

Figure 6 Qualification of the damage by acoustic emission parameters.

than 50 hits. It is noted that the RA values may vary depending on the threshold level. But, Figure 6 shows that the selection of AE sensors does not provide the critical effect on the classified results.

For plotting data, the ordinate is expressed by a physical unit of kHz and the abscissa scale is ms/volt, where the amplitude shall be calibrated as the sensor output, compensating the effect of amplifiers. Since the amplifier gain is normally expressed in dB, using the relationship:

$$\mathrm{dB} = 20\log(V_{\max}/1\,\mu\text{-volt}) - (\text{preamplifier gain in dB}). \tag{7}$$

If the preamplifier gain is 40 dB, the maximum amplitude recorded as 80 dB corresponds to 1 V. In the Figure 6, the ratio of the abscissa scale to the ordinate scale is set to 10. But, it just means a suggestive value. A proper ratio shall be determined, depending on materials and structures. It is recommended to set the ratio in advance to the classification of active cracks. In a reference, it is recommended to apply the ratio of 50, based on the moment tensor analysis (Ohno & Ohtsu, 2008). In another reference, just a trend of these RA value in Eqn (5) and Fa in Eqn (6) is applied to identify the corrosion process in reinforced concrete (Ohtsu & Tomoda, 2008), and to characterize the transition from tensile to shear cracking in steel-fiber-reinforced concrete (Soulioti et al., 2009).

6 Concluding remarks

Recently, research activities on AE techniques are very high in a variety of laboratory studies as well as theoretical researches. Focusing on crack detection and damage evaluation in concrete for diagnosis and prognosis, AE techniques and related NDE techniques play a key role for inspection and maintenance of infrastructures.

Toward the sustainable society, the long service life of infrastructure is going to be an evolutional target. Aging problems and damages due to natural disasters in concrete structures have updated the urgent demand for continuing maintenance of the structures in service. Because this issue is critical for the sustainable infrastructure, a variety of techniques and evaluation methods for diagnosis and prognosis are under development in concrete engineering. In this regard, AE and related NDE techniques are to be developed as practically applicable to on-site measurement.

References

ASNT (American Society for Nondestructive Testing) DGZfP-SE1 nondestructive testing: acoustic emission terms.

ASTM E750 standard practice for characterizing AE instrumentation.

Colombo, S., Forde, M. C., Main, I. G., Halliday, J., & Shigeishi, M. (2005). AE energy analysis on concrete bridge beams. *Materials and Structures, 38*, 851–856.

Colombo, S., Forde, M. C., Main, I. G., & Shigeishi, M. (2005). Predicting the ultimate bending capacity of concrete beams from the "relaxation ratio" analysis of AE signals. *Construction and Building Materials, 19*, 746–754.

EWGAE Codes for AE examination: Code IV-definition of terms in AE.

Fowler, T. J. (1986). Experience with acoustic emission monitoring of chemical process industry vessels. *Progress in AE III*, 150–162.

Grosse, C. U., & Ohtsu, M. (Eds.). (2007). *Acoustic emission testing*. Springer.

Hsu, N. N., & Breckenridge, F. R. (1981). Characterization and calibration of acoustic emission sensors. *Materials Evaluation, 39*, 60–68.

Lilliu, G., & van Mier, J. G. M. (2003). 3D lattice-type fracture model for concrete. *Engineering Fracture Mechanics, 70*(7/8), 927–941.

Liu, Z., & Ziehl, P. (2009). Evaluation of reinforced concrete beam specimens with acoustic emission and cyclic load test methods. *ACI Structural Journal, 106*(3), 288–299.

Nielsen, A. (1977). *"Acoustic emission source based on pencil Lead breaking," presented at EWGAE Meeting in Rome.* September 21.

Ohno, K., & Ohtsu, M. (2008). Comparison of crack classification in concrete by parameter analysis and SiGMA in acoustic emission. In *Proc. structural faults and repair 2008, 12th International Conference and Exhibition.* Edinburgh, U.K. (CD-ROM).

Ohtsu, M. (2010a). Measurement method of acoustic emission signals in concrete. *Materials and Structures, 43*, 1177–1182.

Ohtsu, M. (2010b). Test method for damage qualification of reinforced concrete beams by AE. *Materials and Structures, 43*, 1183–1186.

Ohtsu, M. (2010c). Test method for classification of active cracks in concrete structures by AE. *Materials and Structures, 43*, 1187–1189.

Ohtsu, M., Okamoto, T., & Yuyama, S. (1998). Moment tensor analysis of acoustic emission for cracking mechanisms in concrete. *ACI Structural Journal, 95*(2), 87–95.

Ohtsu, M., & Tomoda, Y. (2008). Phenomenological model of corrosion process in reinforced concrete identified by acoustic emission. *ACI Materials Journal, 105*(2), 194–199.

Ohtsu, M., Uchida, M., Okamoto, T., & Yuyama, S. (2002). Damage assessment of reinforced concrete beams qualified by acoustic emission. *ACI Structural Journal, 99*(4), 411–417.

Ohtsu, M., & Yoshimura, S. (1997). Analysis of crack propagation and crack initiation due to corrosion of reinforcement. *Construction and Building Materials, 11*(7–8), 437–442.

Ohtsu, M., & Yoshimura, S. (1998). LIFEM prediction and repair strategy for crack extension due to corrosion of reinforcement. In *Proc. of FRAMCOS-3* (Vol. II, pp. 1829–1840). AEDIFICATIO publishers.

Soulioti, D., Barkoula, N. M., Paipetis, A., Matikas, T. E., Shiotani, T., & Aggelis, D. G. (2009). Acoustic emission behavior of steel fiber reinforced concrete under bending. *Construction and Building Materials, 23*, 3532–3536.

van Mier, J. G. M. (2007). Multi-scale interaction potentials (*F-r*) for describing fracture of brittle disordered materials like cement and concrete. *International Journal of Fracture, 143*, 41–78.

Related titles

Understanding the rheology of concrete
(ISBN 978-0-85709-028-7)

Non-destructive evaluation of reinforced concrete structures
Volume 1: Deterioration processes and standard test methods
(ISBN 978-1-84569-560-6)

Non-destructive evaluation of reinforced concrete structures
Volume 2: Non-destructive testing methods
(ISBN 978-1-84569-950-5)

Woodhead Publishing Series in Civil and Structural Engineering

1 **Finite element techniques in structural mechanics**
C. T. F. Ross
2 **Finite element programs in structural engineering and continuum mechanics**
C. T. F. Ross
3 **Macro-engineering**
F. P. Davidson, E. G. Frankl and C. L. Meador
4 **Macro-engineering and the earth**
U. W. Kitzinger and E. G. Frankel
5 **Strengthening of reinforced concrete structures**
Edited by L. C. Hollaway and M. Leeming
6 **Analysis of engineering structures**
B. Bedenik and C. B. Besant
7 **Mechanics of solids**
C. T. F. Ross
8 **Plasticity for engineers**
C. R. Calladine
9 **Elastic beams and frames**
J. D. Renton
10 **Introduction to structures**
W. R. Spillers
11 **Applied elasticity**
J. D. Renton
12 **Durability of engineering structures**
J. Bijen
13 **Advanced polymer composites for structural applications in construction**
Edited by L. C. Hollaway
14 **Corrosion in reinforced concrete structures**
Edited by H. Böhni
15 **The deformation and processing of structural materials**
Edited by Z. X. Guo
16 **Inspection and monitoring techniques for bridges and civil structures**
Edited by G. Fu
17 **Advanced civil infrastructure materials**
Edited by H. Wu
18 **Analysis and design of plated structures Volume 1: Stability**
Edited by E. Shanmugam and C. M. Wang

19 **Analysis and design of plated structures Volume 2: Dynamics**
Edited by E. Shanmugam and C. M. Wang
20 **Multiscale materials modelling**
Edited by Z. X. Guo
21 **Durability of concrete and cement composites**
Edited by C. L. Page and M. M. Page
22 **Durability of composites for civil structural applications**
Edited by V. M. Karbhari
23 **Design and optimization of metal structures**
J. Farkas and K. Jarmai
24 **Developments in the formulation and reinforcement of concrete**
Edited by S. Mindess
25 **Strengthening and rehabilitation of civil infrastructures using fibre-reinforced polymer (FRP) composites**
Edited by L. C. Hollaway and J. C. Teng
26 **Condition assessment of aged structures**
Edited by J. K. Paik and R. M. Melchers
27 **Sustainability of construction materials**
J. Khatib
28 **Structural dynamics of earthquake engineering**
S. Rajasekaran
29 **Geopolymers: Structures, processing, properties and industrial applications**
Edited by J. L. Provis and J. S. J. van Deventer
30 **Structural health monitoring of civil infrastructure systems**
Edited by V. M. Karbhari and F. Ansari
31 **Architectural glass to resist seismic and extreme climatic events**
Edited by R. A. Behr
32 **Failure, distress and repair of concrete structures**
Edited by N. Delatte
33 **Blast protection of civil infrastructures and vehicles using composites**
Edited by N. Uddin
34 **Non-destructive evaluation of reinforced concrete structures Volume 1: Deterioration processes**
Edited by C. Maierhofer, H.-W. Reinhardt and G. Dobmann
35 **Non-destructive evaluation of reinforced concrete structures Volume 2: Non-destructive testing methods**
Edited by C. Maierhofer, H.-W. Reinhardt and G. Dobmann
36 **Service life estimation and extension of civil engineering structures**
Edited by V. M. Karbhari and L. S. Lee
37 **Building decorative materials**
Edited by Y. Li and S. Ren
38 **Building materials in civil engineering**
Edited by H. Zhang
39 **Polymer modified bitumen**
Edited by T. McNally
40 **Understanding the rheology of concrete**
Edited by N. Roussel
41 **Toxicity of building materials**
Edited by F. Pacheco-Torgal, S. Jalali and A. Fucic

42 **Eco-efficient concrete**
Edited by F. Pacheco-Torgal, S. Jalali, J. Labrincha and V. M. John
43 **Nanotechnology in eco-efficient construction**
Edited by F. Pacheco-Torgal, M. V.Diamanti, A. Nazari and C. Goran-Granqvist
44 **Handbook of seismic risk analysis and management of civil infrastructure systems**
Edited by F. Tesfamariam and K. Goda
45 **Developments in fiber-reinforced polymer (FRP) composites for civil engineering**
Edited by N. Uddin
46 **Advanced fibre-reinforced polymer (FRP) composites for structural applications**
Edited by J. Bai
47 **Handbook of recycled concrete and demolition waste**
Edited by F. Pacheco-Torgal, V. W. Y. Tam, J. A. Labrincha, Y. Ding and J. de Brito
48 **Understanding the tensile properties of concrete**
Edited by J. Weerheijm
49 **Eco-efficient construction and building materials: Life cycle assessment (LCA), eco-labelling and case studies**
Edited by F. Pacheco-Torgal, L. F. Cabeza, J. Labrincha and A. de Magalhães
50 **Advanced composites in bridge construction and repair**
Edited by Y. J. Kim
51 **Rehabilitation of metallic civil infrastructure using fiber-reinforced polymer (FRP) composites**
Edited by V. Karbhari
52 **Rehabilitation of pipelines using fiber-reinforced polymer (FRP) composites**
Edited by V. Karbhari
53 **Transport properties of concrete: Measurement and applications**
P. A. Claisse
54 **Handbook of alkali-activated cements, mortars and concretes**
F. Pacheco-Torgal, J. A. Labrincha, C. Leonelli, A. Palomo and P. Chindaprasirt
55 **Eco-efficient masonry bricks and blocks: Design, properties and durability**
F. Pacheco-Torgal, P. B. Lourenço, J. A. Labrincha, S. Kumar and P. Chindaprasirt
56 **Advances in asphalt materials: Road and pavement construction**
Edited by S.-C. Huang and H. Di Benedetto
57 **Acoustic emission (AE) and related non-destructive evaluation (NDE) techniques in the fracture mechanics of concrete: Fundamentals and applications**
Edited by M. Ohtsu

Woodhead Publishing is an imprint of Elsevier
80 High Street, Sawston, Cambridge, CB22 3HJ, UK
225 Wyman Street, Waltham, MA 02451, USA
Langford Lane, Kidlington, OX5 1GB, UK

Copyright © 2015 Elsevier Ltd. All rights reserved.

No part of this publication may be reproduced, stored in a retrieval system or transmitted in any form or by any means electronic, mechanical, photocopying, recording or otherwise without the prior written permission of the publisher.

Permissions may be sought directly from Elsevier's Science & Technology Rights Department in Oxford, UK: phone (+44) (0) 1865 843830; fax (+44) (0) 1865 853333; email: permissions@elsevier.com. Alternatively you can submit your request online by visiting the Elsevier website at http://elsevier.com/locate/permissions, and selecting Obtaining permission to use Elsevier material.

Notice
No responsibility is assumed by the publisher for any injury and/or damage to persons or property as a matter of products liability, negligence or otherwise, or from any use or operation of any methods, products, instructions or ideas contained in the material herein. Because of rapid advances in the medical sciences, in particular, independent verification of diagnoses and drug dosages should be made.

British Library Cataloguing-in-Publication Data
A catalogue record for this book is available from the British Library

Library of Congress Control Number: 2014959677

ISBN: 978-1-78242-327-0 (print)
ISBN: 978-1-78242-345-4 (online)

For information on all Woodhead Publishing publications visit our website at http://store.elsevier.com/

Typeset by TNQ Books and Journals
www.tnq.co.in
Printed and bound in the United Kingdom

Index

Note: Page numbers followed by "f" and "t" indicate figures and tables respectively.

Damage evaluation in concrete materials by acoustic emission

1

T. Suzuki
Niigata University, Niigata, Japan

1.1 Introduction

The durability of concrete structures easily decreases as a result of environmental attacks. The degree of damage in concrete is, in most cases, evaluated by mechanical properties such as the strength and the modulus of elasticity. For effective maintenance and management of concrete structures, it is necessary to evaluate explicitly the degree of damage. To inspect concrete structures for maintenance, the acoustic emission (AE) technique is known to be useful (Grosse & Ohtsu, 2008). Crack nucleation and extension are readily detected by AE measurement. In this respect, monitoring of AE activity in the uniaxial compression test of core samples was proposed (Ohtsu, Kawai, & Yuji, 1988). AE behavior under compression is formulated by the rate-process theory.

Here, quantitative evaluation of damage has been performed by correlating AE rate-process analysis and damage mechanics. Concrete samples drilled out from structures are tested under compression, and AE measurement is carried out. By calculating Young's modulus of intact concrete, E^*, from the AE database, the degree of damage was estimated as a relative damage in a road bridge (Suzuki, Shigeishi, et al., 2007). Thus, the procedure to estimate the relative moduli, E_0/E^*, of concrete is implemented as DeCAT (Damage Estimation of Concrete by Acoustic Emission Technique) (Suzuki, & Aoki, 2010; Suzuki, Ogata, Takada, Aoki, & Ohtsu, 2010).

1.2 Damage estimation of concrete by acoustic emission technique (DeCAT) procedure

1.2.1 Acoustic emission rate-process analysis

The concept that the AE activity of concrete under compression is associated with the rate-process theory was introduced (Ohtsu & Suzuki, 2004) in order to analyze AE-generating behavior associated with the generation of micro-cracks. It is well known that these cracks tend to gradually accumulate until final failure. Since this process could be referred to as stochastic, the following equation of the rate process is derived to formulate the number of AE events, dN, generated by the increment of stress from V to $V + \mathrm{d}V$.

Acoustic Emission (AE) and Related Non-destructive Evaluation (NDE) Techniques in the Fracture Mechanics of Concrete
http://dx.doi.org/10.1016/B978-1-78242-327-0.00001-5
Copyright © 2015 Elsevier Ltd. All rights reserved.

$$f(V)\mathrm{d}V = \frac{\mathrm{d}N}{N} \tag{1.1}$$

where N is the total number of AE events and $f(V)$ is the probability function of AE generation at stress level $V\%$. For $f(V)$ in Eqn (1.1), the following hyperbolic function is assumed:

$$f(V) = \frac{a}{V} + b \tag{1.2}$$

where a and b are empirical constants. Here, the value a is named the rate. As shown in Figure 1.1, the probability varies, in particular at low stress level, depending on whether rate a is positive or negative. In the case that the rate a is positive, the probability of AE generation is high at low stress level. This indicates that a tested concrete core could be damaged. In contrast, in the case that the rate a is negative, the probability is low at low stress level, implying that the concrete is in sound condition. Therefore, it is possible to quantitatively evaluate the damage of concrete from AE activity under uniaxial compression by AE rate-process analysis.

Substituting Eqn (1.2) into Eqn (1.1), a relationship between the total number of AE events, N, and stress level, V, is obtained as follows:

$$N = CV^a \exp(bV) \tag{1.3}$$

where C is the integration constant.

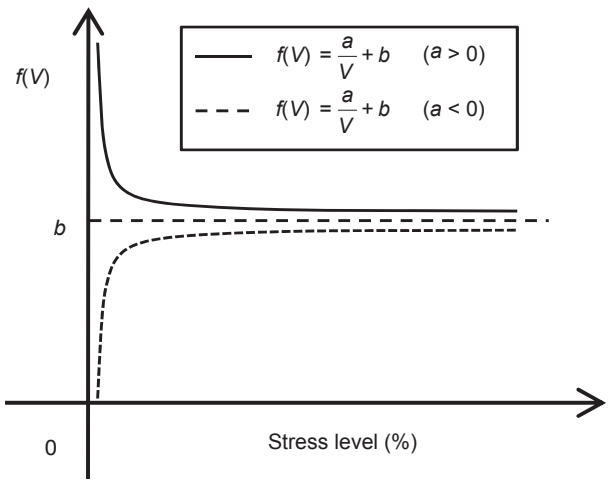

Figure 1.1 Two possible relations of probability function $f(V)$.

1.2.2 Damage mechanics

Damage parameter Ω in continuum damage mechanics is defined as a relative change in the modulus of elasticity, as follows:

$$\Omega = 1 - \frac{E}{E^*} \tag{1.4}$$

where E is the modulus of elasticity and E^* is the modulus of concrete that is assumed to be intact and undamaged. Loland (1989) assumed that the relationship between damage parameter Ω and strain ε under uniaxial compression is as follows:

$$\Omega = \Omega_0 + A_0 \varepsilon^{\lambda} \tag{1.5}$$

where Ω_0 is the initial damage at the onset of the uniaxial compression test, and A_0 and λ are empirical constants of concrete. The following equation is derived from Eqns (1.4) and (1.5):

$$\sigma = \left(E_0 - E^* A_0 \varepsilon^{\lambda}\right)\varepsilon \tag{1.6}$$

where

$$E_0 = E^*(1 - \Omega_0) \tag{1.7}$$

$$E_c = E_0 - E^* A_0 \varepsilon_c^{\lambda} \tag{1.8}$$

From Eqn (1.7), to estimate the initial damage, Ω_0, it is essential to obtain the modulus of intact concrete E^*. However, it is not feasible to determine E^* of concrete in an existing structure. To estimate E^* from AE measurement, the relation between the total number of AE events and the stress level in Eqn (1.3) is correlated with the Loland model. In the compression test, a relation between stress and strain is shown in Figure 1.2. The modulus of elasticity varies from E_0 to final E_c. Note that the former is defined as a tangential modulus, whereas the latter is a secant modulus. Following Eqn (1.5), damage Ω increases from Ω_0 to Ω_c, as shown in Figure 1.3.

1.2.3 Database development

The static initial modulus of elasticity E_0 is to be quantitatively determined as a tangential gradient of the stress−strain curve, from Eqn (1.6):

$$\sigma = E_0 \varepsilon - E^* A_0 \varepsilon^{\lambda+1} \tag{1.9}$$

Thus, the static modulus, E_0, is uniquely determined as a tangential modulus: $\mathrm{d}\sigma/\mathrm{d}\varepsilon$ at $\varepsilon = 0$.

As shown in Figure 1.2, two moduli of elasticity, E_0 and E_c, are determined in the core test. Then, the rate-process analysis is conducted in the stress level range from 30% to 80%. This is because AE events at initial loading below 30% stress are

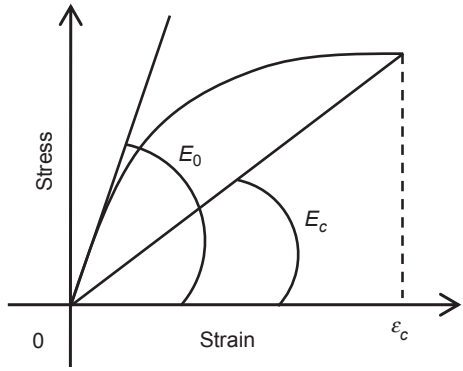

Figure 1.2 Stress−strain relation and two Young's moduli.

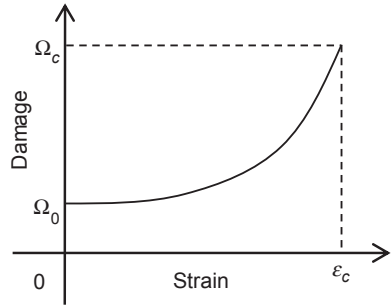

Figure 1.3 Evolution of damage in concrete.

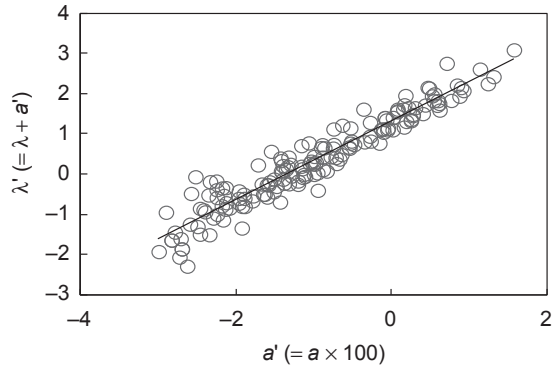

Figure 1.4 Acoustic emission database.

normally associated with contact with the loading plate, and those at an accelerated stage above 80% have little to do with the damage.

We have found the highest correlation between the damage parameter λ and the rate a (Suzuki & Ohtsu, 2011). Results of all samples damaged due to the freezing−thawing process in previous experiments are plotted with open circles in Figure 1.4.

The AE database consists of 200 samples tested at Kumamoto University from 1988 to 2013. A linear correlation between λ' and the rate a' value is reasonably assumed. Thus, the equation of λ' is expressed as follows:

$$\lambda' = a'X + Y$$

$$\lambda + (a \times 100) = (a \times 100)X + Y \tag{1.10}$$

where

$$\lambda = \frac{E_c}{E_0 - E_c} \tag{1.11}$$

Here, it is assumed that $E_0 = E^*$ when $a = 0.0$. This allows us to estimate Young's modulus of intact concrete E^* from the AE database as follows:

$$E^* = E_c + \frac{E_c}{Y} \tag{1.12}$$

In this study, the damage of concrete is evaluated by relative moduli E' as presented.

$$E' = \frac{E^*}{E_0} \times 100 \tag{1.13}$$

Here E_0 is the tangent modulus of elasticity in the compression test. The procedure to estimate the relative moduli E' is named DeCAT (damage estimation of concrete by acoustic emission technique).

1.3 Comparison of concrete damage with crack distribution

In a water canal constructed around the 1970s, where concrete was heavily cracked as shown in Figure 1.5, core samples were taken from the concrete walls. Damage estimation of concrete-core samples was conducted applying DeCAT and X-ray computed tomography (CT) methods. Testing samples were strongly influenced by the freeze−thawed process (Suzuki et al., 2010). These samples were drilled out from the left- and right-side walls. Crack distributions observed are not similar in the left- and right-side walls (Figure 1.6(a)−(c)). Concrete from the left-side wall had been damaged due to the freezing and thawing effect as shown in Figure 1.6(a) (Type A) and Figure 1.6(b) (Type B), whereas that at the right-side wall seems to be sound without inner cracks as found in Figure 1.6(c) (Type C). Inner cracks in concrete cores were inspected with helical CT scans. After the helical CT scan, damage of core samples was evaluated by the DeCAT procedure.

Figure 1.5 Overview of sampling site.

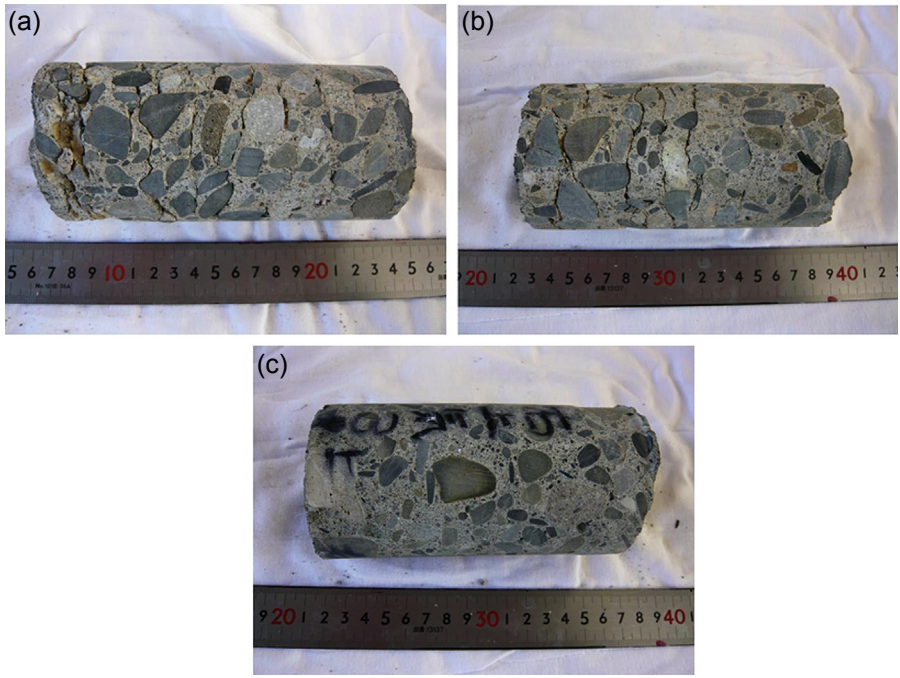

Figure 1.6 (a) Type A sample (heavily damaged concrete). (b) Type B sample (somewhat damaged concrete). (c) Type C sample (non-cracked concrete).

1.3.1 Visualization of cracks in concrete using X-ray CT

The core samples were inspected with helical CT scans, shown in Figure 1.7, which were undertaken at 1-mm intervals before the compression test. In X-ray CT tests of concrete samples, the CT numbers are detected from +127 to +1472 for pores and

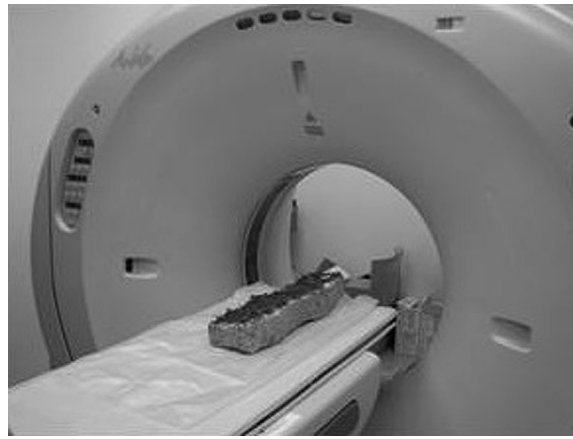

Figure 1.7 A general view of the helical computed tomography machine and a sample.

+2000 over for aggregates. At cross-sections of intact concrete, the average CT numbers are between +1625 and +1993. At the regions where cracks were generated, the average CT numbers are between −124 and +1141, which are about 30% lower than those of non-damaged concrete. Variations of the CT numbers in tested cores are given in Figure 1.8. In Type A samples, the CT number clearly drops at cracked portions. The averaged CT number of non-cracked cores (Type C) is +1895. In contrast, the averaged CT numbers in the damaged cores are +1743 (Type A) and +1859 (Type B). These results imply that the decrease in the CT number could reflect accumulation of damage.

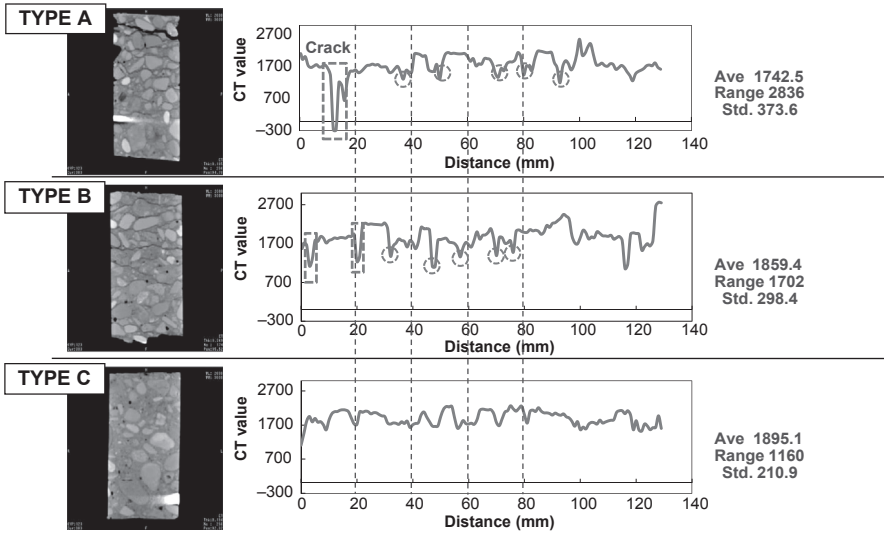

Figure 1.8 Results of X-ray density analysis from top to bottom in a core sample.

1.3.2 Quantitative damage evaluation of cracked concrete by relative moduli E′

After X-ray CT tests, uniaxial compression tests of core samples were conducted, measuring AE activities, as shown in Figure 1.9. Two strain gauges were attached in the axial and lateral directions to measure strain. AE monitoring was conducted by employing an AE sensor of 150 kHz resonance (R15α, PAC) that was attached at the middle height of the specimen. Amplification was 60 dB gains in total. The frequency range was set from 60 kHz to 1 MHz. AE hits were detected at a threshold level of 42 dB by an AE system (SAMOS-AE, PAC).

Using the results of AE tests, relative damages were estimated by the ratio of initial Young's moduli E_0 to intact E^* (Eqn (1.13)). These relative moduli (E_0/E^*) are compared with the compressive strengths shown in Figure 1.10. The figure also presents the previous results of structural concrete cores in addition to the present study (Suzuki, Ohtsu, et al., 2007). Those samples were collected from other concrete canal

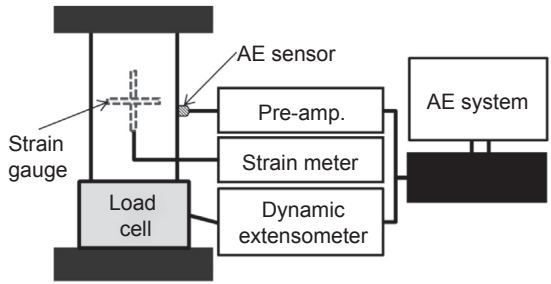

Figure 1.9 Test setup for acoustic emission (AE) monitoring in core testing.

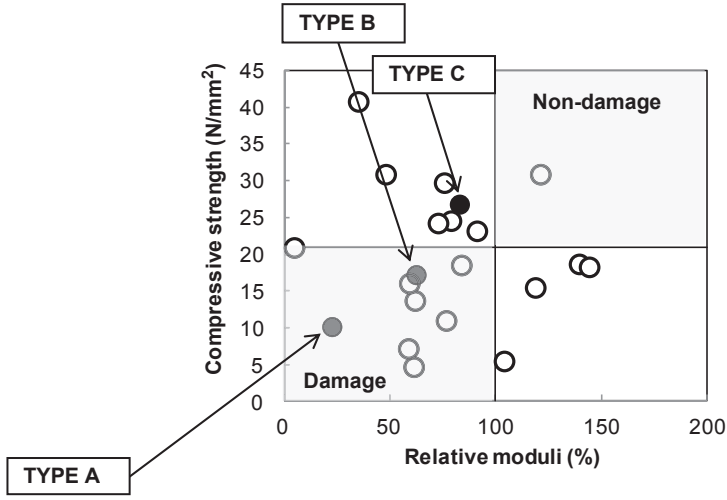

Figure 1.10 Comparison between the relative moduli and compressive strengths.

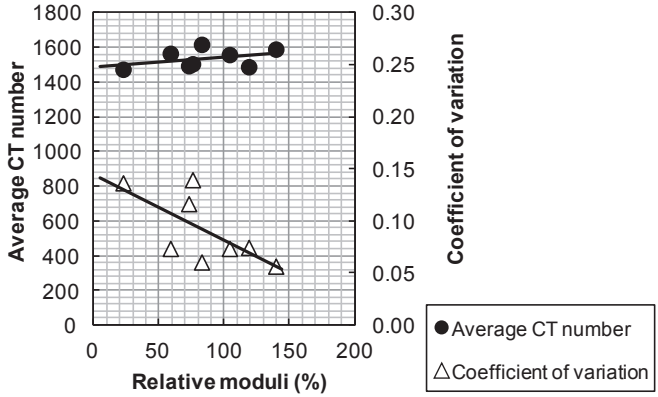

Figure 1.11 Relationship between the relative moduli and statistical properties of computed tomography (CT) data.

structures in service. Relations between the relative moduli and the compressive strengths are classified by one criterion (Suzuki, Shigeishi, et al., 2007) because the baseline of the compressive strength is 21 N/mm^2, as defined in the standard design strength for concrete water canals of Japan (MAFF, 2001). The damaged samples (Types A and B) are plotted in the "Damage" zone because relative moduli are lower than 100% and the compressive strength is lower than 21 N/mm^2. The sample (Type C) is found in the intermediate zone, as the relative damage is slightly lower than 100%, but the strength is over 21 N/mm^2.

The relative moduli are compared with statistical properties of the CT numbers in Figure 1.11. The coefficients of variations are negatively correlated with relative moduli, whereas the averaged CT numbers increase with the increase in the relative damages. Therefore, the decrease in the relative damages is associated with the decrease in the CT numbers, which reflect accumulation of micro-cracks.

1.4 Application of DeCAT to an in-service concrete structure damaged by earthquake

1.4.1 Great East Japan earthquake

The Great East Japan Earthquake hit the Tohoku area in Japan on March 11, 2011 (Figure 1.12). The seismic wave recorded is shown in Figure 1.13, comparing it with another two large earthquakes in Japan. A large number of concrete structures were damaged due to the 9.0 Richter-scale magnitude earthquake. Prior to reconstruction and retrofitting of these structures, damage evaluation of *in situ* concrete structures is now in urgent demand. In this concern, quantitative damage estimation of concrete has been performed, applying DeCAT procedure to core samples (Suzuki & Ohtsu, 2012).

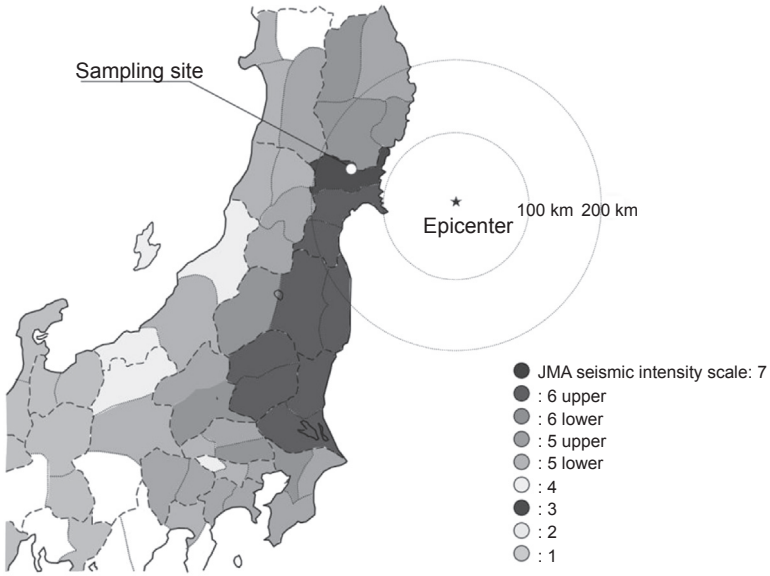

Figure 1.12 Earthquake epicenter and location of sampling site.

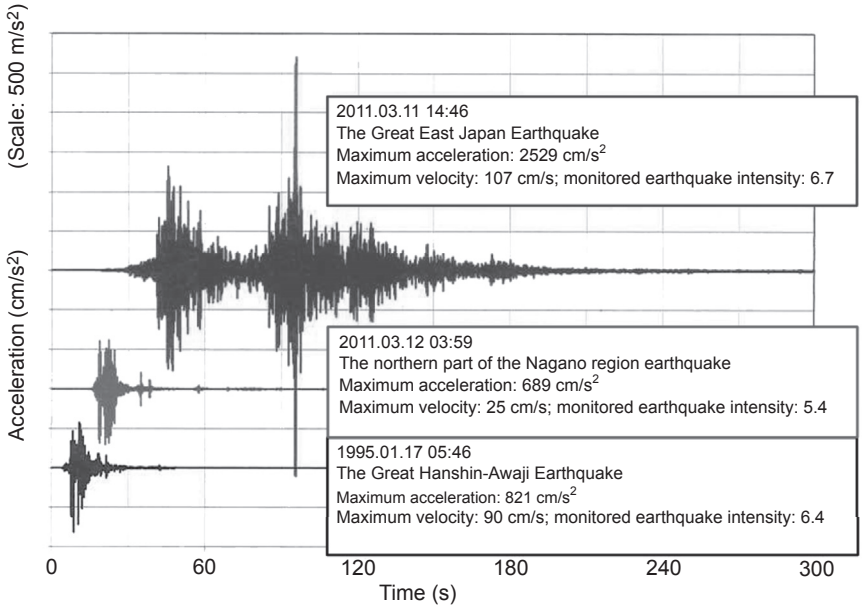

Figure 1.13 Seismic waves recorded in Japan.

1.4.2 Damage estimation of concrete by DeCAT

Concrete-core samples were taken from reinforced concrete columns of an existing canal of both periods of pre- and post-earthquake. These samples are classified into two types of Type 1 and Type 2 samples. Type 1 samples were drilled out in October, 2009, prior to the Great East Japan Earthquake hitting the Tohoku area. Then, Type 2 samples were drilled out in the same canal in January, 2012, after the earthquake at locations close to where the Type 1 cores were drilled.

The compressive strengths and the relative moduli were determined. Results are summarized in Figure 1.14. A relationship between the compressive strengths and the relative moduli in Type 1 is similar to that of Type 2 with the increasing trend. However, the relative damages of Type 2 are definitely lower than those of Type 1. These results suggest that the strength may not be a key factor for durability. However, the relative moduli E_0/E^* are really sensitive to damage because high AE activities in low stress level are closely associated with existing micro-cracks, which may not be explicitly related with the strength.

In Figure 1.15, along with the distances from the reference point, all relative moduli determinations are compared with the compressive strengths at their locations. It is clearly observed that the relative moduli estimated are in reasonable agreement with the compressive strengths after the earthquake (Type 2). Here, the relative moduli vary from 0.696 to 0.925 and are estimated to be below 1.0, which implies a damaged condition. Comparing the results of Type 1 with those of Type 2, the relative damages estimated in Type 2 are quantitatively lower than those of Type 1.

1.4.3 Non-destructive damage estimation of concrete with dynamic Young's modulus E_d

Along the canal wall of 1.2 km, the longitudinal-wave velocities were measured before and after the earthquake with a 100-m interval. The dynamic modulus of elasticity E_d

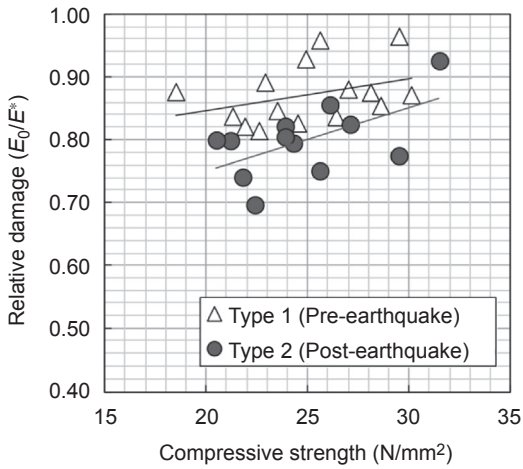

Figure 1.14 Relation between relative damages E_0/E^* and compressive strengths.

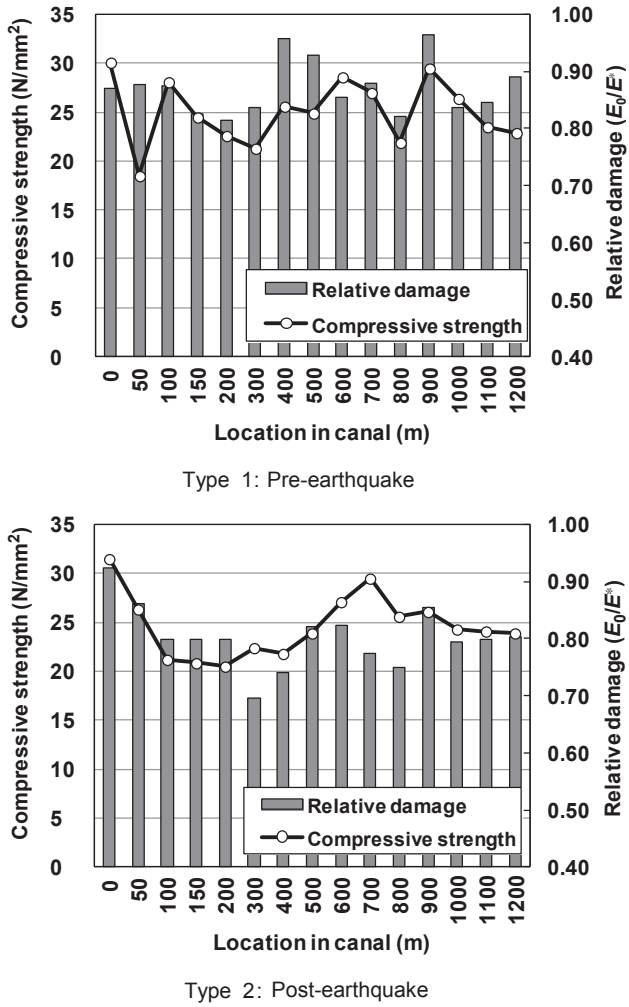

Figure 1.15 Spatial damage distribution of the strengths and relative moduli.

was calculated from the *P*-wave velocity using Eqn (1.14), which is based on the JSCE TC-326 report (JSCE TC326, 2004).

$$E_d = \frac{(1+\nu)(1-2\nu)\rho}{1-\nu} V_p^2 \tag{1.14}$$

Here, ρ is the density of the concrete specimen and ν is Poisson's ratio. V_p is the longitudinal-wave velocity. Thus, dynamic moduli at the location of the velocity measurement were estimated as E_d/E^*, where the modulus E^* of the core sample closest to the location was applied.

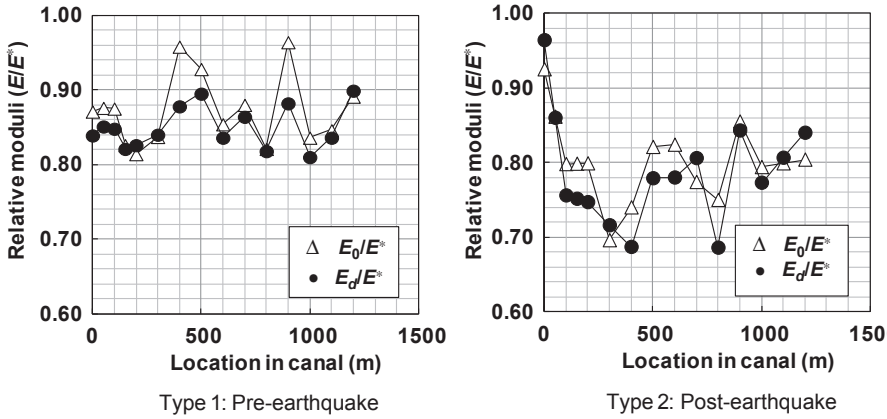

Figure 1.16 Comparison between relative moduli E/E^* and E_d/E_0.

In Figure 1.16, comparisons of relative moduli, E/E^*, using E_d and E_0 are shown. The static modulus of elasticity E_0 is obtained as a tangential modulus in the compression test, while the dynamic modulus of elasticity E_d is obtained by ultrasonic testing (UT). Reasonable agreement is observed between the static moduli E_0/E^* and the dynamic moduli E_d/E^*. These results confirm that the non-destructive indicator E_d is also effective for damage evaluation of concrete by means of E_d/E^*. The experimental results suggest that the damage of concrete could be quantitatively estimated from damage parameter E_0/E^* without knowing the original state of the concrete at construction. Because the static moduli (relative moduli) E_0/E^* and dynamic moduli E_d/E^* are closely correlated, these are useful for compensating relative moduli E_0/E^* in large structures.

1.5 Concluding remarks and future trends

For quantitative estimation of damage in concrete, AE monitoring is applied to uniaxial compression testing of concrete samples. The procedure is based on estimating the intact modulus of elasticity in concrete using damage mechanics. In addition, by applying *P*-wave velocity measurement, spatial distribution of the damage is readily determined, which is based on an estimation of dynamic Young's modulus calculated from *P*-wave velocity. Reasonable agreement with the spatial distribution of dynamic moduli E_d/E^* is confirmed by the results of static moduli E_0/E^* based on AE generation behavior in the core test.

Applications for damage evaluation using AE are extensively discussed. Results are really promising for actual monitoring and *in situ* observation. AE monitoring in a core test will be a useful method for damage estimation of concrete. In the future, a non-destructive inspection method for damage detection in concrete will be developed based on the relation between AE rate in the core test and *P*-wave velocity.

References

Grosse, C. U., & Ohtsu, M. (2008). *Acoustic emission testing*. Berlin: Springer. pp. 3−10.

Japan Society of Civil Engineers (JSCE) TC-326 Edit. (2004). *Nondestructive inspection of concrete by elastic wave method*. JSCE. pp. 31−37.

Loland, K. E. (1989). Continuous damage model for load - response estimation of concrete. *Cement and Concrete Research, 10*, 395−402.

Ministry of Agriculture, Forestry and Fisheries of Japan (MAFF). (2001). *Japanese standard for design and construction of agricultural water canal structure*. JSIDRE. pp. 302−303.

Ohtsu, M., Kawai, Y., & Yuji, S. (1988). Evaluation of deterioration in concrete by acoustic emission activity. *Proceedings of the Japan Concrete Institute, 10*(2), 849−854.

Ohtsu, M., & Suzuki, T. (2004). Quantitative damage evaluation of concrete core based on AE rate-process analysis. *Journal of Acoustic Emission, 22*, 30−38.

Suzuki, T., & Aoki, M. (2010). Evaluation of durability in agricultural concrete open canal by damage mechanics. *Journal of JASRAD, 20*(3), 19−25.

Suzuki, T., Ogata, H., Takada, R., Aoki, M., & Ohtsu, M. (2010). Use of acoustic emission and X-ray computed tomography for damage evaluation of freeze-thawed concrete. *Construction and Building Materials, 24*, 2347−2352.

Suzuki, T., & Ohtsu, M. (2011). Damage evaluation of core concrete by AE. *Concrete Research Letters, 2*(3), 275−279.

Suzuki, T., & Ohtsu, M. (2012). Application of DeCAT system for damage evaluation of concrete in disaster areas due to the Great East Japan earthquake. In *14th International conference structural faults and repair-2012*.

Suzuki, T., Ohtsu, M., Aoki, M., & Nakamura, R. (2007). Damage identification of a concrete water-channel in service by acoustic emission. *Advance Acoustic Emission* (CD-R).

Suzuki, T., Shigeishi, M., & Ohtsu, M. (2007). Relative damage evaluation of concrete in a road bridge by AE rate - process analysis. *Materials and Structures, 40*(2), 221−227.

Acoustic emission wireless monitoring of structures

2

G. Lacidogna, A. Manuello, G. Niccolini, F. Accornero, A. Carpinteri
Department of Structural, Geotechnical and Building Engineering, Politecnico di Torino, Torino, Italy

2.1 Introduction

Continuous structural health monitoring should provide data in order to better understand structural performances and to predict durability and remaining lifetime. Since around 2005, the acoustic emission (AE) technique has been used in several applications due to its capability to detect crack growth, damage accumulation and AE source localizations in historical monuments, concrete structures and infrastructures (Accornero, Invernizzi, Lacidogna, & Carpinteri, 2012; Carpinteri & Lacidogna, 2006a, 2006b, 2007; Carpinteri, Lacidogna, & Pugno, 2007; Carpinteri, Lacidogna, & Manuello, 2011; Carpinteri, Lacidogna, Invernizzi, et al., 2013). In particular, recent events, such as the reconstruction of the Noto Cathedral in 2007 (Anzani, Binda, Carpinteri, Lacidogna, & Manuello, 2008) after its collapse and the effects of the L'Aquila earthquake in April 2009, have brought the problem of structural safety to be a priority in the maintenance of Italian civil structures and monuments (Han, Carpinteri, Lacidogna, & Xu). These recent events lead to the conclusion that a large number of structures need monitoring and inspection procedures that are reliable, inexpensive and easy to implement. During the last few years, the AE technique has been used for materials damage analysis and long-term monitoring in order to analyze the time evolution of micro-cracking phenomena (Brindley, Holt, & Palmer, 1973; Carpinteri, Lacidogna, & Niccolini, 2007; Carpinteri et al., 2013; Grosse, Reinhardt, & Finck, 2003; Lacidogna, Manuello, Niccolini, & Carpinteri, (2012); Niccolini, Xu, Manuello, Lacidogna, & Carpinteri, 2012; Ohtsu, 1996; Pollock, 1973; Yoon, Lee, Kim, & Seo, 2007). According to this technique, it is possible to detect the onset and the evolution of stress-induced cracks. Crack opening, in fact, is accompanied by the emission of elastic waves that propagate within the bulk of the material. These waves can be detected and recorded by transducers applied to the surface of the structural elements. AE monitoring is performed by means of piezoelectric (PZT) sensors, using crystals that give out signals when subjected to mechanical stress (Carpinteri & Lacidogna, 2006a, 2006b, 2007). In this way, the AE technique makes it possible to estimate the amount of energy released during the fracture process, to obtain information on the criticality of the process underway and to localize the damage source locations (Carpinteri, Lacidogna, & Niccolini, 2006; Ohtsu, 1996; Shah & Li, 1994). In the present chapter, a new AE equipment based on a wireless data acquisition system is presented (Carpinteri, Lacidogna, Manuello, et al., 2013).

Acoustic Emission (AE) and Related Non-destructive Evaluation (NDE) Techniques in the Fracture Mechanics of Concrete
http://dx.doi.org/10.1016/B978-1-78242-327-0.00002-7
Copyright © 2015 Elsevier Ltd. All rights reserved.

Due to the attenuation of acoustic waves and geometrical spreading in concrete structures, numerous sensors have to be applied to cover all critical parts. These circumstances make the traditional way of applying AE techniques too expensive. Monitoring systems for large structures should be based on a new kind of AE equipment using wireless transmission systems. In the new monitoring system, AE signals are detected by the sensor array, recorded *in situ* by a synchronization and storage unit, and subsequently, they are sent via the GPRS/UMTS system to the central server for the elaboration phases. In this way, it is possible to use a centralized station to control continuously and simultaneously, in real time, individual structures situated at different sites (Carpinteri, Lacidogna, Manuello, et al., 2013; Grosse et al., 2003; Yoon et al., 2007).

2.2 Acoustic emission (AE) equipment and wireless transmission system

In the last few years a computer-based procedure including AE source location, AE event counting and statistical analysis applied to AE time series has been developed by the authors (Carpinteri et al., 2011; Carpinteri, Lacidogna, & Niccolini, 2007; Lacidogna et al.). The final output of the AE data processing code returns a complete description of damage characterization and evolution. Today, the most critical cases or those demanding long, *in situ* observation periods (infrastructural or monumental buildings) require AE monitoring based on a telematics working procedure. Huge structures, such as large concrete structures and infrastructures, should be monitored by means of new types of sensors, using efficient algorithms for processing large quantities of data.

To this purpose, the authors are working on a new type of AE equipment able to execute the AE data acquisition in real time by wireless technology. By means of this new equipment, AE signals detected by the sensor array are recorded *in situ* by a synchronization storage device, and successively sent via a GPRS/UMTS system to the central server for the elaboration phase (Carpinteri, Lacidogna, Manuello, et al., 2013).

In this way, it will be possible to use a centralized station to control continuously and simultaneously individual structural elements or entire structures, possibly situated in different places. Moreover, because a correlation exists between the regional seismic activity and the AE signals collected during structural monitoring (Carpinteri, Lacidogna, Invernizzi, et al., 2013; Carpinteri, Lacidogna, & Niccolini, 2007), AE wireless equipment can be also used for the preservation of concrete structural and infrastructural networks from seismic risk. The new AE instrumentations and the prototype are the result of a technical collaboration between the AE research unit of the Politecnico di Torino and LEANE NET Ltd, an Italian company which is a leader in the design and implementation of structural monitoring systems. The new AE sensors are designed to optimize weight, size and applicability to different structural supports (Figure 2.1(a) and (b)). The connection between the sensors and the acquisition module is realized by coaxial cables optimized to reduce the effects of electromagnetic noise. The modules for the signal storage are integrated within the central acquisition unit. The AE data coming from each channel are synchronized and analyzed by a mini-processor.

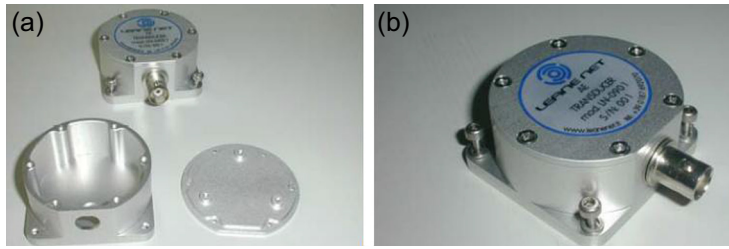

Figure 2.1 (a) New PZT acoustic emission (AE) sensors. (b) The new AE sensors, working in a frequency range between 50 and 800 kHz, are designed to optimize weight, size and applicability to different structural supports.

During this phase, the main characteristics of AE signals are recognized (AE amplitude, signal arrival time, duration and signal frequency).

In Figure 2.2(a) and (b) the central unit interface and the modem for the AE wireless transmission system are reported. The scheme of acquisition, pre-processing and data transmission adopted in the prototype is reported in Figure 2.3. Each channel consists of an analogy to digital converter module (ADC) with the capacity to acquire 10 Ms/s (mega-sample/second) in order to cover the wide band of AE signal frequency range (50−800 kHz). The data exchange is run using a field programmable gate array (FPGA) connected with a parallel bus and integrated into the central unit (Figure 2.3). Each channel, connected with the central processor, has a devoted memory of 64 Mb and is able to perform the data synchronization.

The central unit is also equipped with a thin film transistor (TFT) touch screen for the human interface and first signal processing executable *in situ* (Figure 2.2(a)). The stored data are collected into a compact flash memory card (CF 64 GB) and then sent in real time to the AE laboratory by GSM/GPRS antenna (Figure 2.3) for AE signal analysis. The AE sensors adopted for the new monitoring system are of two types: resonant and broadband piezoelectric transducers. These two kinds of sensors were used according to different conditions and considering the different structures to be

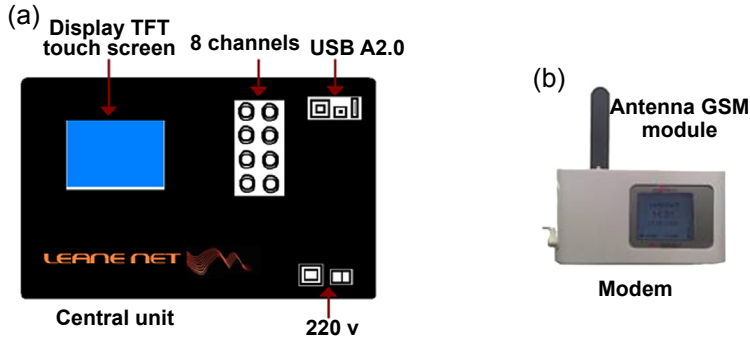

Figure 2.2 Central unit interface (a). Modem for acoustic emission wireless data transmission (b).

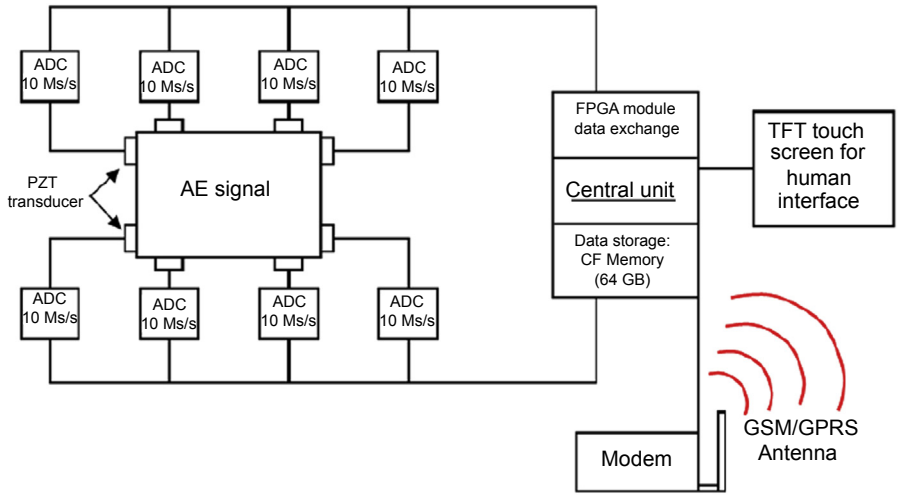

Figure 2.3 Acquisition, pre-processing and data transmission of acoustic emission (AE) signals for the new AE equipment.

monitored. The sensitivity of the broadband sensor is lower, but these sensors are able to acquire data clouds in a wide frequency band and can be used in structures and components of reduced dimensions. In other conditions, and especially when the localization of the damage must be particularly accurate, the resonant sensors will be used according to their greater sensitivity.

2.3 Real-time AE analysis: damage evaluation

The new AE equipment automatically performs different kinds of analysis. The first analysis is devoted to evaluating the damage evolution of the monitored structure. According to this objective, different parameters are computed using the acquired data. The first indicator is represented by the cumulative number of AE signals, N, detected during the monitoring time. In addition, the time dependence of the structural damage observed during the monitoring period, identified by parameter η, can also be correlated to the rate of propagation of the micro-cracks. If we express the ratio between the cumulative number of AE counts recorded during the monitoring process, N, and the number obtained at the end of the observation period, N_d, as a function of time, t, we get the damage time dependence on AE (Carpinteri & Lacidogna, 2006b; Carpinteri et al., 2011):

$$\eta = \frac{E}{E_d} = \frac{N}{N_d} = \left(\frac{t}{t_d}\right)^{\beta_t} \tag{2.1}$$

In Eqn (2.1), the values of E_d and N_d do not necessarily correspond to critical conditions ($E_d \leq E_{\max}$; $N_d \leq N_{\max}$), and the t_d parameter must be considered as the

time during which the structure has been monitored. By working out the β_t exponent from the data obtained during the observation period, we can make a prediction as to the structure's stability conditions. If $\beta_t < 1.0$, the damaging process slows down, and the structure evolves towards stability conditions, in as much as energy dissipation tends to decrease; if $\beta_t > 1.0$ the process diverges and becomes unstable; if $\beta_t = 1.0$ the process is metastable, that is, though it evolves linearly over time, it can reach indifferently either stability or instability conditions (Carpinteri, Lacidogna, & Pugno, 2007; Carpinteri et al., 2011). Damage assessment in the structure may be also investigated by the statistical distribution of the AE signal magnitudes fitted by the Gutenberg−Richter (GR) law (Carpinteri, Lacidogna, & Pugno, 2007; Carpinteri et al., 2011):

$$\log_{10} N(\geq M) = a - bM \tag{2.2}$$

where N is the number of AE events with magnitude greater than M, and a and b (or b-value) are fitting parameters. The b-value is an important parameter for damage assessment of structures as it decreases during damage evolution, reaching final values close to 1.0 when the failure is imminent (Carpinteri et al., 2011).

2.4 Post-process analysis

The new AE monitoring system is also provided with a computer-based procedure, including the improved AE source location based on the Akaike algorithm (Carpinteri, Xu, Lacidogna, & Manuello, 2012). These procedures are performed by automatic AE data processing and are used to evaluate the AE results in concrete notched beams subjected to three-point bending loading conditions up to the final failure.

Traditionally, picking the signal onset times was carried out by checking the signal traces based on an analyst's experience. Nowadays, handling large volumes of digital and real-time data impose less time-consuming and equally objective alternatives. Here, the onset of AE signals is determined by modelling the noise and the signal in windows using the Akaike Information Criterion (AIC) with an automatic procedure for signal data processing able to eliminate false or doubtful onset times.

Initially developed to predict the optimal order of the auto-regressive (AR) process fitting the time series in seismology (Earle & Shearer, 1994; Sleeman & Eck, 1999; Tong & Kennett, 1996), the AIC can be used to demark the point of two adjacent time series (noise and signal) with different underlying statistics (Akaike, 1974; Hafez, Khan, & Kohda, 2010; Kurz, Grosse, & Reinhardt, 2005; Maeda, 1985; Yokota, Zhou, Mizoue, & Nakamura, 1981; Zhang, Thurber, & Rowe, 2003).

Suppose that a voltage time series, $\{x_1, x_2, \ldots, x_n\}$, containing the AE signal is divided into two segments, $i = 1,2$, $\{x_1, x_2, \ldots, x_k\}$ and $\{x_k+1, x_2, \ldots, x_n\}$, where k identifies the unknown signal onset time. Both segments are assumed to be two

different pseudo-stationary time series, either modelled as an AR process of order M with coefficients $\{a_m^i\}$:

$$x_j = \sum_{m=1}^{M} a_m^i x_{j-m} + e_j^i, \quad i = 1, 2 \tag{2.3}$$

where $j = M+1, \ldots, k$ for interval $i = 1$, and $j = k+1, \ldots, n-M$ for $i = 2$.

The model divides either time series into a deterministic and a non-deterministic part, e_j^i, the latter assumed to be a white noise. Thus, the time series $\{e_j^i\}$ is a sample of independent and identically distributed random variables, with mean zero, variance σ_i^2 and density function $f(e_j^i) = (\sigma_i 2\pi)^{-1/2} \exp[-(e_j^i/\sigma_i)^2/2]$, to which the maximum likelihood estimation (MLE) can be applied. Then, we look at the joint density function of all variables $\{e_j^i\}$ – expressed in terms of the observations $\{x_j\}$ by means of Eqn (2.3) – considered as fixed parameters, whereas the model parameters $\Theta_i = \Theta_i(a_1^i, \ldots a_m^i, \sigma_i^2)$ for the i-th interval are allowed to vary freely. In this perspective, the joint density function is the likelihood function L (Akaike, 1974; Hafez et al., 2010; Kurz et al., 2005; Maeda, 1985; Yokota et al., 1981; Zhang et al., 2003):

$$L(\Theta_1, \Theta_2, k, M|x) = \prod_{i=1}^{2} \left(\frac{1}{\sigma_i^2 2\pi} \right)^{\frac{n_i}{2}} \exp\left[-\frac{1}{2\sigma_i^2} \sum_{j=p_i}^{q_i} \left(x_j - \sum_{m=1}^{M} a_m^i x_{j-m} \right)^2 \right] \tag{2.4}$$

where $p_1 = M+1$, $p_2 = k+1$, $q_1 = k$, $q_2 = n-M$, $n_1 = k-M$ and $n_2 = N-k-M$.

As it is known, the MLE finds the particular values of the model parameters that make the observed results the most probable or, in other words, that maximize the likelihood of function L.

Working equivalently with the logarithm of Eqn (2.4) and searching for the MLE of the model parameters we get the following:

$$\frac{\partial \ln L}{\partial \sigma_i} = 0, \quad i = 1, 2 \tag{2.5}$$

which has the solution:

$$\sigma_{i,\max}^2 = \frac{1}{n_i} \sum_{j=p_i}^{q_i} \left(x_j - \sum_{m=1}^{M} a_m^i x_{j-m} \right)^2, \quad i = 1, 2 \tag{2.6}$$

Inserting Eqn (2.6) into Eqn (2.4), we get the maximized logarithmic likelihood function (Akaike, 1974; Maeda, 1985; Yokota et al., 1981):

$$\ln L = -\frac{k-M}{2} \ln \sigma_{1,\max}^2 - \frac{n-k-M}{2} \ln \sigma_{2,\max}^2 + C_1 \tag{2.7}$$

where C_1 is a constant.

The expression in Eqn (2.7) is the basis for the AIC, in which the AIC function is defined as AIC = $2P - 2\ln$ (maximized likelihood function), where P is the number of parameters in the statistical model. Generally, a model with the minimum AIC value is thought to be the most suitable one among the competing models.

Originally, this function was designed to determine the optimal order for an AR process fitting a time series. In the current application, the order M of the AR process is fixed, and therefore, the AIC function is a measure for the model fit. The point k where AIC is minimized, or L is maximized, determines the optimal separation of the two time series – the first representing noise and the second containing the signal – in the least square sense, and it is interpreted as the onset time of the signal. In this sense, the AIC as a function of k is known as the AIC picker (Akaike, 1974):

$$\mathrm{AIC}(k) = (k - M)\ln \sigma^2_{1,\max} + [n - k - M]\ln \sigma^2_{2,\max} + C_2 \tag{2.8}$$

where C_2 is a constant.

Alternatively, the AIC value can be directly calculated from the signal without dealing with the AR coefficients. As $M << n$, Eqn (2.8) can be simplified (Akaike, 1974):

$$\mathrm{AIC}(k) = k\ln(\mathrm{var}(x[1,k])) + (n - k - 1)\ln(\mathrm{var}(x[1+k,n])) \tag{2.9}$$

where k goes through all the signal trace and var is the sample variance.

As the AIC picker finds the onset point as the global minimum, it is necessary to choose a time window that includes only the segment of interest of the signal. If the time window is chosen properly, the AIC picker can find the first arrival of the signal (P-wave arrival for AE) accurately. In the case of low *S/N* ratios (as for noisy EM signals) or more seismic phases (as P-wave and S-wave for AE signals) in a time window, the global minimum cannot guarantee to indicate the first arrival of the signal. For this reason, a pre-selection of this window is necessary to apply the procedure. Here, the onset time is first pre-determined using a threshold amplitude level:

$$\left(\sum_{k=i+1}^{10} |x_k|\right) \Big/ 10 \geq 4\left(\sum_{k=1}^{i} |x_k|\right) \Big/ i \tag{2.10}$$

The first value for the index k that makes relation (2.10) fulfilled is named k_0, and it is the first estimation for the onset time. This first estimation is always localized after the actual onset time.

Thus, we apply the AIC picker to the interval $[1,k_0]$ for a rough determination of the onset time, k_1.

Then, the application of the AIC picker to the time window with centre in k_1 and width $2(k_1-k_0)$ gives the value $k_{\min}$, which is regarded as the actual onset time of the analyzed signal.

For a practical application, see in the following the results of this method on a three-point bending test.

2.5 Damage classification

AE signals generally depend on their source and, specifically, the intensity and the mode of fracture. Therefore, key waveform features like the amplitude, energy and frequency carry information from the damage mode and the fracture process (Shiotani, Fujii, Aoki, & Amou, 1994; Watanabe, Hosomi, Yuno, & Hashimoto, 2010). In general, the characterization of cracks as to their mode provides a warning before failure (Ohtsu, 2010). The received wave depends on the cracking mode, as well as on the orientation of the crack relative to the receivers and the distance between the cracking source and the sensor. When a cracking event occurs, all possible wave modes (longitudinal, transverse and Rayleigh if the crack is surface breaking) are excited. A tensile cracking incident (Figure 2.4) excites most of the energy in the form of longitudinal waves. Therefore, most of the energy arrives in the initial part of the acquired waveform since longitudinal waves are the fastest type. When shear cracking occurs, the percentage of energy emitted in the shear wave mode is increased, resulting in a delay of the main energy cycles of the waveform.

The connection between the mode of crack and the waves recorded depends on different factors like geometric conditions, relative orientation and propagation distance (Aggelis, Mpalaskas, Ntalakas, & Matikas, 2012). The AE waveform parameters, which have been correlated with the cracking mode, are mainly the rise time and peak amplitude, used to calculate the rise angle (RA) value (RILEM Technical Committee, 2010a, 2010b; 2010c, 2010d), defined as the ratio of the rise time (expressed in ms) over the peak amplitude (expressed in V).

Another parameter used to characterize the cracking mode is the average frequency (AF) measured in kHz. The AF values are obtained from the AE ring-down count divided by the duration time of the signal. The AE ring-down count corresponds to the number of threshold crossings within the duration time.

The fracture mode is characterized by the shape of the AE waveforms. Low rise time values and high frequency are typical of tensile crack propagations that include opposing movement of the crack sides (Mode I); whereas shear events usually result in longer waveforms, with longer rise times and lower frequency (Mode II), as shown in Figure 2.5 (Aggelis et al., 2012). These conditions are synthesized by the RA

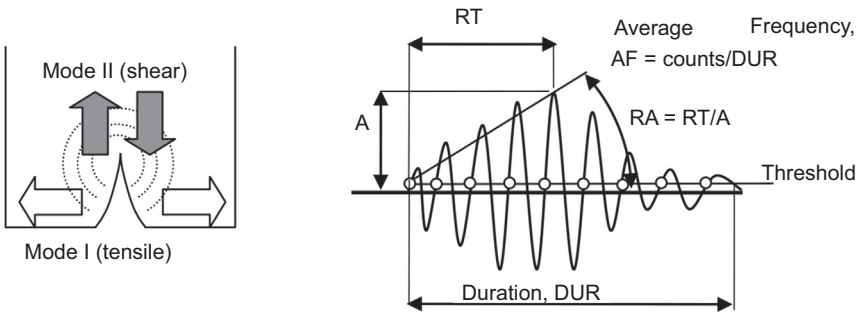

Figure 2.4 Cracking modes and typical acoustic emission signals.

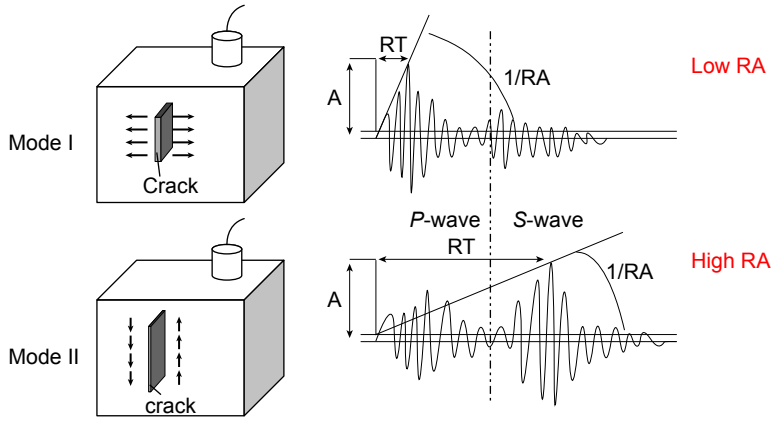

Figure 2.5 Typical waveforms of tensile and shear events. *A* is the amplitude, and RT is the rise time (time between the onset and the point of maximum amplitude) of the waveforms (Aggelis et al., 2012).

value (Aggelis, 2011; Aldahdooh & Muhamad Bunnori, 2013; Ohno & Ohtsu, 2010; Soulioti et al., 2009).

2.6 Structural monitoring systems for seismic risk evaluation

Among the various studies on earthquake space−time correlation, there is a statistical method that allows the calculation of the degree of correlation both in space and time between a series of AE and local seismic recordings, collected in the same period (Carpinteri, Lacidogna, Invernizzi, et al., 2013, Carpinteri, Lacidogna, & Niccolini, 2007). This analysis is based on the generalization of the space−time correlation known as the integral of Grassberger−Procaccia (Grassberger & Procaccia, 1983), defined as follows:

$$C(r,\tau) \equiv \frac{1}{N_{EQ}N_{AE}} \sum_{k=1}^{N_{EQ}} \sum_{j=1}^{N_{AE}} \Theta\left(r - \left|x_k - x_j\right|\right)\Theta\left(\tau - \left|t_k - t_j\right|\right) \tag{2.11}$$

where N_{AE} is the number of peaks of AE activity registered in site and at a defined time window, N_{EQ} is the number of earthquakes recorded in the surrounding area during the same time window and Θ is the step function of Heaviside ($\Theta(x) = 0$ if $x \leq 0$, $\Theta(x) = 1$ if $x > 0$). The index k refers to the recorded seismic events $\{x_k, t_k\}$, while the index j refers to the recorded AE events $\{x_j, t_j\}$.

Therefore, between all possible pairs of recorded AE and seismic events, the sum expressed by the integral of Grassberger−Procaccia can be calculated for those having the epicentral distance $\left|x_k - x_j\right| \leq r$ and the temporal distance $\left|t_k - t_j\right| \leq \tau$. Hence, $C(r,\tau)$ is the probability of the occurrence of two events, an earthquake and an AE

event, whose mutual spatial distances are smaller than r and mutual temporal distances are smaller than τ.

Note that, in order to evaluate Eqn (2.11), the numbers of N_{AE} and N_{EQ} are not required to assume the same value, and x_j correspond to the geographical position of the monitoring site.

Anyway, this approach does not consider the chronological order of the two types of event. Since the AE time series and the earthquake sequences are closely intertwined in the time domain, the problem of the predictive ability of the AE peaks is still open. The records of AE could be both the consequences of the progressive development of micro-damage and the effect of widespread micro-seismicity. Therefore, a probabilistic analysis can be carried out discriminating between the AE events prior to the earthquake, which are precursors, and the AE following the earthquake, which are aftershocks. This analysis can be performed adopting a modified correlation integral (Carpinteri Lacidogna, Invernizzi, et al., 2013; Carpinteri, & Lacidogna, 2007):

$$C_{\pm}(r,\tau) \equiv \frac{1}{N_{EQ}N_{AE}} \sum_{k=1}^{N_{EQ}} \sum_{j=1}^{N_{AE}} \Theta\left(r - \left|x_k - x_j\right|\right)\Theta\left(\tau - \left|t_k - t_j\right|\right)\Theta\left(\pm\left(t_k - t_j\right)\right) \tag{2.12}$$

where "+" and "−" in the Heaviside function are used to take into account that the AE events could be seismic precursors and aftershocks, respectively.

In this way, the function $C^{+}(r, \tau)$ gives the probability that a peak of AE, detected at a certain time, will be followed by an earthquake in the subsequent days within a radius of r kilometers from the AE monitoring site. Varying the thresholds r and τ in Eqn (2.12), two cumulative probability distributions can be constructed, one for each condition (sign "+" or "−") and then the corresponding probability density functions can be derived and represented.

2.7 Applications, observations and results: laboratory tests

The first application was conducted using a servo-controlled machine (MTS) with a closed loop control. A three-point bending test was realized with a linear actuator (hydraulic jack) by passing the stem acting in the middle point of the upper side of the beam. For the test, a concrete element measuring $1190 \times 100 \times 200\ mm^3$ was cast, a central notch of 100 mm was made starting from the middle point at the lower side, and the beam was tested up to the final failure of the specimen (see Figure 2.6).

The results of AE real-time analysis are reported in Figure 2.7 for the monitored specimen. The cumulated number of AEs computed using the new AE equipment shows a strong increment at the beginning of the test up to the final failure of the concrete beam. In correspondence of this phase, the b-value decreases from 1.8 down to values smaller than 1. This parameter shows a damage evolution from

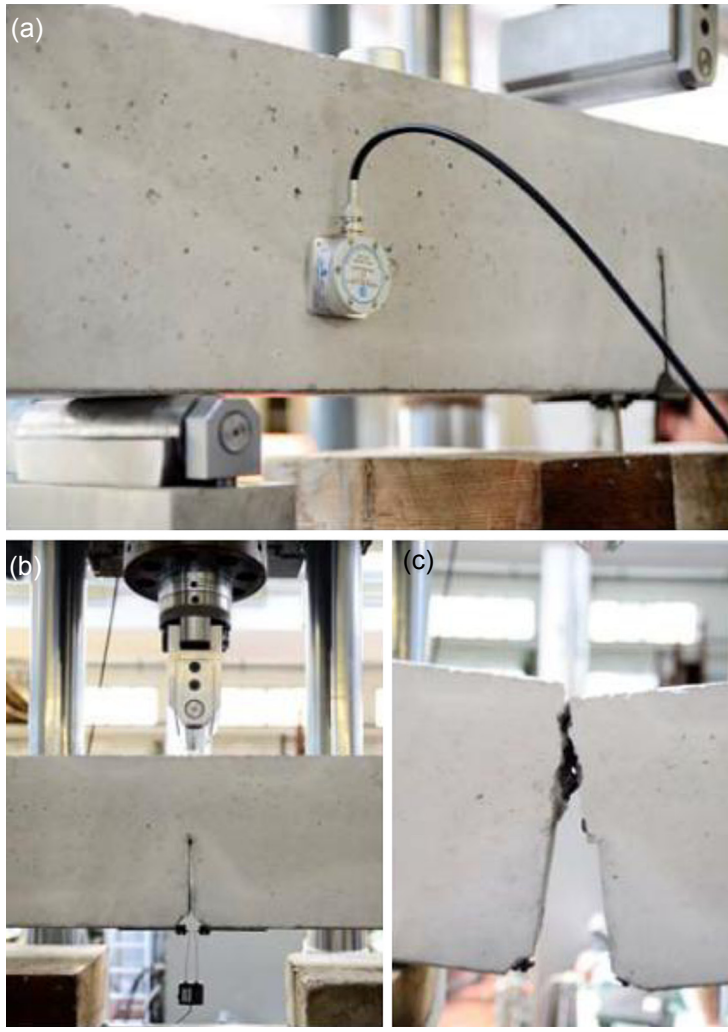

Figure 2.6 (a) New acoustic emission equipment applied to the monitored specimen. (b) Notched beam during the test. (c) Concrete beam after the final failure.

micro-cracks to macro-cracks with dimensions comparable with the ligament. The β_t is significant before the failure of the specimen, and in this stage between 0 and 60 s from the beginning of the test, a mean value greater than 1 is shown, which indicates that the process diverges and becomes unstable. The new automatic data acquisition system also computes in real time the AE amplitude and the frequency of the acquired signals.

The improved AIC is also employed to determine the onset times of AE events generated during a three-point bending tests of concrete beam monitored by seven AE piezoelectric transducers, working in a frequency range between 50 and 500 kHz and applied on the external surface of the element as shown in

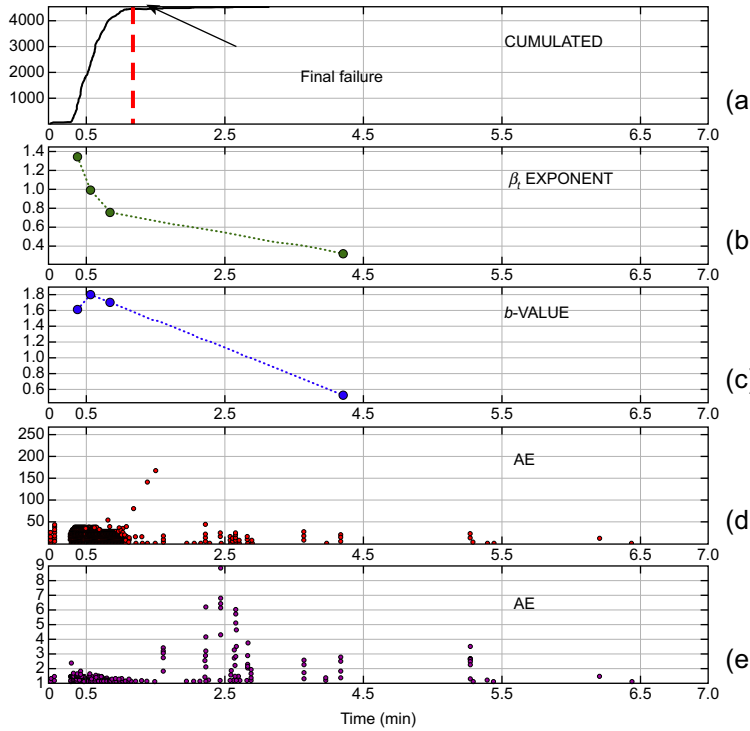

Figure 2.7 Real-time acoustic emission (AE) analysis: cumulated AE (a), β_t exponent (b), *b*-value (c), AE amplitude (d) and frequency (e) during time.

Figures 2.8(a) and 2.8(b). The onset times of the AE signals detected during the test are successively used in the localization procedure to determine the crack positions in the element. The monitored notched beam has been conducted up to failure controlling the crack mouth opening displacement (CMOD) with an opening velocity equal to 0.001 mm/s. The geometrical characteristic of the beam and the testing scheme are reported in Figure 2.8(a)−(c).

Concerning the AE monitoring, a total number of 26 AE points have been localized by means of the triangulation based on the improved AIC. A very good agreement is obtained between the localized points and the crack pattern configuration (see Figures 2.8(b) and (c)).

The AE source location algorithm, based on the improved AIC, can be included in a computer procedure for AE data analysis. This method can be very useful for a telematics working approach, using wireless transmission systems, where efficient algorithms for processing a very large amount of data are necessary.

The second application was conducted on two different types of beams. A scheme of a specimen is shown in Figure 2.9, where h is the height, l is the length and d is the depth. Their main geometrical characteristics are reported in Table 2.1.

A central notch of half the height of the beam was made, starting from the middle point at the lower side. The specimen was tested until the final failure was reached.

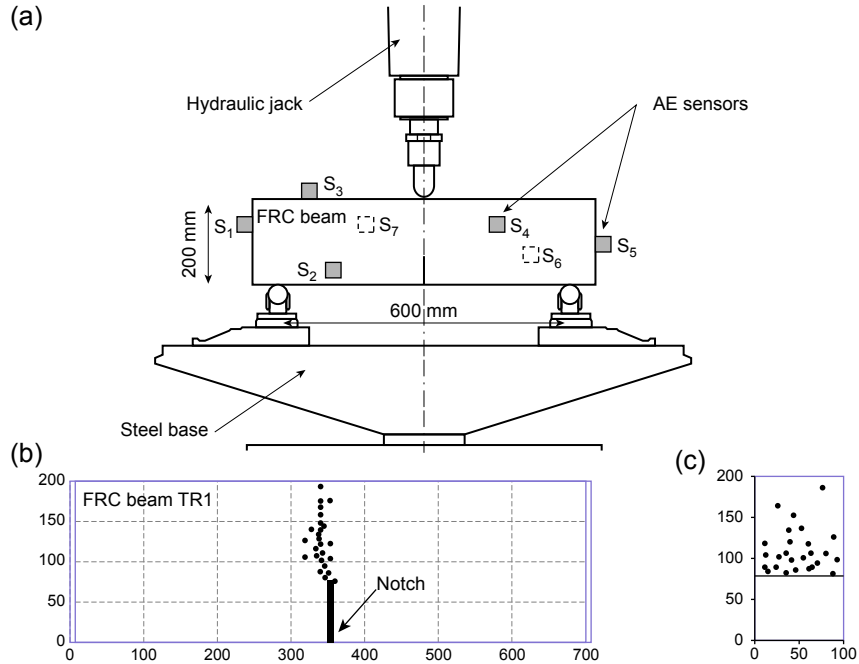

Figure 2.8 (a) Three-point bending test and acoustic emission (AE) sensor positions. (b), (c) AE localizations: During the tests, 26 AE sources were localized by the improved Akaike Information Criterion method.

The maximum aggregate size changed from 15 mm for the first beam to 45 mm for the third one. The water-to-cement ratio by mass (w/c) varied from 0.53 to 0.63; whereas, the compressive strength had an average value of 25 MPa.

The specimens were subjected to three-point bending according to RILEM Technical Committee TC-50 on Fracture Mechanics of Concrete: "Determination of the fracture energy of mortar and concrete by means of three-point bend tests on notched beams", Draft Recommendation, Materials And Structures, Vol. 18, 1985. The experimental test was conducted using a servo-controlled machine (MTS) with a

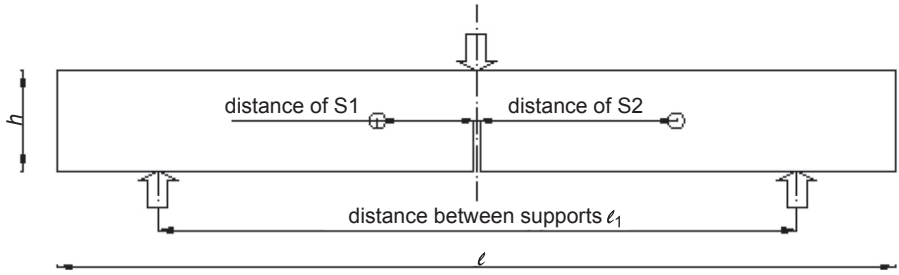

Figure 2.9 Schematic representation of the specimen tested in three-point bending.

Table 2.1 Main geometrical characteristics of beams

	Specimen 1	Specimen 2
Beam height h [mm]	840	1190
Beam length l [mm]	100	200
Beam depth d [mm]	100	100
Distance between supports l_1 [mm]	640	990
Distance of S1 from the notch [mm]	37.5	150
Distance of S2 from the notch [mm]	112.5	300

closed loop control. The monitored notched beam was conducted up to failure controlling the CMOD with an opening velocity equal to 0.002 mm/s.

For each beam, average values of the AE parameters recorded by the first sensor until the final failure have been compared to those of the second sensor. The load versus time diagram compared with the average values of AF and RA (for the two sensors) and cumulated AE events of the beam having dimensions 840 × 100 × 100 mm^3 (specimen 1) is reported in Figure 2.10. From a mechanical point of view, the overall behavior is characterized by a normal softening post−peak phase. During the test, an increase in the AE events was obtained approaching the peak load.

An important AE parameter used to characterize the cracking mode is the AF. It decreases for the duration of the trial (Figure 2.10) and also between the two receivers from 145 to 102 kHz (Figure 2.11(a)). Thus, a shift in frequencies from higher to lower values is observed.

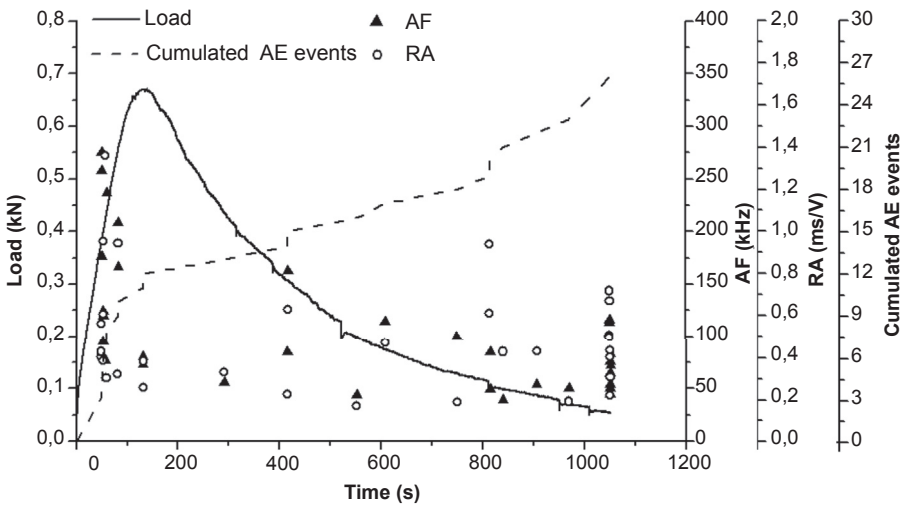

Figure 2.10 Specimen 1. Load versus time diagram compared with the average values of average frequency (AF), rise (RA) and cumulated acoustic emission (AE) events.

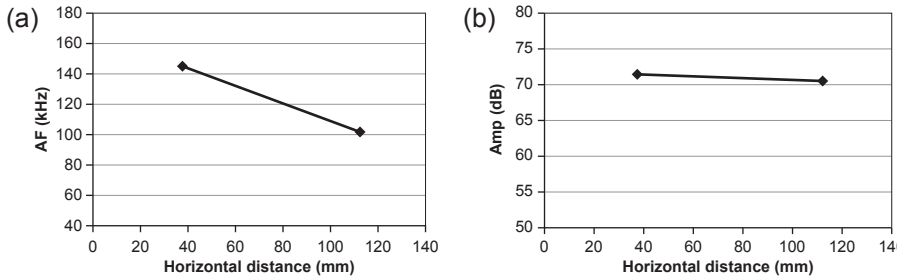

Figure 2.11 Specimen 1. (a) Average frequency (AF) values obtained by the two sensors. (b) Average amplitude values obtained by the two sensors.

Regarding the signal amplitude, a decrease of its average value between the two sensors is expected due to damping and scattering effects. The results obtained are reported in Figure 2.11(b). The average amplitude recorded by the nearest receiver is 71.3 dB; while there is a drop of about 1 dB for the second sensor.

The fracture mode criteria have been studied by means of the relationship between RA and AF values estimated for each sensor, as shown in Figure 2.12(a). Considering that a shift in frequencies from higher to lower values are observed for each sensor and taking into account that the average RA values are approximately constant, but rather low (less than 1 ms/V), a dominant presence of tensile cracks seems to lead the damage evolution up to the final collapse. As a matter of fact, for high-frequency waves, it is possible to propagate only through small inhomogeneities, whereas low-frequency waves can also propagate through large inhomogeneities (Carpinteri et al., 2013; Landis & Shah, 1995).

From the analysis of the energy content obtained from AE signals (Figure 2.12(b)), it is verified that the damage evolution carries more powerful signals after the peak load. During this test, the amount of released energy, calculated by the AE signals energy, is estimated as 329.08 ms $V \cdot 10^2$. The value for the total dissipated energy

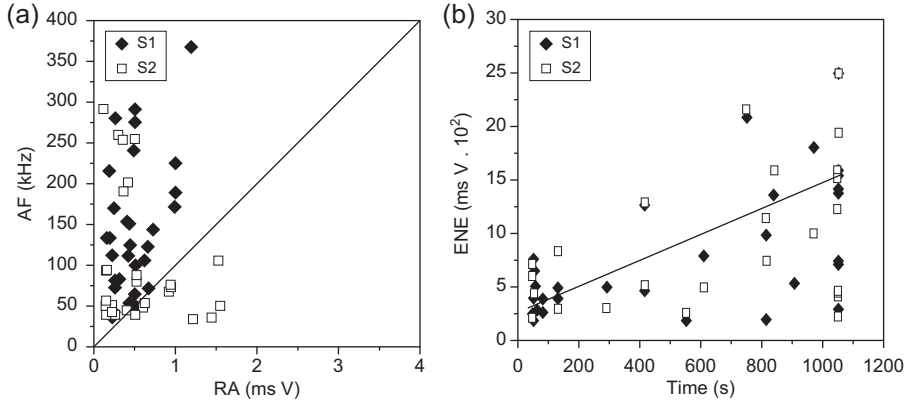

Figure 2.12 Specimen 1. (a) Fracture mode criteria by the relationship between rise angle (RA) and average frequency (AF) values for each sensor. (b) Acoustic emission signals energy versus time diagram.

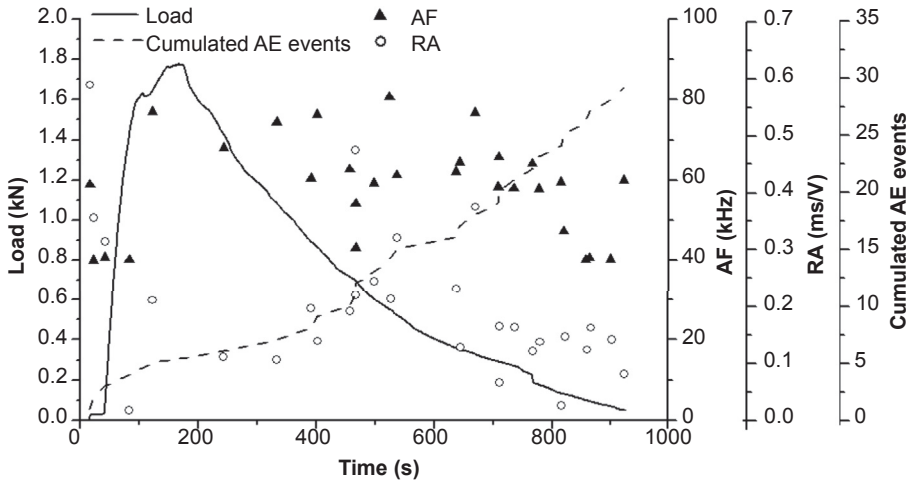

Figure 2.13 Specimen 2. Load versus time diagram compared with the average values of average frequency (A)F, rise angle (RA) and cumulated acoustic emission (AE) events.

is 0.15 J, which is computed as the area beneath the load vs. crack mouth opening displacement curve (RILEM 50-FMC Committee, 1986).

As regards the beam having dimensions 1190 × 200 × 100 mm^3 (specimen 2), the load versus time diagram compared with the average values of AF and RA (for the two sensors) and cumulated AE events is shown in Figure 2.13. The overall mechanical behavior has a similar trend compared to the previous case, even if there is an increase in the cumulative number of AE events at the end of the test.

The average values of AE frequencies decreases during the loading test (Figure 2.13) and also between the two sensors (Figures 2.14(a) and (b)) from 66 kHz to 51 kHz, as well as the average amplitude. Their values change from 58.7 dB for the first sensor to 55.2 dB for the second one, due to scattering and

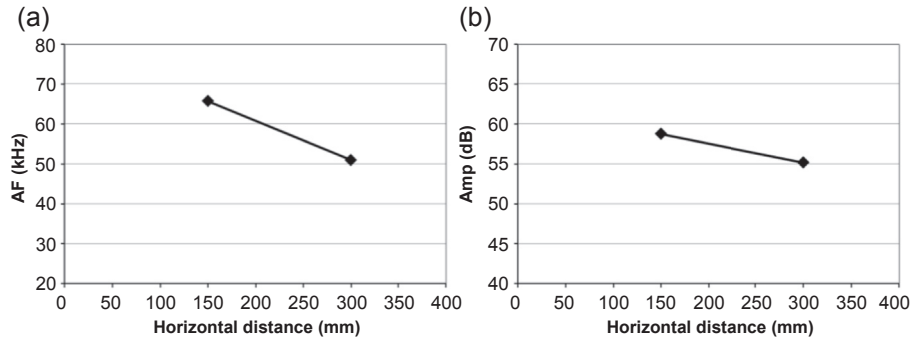

Figure 2.14 Specimen 2. (a) Average frequency values obtained by the two sensors. (b) Average amplitude values obtained by the two sensors.

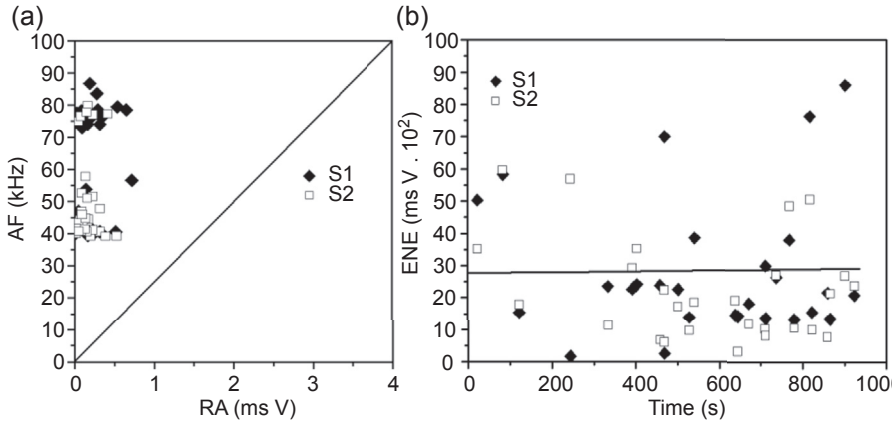

Figure 2.15 Specimen 2. (a) Fracture mode criteria by the relationship between rise angle (RA) and average frequency (AF) values for each sensor. (b) Acoustic emission (AE) signals energy versus time diagram.

dumping phenomena. Therefore, also in this case, a shift in frequencies and amplitude from higher to lower values had been observed. Considering the relationship between RA and AF values obtained from both sensors, it has been possible to study the type of crack. The RA values are approximately constant (Figure 2.15(a)) but less than 1 ms/V, thus the evolution of the damage from the initial notch was dominated by a Mode I crack.

The signal energy of the AE events detected during the loading is reported in Figure 2.15(b), separately for each sensor. It is evident that with respect to the previous trial, the released AE signals energy is almost constant for the whole duration of the test. The amount of the total released AE signals energy is estimated as 915 ms $V \cdot 10^2$; while the value for the total dissipated energy is 0.67 J.

As a third application, a compression example is used to verify that the fracture mode criteria by means of the relationship between RA and AF is appropriate. The results of the test are reported as follows.

The compression test was carried out by means of an MTS servo-hydraulic press, with a maximum capacity of 1000 kN, working by a digital-type electronic control unit (Figure 2.16). The force applied was determined by measuring the pressure in the loading cylinder by means of a transducer. The uncertainty in the determination of the force is 1%, which makes it a class 1 mechanical press. The specimen was arranged with the two smaller surfaces in contact with the press platens, without coupling materials in between, according to the testing modalities known as "test by means of rigid platens with friction". The platen was controlled by means of a wire-type potentiometric displacement transducer. The test was performed under displacement control, with the planned displacement velocity fixed at 0.001 mm/s.

Moreover, the loading process was also controlled by the circumferential strain, measured by means of a linked chain placed around the cylinder at mid-height. Such a control has permitted to completely detect the load−displacement curve,

Figure 2.16 Experimental setup of the compression test on the concrete specimen.

even in case of severe, unstable phenomena such as snap-back. More in details, the tests were controlled by the circumferential strain up to the maximum displacement for the extensometer (Carpinteri, Corrado, & Lacidogna, 2013).

In Figure 2.17, the load versus time diagram together with cumulated AE events, RA and AF values are reported. During the test, a shift from higher to lower frequencies involves both tensile cracks (low RA) and shear cracks (high RA), as shown in Figure 2.18.

Therefore, the final collapse of the specimen is reached for different types of fracture, showing in this way, the difference with the TPB tests.

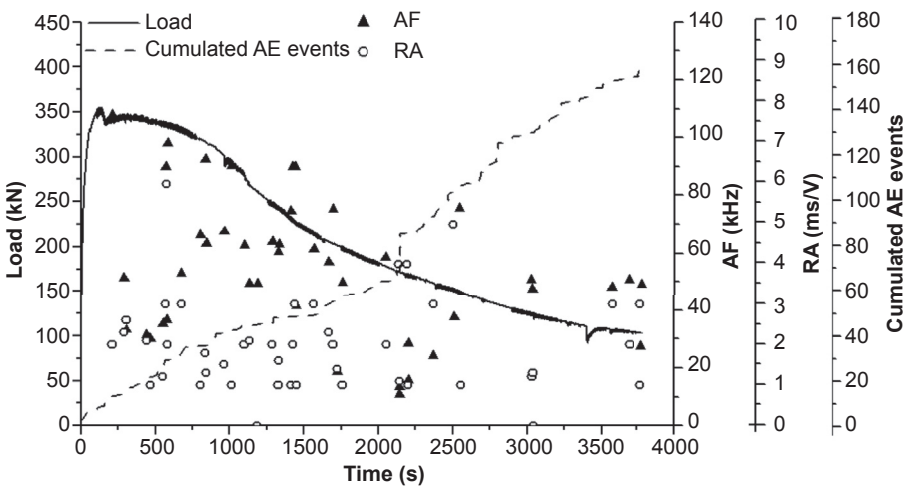

Figure 2.17 Load versus time diagram compared with average frequency (AF), rise angle (RA) values and cumulated acoustic emission (AE) events for a concrete specimen under compression.

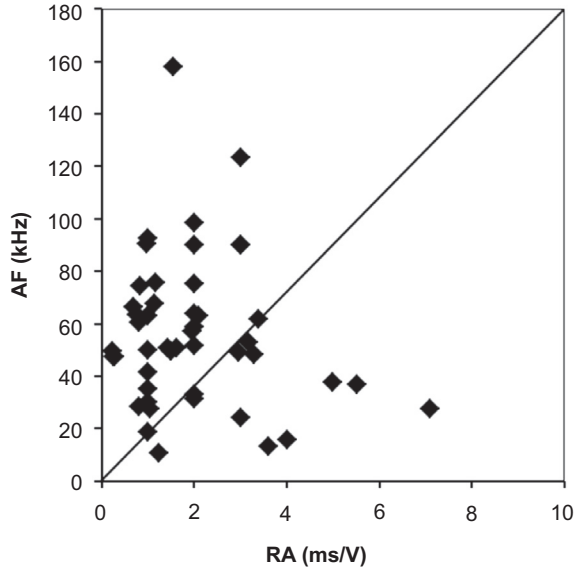

Figure 2.18 Fracture mode criteria with the relationship between rise angle (RA) and average frequency (AF) for a concrete specimen under compression.

2.8 Applications, observations and results: *in situ* monitoring

As an application of the AE technique for recognizing impending earthquakes, we obtain a correlation between seismic and acoustic events registered at the Historical Renaissance Complex of the Sacred Mountain of Varallo, Italy (Figures 2.19 and 2.20), through the application of the modified integral of Grassberger–Procaccia (Carpinteri, Lacidogna, Intermezzo, et al., 2013).

The AE monitoring was conducted on the frescoed masonry walls of the Chapel XVII of the Sacred Mountain of Varallo: the Chapel of the Transfiguration of Christ on Mount Tabor (Figure 2.20). The construction of the Chapel XVII began in 1572, but the structure was only completed in 1647 (Accornero et al., 2012). One of the

Figure 2.19 The Sacred Mountain of Varallo. The square of Tribunals.

Figure 2.20 The Sacred Mountain of Varallo. Chapel XVII: The Transfiguration of Christ on Mount Tabor.

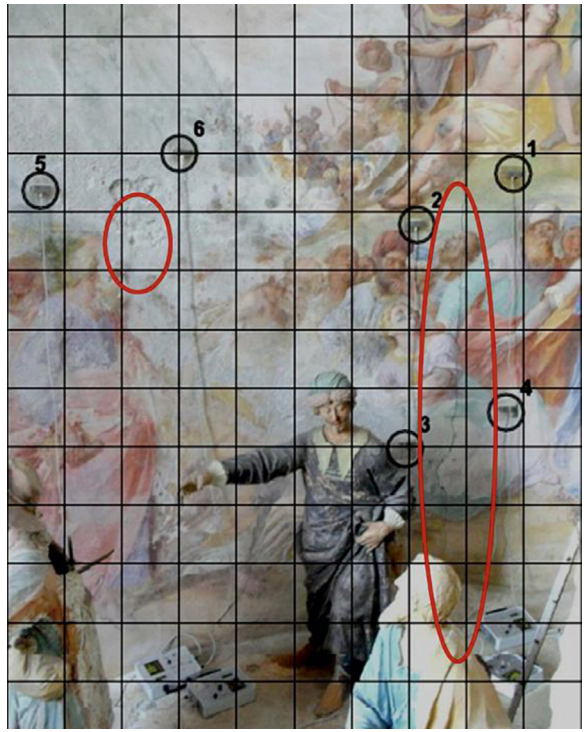

Figure 2.21 Chapel XVII. View of the monitored areas (Carpinteri, Lacidogna, & Pugno, 2007). Left side: sensors 5, 6, and the frescos detachment. Right side: Sensors 1−4 and the vertical crack.

purposes of monitoring by means of AE sensors applied to the frescoed wall was to detect the AE signals from regions of the wall in which the frescos show a plaster detachment and a vertical crack (Figure 2.21).

The data series of analyzed AE are shown in Figures 2.8 and 2.9, and are related to the following time intervals: the first time window started May 9, 2011, and finished June 16, 2011. The second time window started July 5, 2011, and finished September 5, 2011. Both time windows involved the monitoring of the vertical crack and the frescos detachment (Accornero et al., 2012; Carpinteri, Lacidogna, Intermezzo, et al., 2013). The seismic events are taken from the seismic catalog of INGV, National Institute of Geophysics and Volcanology Website (http://iside.rm.ingv.it/iside/standard/result.jsp?page=EVENTS#result), selecting the events comprised in a circle of 100 km radius around the site of Sacred Mountain of Varallo during the defined AE monitoring periods (Figure 2.22).

Looking at the temporal distribution of earthquakes in relation to the cumulative AE trend, a good correspondence between AE peaks and earthquake events can be observed (Figures 2.23 and 2.24).

By applying the modified correlation integral of Grassberger–Procaccia to the data series (Carpinteri, Lacidogna, Invernizzi, et al., 2013), we obtain the cumulative probabilities, as a function of the radius of interest r and of the interval of occurrence τ, both considering the peak of AE as earthquake precursor or as aftershock (Figure 2.25), after distinguishing between the environmental contributions due to crustal trembling (external source) and the structural damage contributions (inner source) to AE activity

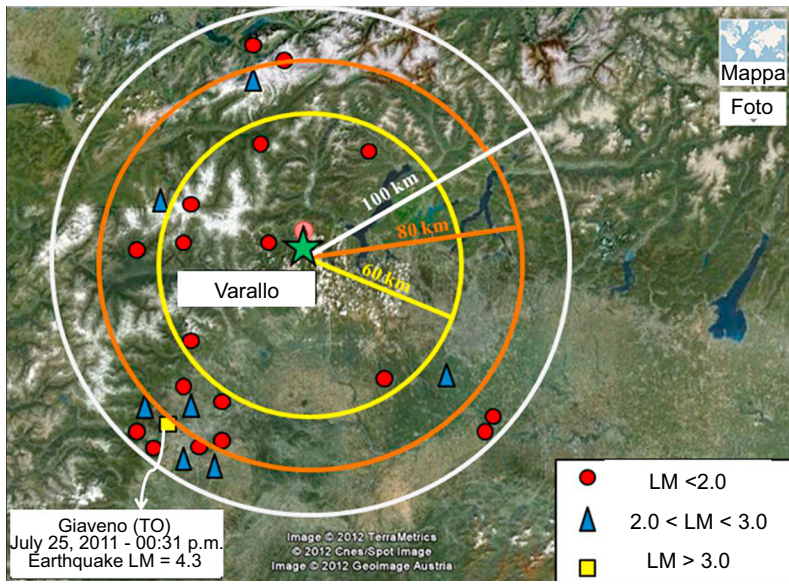

Figure 2.22 Seismic events around Varallo (Italy) from May, 2011 to September, 2011 (LM: local magnitude).

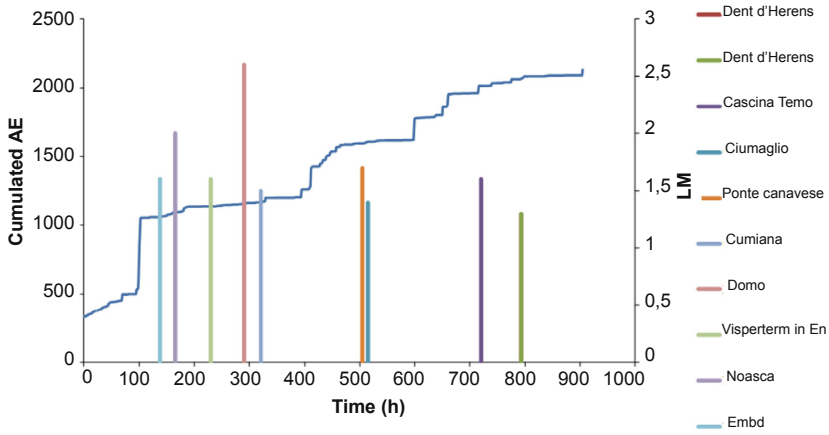

Figure 2.23 Sacred Mountain of Varallo: cumulated AE and seismic events from May 9, 2011 to June 16, 2011 (LM: local magnitude).

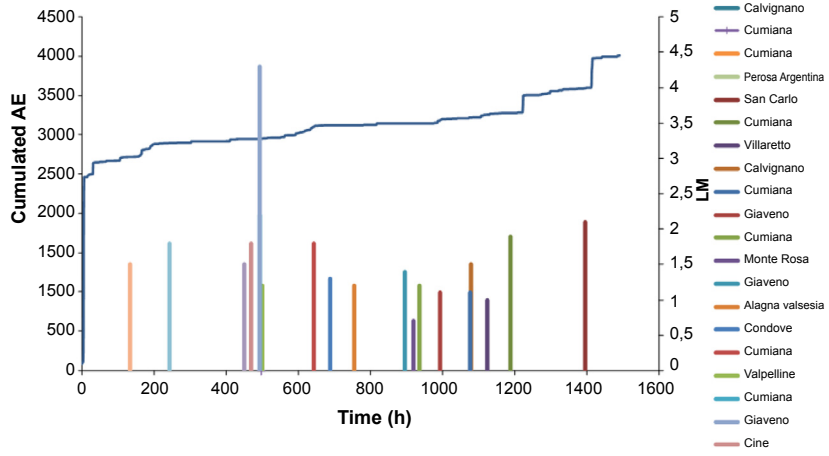

Figure 2.24 Sacred Mountain of Varallo: cumulated AE and seismic events from July 5, 2011, to September 5, 2011 (LM: local magnitude).

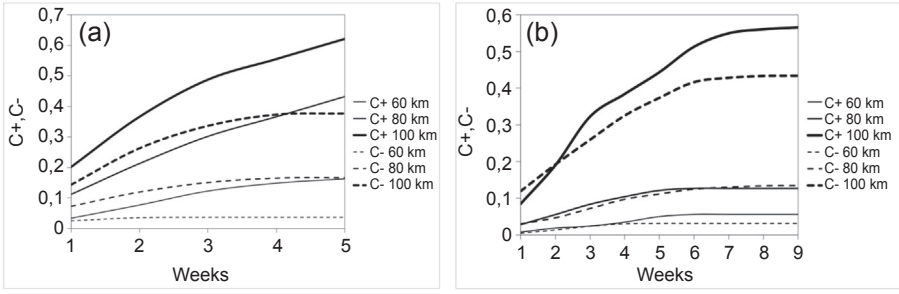

Figure 2.25 Evolution of the modified correlation integral for different time windows, during the two monitoring periods. (a) Monitoring time from May 9, 2011 to June 16, 2011. (b) Monitoring time from July 5, 2011 to September 5, 2011.

on the Chapel XVII. The probability values obtained for the monitoring periods show that, regardless of the distance and of the correlation time, the probability of a seismic event following a peak of acoustic emission (AE *Precursor*) is always greater than the probability of the same AE peak being an effect of the damage caused by the earthquake (*AE Aftershock*). In practice, we see that the monitored structure behaves as a sensitive seismic receptor.

2.9 Conclusions

The present chapter shows the capability of a new acoustic emission data processing system based on wireless AE data transmission. The new AE equipment can be employed to realize at the same time long-time monitoring of different civil structures, performing in real time the AE signal analysis. This system, cost efficient, easy to install and adaptive to different types of concrete structural and infrastructural networks, seems to be also very promising for seismic risk monitoring of civil structures and historical monuments. The AE cumulative number, the β_t exponent, and the b-value can be computed in order to evaluate the damage evolution of a concrete specimen subjected to different stress conditions. This analysis is the first parameter extrapolated from the AE data and represents damage indicators obtained in real time by the new AE equipment.

After the AE data acquisition, it is possible to perform the localization of the AE sources (micro-cracks). This analysis represents the second kind of data available by the AE monitoring. The location of damage, in point of fact, is particularly useful in damage evaluation of concrete and masonry structures. In particular, the onset of AE signals from fracture can be determined through the application of the AIC by using the onset time parameter.

Moreover, AE signals generally depend not only on their source, but also on the dimension and the mode of fracture. Therefore, key waveform features, like the amplitude, energy and frequency, can provide information on the damage mode and the fracture process. These conditions are synthesized by the RA and AF values.

Finally, the presented study suggests the use of AE measurements to enhance monitoring, especially applied to micro-seismicity with potential applications in earthquake forecasting.

2.10 Future trends

The AE data acquired from the sensor network with the presented monitoring system fine-tuned, will be sent electronically to a central server for real-time monitoring of the condition of the buildings, by means of correlation algorithms applied to data from the different measured variables. This remote monitoring system will be maintained after the conclusion of the restoration work, allowing for detection and real-time monitoring of possible structural deterioration processes of the buildings, thus constituting a useful

tool for prevention of structural collapses. This monitoring system, if properly extended, may use the buildings as points of a monitoring network on the territory, useful for reducing the seismic hazard and securing entire metropolitan areas by monitoring the seismic activity.

Acknowledgements

The authors are grateful to the firm LEANE NET Ltd for their partnership in the creation of the AE wireless monitoring system.

References

Accornero, F., Invernizzi, S., Lacidogna, G., & Carpinteri, A. (2012). Acoustic emission and damage analysis of decorated surface structural supports. In *Proceedings of the 19th European Conference on fracture - ECF19*. Kazan: Russia.

Aggelis, D. G. (2011). Classification of cracking mode in concrete by acoustic emission parameters. *Mechanics Research Communications, 38*, 153−157.

Aggelis, D. G., Mpalaskas, A. C., Ntalakas, D., & Matikas, T. E. (2012). Effect of wave distortion on acoustic emission characterization of cementitious materials. *Construction and Building Materials, 35*, 183−190.

Akaike, H. (1974). A new look at the statistical model identification. *IEEE Transactions on Automatic Control, 19*, 716−723.

Aldahdooh, M. A. A., & Muhamad Bunnori, N. (2013). Crack classification in reinforced concrete beams with varying thicknesses by means of acoustic emission signal features. *Construction and Building Materials, 45*, 282−288.

Anzani, A., Binda, L., Carpinteri, A., Lacidogna, G., & Manuello, A. (2008). Evaluation of the repair on multiple leaf stone masonry by acoustic emission. *Materials and Structures, 41*, 1169−1189.

Brindley, B. J., Holt, J., & Palmer, I. G. (1973). Acoustic emission − 3: the use of ring-down counting. *Non-Destructive Test, 6*, 299−306.

Carpinteri, A., Corrado, M., & Lacidogna, G. (2013). Heterogeneous materials in compression: correlations between absorbed, released and acoustic emission energies. *Engineering Failure Analysis, 33*, 236−250.

Carpinteri, A., & Lacidogna, G. (2006a). Damage monitoring of an historical building by the acoustic emission technique. *Materials and Structures, 39*, 164−167.

Carpinteri, A., & Lacidogna, G. (2006b). Structural monitoring and integrity assessment of medieval towers. *Journal of Structural Engineering (ASCE), 132*(2006), 1681−1690.

Carpinteri, A., & Lacidogna, G. (2007). Damage evaluation of three masonry towers by acoustic emission. *Engineering Structures, 29*, 1569−1579.

Carpinteri, A., Lacidogna, G., Accornero, F., Mpalaskas, A., Matikas, T., & Aggelis, D. (2013). Influence of damage in the acoustic emission parameters. *Cement and Concrete Composites, 44*, 9−16.

Carpinteri, A., Lacidogna, G., Invernizzi, S., & Accornero, F. (2013). The Sacred Mountain of Varallo in Italy: seismic risk assessment by acoustic emission and structural numerical models. *The Scientific World Journal*. Article ID 170291, 10, http://dx.doi.org/10.1155/2013/170291.

Carpinteri, A., Lacidogna, G., & Manuello, A. (2011). Stability of the ancient Athena temple in Syracuse investigated by the *b*-value analysis. *Strain, 47*, 243−253.

Carpinteri, A., Lacidogna, G., Manuello, A., & Niccolini, G. (2013). Acoustic emission wireless transmission system for structural and infrastructural networks. In *Proceedings of the 8th international conference on fracture mechanics of concrete and concrete structures − FraMCoS8*. Toledo: Spain.

Carpinteri, A., Lacidogna, G., & Niccolini, G. (2006). Critical behaviour in concrete structures and damage localization by acoustic emission. *Key Engineering Materials, 312*, 305−310.

Carpinteri, A., Lacidogna, G., & Niccolini, G. (2007). Acoustic emission monitoring of medieval towers considered as sensitive earthquake receptors. *Natural Hazards and Earth System Sciences, 7*, 251−261.

Carpinteri, A., Lacidogna, G., & Pugno, N. (2007). Structural damage diagnosis and lifetime assessment by acoustic emission monitoring. *Engineering Fracture Mechanics, 74*, 273−289.

Carpinteri, A., Xu, J., Lacidogna, G., & Manuello, A. (2012). Reliable onset time determination and source location of acoustic emission in concrete structures. *Cement and Concrete Composites, 34*, 529−537.

Earle, P., & Shearer, P. M. (1994). Characterization of global seismograms using an automatic-picking algorithm. *Bulletin in the Seismological Society of America, 84*, 366−376.

Grassberger, P., & Procaccia, I. (1983). Characterization of strange attractors. *Physical Review Letters, 50*, 346−349.

Grosse, C. U., Reinhardt, H. W., & Finck, F. (2003). Signal based acoustic emission techniques in civil engineering. *ASCE Journal of Materials in Civil Engineering, 15*, 274−279.

Hafez, A. G., Khan, T. A., & Kohda, T. (2010). Clear P-wave arrival of weak events and automatic onset determination using wavelet filter banks. *Digital Signal Processing, 20*, 715−732.

Han, Q., Carpinteri, A., Lacidogna, G., Xu, J. Fractal analysis and Yule statistics for seismic prediction based on 2009 L'Aquila earthquake in Italy. *Arabian Journal of Geosciences*. doi: http://dx.doi.org/10.1007/s12517-014-1386-y.

Kurz, J., Grosse, C., & Reinhardt, H. (2005). Strategies for reliable automatic onset time picking of acoustic emissions and of ultrasound signals in concrete. *Ultrasonics, 43*, 538−546.

Lacidogna, G., Manuello, A., Niccolini, G., & Carpinteri, A. (2012). "Acoustic emission monitoring of Italian historical buildings and the case study of the Athena temple in Syracuse". *Architectural Science Review*. doi: http://dx.doi.org/10.1080/00038628.2012.720246.

Landis, E. N., & Shah, S. P. (1995). Frequency-dependent stress wave attenuation in cement-based materials. *Journal of Engineering Mechanics, 121*, 737−743.

Maeda, N. (1985). A method for reading and checking phase times in auto-processing system of seismic wave data. *Zisin, 38*, 365−379.

Niccolini, G., Xu, J., Manuello, A., Lacidogna, G., & Carpinteri, A. (2012). Onset time determination of acoustic and electromagnetic emission during rock fracture. *Progress in Electromagnetics Research Letters, 35*, 51−62.

Ohno, K., & Ohtsu, M. (2010). Crack classification in concrete based on acoustic emission. *Construction and Building Materials, 24*, 2339−2346.

Ohtsu, M. (1996). The history and development of acoustic emission in concrete engineering. *Magazine of Concrete Research, 48*, 321−330.

Ohtsu, M. (2010). Recommendation of RILEM TC 212-ACD: acoustic emission and related NDE techniques for crack detection and damage evaluation in concrete: test method for classification of active cracks in concrete structures by acoustic emission. *Materials and Structures, 43*(9), 1177−1181.

Pollock, A. A. (1973). Acoustic emission-2: acoustic emission amplitudes. *Non-Destructive Test, 6*, 264−269.

RILEM 50-FMC Committee. (1986). Determination of the fracture energy of mortar and concrete by means of three-point bend tests on notched beams. *Materials and Structures, 18*, 286−290.

RILEM Technical Committee TC212- ACD. (2010a). Acoustic emission and related NDE techniques for crack detection and damage evaluation in concrete: measurement method for acoustic emission signals in concrete. *Materials and Structures, 43*, 1177−1181.

RILEM Technical Committee TC212- ACD. (2010b). Acoustic emission and related NDE techniques for crack detection and damage evaluation in concrete: test method for damage qualification of reinforced concrete beams by acoustic emission. *Materials and Structures, 43*, 1183−1186.

RILEM Technical Committee TC212- ACD. (2010c). Acoustic emission and related NDE techniques for crack detection and damage evaluation in concrete: test method for classification of active cracks in concrete by acoustic emission. *Materials and Structures, 43*, 1187−1189.

RILEM Technical Committee TC212- ACD. (2010d). Acoustic emission and related non-destructive evaluation techniques for crack detection and damage evaluation in concrete. *Final Report of RILEM Tech Committee 212 ACD*. M. Ohtsu (Ed.), RILEM Publications SARL, 1−12.

Shah, S. P., & Li, Z. (1994). Localization of microcracking in concrete under uniaxial tension. *ACI Materials Journal, 91*, 372−381.

Shiotani, T., Fujii, K., Aoki, T., & Amou, K. (1994). Evaluation of progressive failure using AE sources and improved *b*-value on slope model tests. *Progress in Acoustic Emission, 7*, 529−534.

Sleeman, R., & Eck, T. (1999). Robust automatic P-phase picking: an on-line implementation in the analysis of broadband seismogram recordings. *Physics of the Earth and Planetary Interiors, 113*, 265−275.

Soulioti, D., Barkoula, N. M., Paipetis, A., Matikas, T. E., Shiotani, T., & Aggelis, D. G. (2009). Acoustic emission behavior of steel fibre reinforced concrete under bending. *Construction and Building Materials, 23*, 3532−3536.

Tong, C., & Kennett, B. L. N. (1996). Automatic seismic event recognition and later phase identification for broadband seismograms. *Bulletin of the Seismological Society of America, 86*, 1896−1909.

Watanabe, T., Hosomi, M., Yuno, K., & Hashimoto, C. (2010). Quality evaluation of concrete by acoustic emission. *Construction and Building Materials, 24*, 2358−2362.

Yokota, T., Zhou, S., Mizoue, M., & Nakamura, I. (1981). An automatic measurement of arrival time of seismic waves and its application to an on-line processing system. *Bulletin of the Earthquake Research Institute, 55*, 449−484.

Yoon, D.-J., Lee, S., Kim, C. Y., & Seo, D. C. (2007). Acoustic emission diagnosis system and wireless monitoring for damage assessment of concrete structures. In *Proceedings of NDT for Safety*. Prague: Czech Republic.

Zhang, H., Thurber, C., & Rowe, C. (2003). Automatic p-wave arrival detection and picking with multiscale wavelet analysis for single-component recordings. *Bulletin of the Seismological Society of America, 93*, 1904−1912.

Identification of the fracture process zone in concrete materials by acoustic emission

3

K. Ohno
Tokyo Metropolitan University, Hachioji-shi, Tokyo, Japan

3.1 Introduction

Crack propagation in concrete is known to be very complex, as is fully understanding its behavior and mechanisms. Crack distribution expands widely due to the existence of aggregate in concrete compared with other brittle materials such as glass. When a crack propagates in concrete, an evolutional area of micro-cracks is developed and observed ahead of the crack tip. The area is well known as the fracture process zone (FPZ), as the existence of FPZ causes the size effect in concrete.

It is reported that the linear elastic fracture mechanics (LEFM) can be applied only when the FPZ is small compared with the relevant dimensions of the specimen. Since the FPZ results in inelastic behaviors and is not small enough to be ignored, it is usually difficult to apply LEFM to concrete. Still, it is important to predict crack propagation in reinforced concrete structures because cracks impair their durability and period of service life. Therefore, much research in concrete engineering has been done to explain the size effect and to predict or accurately estimate the ultimate load-bearing capacity of concrete structures (Bazant, 1984; Bazant & Pfeiffer, 1987; Shah, 1990; Hu & Wittmann, 2000; Hu, 2002).

Currently, in the fracture mechanics of concrete, the fracture energy is a key issue for the size effect and prediction of crack propagation. The fracture energy is defined as the required amount of energy to nucleate a crack by a unit length. The fracture energy in concrete is normally determined by a three-point bending on a notched concrete beam as defined by RILEM (RILEM TC-50 FMC, 1985). It is well known that the fracture energy varies with the specimen size and geometry even if the proportion and materials of concrete are the same. In addition, development and size of the FPZ play an important role in estimating the fracture energy in concrete. In this chapter, the application of acoustic emission (AE) technique to characterization of the FPZ is presented as an experimental technique and is discussed.

3.2 Characterization of the fracture process zone (FPZ)

A structural design is generally based on strength theories. It is assumed that failure occurs when applied stress reaches the material strength. Hence, the compressive

Acoustic Emission (AE) and Related Non-destructive Evaluation (NDE) Techniques in the Fracture Mechanics of Concrete
http://dx.doi.org/10.1016/B978-1-78242-327-0.00003-9
Copyright © 2015 Elsevier Ltd. All rights reserved.

strength is normally used for design and numerical analysis, in order to determine various capacities of concrete structures. Since a test for the compressive strength can be handled easily and variations of test results are reasonably low compared with such tests as for the tensile and the flexural strength, the compressive strength is widely applied to evaluate the mechanical properties of concrete. On the micro- or meso-level of fracture in concrete, it is found that cracks are first opened under tensile force, and then coalesce to fracture. Thus, key issues for concrete fractures are the strength of crack initiation under tension and the resistance for crack progress. The size effect, well known in the fracture mechanics of concrete, results from the fact that the strength decreases with the increase in the size of concrete members under tension. In this regard, nucleation of the FPZ plays an important role.

Characteristics of the FPZ are important in the development of modern nonlinear fracture mechanics for concrete. In order to understand fracture mechanisms and to model the tensile-softening relationship of the FPZ under uniaxial tension, Hillerborg has proposed a fictitious crack model or cohesive crack model as the fracture energy is assumed to be consumed in a small zone (Hillerborg, 1985, 1991). The relation between tensile stress and opening displacement in the FPZ is illustrated in Figure 3.1. The fictitious crack is modeled as the relationship between the damage zone (FPZ) and tensile stress in concrete under tension, as shown in Figure 3.2 (Gustafsson & Hillerborg, 1988). Before reaching the peak stress, the elongation, Δl, of a specimen in uniform tension is assumed to be uniform along the length of the specimen.

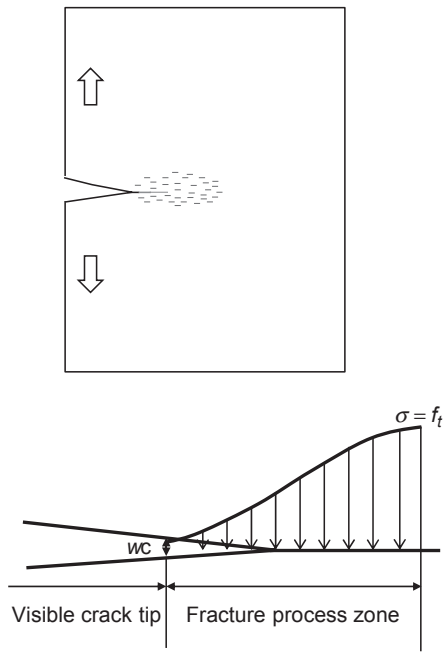

Figure 3.1 The fictitious crack model of fracture process zone.

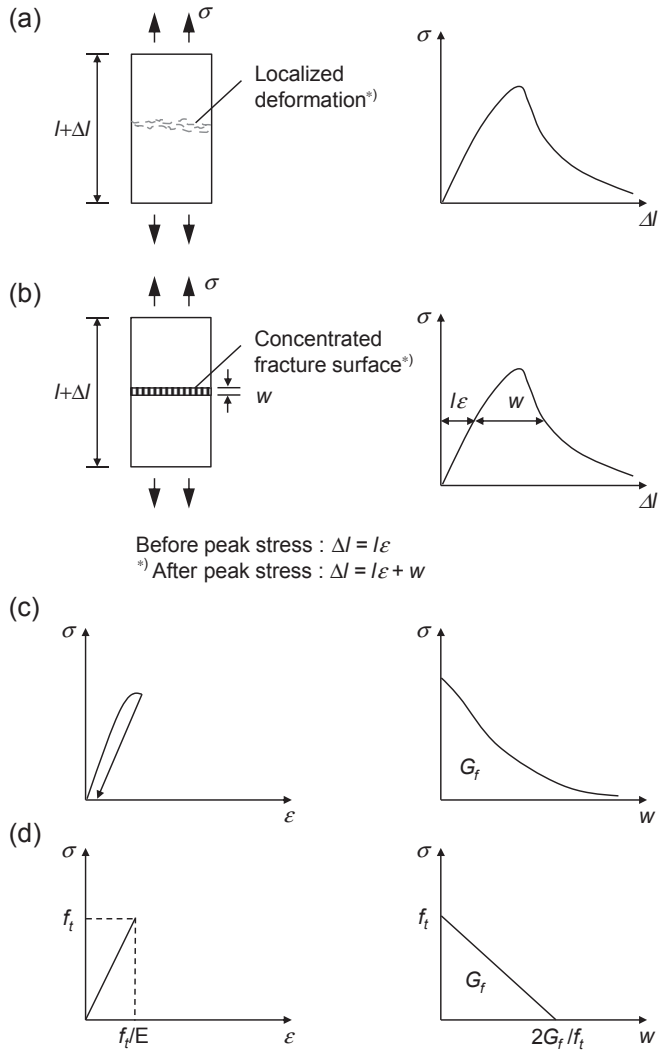

Figure 3.2 Fictitious crack model description of tensile fracture: (a) realistic structure behavior; (b) model of structural behavior; (c) model for description of properties of material; and (d) simplified properties of material.
Hillerborg (1991). Application of the fictitious crack model to different types of materials. *International Journal of Fracture*, *51*(2), 95−102.

A fracture zone starts to be developed just after the applied tensile load reaches the maximum. After the fracture zone has started to develop, the stress decreases, and the outside area of the fracture zone becomes the unloading state, while the inside area indicates strain-softening. Two relationships are described to express the mechanical behavior of concrete in tension: (1) a stress−strain ($\sigma-\varepsilon$) relationship for the outside area of the fracture zone, and (2) a stress−elongation ($\sigma-w$) relationship for

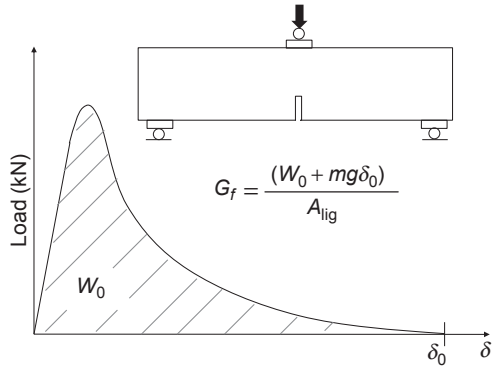

Figure 3.3 Determination method of fracture energy by RILEM recommendation.

the fracture zone. Here, fracture energy G_f is defined by the area under the stress−elongation curve as represented by the following equation:

$$G_f = \int_0^\infty \sigma(w)\mathrm{d}w \tag{3.1}$$

At present, the fracture energy is determined experimentally. According to the RILEM recommendation (RILEM TC-50 FMC, 1985), the fracture energy is determined by a notched concrete beam under three-point bending as shown in Figure 3.3. It has been reported, so far, that the fracture energy obtained varies with the specimen size, the geometry, the type of aggregate, and the aggregate size in concrete. Mihashi (Mihashi & Nomura, 1996, Mihashi, Kirikoshi, Nomura, Ohtsuka, & Kaneko, 1998) and Ohtsuka (Ohtsuka & Date, 2000) experimentally showed that development of the FPZ varies with the aggregate size and the specimen size in concrete. Figure 3.4 illustrates the results of the X-ray observation of the FPZ in concrete with different aggregate sizes ($d_{max} = 5, 10, 15, 20$ mm) (Ohtsuka & Date, 2000). It is clearly found that the width of FPZ increases with the increase in the aggregate size. The fracture energy also increases as the aggregate size in concrete becomes larger. Therefore, the FPZ is directly related to the fracture energy. The size of the FPZ could vary with microstructure, aggregate size, rate of loading, shape of specimen, and so forth.

3.3 The process of crack growth and fracture

Figure 3.5 shows the stress−deformation relationship in concrete under tensile force. At low stress level (from O to point A in Figure 3.5), stress and deformation represent a linear relationship. After the stress level exceeds point A, the relationship between stress

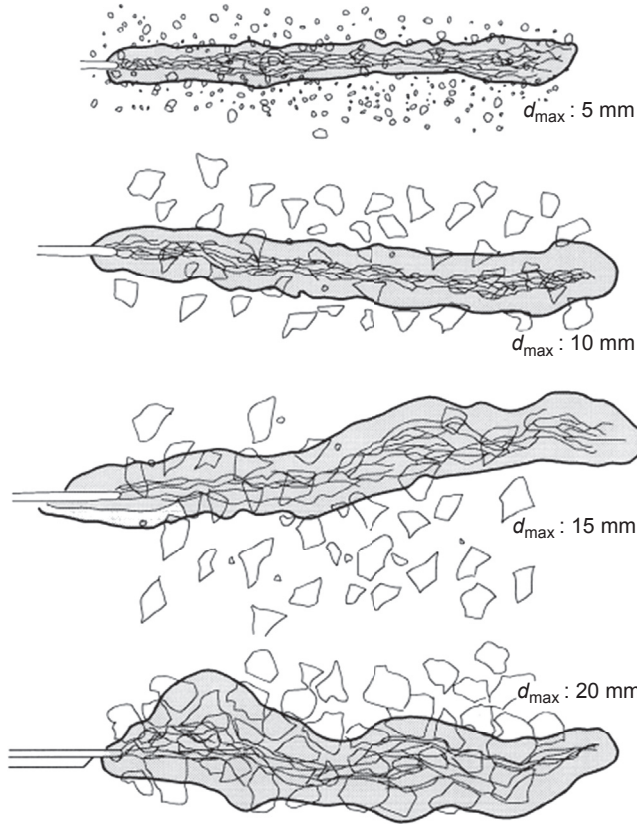

Figure 3.4 Results of X-ray observation in the fracture process zone.
Ohtsuka, K., & Date, H. (2000). Fracture process zone in concrete tension specimen. *Engineering Fracture Mechanics*, *65*, 111−131.

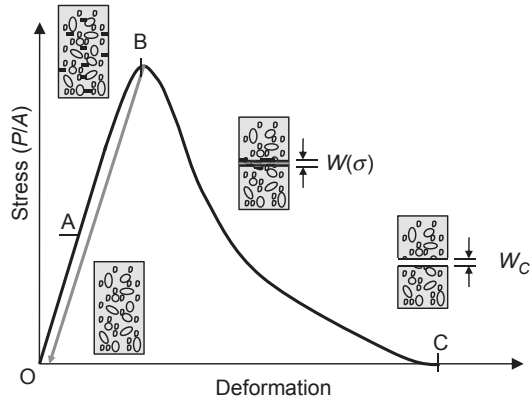

Figure 3.5 Relationship between stress and deformation in tension.

and deformation shows a nonlinear relationship. This phenomenon is explained as follows:

1. Micro-cracks occur at small defects or voids that exist in cement paste and between cement paste and aggregate particles, and then the propagation of cracks could be prevented by the aggregate.
2. If the specimen is unloaded when the stress reaches the maximum (point B), micro-cracks cannot be observed. In this stage, it is thought that damage of concrete is low at the macroscopic level.
3. When the stress exceeds the tensile strength (from point B to point C in Figure 3.5), micro-cracks concentrate at limited areas (around the fracture plane), and the FPZ is nucleated. In this stage, tension-softening behavior is observed in the FPZ.
4. Because concrete is assumed to consist of two phases of cement paste and aggregate at the meso-level, the resistance for crack propagation in cement paste phase is different from that of aggregate phase. As a result, a crack cannot propagate at once, and crack growth and stopping are repeated in concrete. When crack growth is arrested, micro-cracks could generate in other weak parts. These micro-cracks coalesce with each other, and eventually a concrete member fails at a certain area.

3.4 Experimental investigation of the FPZ by acoustic emission (AE) source location

The FPZ can be developed as an accumulation of micro-cracks that occur in front of the crack tip. It is important to determine the size of the FPZ because the fracture energy directly relates to its size. In order to identify the size of the FPZ in concrete, techniques have been employed such as X-ray (Mihashi & Nomura, 1996; Mihashi et al., 1998; Ohtsuka & Date, 2000) and scanning electron microscopy (Diamond & Mindess, 1982). These techniques have limitations in that the observation must be conducted after the loading and/or it takes a lot of time to obtain the result.

AE technique is a powerful technique because the fracture process in concrete can be estimated in real time by three-dimensional locations of AE sources. The AE phenomenon is associated with the release of strain energy resulting from nucleation of a micro-crack. Locations of AE sources can be determined from arrival-time differences, sensor locations, and *P*-wave velocity in concrete. Several techniques for determination of arrival time of the AE signal have been proposed. Shah et al. developed a way to determine the onset time of AE by applying differences between the standard deviation of noise and the AE signal (Maji & Shah, 1988; Li & Shah, 1994). An automated method was also developed by employing the Akaike Information Criteria (AIC) (Ohno, Shimozono, Sawada, & Ohtsu, 2008). In this method, the onset time is determined when the AIC value becomes the global minimum. The AIC value at point $i = k$ is calculated by the following equation:

$$\mathrm{AIC}_k = k \cdot \log\{\mathrm{var}(X[1,k])\} + (N-k) \cdot \log\{\mathrm{var}(X[k,N])\} \tag{3.2}$$

where N is the number of amplitudes of a digitized AE wave, X_i is an amplitude of a signal ($i = 1,2,\ldots,N$), var(X[1,k]) indicates the variance between X_1 and X_k, and var(X[k,N]) is also the variance between X_k and X_N.

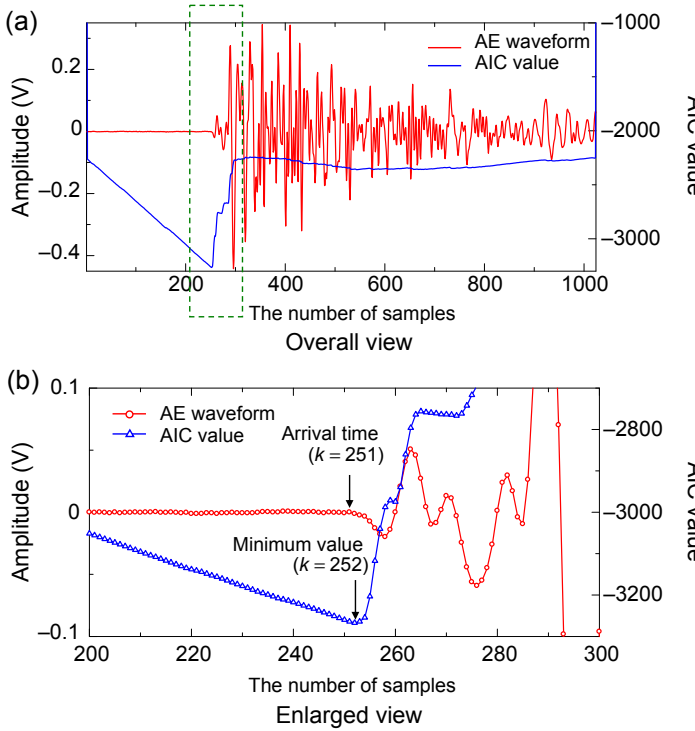

Figure 3.6 Calculated Akaike information criteria (AIC) function for a detected acoustic emission (AE) waveform. (a) Overall view of detected AE signal and AIC value, (b) enlarged view of detected AE signal and AIC value.

Figure 3.6 shows an example in which Eqn (3.2) is applied to a detected AE wave. The arrival time at $k = 251$ is determined manually; the minimum value of AIC indicates at $k = 252$ after the onset point ($k = 251$). Therefore, the arrival time is determined by applying the following equation:

$$T = T_k\{\mathrm{Min}(\mathrm{AIC}_k)\} - \Delta t \tag{3.3}$$

where $T_k\{\mathrm{Min}(\mathrm{AIC}_k)\}$ represents the sampling time number when AIC_k becomes the minimum value at $i = k$, and Δt is the sampling time.

3.5 Measurement and results of SiGMA analysis

The FPZ is mainly developed under tensile stress. Consequently, a direct tension test, a compact-tension test, and a three-point bending test have been conducted to investigate the FPZ, and the fracture energy in concrete has been estimated. Each test method has some advantages and disadvantages. Presently, the three-point bending test of a notched

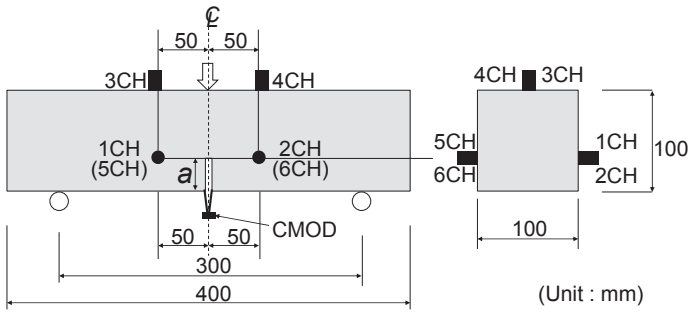

Figure 3.7 Geometry of specimen and position of transducers.

concrete beam is widely used because its test method is proposed as the RILEM recommendation as mentioned in Section 3.2.

Ohno, Uji, Ueno, and Ohtsu (2014) conducted three-point bending tests in accordance with the code of Japan Concrete Institute (2003) to investigate the development of the FPZ. Beam specimens with varying notch depths and the maximum sizes of aggregate were tested. Figure 3.7 shows the schematic setup of the experiment. The maximum aggregate sizes (d_{max}) in concrete were 5, 10, and 20 mm. The specimens with dimensions of length 400 mm, width 100 mm, and height 100 mm were tested with the notch depths *a,* as shown in Figure 3.7. The notch depths (a) are 30, 50, 70, and 80 mm. AE signals were detected by six AE sensors of 150 kHz resonance. AE signals were amplified with 40 dB gain by a preamplifier, and then they were recorded using the AE measurement system (μSAMOS, PAC). AE waveform was recorded at 1-MHz sampling frequency. The threshold level was 35 dB. Detected AE waveforms were applied to SiGMA (simplified Green's functions for moment tensor analysis) procedure (Ohtsu, 1991) to identify the kinematics of AE sources.

Results of the SiGMA analysis of $a/W = 0.3$ and 0.8 are shown in Figure 3.8. It is clearly found that the width of an AE cluster increases with the increase in the maximum size of aggregate and decrease with the values in a/W. In these figures, the numbers of AE sources are too many to understand the predominant crack type. Therefore, the numbers of each crack mode in the two notch depths are summarized in Figure 3.9. The number of AE sources is not constant, depending on the ligament length. In the case $a/W = 0.3$ for all the maximum sizes of aggregate, dominant motions of micro-crack are of the shear crack type, while a lot of tensile cracks are identified in the case $a/W = 0.8$, regardless of the maximum size of aggregate. These results suggest that the opening crack (mode I) occurs in the large a/W specimens, whereas not only mode I but also shear cracks (modes II and III) might take place in the small a/W specimens in the three-point bending. Landis and Shah (1993) have also applied the moment tensor analysis to investigate characteristics of AE sources in mortar beams, which consist of 2-mm grains under four-point bending. In their experiment, dominant motions of AE sources were mode II (shear) and mixed mode. Thus, it is suggested that mixed mode and mode II could be the exclusive fracture modes at the interfacial zone between the cement paste and aggregate, as illustrated in Figure 3.10. In addition, initial damage is characterized by tensile fracture between cement particles and the

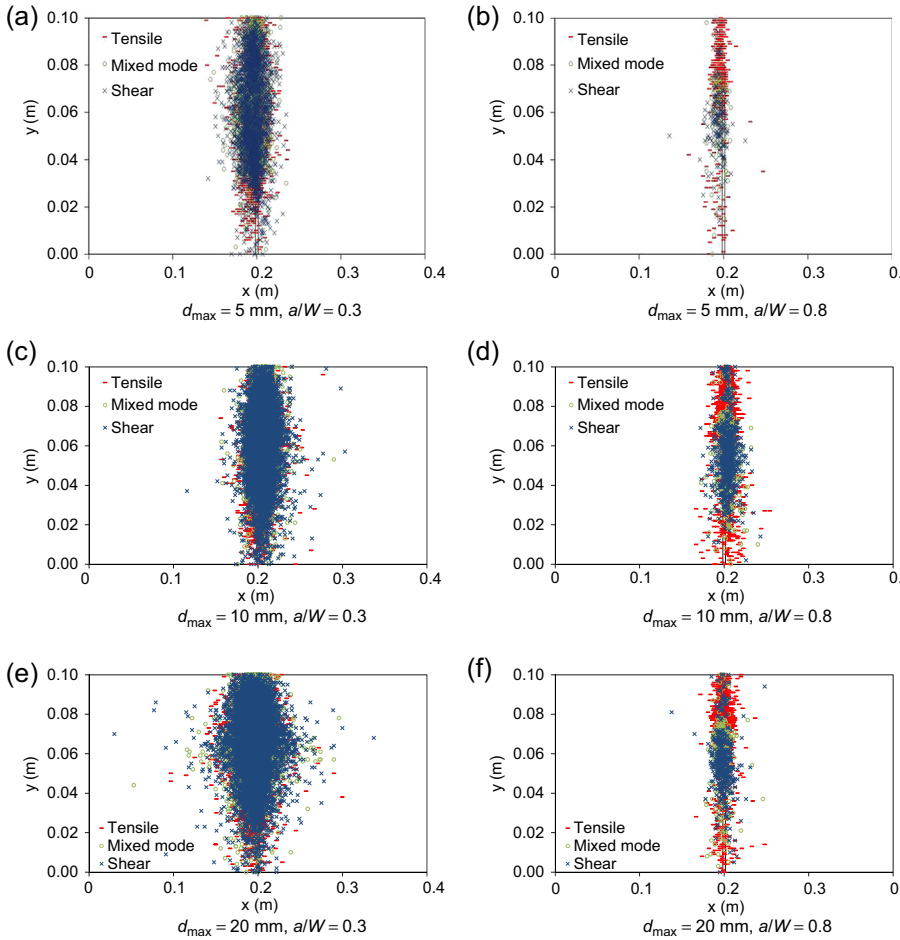

Figure 3.8 (a–f) Results of the SiGMA analysis in a notched concrete beam. Ohno, K., Uji, K., Ueno, A., and Ohtsu, M. (2014). Fracture process zone in notched concrete beam under three-point bending by acoustic emission. *Construction and Building Materials*, 139–145.

cement–aggregate interface. Then, steady-state damage growth could be characterized by friction along the crack surfaces. These findings suggest that the frictional area between crack surfaces becomes small in the case of large a/W. As a result, tensile cracks, which are associated with fracture of cement paste, become relatively dominant. However, in the case of small a/W, the friction area between macroscopic crack surfaces becomes large. This implies that mixed mode and shear mode could be the exclusive modes.

The FPZ can be estimated by AE sources that include high AE energy (Ohtsuka & Date, 2000). AE energy of one AE source is readily calculated by the following equation by employing the maximum amplitude and the duration time of an AE signal at each sensor:

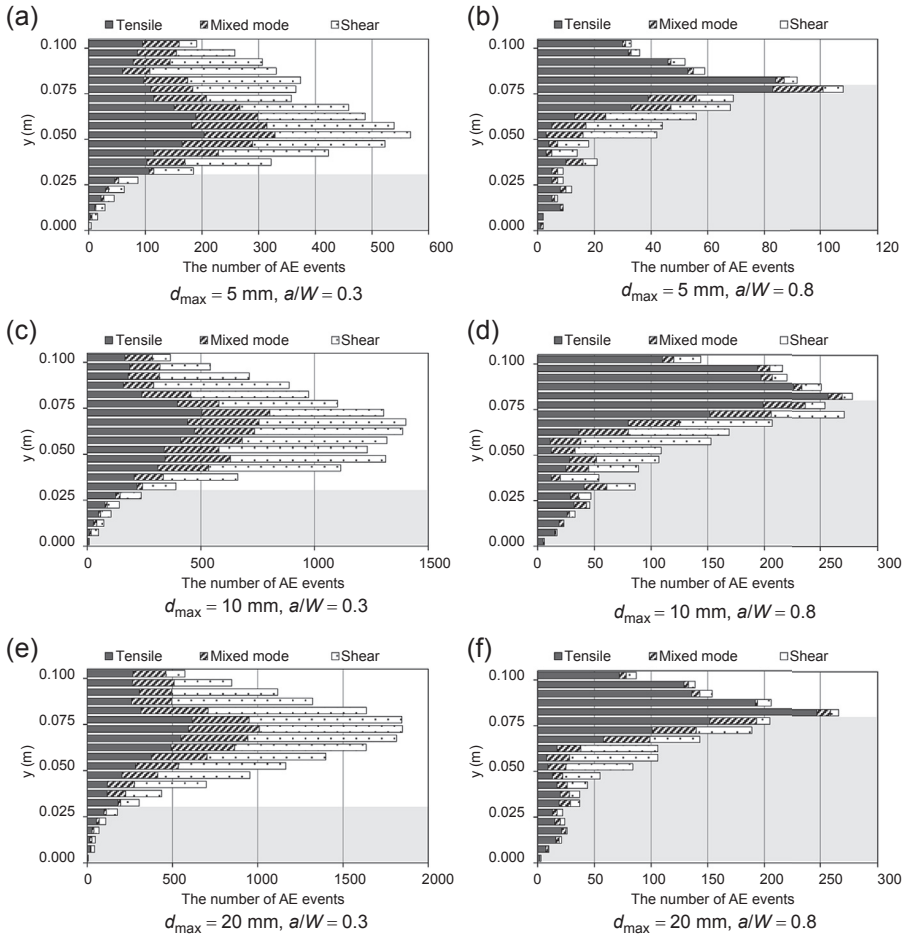

Figure 3.9 (a–f) The numbers of crack modes at two notch depths.
Ohno, K., Uji, K., Ueno, A., and Ohtsu, M. (2014). Fracture process zone in notched concrete beam under three-point bending by acoustic emission. *Construction and Building Materials*, 139–145.

$$E_{AE} = \frac{\sum_{i=1}^{N} V^2 \times T}{N} \tag{3.4}$$

where E_{AE} is AE energy of an AE source (V^2*μs), V is maximum amplitude of an AE signal (volt), T is duration time of an AE signal (μs), and N is the number of AE sensors ($N = 6$ in this experiment).

Here, the AE energy of an AE source is divided into two categories of $1 > E_{AE}$ and $1 \leq E_{AE}$. The relation between AE energy and AE source location in the case of the maximum aggregate size (20 mm) and $a/W = 0.3$ is shown in Figure 3.11. It is obvious that the lower energy sources are distributed over a wider area, and the higher energy sources tend to localize near the notch tip. In order to investigate the relation between

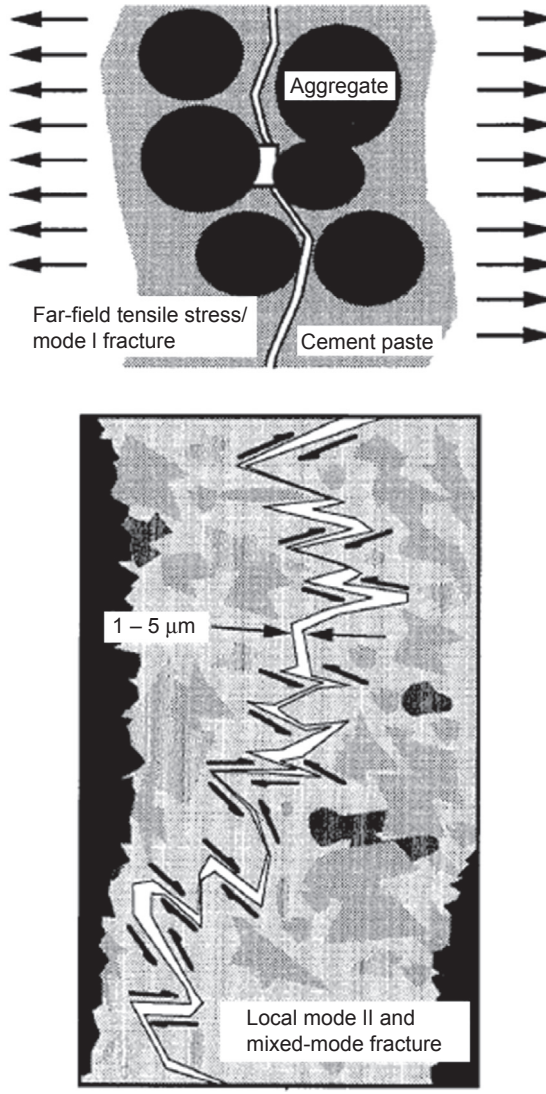

Figure 3.10 Microstructural mechanisms for mode II and mixed-mode micro-craking. Landis, E. N., & Shah, S. P. (1993). Recovery of micro-crack parameters in mortar using quantitative acoustic emission. *Journal of Nondestructive Evaluation*, *12*(4), 219−232.

the width of the FPZ and the fracture energy, the widths of the AE cluster are determined from results of AE source locations, where $1 \leq E_{AE}$. The relations between the fracture energy and the width of the AE cluster for all specimens are shown in Figure 3.12. The distribution of width of the AE cluster increases with the increase in the maximum size of aggregate. From Figure 3.12, it is clearly found that the fracture energy correlates with the width of an AE cluster.

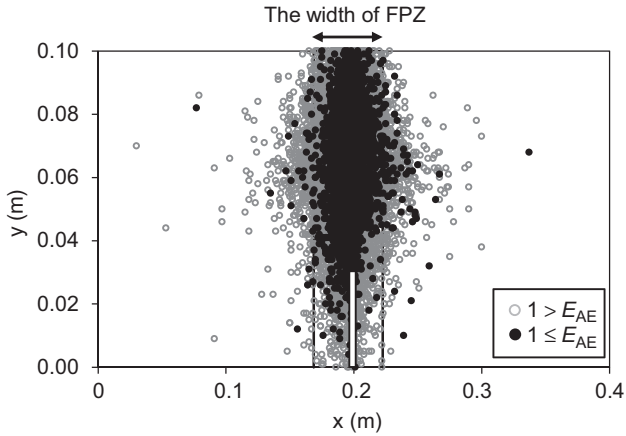

Figure 3.11 The relation between AE source location and acoustic emission (AE) energy ($d_{max} = 20$ mm, $a/W = 0.3$).

3.6 Conclusions

The identification of the FPZ is discussed. Fracture of concrete is characterized by the FPZ, which is nucleated ahead of the crack tip. The existence of the FPZ causes the size effect in concrete. This is because the size of the FPZ varies with the specimen size and the geometry, even if the same materials and the same mixture proportions are employed in concrete.

The evolution of the FPZ can be estimated by AE technique. In particular, AE-SiGMA analysis could clarify micro-cracking mechanisms in the FPZ. The specimen geometry (the ratio of initial crack to specimen height, a/W) influences the micro-cracking mode in the three-point bending. In the generation mechanisms at the FPZ, the mode I cracks dominantly occur in the higher a/W specimens, whereas not only mode I cracks but also mode II and III cracks could take place in the lower a/W specimens. The width of an AE cluster could be associated with the ratios of specimen height to maximum the size of aggregate. These results imply that the characteristics of micro-cracking in the FPZ are readily identified by the AE method.

3.7 Future trends and further related information

The PFZ is nucleated under various stress conditions in a concrete structure (Bazant & Planas, 1998; Duan, Hu, & Wittmann, 2002; Hu & Wittmann, 1992; van Mier, 1997). In other to understand fractures of concrete members or structures, cracking mechanisms in the PFZ are to be identified. As discussed, these mechanisms are easily estimated by applying AE technique (Grosse & Ohtsu, 2008). Ohno et al. have applied AE technique to a bending test, a splitting tensile test, and a shear-bonding test between base concrete and repaired material to identify crack mode from the initial state to the end of the failure

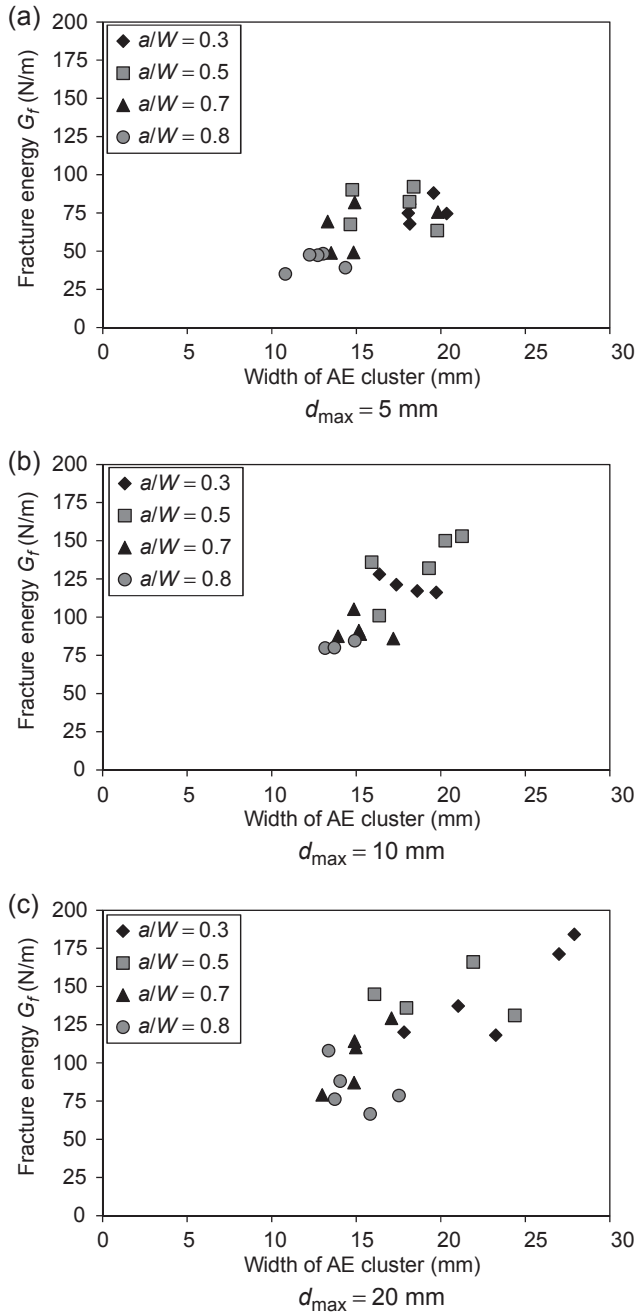

Figure 3.12 (a–c) The relation between fracture energy and width of acoustic emission cluster. Ohno, K., Uji, K., Ueno, A., and Ohtsu, M. (2014). Fracture process zone in notched concrete beam under three-point bending by acoustic emission. *Construction and Building Materials*, 139–145.

process (Ohno, Kurohara, Uji, & Ueno, 2011, 2012; Ohno & Ohtsu, 2010). Other mechanisms are to be identified readily in concrete members and structures.

References

Bazant, Z. P. (1984). Size effect in blunt fracture : concrete, rock, metal. *Journal of Engineering Mechanics, ASCE, 110*, 518−535.

Bazant, Z. P., & Pfeiffer, P. A. (1987). Determination of fracture energy from size effect and brittleness number. *ACI Materials Journal, 84*(6), 463−480.

Bazant, Z. P., & Planas, J. (1998). *Fracture and size effect in concrete and other quasibrittle materials*. BocRaton and London: CRC Press.

Diamond, S., & Mindess, S. (1982). A device for direct observation of cracking of cement paste and mortar under compressive loading within a scanning electron microscope. *Cement and Concrete Research, 12*(5), 569−576.

Duan, K., Hu, X. Z., & Wittmann, F. H. (2002). Explanation of size effect in concrete fracture using non-uniform energy distribution. *Materials and Structures, 35*, 326−331.

Grosse, C. U., & Ohtsu, M. (2008). *Acoustic emission testing*. Springer.

Gustafsson, P. J., & Hillerborg, A. (1988). Sensitivity in shear strength of longitudinally reinforced concrete beams to fracture energy of concrete. *ACI Structural Journal, 85*, 286−294.

Hillerborg, A. (1985). The theoretical basis of a method to determine the fracture energy G_f of concrete. *Materials and Structures, 18*(106), 25−30 (RILEM).

Hillerborg, A. (1991). Application of the fictitious crack model to different types of materials. *International Journal of Fracture, 51*(2), 95−102.

Hu, X. Z. (2002). An asymptotic approach to size effect on fracture toughness and fracture energy of composites. *Engineering Fracture Mechanics, 69*, 555−564.

Hu, X. Z., & Wittmann, F. H. (1992). Fracture energy and fracture process zone. *Materials and Structures, 25*, 319−326.

Hu, X. Z., & Wittmann. (2000). Size effect on toughness induced by crack close to free surface. *Engineering Fracture Mechanics, 65*, 209−221.

Japan concrete institute. (2003). *Method of test for fracture energy of concrete by use of notched beam* (JCI-S-001), (in Japanese).

Landis, E. N., & Shah, S. P. (1993). Recovery of microcrack parameters in mortar using quantitative acoustic emission. *Journal of Nondestructive Evaluation, 12*(4), 219−232.

Li, Z., & Shah, S. P. (1994). Localization of microcracking in concrete under uniaxial tension. *ACI Material Journal, 91*, 372−381.

Maji, A., & Shah, S. P. (1988). Process zone and acoustic-emission measurements in concrete. *Experimental Mechanics, 28*, 27−33.

Mihashi, H., Kirikoshi, K., Nomura, N., Ohtsuka, K., & Kaneko, Y. (1998). Microcracking behavior and softening properties of concrete. *Proceedings FRAMCOS-3*, 181−192.

Mihashi, H., & Nomura, N. (1996). Correlation between characteristics of fracture process zone and tension-softening properties of concrete. *Nuclear Engineering and Design, 165*, 359−376.

Ohno, K., Kurohara, S., Uji, K., & Ueno, A. (2011). Failure process in shear bonding strength tests between existing Concrete and repairing material by acoustic emission technique. In *Proceedings of international RILEM conference on advances in construction materials through science and engineering* (in CD-ROM).

Ohno, K., Kurohara, S., Uji, K., & Ueno, A. (2012). Comparison of failure processes in bond strength tests between shear and splitting tensile in concrete with repairing material by acoustic emission. *Progress in acoustic emission, XVI*, 13−18. JSNDI.

Ohno, K., & Ohtsu, M. (2010). Crack classification in concrete based on acoustic emission. *Construction and Building Materials, 24*, 2339−2346.

Ohno, K., Shimozono, S., Sawada, Y., & Ohtsu, M. (2008). Mechanisms of diagonal-shear failure in reinforced concrete beams analyzed by AE-SiGMA. *Journal of Solid Mechanics and Materials Engineering, 2*(4), 462−472.

Ohno, K., Uji, K., Ueno, A., & Ohtsu, M. (2014). Fracture process zone in notched concrete beam under three-point bending by acoustic emission. *Construction and Building Materials*, 139−145.

Ohtsu, M. (1991). Simplified moment tensor analysis and unified decomposition of AE source: application in situ hydrofracturing test. *Journal Geophysics Research, 96*(B4), 6211−6221.

Ohtsuka, K., & Date, H. (2000). Fracture process zone in concrete tension specimen. *Engineering Fracture Mechanics, 65*, 111−131.

RILEM TC-50 FMC. (1985). Determination of the fracture energy of mortar and concrete by means of three-point bend tests on notched beams. *Materials and Structural, 18*, 287−290.

Shah, S. P. (1990). Size-effect method for determining fracture energy and process zone size of concrete. *Materials and Structures, 23*(6), 461−465.

van Mier, J. G. M. (1997). *Fracture processes of concrete assessment of material parameters for fracture models*. Boca Raton, Fl: CRC Press.

Corrosion-induced cracks in concrete and hybrid non-destructive evaluation (NDE) for evaluation in rebar corrosion

4

Y. Kawasaki, T. Okamoto, K. Izuno
Ritsumeikan University, Kusatsu, Shiga, Japan

4.1 Introduction

A variety of concrete structures, widely recognized as an important material in the world, have been constructed to build social infrastructures such as bridges, tunnels, dams, and harbor structures. Recently, many issues with the deterioration of concrete have been reported (Emmons & Vaysburd, 1997; Qian, 2006). In particular, the corrosion of reinforcing steel bar (rebar) in concrete is an important problem (Rodriguez, Ortega, & Casal, 1997; Rodriguez, Ortega, & Casal, 1994). This is well known as salt damage in reinforced concrete (RC). The damage could start with rusting at the rebar surface, and then corrosion-induced cracks are nucleated in concrete due to expansion of corrosion products. The latter results in surface cracks that begin to delaminate cover concrete. Eventually, the reduction of load-bearing capacity of the concrete structure and cross-sectional loss of rebar become a major problem in the maintenance of RC. Consequently, early detection of the rebar-corrosion process in concrete by nondestructive evaluation (NDE) is in demand for estimation of the progress in deterioration and damage.

In this chapter, we clarify the mechanisms of corrosion-induced cracks in concrete by applying acoustic emission (AE) measurement. Then, we present a basic study on the hybrid-NDE method for evaluation of the corrosion of rebar inside RC members.

4.2 The corrosion process in concrete

In the case of sound concrete, the rebar surface in concrete is covered with a passive film that is very thin and consists of hydrous oxide under a strongly alkaline environment. Therefore, the rebar surface is protected from the corrosive action. Chemically, halide ions (Cl^-, Br^-, I^-), sulfate ion (SO_4^{2-}), and sulfide ion (S^{2-}) exist as harmful components to destroy the passive film on rebar. Due to salt attack, chloride ions (Cl^-) could become a leading cause of rebar corrosion. In the case that the passive film is broken, ferrous ions are activated, and thus rebar is likely to be corroded.

The salt damage in RC structures might result from the quality of concrete itself, environmental conditions, design, construction, and so forth. To quantitatively evaluate

Acoustic Emission (AE) and Related Non-destructive Evaluation (NDE) Techniques in the Fracture Mechanics of Concrete
http://dx.doi.org/10.1016/B978-1-78242-327-0.00004-0
Copyright © 2015 Elsevier Ltd. All rights reserved.

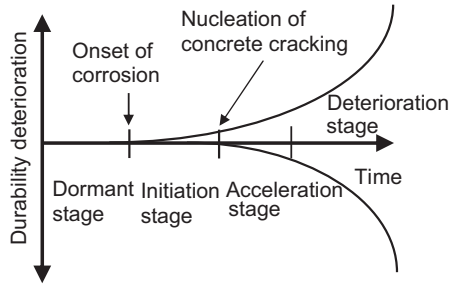

Figure 4.1 Deterioration process due to corrosion.

the deterioration process of the corrosion in RC structures is a hard task. In the standards, the deterioration process of the salt damage is divided into four stages: a dormant stage, initiation stage, acceleration stage, and deterioration stage, as shown in Figure 4.1.

The corrosion of rebar results from an electrochemical reaction. After chloride concentration around rebar exceeds the threshold level of the chloride ion, the passive film of rebar is broken, and then electrochemical reaction occurs. In this case, water and oxygen are necessary, as given in the following equations:

$$F_e \rightarrow F_e^{2+} + 2e^- \quad \text{Anodic reaction} \tag{4.1}$$

$$O_2 + 2H_2O + 4e^- \rightarrow 4OH^- \quad \text{Cathodic reaction} \tag{4.2}$$

Thus, the corrosion cell is formed, as shown in Figure 4.2. Here, a macro-cell is generated in an area at a distance, while a micro-cell occurs in close proximity (Subramaniam & Bi, 2010; Elsener, 2002; Hansson, Poursaee, & Laurent, 2006; Qian, Zhang, & Qu, 2006; Raupach, 1996). As realized in Eqns (4.1) and (4.2), chloride ions are not included in reactions. They act to destroy the passive film on the rebar

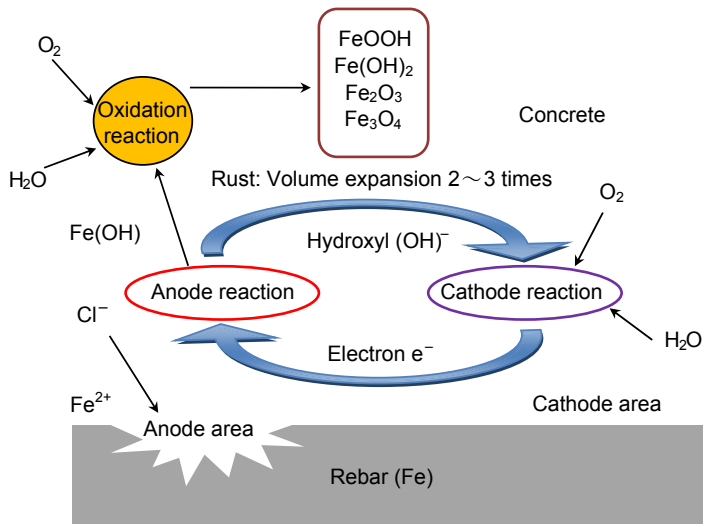

Figure 4.2 Action of the corrosion cell.

surface, and then ferrous ions are activated. Following the reactions, rust (corrosion product) is generated in rebar. Since the volume-expansion coefficient of the corrosion product is two to three times larger than steel, the expansion pressure in concrete nucleates cracks. After surface cracks appear due to the expansion of corrosion products, water and oxygen are readily supplied and further accelerate the corrosion in rebar.

4.3 Non-destructive evaluation (NDE) for corrosion in rebar

NDE techniques are effective to repeatedly inspect materials and structures without causing damage. Those available for rebar corrosion in concrete are summarized in Table 4.1. One category is the electrochemical methods, such as half-cell potentials and polarization resistances. The other is physical methods such as visual (optical) inspection and the AE method, which is currently proposed as a useful method (Kawasaki, Kitaura, Tomoda, & Ohtsu, 2010).

4.3.1 Half-cell potential method

A polarization diagram illustrating both the anode and the cathode in the corrosion reaction is shown in Figure 4.3. When rebar inside concrete is passivated by high

Table 4.1 NDT methods for rebar corrosion

Electrochemical methods	Half-cell potential
	Polarization resistance
	Other
Physical methods	Visual observation
	Acoustic emission

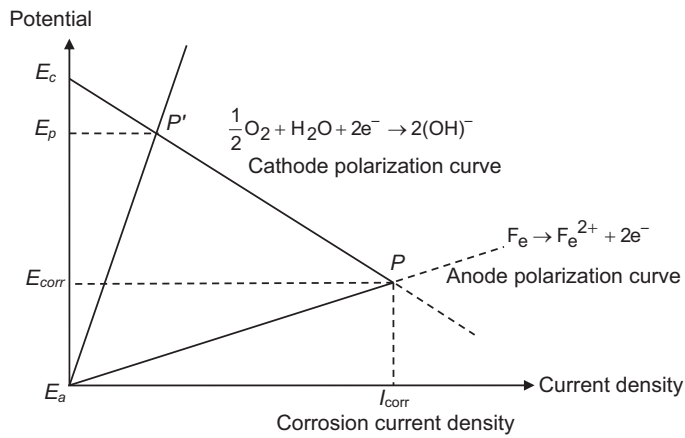

Figure 4.3 Polarization diagram of rebar.

Table 4.2 ASTM criteria of corrosion evaluation

Potential	Probability of corrosion
$-200\ \text{mV} < E$	No corrosion (more than 90%)
$-350\ \text{mV} < E \leq -200\ \text{mV}$	Indetermination
$-350\ \text{mV} > E$	Corrosion (more than 90%)

Note: in the case of CSE (saturated copper sulfate electrode).

alkalinity, half-cell potentials are −100 mV to −200 mV, measured by CSE (saturated copper sulfate electrode), and the corrosion current density is low. In the case when rebar is activated by the ingress of chloride ions, the potentials decrease as more negative values, and the corrosion current density increases. Thus, the half-cell potentials measured could be an indicator of the corrosion activity. The criterion for evaluation of rebar corrosion by the half-cell potentials is given in Table 4.2 (ASTM, 1999).

4.3.2 Polarization resistance method

The polarization resistance method has been employed as a method for estimating the corrosion rate. When an electrical current flows through rebar in concrete, the polarization resistance decreases with the increase in corrosion. As an intersection between the cathode polarization and the anode polarization in the polarization diagram shown in Figure 4.3, the corrosion current density is determined. The reciprocal relation between the corrosion rate and the polarization resistance is established as the Stern−Geary equation in Eqn (4.3) (Stern & Geary, 1957):

$$I_{corr} = B \times \frac{1}{R_p} \tag{4.3}$$

Here, I_{corr} is the corrosion current density (A/cm^2), R_p is the polarization resistance (Ωcm^2), and B is a constant determined from the type of metal and environmental conditions. The value usually used as B is 0.026 V. One criterion for estimating the corrosion rate from the polarization resistance is reported as given in Table 4.3 (BBRI, 1997).

Table 4.3 Criteria of corrosion rate

Corrosion rate I_{corr} (μm/year)	Corrosion activity	Polarization resistance Rct (kΩcm^2)	Penetration (mm/year)
0.1 ~ 0.2	No corrosion	130 ~ 260	0.0011 ~ 0.0023
0.2 ~ 0.5	Low ~ middle	52 ~ 130	0.0023 ~ 0.0058
0.5 ~ 1.0	Middle ~ high	26 ~ 52	0.0058 ~ 0.0116
1.0~	Intense, high	~26	0.0116~

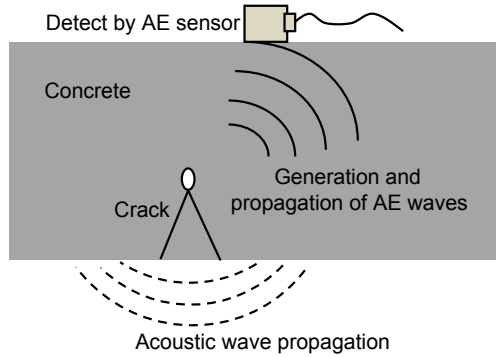

Figure 4.4 Acoustic emission (AE).

4.3.3 AE method

AE is a phenomenon where the emission and propagation of elastic waves are generated due to the release of internal energy as micro-fracturing in an elastic material, as shown in Figure 4.4 (Ohtsu & Grosse, 2008; Ohtsu, 1996). During the corrosion process in rebar, AE activities are observed. Thus, AE measurement is useful for detecting the corrosion activity (Kawasaki, Kitaura, Kobarai, & Ohtsu, 2011; Ohtsu, Mori, & Kawasaki, 2011).

4.4 Estimation of potentials on rebar surface by PiBEM

In the case that concrete is homogeneous, the potential $u(x)$ at an internal point x is obtained by the boundary integral equation (Brebbia, 1987):

$$u(x) = \int_S \left\{ G(x,y)\frac{\partial u}{\partial n}(y) - \frac{\partial G}{\partial n}(x,y)\cdot u(y) \right\} \mathrm{d}S \tag{4.4}$$

Here points y are located on the boundary S of concrete. $G(x,y)$ is the fundamental solution. From Eqn (4.4), potentials at the interface, $u(x)$, between concrete and rebar are discretized as follows:

$$u(x) = \sum_{j=1}^{N} G\left(x,y_j\right)\frac{\partial u}{\partial n}\left(y_j\right)S_j - \sum_{j=1}^{N}\frac{\partial G}{\partial n}\left(x,y_j\right)u(j)S_i \tag{4.5}$$

Setting all variables at the boundary elements as discretized values, Eqn (4.5) is further simplified as shown:

$$u_i = \sum_{j=1}^{N} G_{ij}\frac{\partial u}{\partial n_j}S_j - \sum_{j=1}^{N}\frac{\partial G_{ij}}{\partial n}u_j S_j \tag{4.6}$$

where u_j represents the half-cell potentials at the concrete surface, S_j is the area of the electrode of the measurement, and $\partial u/\partial x_j$ represents the corrosion current. From Eqn (4.3), the following relation with the polarization resistances R_j is assumed:

$$\frac{\partial u}{\partial n_j} \propto \frac{B}{R_j} \tag{4.7}$$

Substituting two coefficients C_1 and C_2 into the potential term and the current term for compensation in Eqn (4.6), we have,

$$u_i = C_1 \left(\sum_{j=1}^{1} \frac{\partial G_{ij}}{\partial n} u_j S_j \right) + C_2 \left(\sum_{j=1}^{N} G_{ij} \frac{1}{R_j} S_j \right) \tag{4.8}$$

In the experiment, half-cell potentials u_j and polarization resistances R_j are measured at the concrete surface (locations y_j), and also by embedded sensors (locations x_1 and x_2). Substituting the half-cell potential u_j at two locations x_1 and x_2 into Eqn (4.8), the coefficients C_1 and C_2 are determined. Then the half-cell potentials at the rebar surface at any locations can be calculated from Eqn (4.8). The procedure is named the potential inverse by BEM (PiBEM) (Kawasaki, Kobarai, & Ohtsu, 2012).

4.5 Acoustic emission (AE) monitoring in the corrosion process

According to a phenomenological model of rebar corrosion in seawater environments (Melchers & Li, 2006), it was reported that a typical corrosion loss during the corrosion process can be divided into four phases, as shown in Figure 4.5. In Phase 1, the

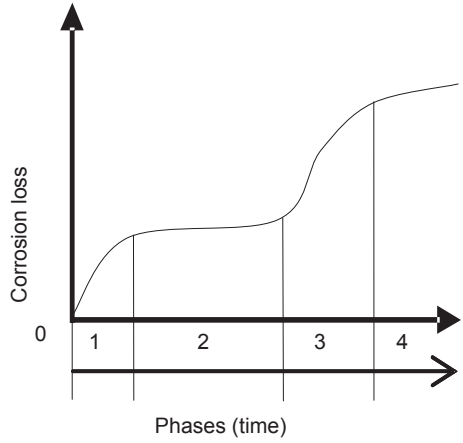

Figure 4.5 Typical corrosion loss for steel immersed in seawater.
Kawasaki, Y., et al. Journal of Construction and Building Materials, 4, 1240−1247.

onset of corrosion occurs. The activity of the corrosion process is dominated by the rate of penetration of oxygen and water. Then a corrosion loss decreases in Phase 2 because the flow of oxygen is eventually inhibited by corrosion products created at the surface of rebar. The corrosion process increases again during Phase 3 because the corrosion penetrates inside the rebar and the expansion of corrosion products occurs. Further, the corrosion of rebar progresses at an almost constant speed in Phase 4. Thus, the phenomenological model is referred to as a two-step process of the onset of corrosion and the expansion of corrosion products.

The expansion caused by corrosion products generates micro-cracks in concrete as corrosion-induced cracks, of which mechanisms can be investigated experimentally by AE. Consequently, continuous AE measurement is applied to identify the transition periods at the onset of corrosion and at the nucleation of corrosion-induced cracks. AE activities under cyclic wet and dry test are investigated, and these results are confirmed by a stereomicroscope. In order to study fracture mechanisms of corrosion-induced cracks, SiGMA (Simplified Green's functions for Moment tensor Analysis) (Ohtsu, 1991, Ohtsu, Okamoto, & Yuyama, 1998) is applied to the corrosion process in RC. To compare with cracking mechanisms identified by SiGMA, a numerical analysis by the two-dimensional boundary element method (BEM) is performed for stress analysis, and applied boundary nodes are determined from a diffusion analysis of chloride contents by the finite element method (FEM). Thus, fracture mechanisms of corrosion-induced cracks are quantitatively evaluated by AE-SiGMA and BEM.

4.5.1 Experiments

RC specimens of dimensions 75 × 100 × 400 mm were made. Configuration of the specimen is illustrated in Figure 4.6. A rebar of 13-mm diameter was embedded with 20 mm cover-thickness for longitudinal arrangement. To promote the corrosion, a notch of dimensions 150 × 10 × 1 mm was set at the bottom of the mold, as shown in Figure 4.7. The mixture proportion of the concrete is given in Table 4.4. Here, NaCl solution is employed as mixing water. Mechanical properties of hardened concrete at 28 days of moisture curing are summarized in Table 4.5. Following the standard curing for 28 days, the corrosion process under salt attack was simulated by cyclic wet and dry conditions.

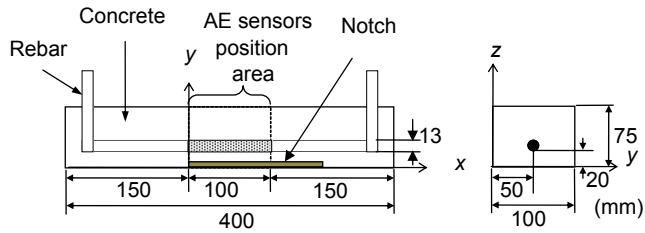

Figure 4.6 RC specimen tested.

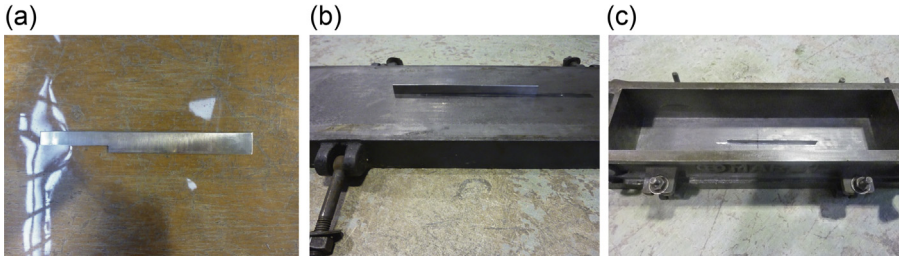

Figure 4.7 Notch and mold. (a) Shape of notch, (b) bottom of the mold, and (c) the mold after setting.

Table 4.4 Mixture proportion of concrete

Maximum gravel size (mm)	W/C (%)	Weight per 1 m^3 concrete					Slump (cm)	Air (%)
		Water (kg)	Cement (kg)	Sand (kg)	Gravel (kg)	Admixture (kg)		
10	55	174	316	758	1117	1.263	7	6

Table 4.5 Mechanical properties of hardened concrete

Compressive strength (MPa)	Poisson's ratio	P-wave velocity (m/s)
36.1	0.2	4500

In the cyclic wet and dry test, the specimens were cyclically put into the container filled with 3% NaCl solution for a week and subsequently taken out of the container to dry under ambient temperature for another week, as shown in Figure 4.8. AE measurement was continuously conducted by using the AE measurement system. Six AE sensors (R15) of 150 kHz resonance were attached to the surface of the specimen as shown in Figure 4.9. The coordinates of AE sensors are given in Table 4.6. The frequency range of the measurement was 10 kHz to 2 MHz, and total amplification was 60 dB gain. For event counting, the dead-time was set to 2 ms, and the threshold

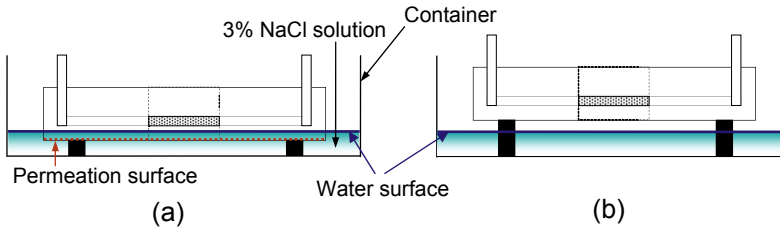

Figure 4.8 Cyclic wet and dry test. (a) Wet condition and (b) dry condition.
Kawasaki, et al. *Journal of Construction and Building Materials*, 4, 1240−1247.

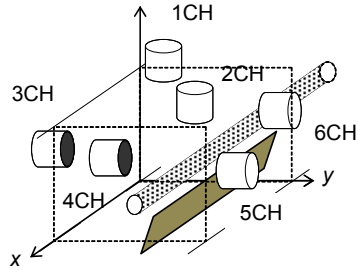

Figure 4.9 Array of six sensors.

Table 4.6 Coordinates of acoustic emission (AE) sensors

	x (m)	*y* (m)	*z* (m)
1CH	0.010	0.020	0.075
2CH	0.080	0.070	0.075
3CH	0.090	0.000	0.045
4CH	0.015	0.000	0.025
5CH	0.080	0.100	0.020
6CH	0.015	0.100	0.055

level was set to 40 dB gain. Every week, AE measurement was temporarily interrupted for the electrochemical measurement.

Half-cell potentials at the surface on the bottom of the specimen were measured by a portable corrosion meter, SRI-CM-II (Yokota, 1999), every week. Results of the half-cell potentials were converted to the probability of corrosion on the basis of ASTM C876 standard prescribed in Table 4.2.

4.5.2 Analysis

Ingress of chloride ions is governed by the diffusion equation. In the case of one-dimensional penetration, the solution is represented in the following error-function, assuming that the chloride concentration $C(x, t)$ at a surface is constant:

$$C(x,t) = C_0\left(1 - \mathrm{erf}\frac{x}{2\sqrt{Dt}}\right) \tag{4.9}$$

Here, D is the diffusion coefficient, C_0 is the surface chloride concentration, x is the distance from the bottom, and t is the measured period. In the analysis, C_0 is estimated as effective surface-chloride concentration, which is obtained as the averaged value from the following:

$$C_0 = \frac{C(x,t)}{1 - \mathrm{erf}\frac{x}{2\sqrt{Dt}}} \tag{4.10}$$

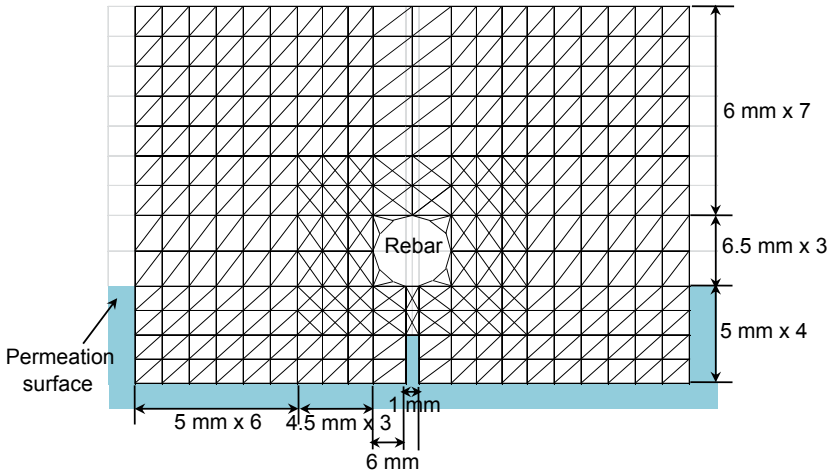

Figure 4.10 Finite element method (FEM) model.

where x and t are substituted from the test. The diffusion coefficient is determined by one equation in the JSCE Standard:

$$\log D = 4.5(W/C) + 0.14(W/C) - 8.47 \tag{4.11}$$

where W/C is the water-cement ratio. The diffusion equation is also solved by using 2-D FEM in order to clarify chloride concentration on a cross-section. The model is shown in Figure 4.10. The number of elements is 620 in total. As for analytical parameters, the initial chloride content is 0.047 kg/m^3, the diffusion coefficient is 6.05 x 10^{-8} cm^2/s, and the corresponding value of the surface chloride content is set to18.2 kg/m^3.

A BEM model is illustrated in Figure 4.11, which corresponds to a half portion of a cross-section in an RC beam. The boundary corresponding to the notch is set to be stress-free from constraints as shown. Expansive pressure due to corrosion products was applied at the cavity, corresponding to the rebar. The pressure was assumed as 1 MPa, which was applied to boundary nodes determined from chloride concentration analyzed by FEM. The number of element and internal elements are 111 and 15 in total, respectively. Poisson's ratio and Young's modulus were set to 0.22 and 0.27 GPa, respectively.

4.5.3 AE activity and half-cell potential

Cumulative AE hits and AE events for every 1 h of all six channels are shown in Figure 4.12. Here, one AE event implies a group of AE hits received from a single source at six channels, of which spatial coordinates could be located. AE hits and AE events start to gradually increase during the first 42 days. Then, AE hits sharply increase at 42 days elapsed. From 49 days to 112 days, AE hits and AE events increase continually. Thus, the onset of corrosion started during the first 42 days, and the corrosion-induced cracks due to the expansion of corrosion products occurred from 42 days in

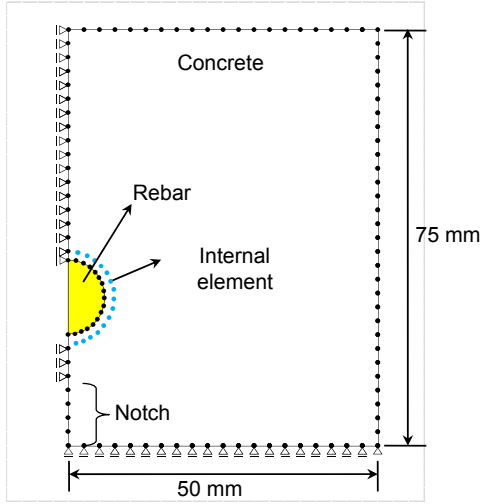

Figure 4.11 Boundary element method (BEM) model.

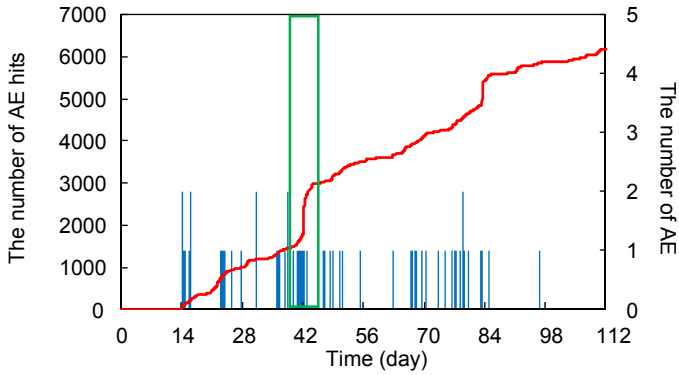

Figure 4.12 Cumulative acoustic emission (AE) hits and AE events.

Phase 1 and Phase 3, respectively (Figure 4.5). This implies that AE events observed from 42 to 112 days could result from corrosion-induced cracks in concrete.

Cumulative AE hits are compared with half-cell potentials in Figure 4.13. The half-cell potentials start to decrease after 42 days. After 56 days elapsed, the potentials became more negative than −350 mV. From these results, the corrosion-induced cracks occurred from 42 days. Thus, after 42 days, rust breaking and other internal cracks around rebar could occur. Then, corrosion-induced cracks in concrete must be nucleated due to expansion of corrosion products in rebar.

4.5.4 Numerical analysis by FEM and BEM

Results of FEM of a half portion of a cross-section at 42 days are shown in Figure 4.14. From the results of the 2-D FEM analysis, the stress distribution around the rebar was

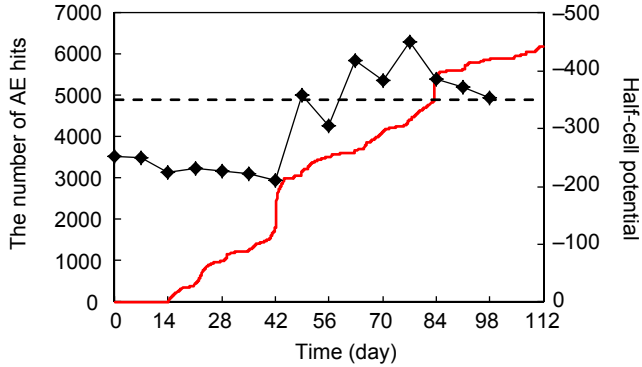

Figure 4.13 Cumulative acoustic emission (AE) hits and half-cell potentials.

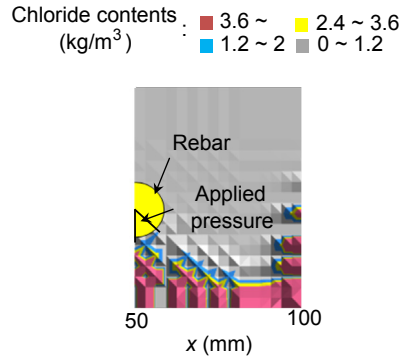

Figure 4.14 Results of finite element method (FEM) analysis.

evaluated by using BEM analysis. Chloride contents were confirmed to exceed 1.2 kg/m^3 at −33.75° orientation. The stress directions of the horizontal and the vertical are shown in Figure 4.15. Thus, expansive pressure (1 MPa) was applied to five points, as shown in Figure 4.16(a).

The number of points where the stress was applied and results of the BEM analysis at 42 days are shown in Figure 4.16(a). Results of the pressure are shown in Figure 4.16(b). In the case of the horizontal pressure applied in Figure 4.16(c), the highest stress and the second highest stress are observed toward the −78.75° and −45° orientations, respectively. It may be the case that the spalling cracks propagate following the surface cracks. The spalling cracks are often observed in when the surface cracks are arrested by aggregate. In the case of the vertical pressure applied in Figure 4.16(d), the highest circumferential stress is only observed toward −78.75° orientation, suggesting nucleation of the surface crack. These results imply that the radial pressure due to the corrosion products could generate the surface crack. The possibility to generate the spalling crack might be stimulated by the horizontal pressure due to expansion of the corrosion products.

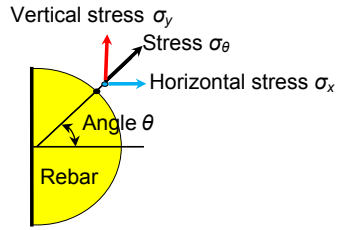

Figure 4.15 Direction of stress.

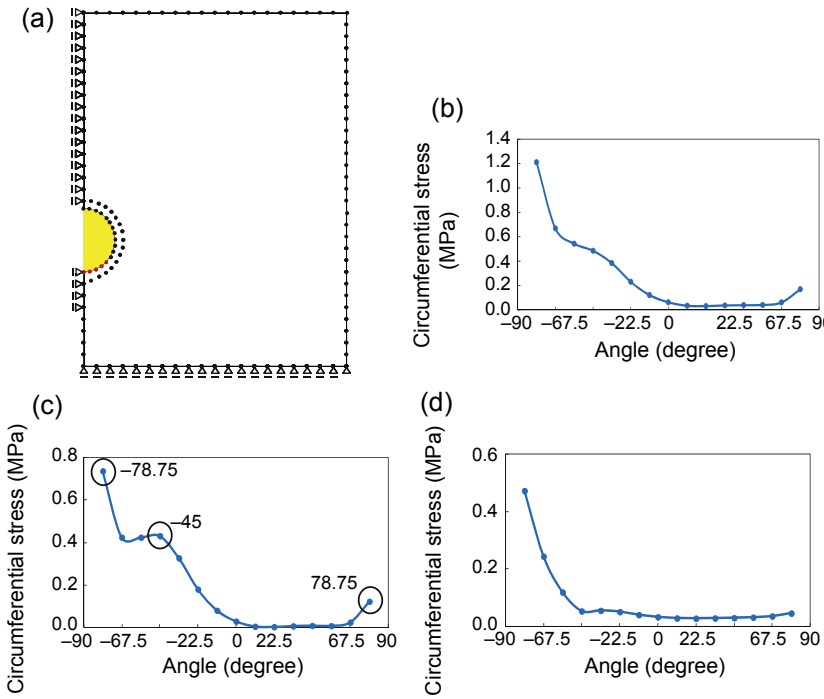

Figure 4.16 Results of boundary element method (BEM) analysis at 42 days. (a) Location of applied pressure, (b) results of pressure, (c) results of horizontal pressure, and (d) results of vertical pressure.

4.5.5 SiGMA analysis and observation

In the SiGMA analysis, AE event definition time (EDT) is set to 100 μs. EDT is applied to recognize AE waves occurring within the specified time from the first-hit and to classify them as part of the current event. Results of the SiGMA analysis at 42 days elapsed are shown in Figure 4.17. Most events are located surrounding the rebar. The events that are located at −78.75° orientation are mostly classified into tensile (opening) cracks. Thus, the surface crack is initiated as tensile cracks, whereas mixed-mode and shear cracks are less active. Additionally, shear cracks (sliding) are

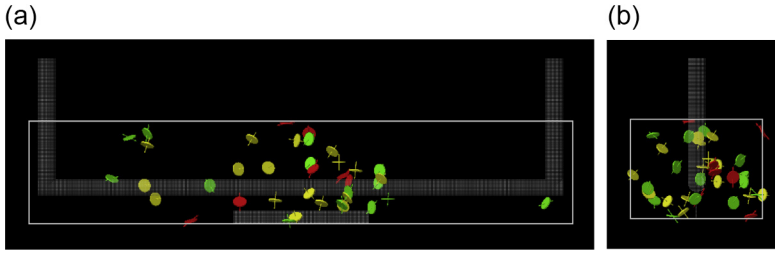

Figure 4.17 Results of SiGMA analysis at 42 days. (a) Side view and (b) cross-section.

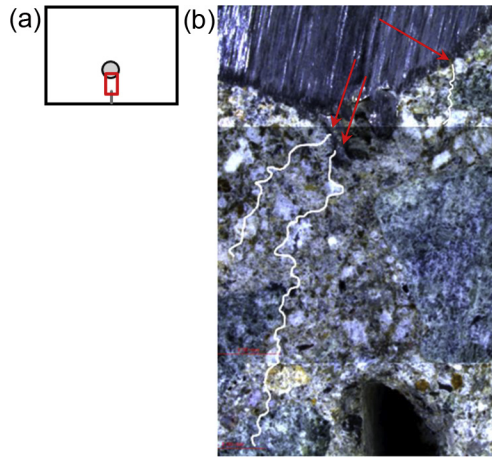

Figure 4.18 Results of stereomicroscope at 56 days. (a) Observed location and (b) cross-section.

observed at 78.75° orientation after the tensile cracks are observed. Referring to Figures 4.16 and 4.17, the vertical pressure could facilitate as a crack-opening action of the surface crack, releasing the horizontal pressure. This result clarifies why the diagonal cracks were generated following the surface cracks in the experiment.

Results of the stereomicroscope view of cross-section at 56 days are shown in Figure 4.18. Three micro-cracks were observed in the cross-section toward the bottom of the RC beam. Orientation of these cracks is about −78.75°. Thus, referring to Figures 4.16−4.18, it is confirmed that tensile cracks are observed at −78.75° orientation as the surface cracks and the spalling cracks.

4.6 Application of hybrid NDE and results

In order to prevent harmful damages from rebar corrosion due to salt attack, many monitoring methods have been developed to evaluate the corrosion before reaching a critical level (Dubravka, Dunja, & Dalibor, 2000). In this concern, NDE techniques are practical and useful in both laboratory tests and on-site measurement. So far, such

electrochemical techniques as half-cell potential and polarization resistance are widely employed, as discussed. In addition, AE measurement has recently become available for detecting both the onset of corrosion and the corrosion-induced cracks in concrete.

In this section, we apply PiBEM analysis and AE measurement in the experiments. Then, we propose the Hybrid-NDE in order to precisely and quantitatively evaluate rebar corrosion.

4.6.1 Experiments

Configuration of a specimen is illustrated in Figure 4.19. One RC slab of dimensions 1000 × 570 × 100 mm was made. A deformed rebar of 13-mm nominal diameter is embedded with 20 mm cover-thickness. Ordinary Portland cement (OPC) was used. Coarse aggregate (gravel) was granite, of which the maximum gravel size is 10 mm. Concerning mixture proportion, the ratios of water, cement, sand, and gravel were 0.55, 1.0, 2.57, and 3.01 by weight, respectively. The slump value and air content of fresh concrete were controlled by admixture as 80 mm and 5.0%, respectively. To accelerate corrosion of rebar, 0.704 kg/m^3 NaCl was mixed in water.

Following moisture curing for 28 days, the corrosion process due to salt attack was simulated by a cyclic wet and dry test. The specimen was cyclically placed into a container filled with 3% NaCl solution for a week and subsequently taken out of the container to dry under ambient temperature for another week.

AE measurement was continuously conducted using an AE measuring system. Two AE sensors of 150 kHz resonance were attached to the surface of the specimen, as shown in Figure 4.19. The frequency range of the measurement was 10 kHz to 2 MHz. AE signals were amplified with 40 dB gain in a preamplifier and 20 dB gain in a main amplifier. For ring-down counting, the dead-time was set to 2 ms and the threshold level to 40 dB gain.

Every week, AE measurement was temporarily interrupted to conduct the half-cell potential measurement. The potentials of the surface of the specimen were measured by using a portable corrosion meter (SRI-CM-II), and C. S. E. values were estimated on the basis of ASTM C876 standard in Table 4.2.

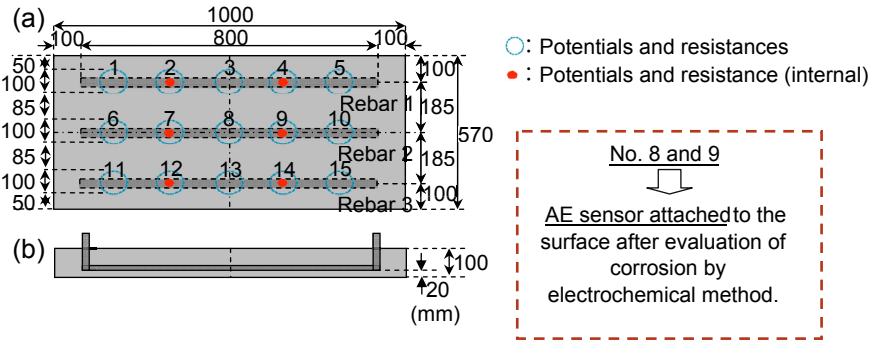

Figure 4.19 Reinforced concrete (RC) slab tested and the location of nondestructive evaluation (NDE). (a) Top view and (b) cross-section.

4.6.2 Electrochemical measurement

Results of half-cell potentials at rebar 1 (measurement areas are 3 and 4) and rebar 2 (measurement areas are 8 and 9) are shown in Figure 4.20. From both results, the half-cell potentials at rebar 1 increased until 105 days elapsed. We found that the potentials drastically decreased after 105 days elapsed. At 133 days elapsed, the potentials became lower than −350 mV, which indicates a 90% corrosion possibility.

However, in the case of results of rebar 2, the half-cell potentials increased until 21 days elapsed. Then, at 49 days elapsed, the potentials became lower than −350 mV. Thus, the potentials at the surface of the concrete at rebar 2 suggested earlier occurrence of the corrosion than rebar 1. After the potentials had become more negative than −350 mV, the potentials were stabilized. At that period, corrosive stains were observed on the bottom surface at rebar 2−8. From these results, we realized that corrosion activities due to half-cell potentials are different, depending on rebar. The corrosion process at rebar 2 is more active than that of rebar 1.

According to results of the internal potentials at rebar 1−4 and rebar 2−9, those potentials are lower than results of the surface potentials. It implies that the potentials at the surface of rebar are very important to electrically evaluate the corrosion initiation.

Based on CEB (Comite Euro-International du Beton) recommendation of polarization resistance in Table 4.7, results at rebar 2 are summarized in Table 4.8. We found that the resistances at all measured points are very low from the beginning. This suggests that the corrosion rates are estimated as from middle to high at 35 days elapsed.

From these results, we assumed that the corrosion started at about 35 days. Then, two AE sensors were attached to the surface of the specimen at rebar 2−8 and rebar 2−9, and AE monitoring was conducted until 147 days.

4.6.3 PiBEM analysis

Results of PiBEM analysis for rebar 2 are given for three periods (21, 63, and 91 days) in Figure 4.21. Although some fluctuations of the potentials are observed along the

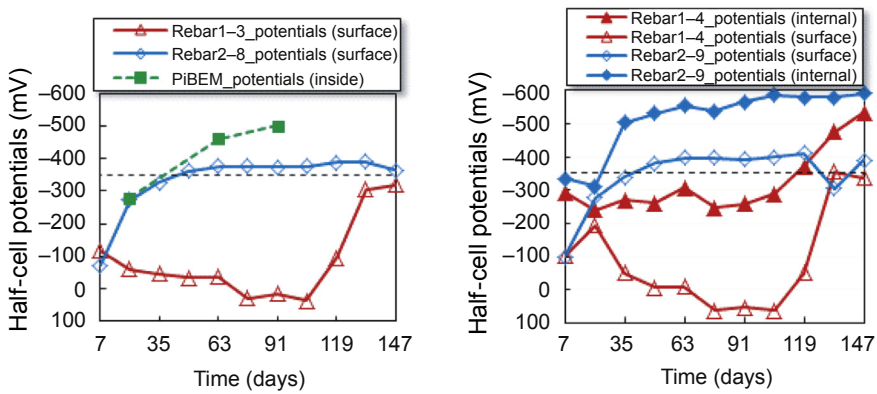

Figure 4.20 Half-cell potentials of rebar 1 and rebar 2.

Table 4.7 CEB recommendation

Resistance Rct ($k\Omega cm^2$)	Corrosion rate
$130 < Rct \leq 260$	No corrosion or very low rate
$52 < Rct \leq 130$	Low ~ medium rate
$26 < Rct \leq 52$	Medium ~ high rate
$Rct \leq 26$	Very high rate

Table 4.8 Results of resistance

	Rebar 2–8	Rebar 2–9
7 days	46	46
21 days	37	37
35 days	30	29
49 days	31	35
63 days	32	35
91 days	38	36

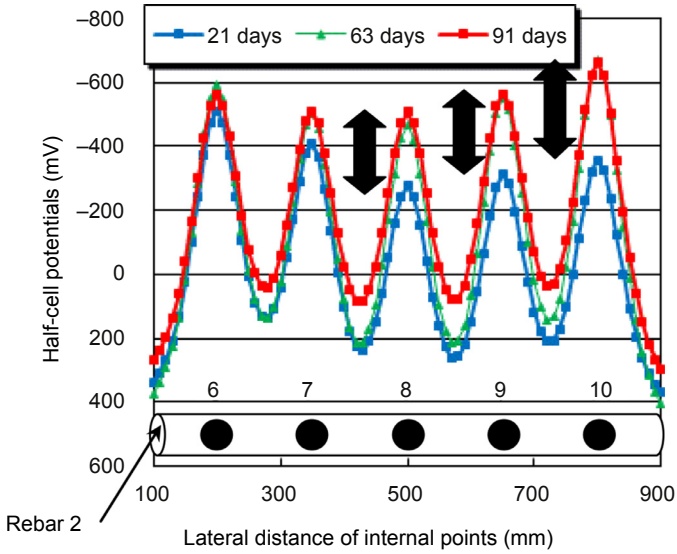

Figure 4.21 Results of PiBEM analysis at rebar 2.

rebar, the potentials of points 8 through 10 decrease from 21 days through 91 days. In contrast, at points 6 and 7, few decreases are realized. This implies that the corrosion activities at points 8 to 10 are higher. In particular, the half-cell potentials at point 10 decrease as the most negative. Thus, the corrosion occurred the most severely at point 10. From these results, the area mostly corroded can be identified along rebar by PiBEM analysis.

4.6.4 AE activity

AE activities of rebar 2 are shown in Figure 4.22. It is already known that the both periods of "the onset of corrosion" and "the nucleation of corrosion-induced crack" could be evaluated by AE monitoring (Kawasaki et al., 2012). Following AE sensor attachment at 35 days elapsed, AE hits start to be detected from 63 days at both areas 8 and 9. In between 70 days and 91 days, no particular AE activities are observed. Then, AE hits drastically increase at 91 days, and the rate of increase at area 9 is higher than at area 8.

4.6.5 Comparison with visual observation

All rebar was removed to visually observe the corrosion state after the cyclic test. These removed rebar are shown in Figure 4.23. Here, red circles indicate the areas where the rust was found. As can be seen, corroded areas in the both rebar 1 and 2 are visually observed. In rebar 2, the rust stain was found at all measured points, and the high corrosion was identified at point 10. Also, at points 8 and 9 where AE measurement was conducted, the corrosion is clearly confirmed. These results are in remarkable agreement with results of the half-cell potentials in Figures 4.20 and 4.21, corresponding to AE activities in Figure 4.22.

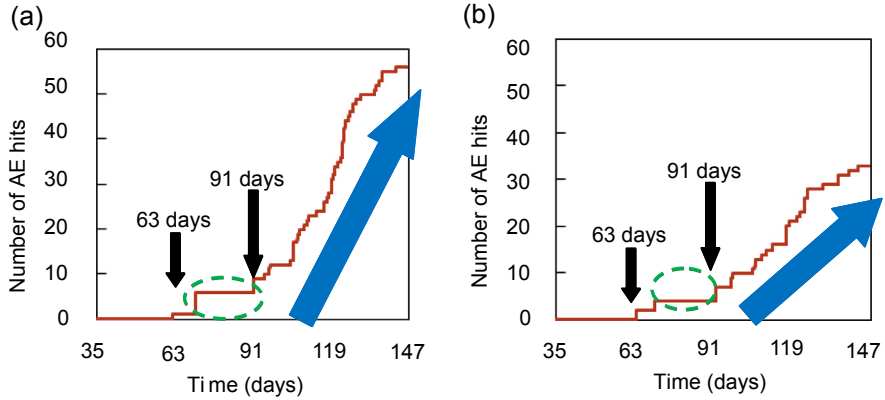

Figure 4.22 Results of acoustic emission (AE) activities. (a) Measurement area 9 and (b) measurement area 8.

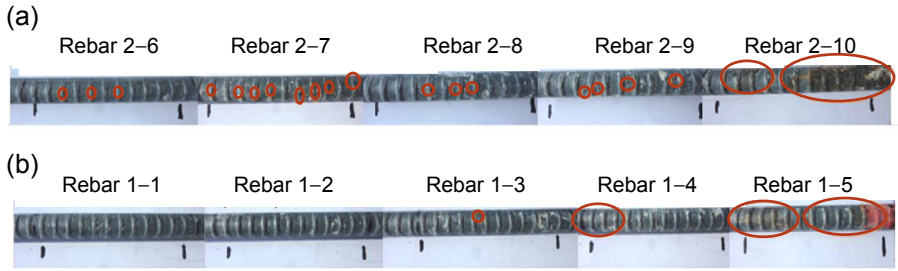

Figure 4.23 Results of visual observation of removed rebar. (a) Rebar 2 and (b) rebar 1.

4.7 Conclusions

Mechanisms of corrosion-induced cracks in RC are clarified analytically and experimentally. Micro-fracture mechanisms for nucleating the surface cracks and the spalling cracks due to expansion of the corrosion products are identified by SiGMA. According to the results, the surface crack is initiated as tensile cracks, whereas mixed-mode and shear cracks are less active. These tensile cracks mostly dominate at the bottom of the beam, especially at -78.75° orientation. After the surface crack is nucleated, the spalling crack is prone to extension as tensile cracks. Then, the mixed-mode and shear cracks are slightly dominant, again around at 78.75° orientation. The results confirm a promise to identify the fracture mechanisms of corrosion-induced cracks by BEM and AE-SiGMA analysis.

AE techniques and electrochemical techniques are applied to evaluate the corrosion process in the RC slab. Corroded areas are estimated by PiBEM analysis, compensating the half-cell potentials. In the half-cell potential measurement, evaluation of the initiation periods of corrosion in RC is possible. However, because the half-cell potentials at the surface of the rebar are distinctly more negative than those of the surface of the specimen, the electrical evaluation at the surface of the rebar is very important. From the results of PiBEM analysis, the internal half-cell potentials at all points were estimated in an RC slab. These results are in remarkable agreement with the results of the visual observation. It implies that the electrical evaluation inside concrete is effective.

The imperceptible difference of the corrosion phenomena, which is difficult to be detected using the electrochemical measurement, can be identified by using AE techniques. AE activities are in remarkable agreement with BEM analysis and visual observation. Thus, it demonstrated that the state of the rebar corrosion in RC can be quantitatively evaluated by using hybrid-NDE techniques of AE techniques and the electrochemical techniques with PiBEM analysis. The potentials evaluated from PiBEM analysis could be confirmed with the corrosion state on the surface of the rebar.

References

ASTM C876-91. (1999). Standard test method for half-cell potentials of uncoated reinforced steel in concrete. *ASTM International.* West Conshohocken, PA, 2009, www.astm.org.

Belgian Building Research Institute (BBRI). (1997). *Strategies for testing and assessment of concrete structures affected by reinforcement corrosion (draft. 4)*. BBRI-CSTC/WTCB, Working Party V/4.1.

Brebbia, C. A. (1987). *Topics in boundary element research* (Vol. 3). Heidelberg: Springer-Verlag.

Dubravka, B., Dunja, M., & Dalibor, S. (2000). Non-destructive corrosion rate monitoring for reinforced concrete structures. *Proceedings of the 15th World Conference on Non Destructive Testing*.

Elsener, B. (2002). Macrocell corrosion of steel in concrete − implications for corrosion monitoring. *Cement and Concrete Composites, 24*, 65−72.

Emmons, P. H., & Vaysburd, A. M. (1997). Corrosion protection in concrete repair: myth and reality. *Concrete International, 19*(3), 45−56.

Hansson, C. M., Poursaee, A., & Laurent, A. (2006). Macrocell and microcell corrosion of steel in ordinary Portland cement and high performance concretes. *Cement and Concrete Research, 36*, 2098−2102.

Kawasaki, Y., Kitaura, M., Kobarai, T., & Ohtsu, M. (2011). Corrosion damage in reinforced concrete identified by AE. *Concrete Research Letters, 2*(3), 263−270.

Kawasaki, Y., Kitaura, M., Tomoda, Y., & Ohtsu, M. (2010). AE monitoring of corrosion process in cyclic wet-dry test. *Construction and Building Materials, 24*(12), 2353−2357.

Kawasaki, Y., Kobarai, T., & Ohtsu, M. (2012). Kinematics of corrosion damage monitored by acoustic emission techniques and based on a phenomenological model. *Advanced Concrete Technology, 10*, 160−169.

Melchers, R. E., & Li, C. Q. (2006). Phenomenological modeling of reinforcement corrosion in marine environments. *ACI Materials Journal, 103*(1), 25−32.

Ohtsu, M. (1991). Simplified moment tensor analysis and unified decomposition of acoustic emission source: application to in situ hydrofracturing test. *Geophysical Research, 96*(B4), 6211−6221.

Ohtsu, M. (1996). The history and development of acoustic emission in concrete engineering. *Magazine of Concrete Research, 48*(177), 321−330.

Ohtsu, M., & Grosse, C. U. (2008). *Acoustic emission testing*. Heidelberg: Springer.

Ohtsu, M., Mori, K., & Kawasaki, Y. (2011). Corrosion process and mechanisms of corrosion-induced cracks in reinforced concrete identified by AE analysis. *Strain, 47*(s2), 179−186.

Ohtsu, M., Okamoto, T., & Yuyama, S. (1998). Moment tensor analysis of acoustic emission for cracking mechanisms in concrete. *ACI Structural Journal, 95*(2), 87−95.

Qian, S., Zhang, J., & Qu, D. (2006). Theoretical and experimental study of microcell and macrocell corrosion in patch repairs of concrete structures. *Cement and Concrete Composites, 28*, 685−695.

Raupach, M. (1996). Chloride-induced macrocell corrosion of steel in concrete—theoretical background and practical consequences. *Construction and Building Materials, 10*, 329−338.

Rodriguez, J., Ortega, L. M., & Casal, J. (1994). Corrosion of reinforcing bars and service life of reinforced concrete structures: corrosion and bond deterioration. *International Conference on Concrete Across Borders, 2*, 315−326.

Rodriguez, J., Ortega, L. M., & Casal, J. (1997). Corrosion of reinforcing bars and service life of reinforced concrete structures: corrosion and bond deterioration. *Construction and Building Materials, 11*(4), 239−248.

Stern, M., & Geary, A. L. (1957). Electrochemical polarization I. A theoretical analysis of shape of polarization curves. *Electrochemical Society, 104*, 1.

Subramaniam, K. V., & Bi, M. (2010). Investigation of steel corrosion in cracked concrete: evaluation of macrocell and microcell rates using Tafel polarization response. *Corrosion Science, 52*, 2725−2735.

Yokota, M. (1999). Study on corrosion monitoring of reinforcing steel bars in 36 years-old actual concrete structures. *Concrete Library of JSCE, 33*, 155−164.

5 Seismology-based acoustic emission techniques for the monitoring of fracture processes in concrete structures

L. Mhamdi[1], *T. Schumacher*[1], *L. Linzer*[2]
[1]University of Delaware, Newark, DE, USA; [2]University of the Witwatersrand, Johannesburg, South Africa

5.1 Introduction and background

Acoustic emissions (AE) are very similar to earthquakes and mining-induced seismic events, except that they occur on a much smaller scale. *They all represent the phenomenon of stress-wave propagation in a solid*. Earthquakes, mining-induced seismicity, and AE are typically caused by the interaction of the Earth's tectonic plates, mining activities, and fracture within a material, respectively. Figure 5.1 presents a scale of the different phenomena with respect to their typical frequency range.

An illustrative comparison between seismology and AE is presented in Figure 5.2. AE activity accompanies almost all processes when a solid medium undergoes an internal stress change (mechanical, thermal, physical, etc.) resulting in a sudden release of stress. It occurs in the microscale due to the movement of small particles at the microscopic level, as well as in the macroscale due to the failure of structural components (e.g., the failure of assemblies, parts, etc.). Earthquakes occur due to the sudden release of stress in the Earth's crust, which results in the generation of elastic disturbances (or seismic waves) that propagate the released energy from the source of the earthquake along the surface of and through the Earth. AE and earthquakes are similar

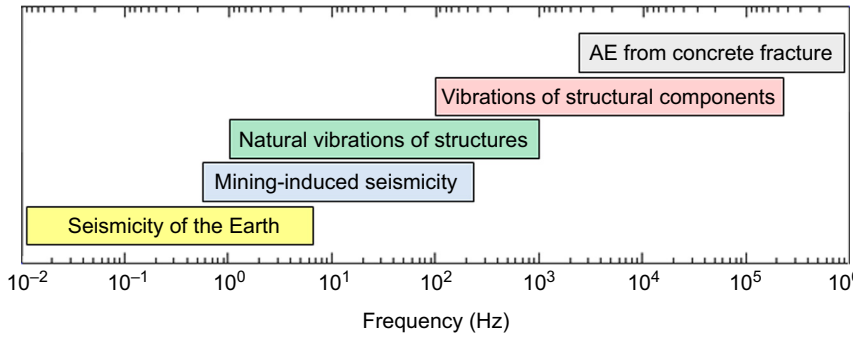

Figure 5.1 Frequency scale of stress-wave phenomena.

Acoustic Emission (AE) and Related Non-destructive Evaluation (NDE) Techniques in the Fracture Mechanics of Concrete
http://dx.doi.org/10.1016/B978-1-78242-327-0.00005-2
Copyright © 2015 Elsevier Ltd. All rights reserved.

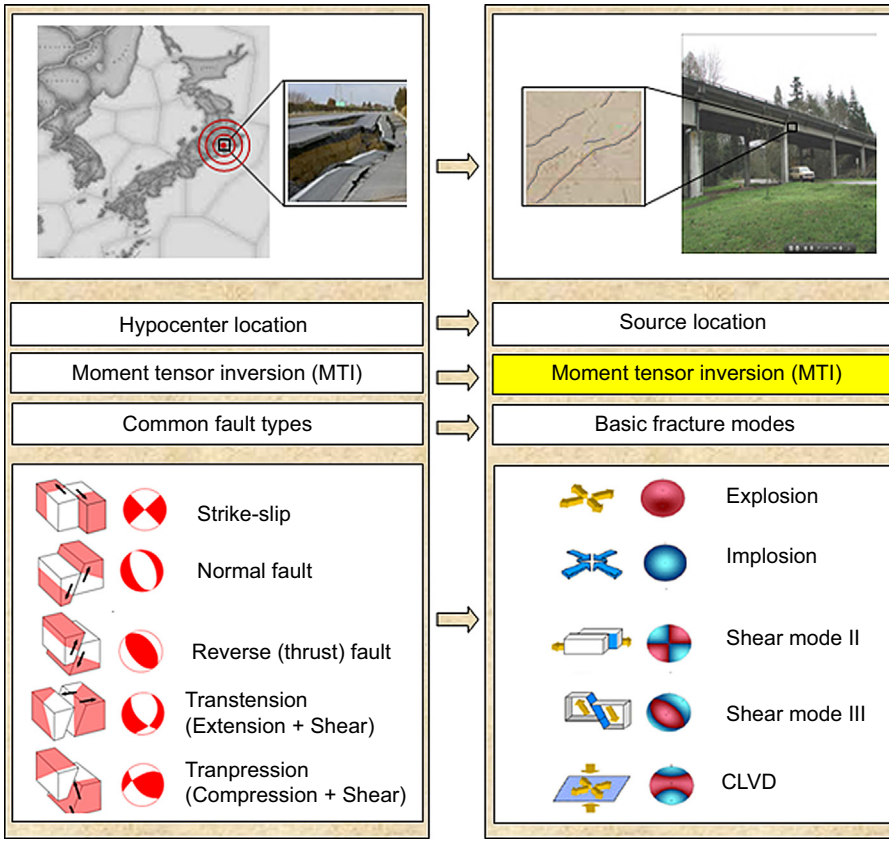

Figure 5.2 Comparison between seismology of the Earth (left column) and AE from concrete fracture (right column).

phenomena even though there are differences in scale (space, time), geometry, loading, boundary conditions, and medium. Despite these differences, AE can be thought of as a form of microseismicity that occurs at much smaller scale. Some authors (e.g., Bonamy, 2009; Mogi, 1962; Scholz, 1968) have proposed that AE generated by brittle fracture in heterogeneous materials can provide a good laboratory-scale model for earthquake studies.

Similar scaling relationships are observed when the source parameters of AE events and mining-induced events are compared. In a study by Sellers, Kataka, and Linzer (2003). to investigate the AE response during an unconfined compression test of quartzite, which is similar to the stress state experienced near slope faces or pillars in deep-level gold mines in South Africa (i.e., high vertical stress and low horizontal confinement), it was found that AE exhibits a similar moment−energy relationship when compared to mine seismicity and natural earthquakes (Figure 5.3). In addition, this study showed that the stress drop is largely independent of the moment

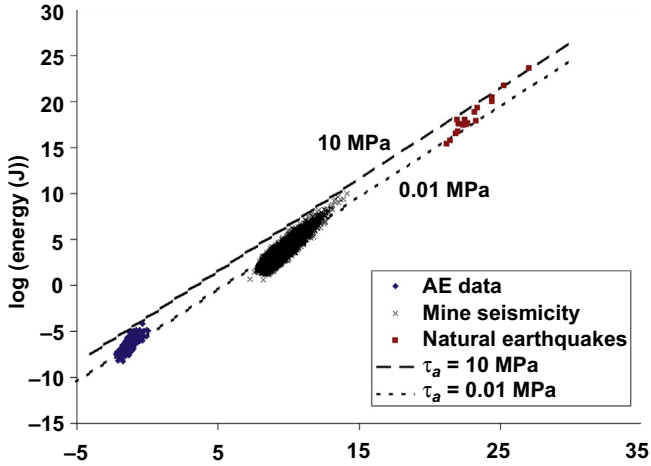

Figure 5.3 Plot of log (energy) versus log (moment) for AE (◆), mining-induced events (×), and natural earthquakes (■). Dashed lines are lines of constant apparent stress.
Sellers, E. J., Kataka, M. O., & Linzer, L. M. (2003). *Journal of Geophysical Research.*

(Figure 5.4), which is similar to observations from mining-induced earthquakes (e.g., Richardson & Jordan, 2001) and natural earthquakes (e.g., Abercombie, 1995; Kanamori, Mori, Heaton, Huttos, & Jones, 1993).

Moreover, the similarity between AE and natural earthquakes can be clearly observed when the signals are plotted next to each other as shown in Figure 5.5.

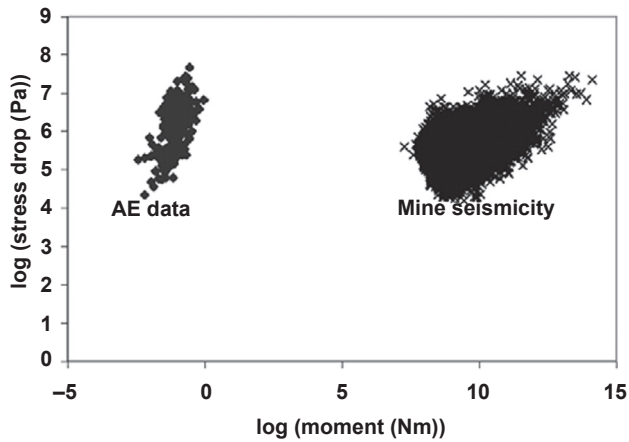

Figure 5.4 Plot of log (stress drop) against log (moment). Diamonds represent AE data and crosses represent mining-induced data from a deep-level gold mine in South Africa.
Sellers, E. J., Kataka, M. O., & Linzer, L. M. (2003). *Journal of Geophysical Research.*

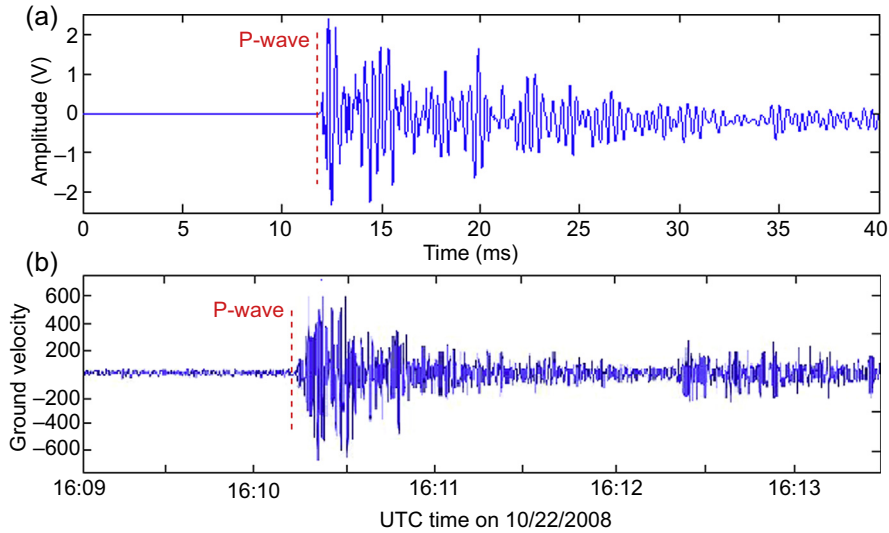

Figure 5.5 Example signals: (a) typical acoustic emission (AE) signal waveform from a concrete fracture recorded by uniaxial sensors showing P-wave arrival time, and (b) seismogram recorded at station Matsushiro in Japan for the magnitude 6.4 event that occurred on November 22, 2008 *(Data taken from IRIS data center)*.

Over the years, the AE literature has documented the studies of numerous authors that have applied both qualitative as well as quantitative seismology-based approaches. The two most important methods for application to concrete fracture, b-value analysis and moment tensor inversion (MTI), are presented in detail in Sections 5.3 and 5.4, respectively.

Over the last few decades, there has been sustained interest in understanding failure mechanisms in concrete structures to achieve full insight into ongoing fracture processes (Bazant & Lee, 1998; Shah & Choi, 1999, etc.). Such understanding would greatly benefit the concrete industry as a whole. The first attempt to study the cracking process in concrete materials dates back to 1961, when Kaplan (1961) first applied the theory of linear elastic fracture mechanics (LEFM) to calculate the fracture parameter K_{IC} in notched three-point and four-point bending of concrete beams. Ever since, there has been an increasing interest in the cracking and fracture mechanisms of concrete materials. A significant amount of work, both theoretical and experimental, has been performed resulting in many scientific contributions that have considerably enhanced the understanding of fracture processes in concrete. McGarr (1984) investigated the applicability of Griffith theory to concrete specimens with notches of varying lengths, tested in flexure and tension. Higgins and Bailey (1976) loaded notched concrete specimens to failure in both flexure and tension and estimated the critical stress intensity factor using LEFM applied to beam geometry. Several other attempts to apply LEFM to concrete have been made. It was subsequently deduced that the theory of

LEFM could not predict the fracture resistance of concrete; nonlinear fracture theory that takes into account the influence of the fracture process zone in concrete was required. A number of nonlinear fracture models were developed. For example, Hillerborg, Modeer, and Peterson (1976) proposed a nonlinear finite element-based fracture mechanics model to estimate the critical fracture energy. Zdenk and Oh (1983) developed the crack band model and showed that a fracture in the material could be characterized by only three properties (fracture energy, strength, and width of crack band front). Several other nonlinear fracture models for the characterization of concrete fracture mechanics were also proposed.

Despite extensive research, the application of fracture mechanics to concrete is still a challenge. For instance, the principles of fracture mechanics are not currently applied in the design of concrete structures because none of the existing code provisions are based on these principles. To address these challenges and fully understand concrete fracture mechanisms, cracking needs to be monitored temporally and spatially. For this reason, monitoring techniques and methodologies have been proposed to verify classic theory of fracture mechanics that describe the complicated fracture process in concrete materials. Possibly the most important and widely used techniques to study and monitor the formation and growth of cracks in concrete structures are parameter-based (or qualitative) AE methods discussed in Section 5.3.

However, these purely qualitative methods cannot provide a complete understanding of fracture mechanics in concrete materials. Further developed AE techniques that can provide a complete understanding of concrete mechanics are needed. As a result, dedicated scientific research programs have been launched to provide the scientific and industrial communities with well-established techniques that can give satisfactory analyses and description of fracture processes in concrete materials. Fortunately, committed researchers have adapted signal-based (or quantitative) AE techniques, which are discussed in Section 5.4, and successfully applied them in concrete engineering. These signal-based methods, also known as quantitative methods, are more sophisticated than the traditional parameter-based methods. They provide good tools to answer more challenging questions such as how, where, and when cracks initiate and how they propagate. These methods rely on different procedures to analyze the recorded AE waveforms and extract informative parameters to constrain the mechanics of sources of cracks (type, location, orientation, intensity, etc.).

5.2 The acoustic emission (AE) measurement process

AE is defined by the American Society for Testing and Standards as "the class of phenomena whereby transient elastic waves are generated by the rapid release of energy from localized sources within a material, or the transient waves so generated ASTM (2014)." The European committee for standardization defines AE as "transient elastic waves generated by the release of energy within a material or by a process EN (2000)." Both definitions state that the term AE describes the sudden release of energy within a medium due to dynamic local arrangements of its internal structure when it undergoes

sudden stress redistributions. The energy released radiates outward in all directions in the form of elastic mechanical waves that cause vibrations of the surface as illustrated in Figure 5.6.

By coupling appropriate physical sensors to the surface of the specimen being tested, these surface displacements can be converted to electrical signals (or AE signals) that can be recorded and stored. These signals are of practical interest because of the wealth of information they contain about the source that caused them. AE can be induced by various processes such as the initiation, formation, growth and coalescence of cracks, internal friction, dislocation movements, etc. At present, it is generally recognized that AE accompanies almost all physical phenomena in solids and their surfaces (Baranov et al., 2007). Thus, recording these AE using appropriate instruments, extracting the desired information and parameters and analyzing the data constitute a very distinctive testing method, namely the AE monitoring technique, suitable for applications that involve monitoring, diagnosis, and assessment of structural elements and structures. Today, technological advancements (microelectronics, high-fidelity sensors, powerful DAQs, etc.) have led to the emergence of the AE technique as a promising nondestructive testing (NDT) technique for characterizing internal fracture among industrial, scientific, and engineering communities. The measurement process can be represented by a convolution of system response functions as follows (Grosse & Schumacher, 2013):

$$R(t) = S(t) * \mathrm{TF_M}(t) * \mathrm{TF_S}(t) * \mathrm{TF_R}(t) \tag{5.1}$$

where $R(t)$ is the recorded (digitized) signal, $S(t)$ the source signal, $\mathrm{TF_M}(t)$ the elasto-dynamic Green's functions (explained in detail in Section 5.4) that describe wave propagation in the medium, $\mathrm{TF_S}(t)$ the sensor response characteristics, and $\mathrm{TF_R}(t)$ the characteristics of the data acquisition system, including preamplifiers and filters, and "*" denotes convolution. It is important to note that every element in the measurement process has an influence on the final, stored AE waveform $R(t)$,

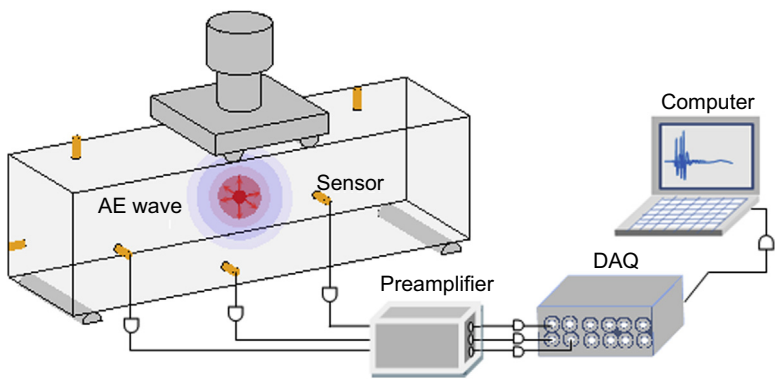

Figure 5.6 Typical acoustic emission (AE) measurement process (the cables of only three sensors are shown for simplicity).

e.g., resonant-type sensors tend to ring at their resonant frequency and can introduce significant signal distortion. This affects both parameter- and signal-based techniques.

In the following two sections, the two main methods that have been adapted from seismology to analyze AE from concrete fracture are presented: *b*-value analysis (Section 5.3) and moment tensor inversion (MTI) (Section 5.4). The first is considered a qualitative (or parameter-based) method that characterizes large numbers of events (earthquakes or AE) using an empirical log-linear frequency−magnitude distribution, from which parameters describing the distribution can be determined (such as mean occurrence time, maximum event size, relative numbers of small to large events, etc.). The dimensionality of populations of events and the ambient stress state of the material can also be inferred. The *b*-value analysis does not attempt to explain the physics of individual events but describes overall patterns of large numbers of events statistically. In contrast, MTI studies individual events and aims to characterize the exact nature of those in terms of temporal and spatial coordinates and mechanism. This method is considered quantitative (or signal-based) and assumed to most accurately represent the mechanics of an event.

5.3 *b*-Value analysis

5.3.1 Introduction and background

Gutenberg and Richter (1949) originally proposed an empirical relationship, in seismology referred to as the Gutenberg−Richter frequency−magnitude relation, to analyze distributions of earthquake populations. After analyzing large numbers of earthquakes in the temporal as well as the spatial domain, they found that the slope of the cumulative frequency−magnitude relationship is usually equal to unity, i.e., $b \approx 1$, in seismically active regions (Stein & Wysession, 2003):

$$\log_{10}(N) = a - b \cdot M_{\mathrm{L}} \tag{5.2}$$

where $M_{\mathrm{L}} = \log_{10} A(r) - \log_{10} A_o(r)$ is the local magnitude of the earthquake. Several magnitude scales are used in seismology: Richter scale, body wave magnitude, surface wave magnitude, local magnitude, duration magnitude, moment magnitude, etc. A is the amplitude of the maximum recorded ground motion (μm), and $A_o(r)$ is an empirical function to correct for the distance r between the recording instrument and the earthquake epicenter. Local magnitude is essentially a measure of the amount of energy released during an earthquake and can be thought of as the strength of the event. N is the number of earthquakes that have a magnitude greater than M_{L}, and a and b are empirical constants to be estimated from the data, where a is the intercept and represents the overall seismicity rate of the region, and b describes the slope of the magnitude−frequency diagram or ratio of small and large earthquake magnitudes (Stein & Wysession, 2003). The magnitude is often calculated in the time domain by integrating the square of the recorded velocity.

A more robust measure of magnitude is moment magnitude, which is calculated in the frequency domain from the spectral plateau of the integrated velocity (i.e., displacement). Each component of the total seismic moment $M_{0\ ijk}$ is calculated for each geophone site i, channel j, and wave-phase k using the following:

$$M_{0\ ijk} = 4\pi\rho v_k^3 r_i \frac{\Omega_{0\ ijk}}{f_{\theta\phi\ k}} \tag{5.3}$$

where ρ is the density of the material (kg/m^3), v is the wave-speed of the P or S phase (m/s), r_i is the hypocentral distance (m), $f_{\theta\phi}$ accounts for the radiation pattern ($f_{\theta\phi 1} = 0.37$ for P-waves and $f_{\theta\phi 2} = 0.57$ for S-waves, Spottiswoode & McGarr, 1975), and Ω_0 is the integrated displacement, $\Omega_0 = \int u\mathrm{d}t$, calculated from the low-frequency displacement spectral plateau for windows over the P and S phase. The moment M_{0ijk} for each phase k of the event, for each geophone site i, is the computed from the vector sum of the moments for each recording channel:

$$M_{0\ ik} = \sum_{j=1}^{3} M_{0\ ijk} \tag{5.4}$$

The total moment M_0 for an event is the sum of its P and S moments, averaged over all geophone sites:

$$M_0 = \frac{1}{2N} \sum_{i=1}^{N} \sum_{k=1}^{2} M_{0\ ik} \tag{5.5}$$

where N is the number of active geophone sites. The moment magnitude can then be calculated from the moment using an empirical relation, for example, $M_\mathrm{L} = 0.77 \log_{10} M_0 - 7.07$.

Typically, the absolute value for the slope of the Gutenberg–Richter relationship, b, is used in b-value analysis. An example of a cumulative frequency–magnitude diagram is given in Figure 5.7. The point of deviation of the curve from the linear trend gives an indication of the minimum event magnitude (indicated as dashed line) reliably recorded by the network, i.e., network sensitivity.

A striking feature of the Gutenberg–Richter frequency–magnitude relation is the logarithmic decay. Such patterns are common in nature and are scale-invariant, i.e., the pattern remains the same regardless of the scale from which it is viewed. This is also called fractal scaling or self-similarity and can be quantified using the fractal dimension D (Stein & Wysession, 2003). The fractal dimension provides a measure of the degree of fractal clustering of epicenters in space and can be calculated from the b-value using $D = 2b$. Studies in mining seismology (e.g., Spottiswoode, Milev, Linzer, & Majiet, 2009) have shown that $D \approx 1$ for populations of events associated with linear structures where the length L is much greater than the width W. Events on

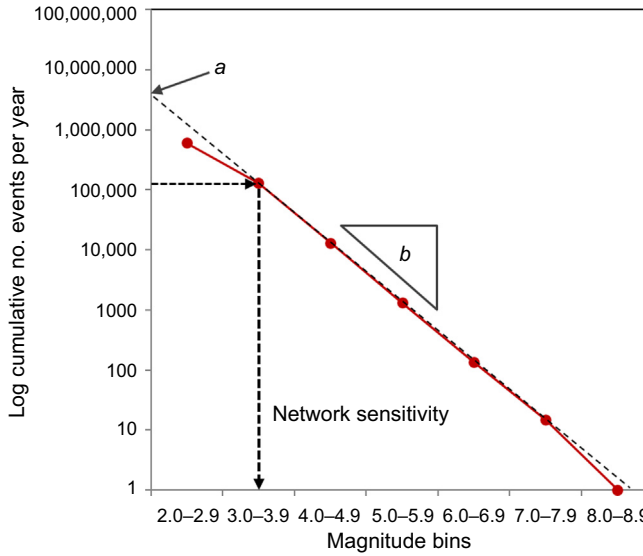

Figure 5.7 Example of cumulative frequency-magnitude diagram (or Gutenberg−Richter distribution) in seismology, world earthquake rates.
Data from USGS (1900−1990). Table of data from the USGS Website titled "Frequency of occurrence of earthquakes." Graph plotted by L. Linzer using Excel.

planar features having $L \sim W$ have $D \approx 2$ (e.g., a fault surface, failure along mine abutments or long walls). Events distributed volumetrically where $L \sim W \sim S$ (and S is the spacing of shear zones) showed $D \approx 3$ (e.g., crush pillars).

5.3.2 Applications in materials science and engineering

Parameter-based methods applied to AE in concrete have focused on the study of the b-value, hence the term b-value analysis. Mogi (1962) showed that the b-value is influenced by the degree of heterogeneity and crack density in the medium. Scholz (1968) demonstrated the strong similarities between natural earthquakes and fracture of rock and suggested that the state of stress, rather than the heterogeneity of the material, played the most important role in the magnitude of the estimated b-values. Although the b-value is generally close to 1, it has been found to vary spatially and with depth (Wiemer and Wyss, 1977). Areas having $b < 1$ imply a shorter recurrence time between events. Such areas have been interpreted as patches of stress concentration or asperities on the fault plane and could possibly indicate variation in frictional properties. Similar approaches were later proposed to study slope stability problems in geotechnical (Miller et al., 2005; Rao & Lakshmi, 2005; Shiotani and Ohtsu, 1998) and fracture processes in material science applications for a variety of materials (e.g., Carpinteri et al., 2009; Cox & Meredith, 1993; Hardy, 1971; Kurz, Finck,

Grosse, & Reinhardt, 2006; Pollock, 1981; Shiotani, Yuyama, & Ohtsu, 2000). *b*-Value analysis is also widely used in mining seismology (e.g., Gibowicz & Kijko, 1994; McGarr, 1984; Nuannin, Kulhanek, Persson, & Tillman, 2002). Establishing the *b*-value for a mining area underground is important in seismic hazard assessment because high levels of ground motion are often associated with damage or rock mass weakening that occurs as a result of seismic events of high magnitude (Kijko & Funk, 1995).

5.3.3 Methodology for application to concrete

The idea of applying *b*-value analysis to AE signals from concrete fracture was first explored by Pollock (1981). Shiotani et al. (2000) proposed an *improved b-value* method for the analysis of fracture processes in concrete and Colombo, Main, and Forde (2003) applied it to a mid-size reinforced concrete beam. The improved *b*-value method proposed that the *b*-value could be calculated from the slope between two points in the distribution curve corresponding to the mean magnitude plus and minus one standard deviation. Colombo et al. (2003) proposed a linear least-squares curve fit to estimate the *b*-value rather than two fixed points. Kurz et al. (2006) studied *b*-values to characterize cracking from a small fiber-reinforced concrete beam and highlighted the need to consider attenuation in large structures. Schumacher, Higgins, and Lovejoy (2011) used a linear least-squares curve-fit over a range of data as suggested by Rao et al. (2005) to analyze *b*-values from full-scale reinforced concrete bridge girders. Since then, other researchers have employed *b*-value analysis and have suggested alternative ways to interpret the results, e.g., Farhidzadeh, Salamone, et al. (2013).

The maximum hit amplitude $A(\mathrm{dB})$ is commonly used in *b*-value analysis for AE applications and is multiplied by a factor of 1/20 to emulate the earthquake magnitude M_L (Colombo et al., 2003; Weiss, 1997). The scaling is empirical and applied so that *b*-values from concrete fracture are in the same range as seen in seismic applications. Thus, the relationship is usually referred to as amplitude−frequency distribution. The amplitude $A(\mathrm{dB})$ is defined as:

$$A(\mathrm{dB}) = 20 \cdot \log_{10}\left(A\ (\mathrm{mV})\right) + 60\ \mathrm{dB} - G(\mathrm{dB}) \tag{5.6}$$

where $A(\mathrm{mV})$ and $G(\mathrm{dB})$ represent the measured sensor output voltage and the signal gain provided by the preamplifiers, respectively. As for earthquake magnitude, the AE signal amplitude is represented on a logarithmic scale. The main difference is that the distance between the source and the AE sensor is not accounted for as it is in the computation of *b*-values from earthquakes (Weiss, 1997). As enumerated by several authors (Landis & Shah, 1995; Lovejoy, 2006; Schumacher, 2008; Uomoto, 1987), attenuation in concrete is significant and *b*-value analysis could be improved if attenuation were to be taken into account. Also, the signal amplitude $A(\mathrm{mV})$ from AE sensors is often not well defined and can be either acceleration, velocity, displacement, or a combination thereof (Schumacher, 2008). Recall that in order for Eqns (5.2)−(5.5) to apply, in theory, displacements are required. The only way to ascertain which of these dynamic quantities $A(\mathrm{mV})$ represents is by performing an absolute calibration

under realistic conditions, as presented in McLaskey and Glaser (2012). Once the sensor response has been calibrated in this manner and the sensor response function $TR_S(t)$ is established, it can be accounted for in Eqn (5.1).

The application of *b*-value analysis to concrete fracture mechanics relies on the assumption that a change in the *b*-value indicates a change in the concrete's cracking behavior. Several researchers have reported that a decrease in the *b*-value below a value of approximately 1.0 may indicate that stresses are redistributed, and the cracking is more localized (e.g., Spottiswoode et al., 2009). In the field of reinforced concrete, *b*-value analysis has been studied by several researchers to monitor structural deterioration using AE monitoring (ASNT, 2005; Colombo et al., 2003; Kurz et al., 2006; Schumacher et al., 2011; Shiotani et al., 2000).

The *b*-value for each set of AE amplitude−frequency distributions was estimated by a linear least-squares curve-fit over the mean ± one standard deviation, as proposed by Colombo et al. (2003) and Rao and Lakshmi (2005). Standard errors are given as $SE = b/\sqrt{n}$, where n is the number of samples (equal to consecutive AE hit amplitudes) used for the computation. Suggested values for n found in the literature range from 50 to 100 (Colombo et al., 2003; Kurz et al., 2006; Rao & Lakshmi, 2005).

Figure 5.8 shows two examples of estimated *b*-values using $n = 50$ collected at different instances during a large-scale laboratory experiment on reinforced concrete bridge girders (Schumacher, 2008). The two plots illustrate how the *b*-value changes when the ratio of the number of strong to weak events changes: high (Figure 5.8(a)) and low (Figure 5.8(b)) *b*-values have been associated with micro-cracking (distributed damage) and macro-crack formation and propagation (localized damage), respectively, as proposed in Carpinteri et al. (2006), Cox and Meredith (1993), Kurz et al. (2006); Pollock (1981); Rao and Lakshmi (2005) Rundle et al. (2003).

b-Value analysis appears particularly appealing for implementation in a structural health monitoring (SHM) system because it is computationally inexpensive, and theoretically, the analysis can be performed using one sensor. An example of such a continuous estimation of *b*-values for a full-scale reinforced concrete bridge girder (discussed in detail in Section 5.3.4) tested in the laboratory is illustrated in Figure 5.9. A selected portion of the complex loading protocol is shown, the a full details of which can be

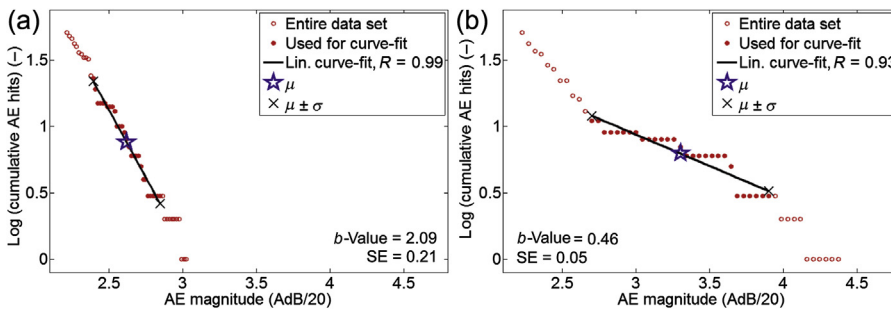

Figure 5.8 Examples of cumulative amplitude−frequency diagrams for AE from reinforced concrete: (a) high *b*-value produced during service-level load, and (b) low *b*-value produced during the application of an overload (OL).

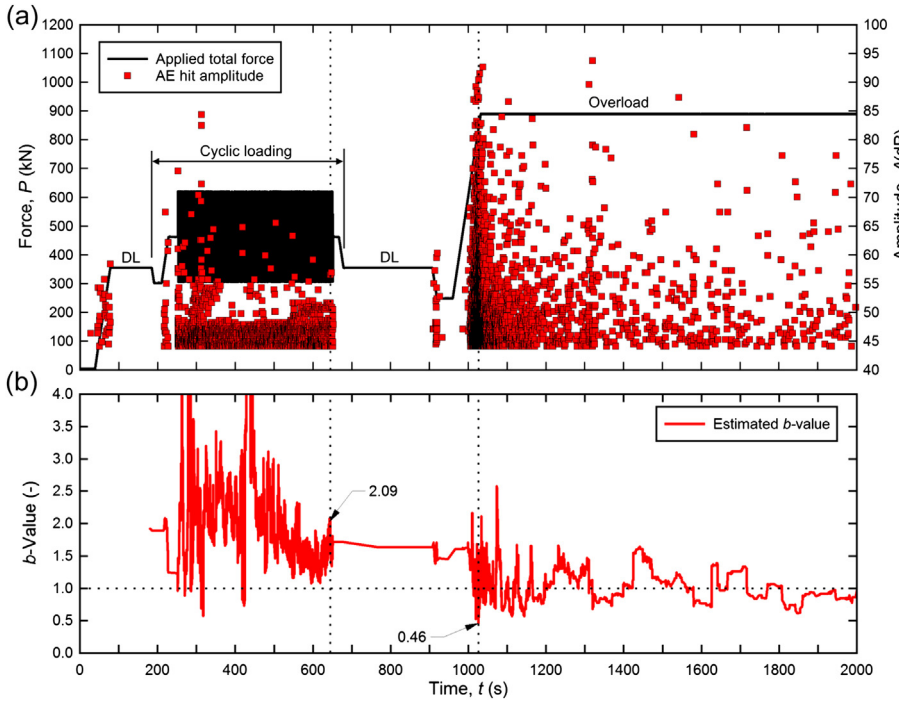

Figure 5.9 (a, b) Example of continuous *b*-value analysis for a full-scale reinforced concrete bridge girder.
Data source: Schumacher (2008).

found in Schumacher (2008). Figure 5.9(a) and (b) show the total applied force and the recorded AE hit amplitudes for one selected sensor, respectively. After applying a dead load (DL) of 356 kN, the girder was loaded between 302 and 623 kN over 2000 cycles to represent ambient traffic. Finally, an overload (OL) of 890 kN was applied to impose new deterioration in the form of cracking. Figure 5.9(b) shows the estimated *b*-values for the selected sensor. The vertical dashed lines indicate the time instances at which the individual b-values shown in Figure 5.8 were computed. It can be observed that the drop in the estimated *b*-value is a good predictor of the point of maximum applied total force, which caused the propagation of existing cracks. During the earlier service-level loads, the *b*-value typically exceeds 1, with a few exceptions. These exceptions could be due to redistribution of stresses in the concrete during repeated loading or noise from the experimental setup.

5.3.4 *Application example: monitoring of reinforced concrete bridge girders*

For routine inspections of in-service bridges, a method called *minimum b-value analysis* was proposed by Schumacher et al. (2011) to quantify the effect of a passing

vehicle on the monitored bridge component or section. The procedure was evaluated on a full-scale reinforced concrete bridge girder in the laboratory. Figure 5.10 shows the experimental setup, the girder specimen, and the sensor locations for one of the specimens. More details can be found in Schumacher (2008). A baseline dataset was created using a realistic loading scenario simulating service-level test trucks (TT) as well as overloaded (OL) trucks.

As explained earlier, a drop in the *b*-value may indicate the localization of damage, i.e., macro-crack formation and propagation. The idea is that the current operating load level of a bridge component can be estimated by computing the *minimum b-value* for TT of known weight driven across the bridge. The *minimum b*-value is defined as the mean of the lowest *b*-values from one complete load event for each of the AE sensors (Schumacher et al., 2011). The standard deviations are also calculated to measure the spread of the data. In contrast to the *b*-value monitoring approach presented in Section 5.3.3, the number of AE hit amplitudes *n* is not fixed to 50 but set to the duration of the considered load event. The study found that when all sensors were included in the computation, a better representation of actual structural deterioration is achieved. Figure 5.11 summarizes the findings of the research. *LR*2 and *LR*3 represent the ratios of *applied force/previously applied overload* and *previously applied overload/ultimate capacity*, respectively. The following example explains the procedure: Assume a TT has a load of 600 kN and is used during a load test of a bridge girder, and the estimated minimum *b*-value is computed as 1.5. Further assuming that the load ratio $LR3 = 0.4$, load ratio *LR*2 is found to be 0.75. This would suggest that the largest previous load the girder has experienced is 600 kN/0.75 = 800 kN. The difficulty with this approach is the estimation of the level of deterioration, which is related to the highest previous load that the bridge girder has experienced and is represented by the load ratio *LR*3.

For comparison purposes, the method was also applied to AE data collected during a structural load test of a real bridge (Schumacher, Higgins, & Lovejoy, 2013). Although it appears that the *b*-values are sensitive to high loads, which may result in macro-cracking, they are also subject to noise as produced by cars with studded tires

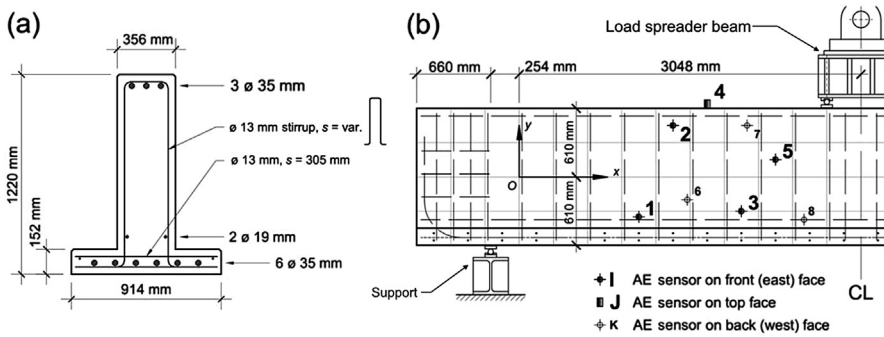

Figure 5.10 Full-scale laboratory reinforced concrete bridge girder: (a) cross-section and (b) elevation view of girder specimen.

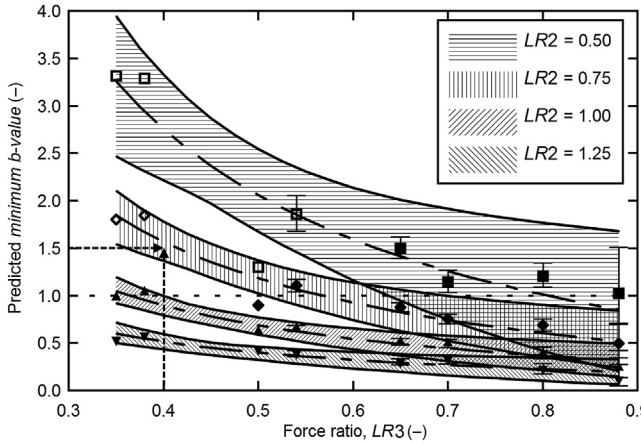

Figure 5.11 Diagram showing how *minimum b-values* relate to operating load conditions and proximity to the ultimate capacity of the girder specimens.
Adapted from Schumacher et al. (2011).

(Schumacher, Higgins, et al., 2010). However, these can be easily discarded by measuring strain or displacement in addition to recording AEs.

5.3.5 Summary and conclusions

The following conclusions can be drawn from *b*-value analysis:

- *b*-Value analysis appears particularly well-suited for the real-time monitoring of concrete fracture processes due to its simplicity and, thus, ease of implementation.
- *b*-Values are sensitive to high loads, in particular loads that significantly exceed a previously experienced level, i.e., the *b*-value typically drops notably below 1 (often below 0.5) when macro-cracking occurs.
- *b*-Value time histories are dependent on the sensor location and, thus, vary from sensor to sensor. Threshold values should thus be established empirically during long-term monitoring and simultaneous observation of the structure's performance.
- The application presented in Section 5.3.4 may help estimate the operating conditions of the monitored element but cannot predict impending failure. Hence, it is unreasonable to use this approach to estimate ultimate capacity. However, it may still provide useful information during regular operation or in-service structural load testing.
- It is crucial that other physical measurements along with AEs, such as strain or displacement, are recorded to verify high amplitude AE events that may be caused by external sources.

5.4 Moment tensor inversion

5.4.1 Introduction and background

The MTI method is a well-established quantitative seismological technique that has shown great potential for providing a full understanding of the fault mechanisms in

seismology (e.g., Gibowicz & Kijko, 1994). The method was pioneered by Dziewonski and Gilbert (1974), further developed by Aki and Richards (1980), and is now routinely applied by seismologists to study earthquake source mechanisms. Ohtsu (1991) successfully adapted the MTI technique for concrete mechanics. He developed an MTI-based code called SiGMA (Simplified Green's functions for Moment Tensor Analysis), which he used to study cracking mechanisms in concrete at the meso-scale. Ever since his leading work, the MTI technique has been the subject of increasing interest in the field of materials science, especially in concrete mechanics, and has been applied by many other authors for the analysis and the study of different types of fractures and cracking mechanisms. Grosse has done remarkable work on the quantitative analysis of AE from concrete elements using the MTI technique. He applied a relative MTI code developed by Dahm (1996) that computes source mechanisms of clusters of events. Yuyama, Li, Ito, and Arazoe (1999) has used MTI extensively to study the fracture mechanics of concrete beams reinforced with FRP sheets and reinforced concrete column foundations.

5.4.2 Methodology for application to concrete

MTI is a quantitative method used to invert recorded surface displacements generated within a test specimen due to ongoing rapid internal strain releases to identify and characterize the sources of AE within the specimen. These techniques are routinely performed in global and mining seismology to characterize earthquake source mechanisms. Due to the profound analogy between earthquakes and AE, these quantitative techniques are being adapted to study the fracture of materials and structures. The application of MTI to engineering materials, however, is a relatively recent innovation. Only a few works related to the use of MTI in fracture mechanics studies of materials have been published (e.g., Grosse, Reinhardt, & Dahm, 1997; Ohtsu, 1998; Sellers, Kataka, & Linzer, 2003; Yuyama et al., 1999), the reason being that the inversion methods are notoriously tedious and prone to errors Andersen (2001).

In 1970, Gilbert introduced the moment tensor concept as a physical representation of an earthquake source and outlined the forward problem, where displacements at the Earth's free surface are expressed as the sum of the moment tensor components multiplied by their corresponding Green's functions. Aki and Richards (1980) later proposed a theoretical expression of the seismic displacement u_k:

$$u_k(x,t) = \sum_{n=0}^{\infty} \frac{1}{n!} G_{ki,j1\ldots jn}(x,t;\xi,t') * M_{ij1\ldots jn}(\xi,t') \tag{5.7}$$

where $G_{ki,j1\ldots jn}(x,t;\xi,t')$ are the components of the elasto-dynamic Green's functions, which describe propagation effects between the source (ξ,t') and the receiver (x,t), and $M_{ij}(\xi,t')$ are the moment tensor components of the source. Note that Einstein summation notation applies.

Further simplifications and assumptions (elastic infinite media, point-source, far-field, synchronous source approximation, etc., see Aki and Richards (1980) for more details) applied to Eqn (5.7) give:

$$u_k(x,t) = G_{ki,j}(x,t) \cdot M_{ij} \tag{5.8}$$

$$u_k(x,t) = \sum_{i=1,\, j=1}^{3,3} G_{ki,j}\left(x,t;\xi,t'\right) \cdot M_{ij} \tag{5.9}$$

The linear relationship between the moment tensor and the Green's functions was first used by Gilbert (1970) to compute moment tensors from recordings of seismic displacements. In this process, Eqn (5.9) is written as an inverse problem and solved using matrix algebra methods. Essentially, the moment tensor components are inverted from recorded displacements and estimated Green's functions.

The seismic moment tensor of a real source is defined as a combination of force couples and dipoles called equivalent forces, which produce displacements at a given point identical to the displacements produced by the actual forces acting at the source, as illustrated in Figure 5.12.

Figure 5.13 shows two distinct sources as explained by the moment tensor: (a) pure shear and (b) pure explosion.

Different disciplines use different terms to describe cracking behavior. Using fracture mechanics terminology, mode II refers to shear cracks, where the forces are parallel to the crack (also called in-plane shear), and mode III describes forces that are normal to the crack surface (out-of-plane shear) (Linzer et al., 2013). In seismology, shear dislocations are referred to as double couple sources. A double couple would consist of two force couples (e.g., M_{xy} and M_{yx}) and is the preferred force system. It is based on observational and theoretical evidence and a thorough understanding of the radiation pattern of P- and S-waves generated by the two types of sources (Linzer et al., 2013). The double couple formulation also allows the simplification of some complex equations and is directly compatible with the tensor formulation for stress and strain used in rock mechanics (e.g., Aki & Richards, 1980; Jäger & Cook, 1976).

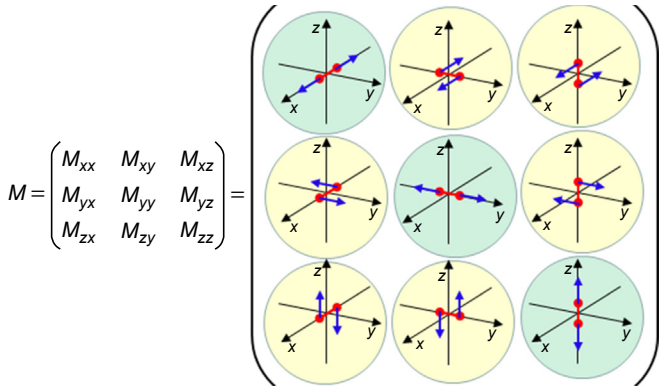

Figure 5.12 Representation of the moment tensor in canonical and spatial forms.

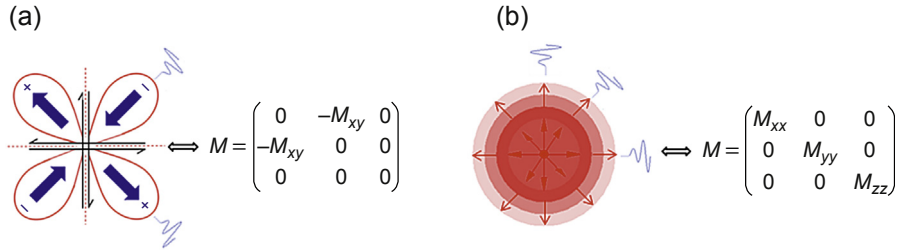

Figure 5.13 Radiation patterns and moment tensors of two distinct sources: (a) pure shear and (b) pure explosion.

It is convenient to view the moment tensor as a radiation pattern around the source i.e., as a 3-D spherical pattern in space that shows the amplitudes and directions of the P-wave field (S-waves are less commonly used). This 3-D sphere is then projected onto a 2-D plane using a stereographic projection (Figure 5.14). Fault-plane solutions, which describe the orientation of the nodal planes (planes in the radiation pattern where there is zero displacement), are also calculated. Due to the symmetry of the radiation pattern, two fault plane solutions are calculated, where only one of which corresponds to the actual fault plane in reality.

Different types of sources produce characteristic patterns, for example, a normal fault (mode II shear where the shear stress is perpendicular to the plane of fracture) resulting from extension would produce the pattern shown in Figure 5.15. The points halfway between the nodal planes are the P- and T-axes, the compressional and tensional axes, respectively.

An important difference exists between seismology and fracture mechanics: the directions of maximum and minimum compressive stress determined from the moment tensor are 45° to the slip plane, whereas laboratory experiments show that the fracture plane is often about 25° from the maximum principal stress direction (Seth & Wysession, 2002).

A large number of MTI methods have been proposed since the pioneering paper of Dziewonski and Gilbert (1974). The methods are tailored to the available data and differ according to models of the seismic source; approaches used to evaluate the Green's functions; noise reduction schemes; and whether the methods are applied in the time or frequency domain, to full waveforms or selected phases.

We recognize two broad classes of MTI according to whether the methods are applied to single events or clusters of recorded events: absolute methods (e.g., Dziewonski & Gilbert, 1974) and relative methods (e.g., Patton, 1980). Absolute

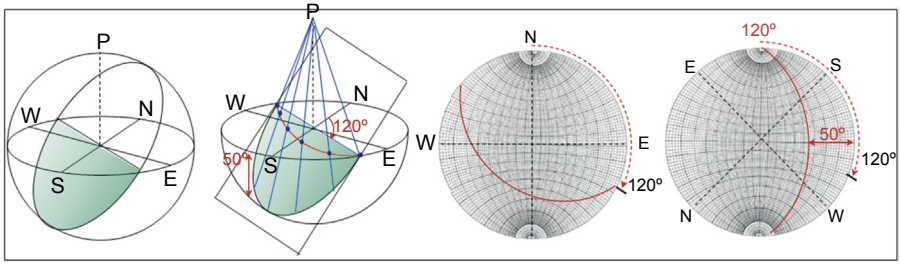

Figure 5.14 Illustrative stereographic projection of a plane having strike of 120° and dip of 50°.

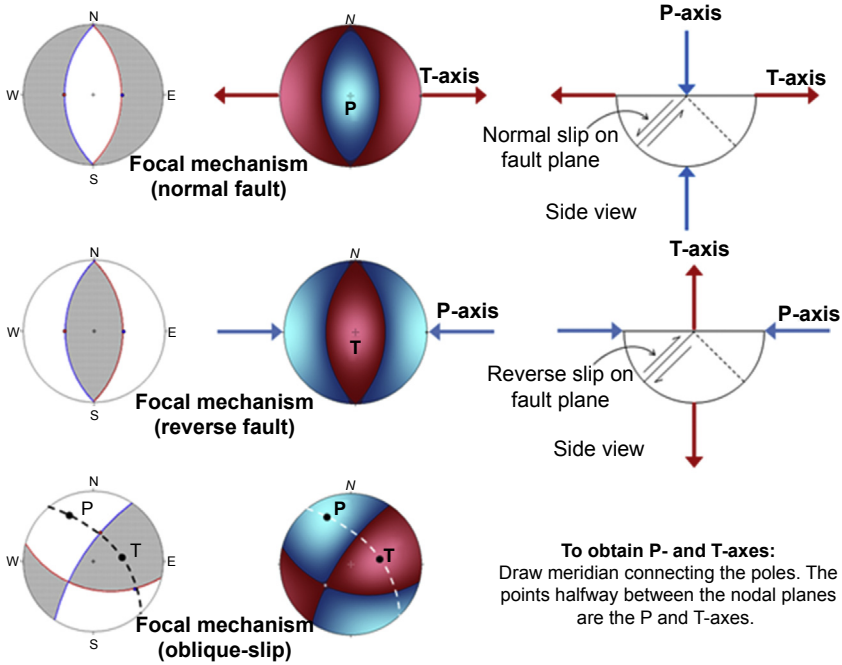

Figure 5.15 Simplistic relationship between the P- and T-axes and normal, reverse, and oblique slip fault types. The P- and T-axes can be obtained by drawing a meridian line that connects the poles to the fault planes. The points halfway between the nodal planes are the P- and T-axes. Redrawn and modified from Stein and Wysession (2003).

methods apply to individual events and require that the Green's function be estimated, either theoretically or empirically. Relative methods apply to spatial clusters of events and assume that all the events in the cluster experience the same wave propagation effects to a given receiver, allowing the Green's functions of a reference event to be used as estimations for other events in the cluster. Under special conditions, the Green's functions can be eliminated analytically avoiding the explicit use of Green's functions (Dahm, 1996).

The hybrid method by Andersen (2001) is a combination approach that applies the absolute method to individual events in a spatial cluster, and then, it computes and applies a relative correction to improve the individual solutions. The correction is essentially a weight, based on the statistical distribution of the residuals between the theoretical and recorded displacements, for events in a cluster having common ray paths. The hybrid method was initially developed for high-frequency mining-induced data recorded by underground networks. Data recorded in the harsh, deep-level mining environment are noisy and suffer from scattering due to mining-induced fracturing associated with the excavations, and often only one channel of a triaxial sensor is operational.

The high-frequency nature of AE and difficulties in identifying wave phase types spurred the development of the simplified MTI method by Ohtsu (1991). Ohtsu's

method is called simplified Green's functions for moment tensor analysis (SiGMA), where concrete cracking is categorized as either tensile, shear, or mixed-mode. This method falls into the class of absolute methods and uses only the P-wave amplitudes in the time domain. An example of how the results are visualized using virtual reality modeling language can be found in Ohtsu and Shigeishi (2003).

Table 5.1 summarizes the strengths and limitations of the different MTI methods, according to the broad classification outlined in this paper. The main difference between these techniques is how the Green's functions are evaluated. The accurate evaluation of these functions using theoretical equations is complex for nonhomogeneous media or media with changing boundary conditions, i.e., due to cracking in concrete. In addition, assumptions are usually made (use of Taylor series, truncation at the first order, etc.) to simplify the problem and reduce the computational time for numerical techniques.

Table 5.1 Comparison of different moment tensor inversion (MTI) techniques

	Strengths	Limitations
Absolute MTI methods	• Applied in single event situations	• Difficult to apply in nonhomogeneous environments • Tedious evaluation of the Green's functions for every AE event • Require a dense network of AE sensors • Noise-sensitive
Relative MTI methods	• Green's functions can be estimated from a reference event, either empirically or theoretically • In special cases, the Green's functions can be eliminated analytically (no need to evaluate them) • Applied to clusters of AE events	• Require a cluster of events, i.e., cannot be applied in single event situations • Events in the cluster must have different radiation patterns • Extremely sensitive to noise if source mechanisms of the cluster events are very similar
Hybrid MTI methods	• Capitalize on the strengths of both the absolute and relative MTI methods • Compensate for different types of systematic errors in the AE waveforms • Achieve accurate and robust measure of the moment tensor	• Require the evaluation of the Green's functions

5.4.3 Application example: fracture of a small notched concrete beam

This case study represents a proof-of-concept that aims to evaluate the usefulness of an MTI-based methodology in characterizing AE sources (fracture, cracks, etc.) Linzer, Mhamdi, & Schumacher (2015). The experiment consists of loading a notched concrete beam of dimensions $6 \times 6 \times 21$ in^3 in a three-point bending configuration (Figure 5.16). The notch was predefined at mid-span and serves as a crack initiator so that the beam fails in pure flexure in the standard "Mode 1" protocol. The beam was driven to failure very slowly to allow the collection of the maximum number of AE events to best reproduce the cracking pattern. The beam was equipped with 12 high-fidelity Glaser/NIST point-contact sensors mounted on the six sides.

The components required to collect AE data along with key characteristics of the measurement system are summarized in Table 5.2.

Typical AE sensors work on the piezoelectric effect, i.e., when a piezoelectric material is deformed it produces an output voltage proportional to the experienced deformation. Most commonly, lead zirconium titanate (PZT) is used for the sensing element. In this experiment, Glaser/NIST sensors are used. These have been be absolutely calibrated (McLaskey & Glaser, 2012) and have shown to have a relatively flat response (within 3 dB) over a frequency response from 20 kHz to 1 MHz with respect to displacement. Figure 5.17 shows the sensor and its basic response characteristics. These sensors were selected specifically because of their high-fidelity response characteristics that would ensure quantitative procedures such as MTI, which rely on unbiased measurements, could be applied.

To evaluate the feasibility of AE monitoring for fatigue crack detection, a number of algorithms had to be developed first. Subsequently, the required steps to perform quantitative AE analyses are described in detail.

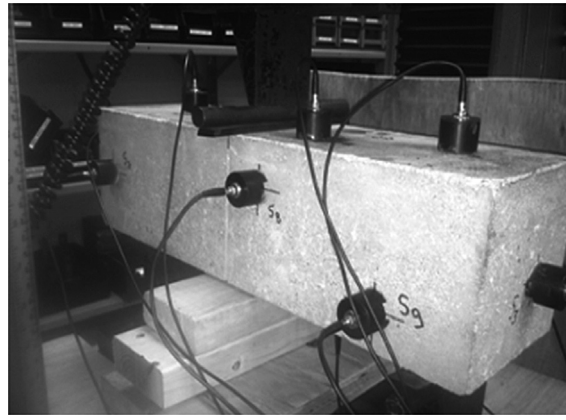

Figure 5.16 Concrete beam in a three-point bending scenario.

Table 5.2 Components and key characteristics of acoustic emission (AE) data acquisition system

Element	Key characteristics
Glaser/NIST sensors, KRN Services, Inc.	• Point-contact sensor • Conical piezoelectric crystal with built-in JFET • High-fidelity broad-band response • High sensitivity
Preamplifiers, KRN Services, Inc.	• Wideband amplification (up to 2 MHz) • Input noise less than 10 mV • Output voltage up to 22 V
Analog filters, Krohn-Hite Corp.	• 15 channels • 20 kHz high-pass 8-pole Butterworth filter
Data acquisition system, Elsys Instruments, LLC	• 16 channels with 14-bit @ 40 MHz/16-bit @ 5 MHz • Up to 128 MS acquisition memory per channel • Flexible parallel triggering mode using all channels for event-based recording • LAN Ethernet connection
Personal computer, Dell Corp.	• Windows 7 Enterprise • Intel® Core™ i7 CPU 2.93 GHz processor • 8 GB RAM

5.4.3.1 P-wave arrival-time picking

Figure 5.18 shows typical AE signals recorded from one sensor with (a) high and (b) low signal-to-noise ratios. The recorded signal clearly shows the arrival of the first body wave mode, the compression, or P-wave. The first step in quantitative AE analysis is to pick these P-wave arrivals (i.e., identify the first onset of the P-wave in time) since they represent the first undisturbed signal that arrives at a sensor. Subsequent modes such as the shear (S-) wave or the surface (R-) wave can be difficult to observe and often contain boundary reflections. An algorithm was implemented in MATLAB to (1) pick the P-wave arrivals based on the Akaike Information Criterion (AIC) (Akaike, 1974) and (2) estimate AE source locations based on Geiger's method (Geiger, 1912). The P-wave picker that was developed for this research consists of computing the AIC function as illustrated in Figure 5.18. The minimum value of the AIC function represents the estimated P-wave arrival. The idea has been used in the AE community for many years and has shown to perform more accurately and reliably compared to other picking schemes Schechinger (2006).

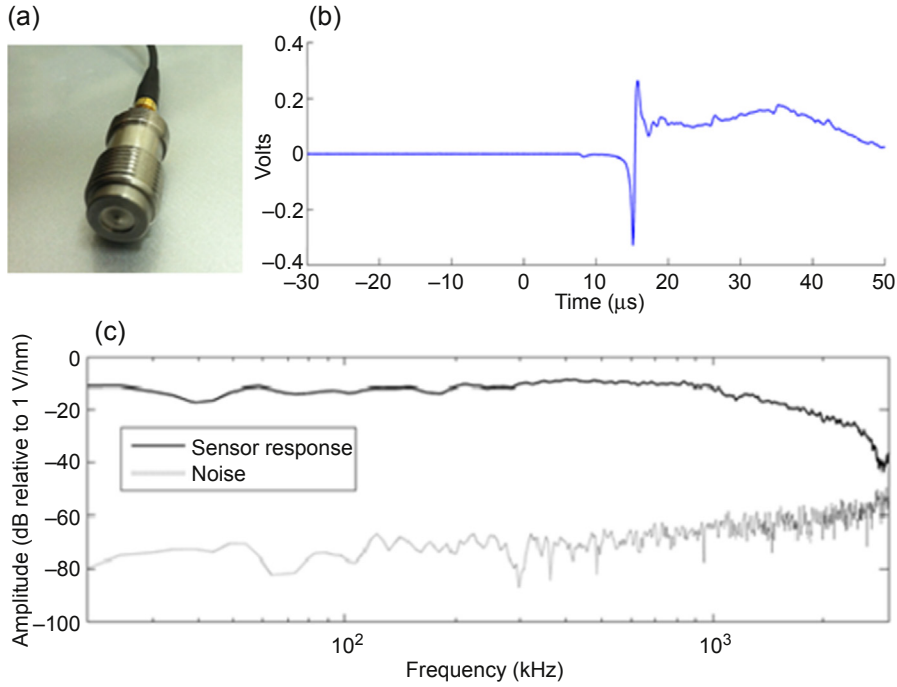

Figure 5.17 The Glaser/NIST point-contact sensor: (a) photo of the sensor connected to cable, (b) typical time-history due to a steel ball drop on a thick steel plate, and (c) typical spectral response obtained from the fracture of a radially loaded glass capillary tube.
Data source: KRN Services, Inc.

Once all the P-wave arrivals have been picked accurately (as illustrated in Figure 5.18), AE events are formed or associated. An event is a group of AE signals that are associated with a common source, i.e., depending on the sensor network, these signals must arrive at every sensor within a specified time period. Because our data acquisition system allows for event-based triggering and recording, events were discriminated and stored as such by the data acquisition system. Next, the source origin (in time and space) can be estimated using an iterative scheme.

5.4.3.2 Estimation of AE source locations

Methods used to determine earthquake epicenters are also applicable to this problem. The aim of event source location techniques is to associate an AE event, formed from a collection of AE signals that arrive within a certain time window, with a physical cause. When the source location is known, the P-wave velocity can be estimated easily using the distance between the source and the sensor and the arrival time of the wave. In Figure 5.19, the calculated velocity is approximately 4549 m/s, which is expected for typical normal strength concrete.

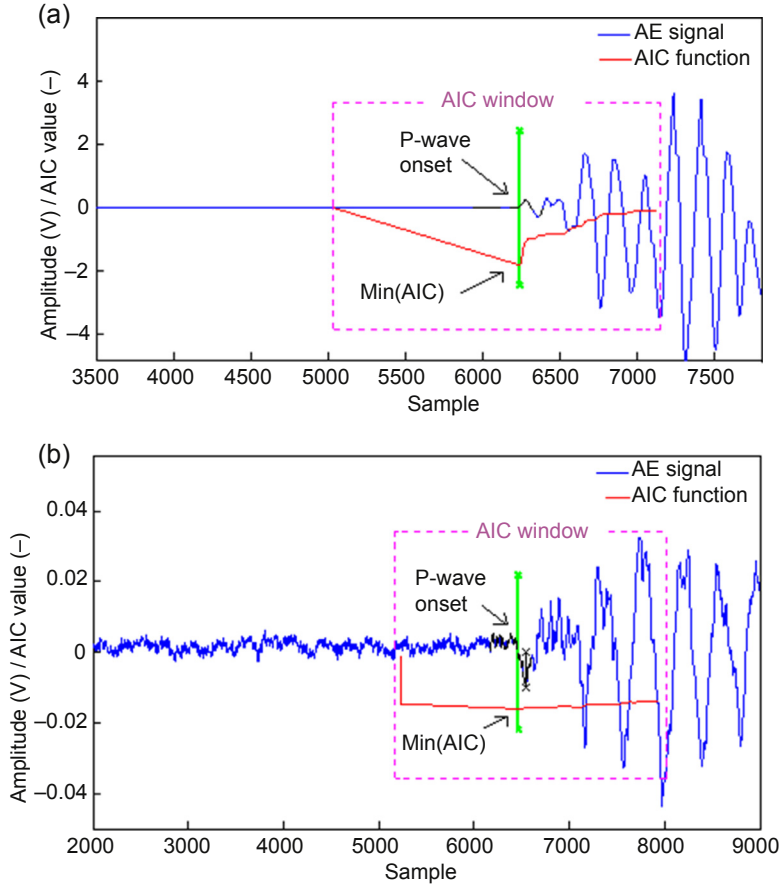

Figure 5.18 P-wave arrival estimation for signals with (a) high and (b) low signal-to-noise ratios.

Although probabilistic source location algorithms have been developed and applied to AE (see e.g. Schechinger (2006) and Schumacher, Straub, & Higgins (2012)), most commonly deterministic methods are employed based on Geiger's method. Geiger's source location method (Geiger, 1912) requires at least four signals to estimate three-dimensional source locations: three spatial coordinates and event time. A detailed description of this source location scheme can be found in Ge's paper (Ge, 2003). The fundamental assumptions are that the medium is elastic, heterogeneous, and isotropic. The governing equation used in Geiger's method is the so-called arrival-time function:

$$f_i(x) = f_i(x_0, y_0, z_0, t_0) = t_0 + \frac{\sqrt{(x_i - x_0)^2 + (y_i - y_0)^2 + (z_i - z_0)^2}}{c_P} \quad (5.10)$$

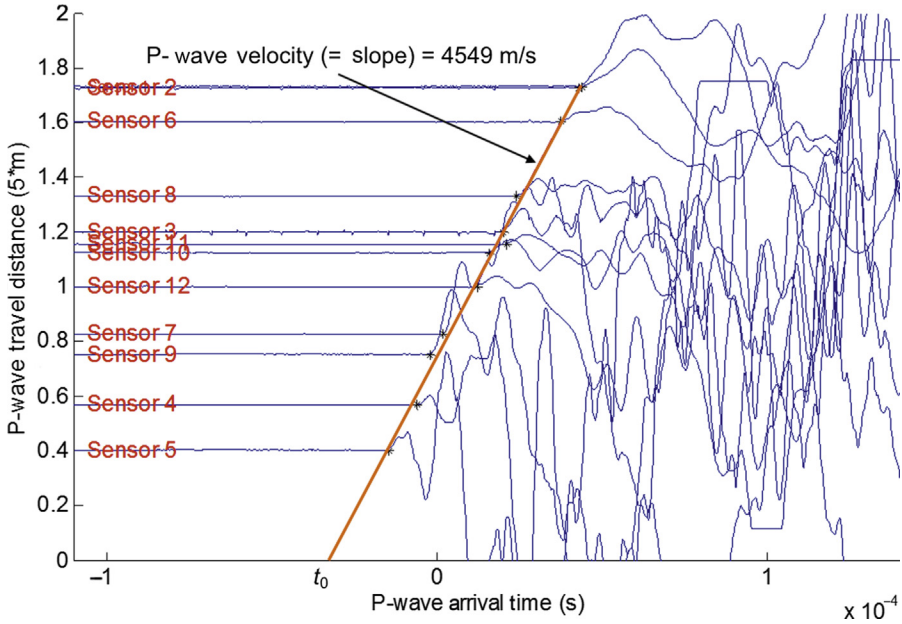

Figure 5.19 Example of recorded AE signals from the concrete beam. The *x*-axis shows time and the *y*-axis shows the calculated distance from the source each of the sensors. The red line is a linear curve fitted through the arrival times of the P-wave, such that the slope represents the P−wave velocity.
Linzer, Mhamdi, & Schumacher, (2015). Application of a moment tensor inversion code developed for mining-induced seismicity to fracture monitoring of civil engineering materials. *Journal of Applied Geophysics, 112*, 256−267.

The subscript i denotes the index of the AE sensor deployed in the network where x_i, y_i, and z_i represent the spatial coordinates, and t_i is the P-wave arrival time. The source event time is denoted by t_0 (time at which the elastic wave, or AE, initiated), and x_0, y_0, and z_0 represent the spatial coordinates of the source. The travel paths between source and sensors are assumed to be straight, having a P-wave velocity, c_P. In all source location estimations, a P-wave velocity of 4000 m/s was used. The goal of the method is to minimize the residuals (r) between calculated, c, and observed, o, arrival time at each sensor:

$$r_i = \min\left(t_{i,o} - t_{i,c}\right) \tag{5.11}$$

This is done by solving the inverse nonlinear problem iteratively. Starting from a trial solution, a first set of source coordinates is calculated using Eqn (5.10). The arrival times calculated for all sensor locations are then compared to the observed arrival times, and sensor residuals are computed according to Eqn (5.11). A correction vector is then computed based on the first derivatives of the linearized arrival-time function (Eqn (5.10)) using a least-squares approach and added to the calculated source location

parameters (Ge, 2003). The process is repeated until a predefined stopping criterion is fulfilled. This iterative algorithm was implemented in MATLAB and was applied to all the AE events in our experiments.

Uncertainties in the actual P-wave speed, travel paths in cracked heterogeneous and anisotropic materials, and the errors in the picking of the arrival times from the AE signals introduce errors into the results. If more than five AE signals are available, the system of equations is overdetermined (five or more equations and only four unknowns), and the covariance matrix of the solution using the least-squares method can be computed. The standard deviations in the principal directions (σ_1, σ_2, and σ_3) can then be obtained by solving for the eigenvalues and eigenvectors of the covariance matrix. These standard deviations are a measure of inconsistency in the observed arrival times and not the absolute error associated with a certain location result. For example, the effect of systematically delayed arrival times would remain unrevealed (Schumacher, 2008). An example of located AE sources for a three-point beam test is given in Figure 5.20.

The last and final step in quantitative AE analysis is the MTI. In this study, the MTI Tool Box developed by Andersen (2001) to investigate mining-induced seismicity was adapted and employed to characterize the nature of AE events Mhamdi, Schumacher, & Linzer (2013). The inputs needed to perform an MTI computation are (1) source

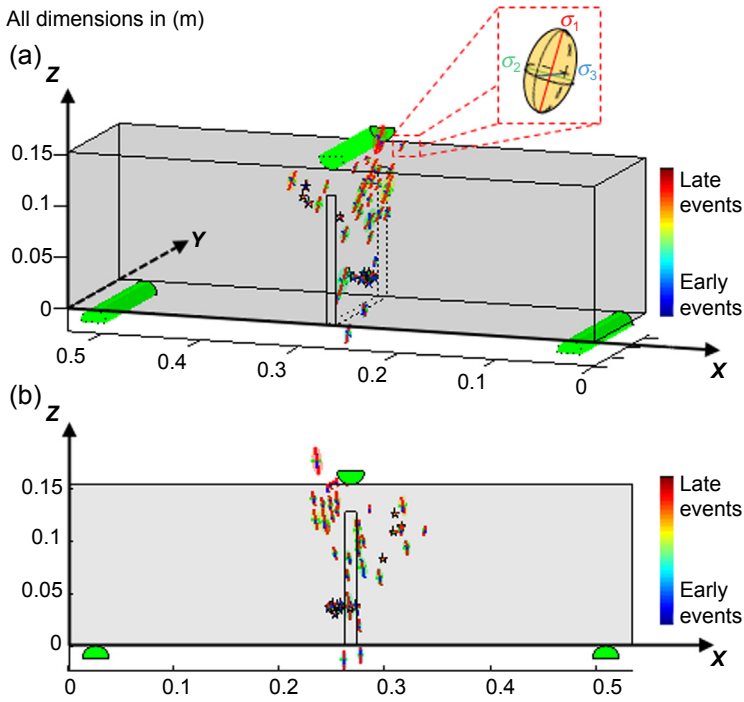

Figure 5.20 Example of results obtained from source location algorithm.
Linzer, Mhamdi, & Schumacher, (2015). Application of a moment tensor inversion code developed for mining-induced seismicity to fracture monitoring of civil engineering materials. *Journal of Applied Geophysics, 112*, 256–267.

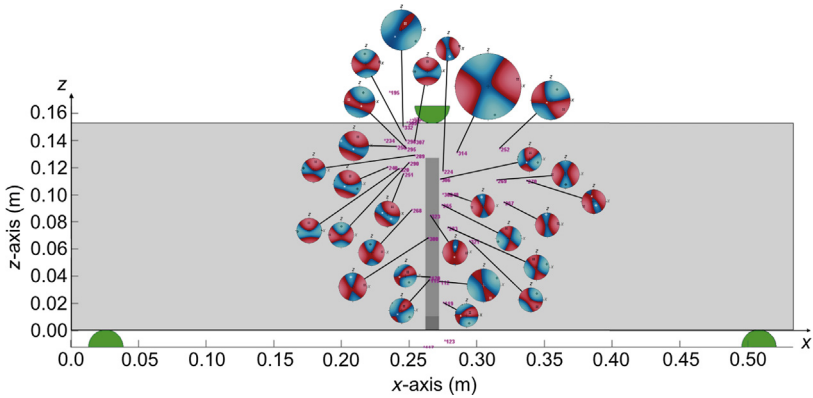

Figure 5.21 Moment tensor inversion results displayed on the beam (x−z, elevation view).

location, (2) P-wave amplitudes, and (3) sensor characteristics. The idea of a moment tensor is that a point source can be represented by a set of nine force couples. Due to symmetry, the off-diagonal terms of the moment tensor are the same, which reduces the number of independent terms to six. Therefore, at least six AE signals need to be recorded in order to perform an MTI to obtain stable and reliable results, and in the presence of noise, it is necessary to have a higher number of signals. In our tests, we typically use at least eight sensors, and we can employ up to 12.

It is convenient to display the radiation pattern described by the moment tensor as a stereographic projection (or "beach ball" plot). These patterns show the changes in P-wave polarity around the source, where red and blue areas represent positive (away from the source) and negative swings (toward the source) of the first motion, respectively. Different types of sources have characteristic patterns related to how the wave field propagates in 3-D away from the source. The P-wave radiation patterns for selected AE events from our concrete beam experiment discussed in detail in Linzer, Mhamdi, & Schumacher (2015) and computed using the MTI Tool Box are visualized in Figure 5.21. It can be observed that most events are of mixed-mode type that can be explained by the complex crack surface leading to a nonuniform wave field.

Figure 5.22(a) shows the stereographic projection (beach ball) for one AE event (Ev. 300) located near the notch of the concrete beam. The stereograph is projected in three different planes (*XY*, *XZ*, and *YZ*). An event dominated by shearing would show approximately equal areas of red and blue; an event dominated by opening would be mostly red; and, an event dominated by closing would be mostly blue. The beach ball in the figure indicates that the opening mode (mode I) is more dominant than the shearing mode (mode II). Figure 5.22(b) shows the detailed graphical and numerical solution available from the MTI Toolbox.

5.5 Strengths and limitations

Seismology-based methods appear particularly well-suited for adaption to AE monitoring of concrete fracture. The presented approaches differ in that one is qualitative

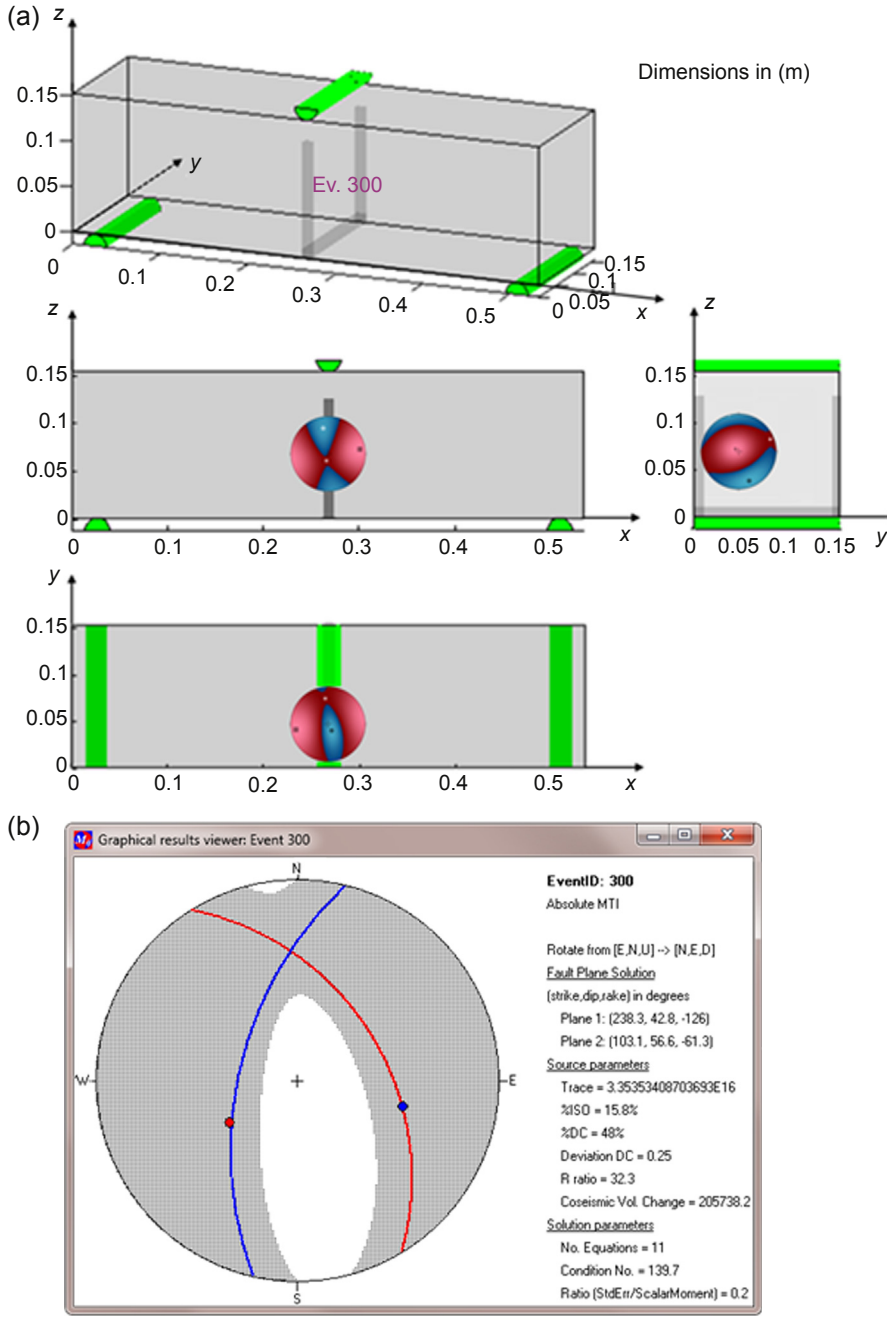

Figure 5.22 Example of an acoustic emission (AE) event with a dominant mode 1: (a) event seen on the concrete beam from the different projection views, (b) graphical result with statistics from the moment tensor inversion (MTI) Toolbox.
Linzer, Mhamdi, & Schumacher, (2015). Application of a moment tensor inversion code developed for mining-induced seismicity to fracture monitoring of civil engineering materials. *Journal of Applied Geophysics, 112*, 256–267.

(or parameter-based), whereas the other one is quantitative (or signal-based). A comparison of these two approaches is presented in Table 5.3.

Table 5.3 highlights the strengths and limitations of both approaches. Although quantitative approaches produce the most meaningful results, they can be challenging to deploy. Current research involves refining already developed or adapted methods and recording new data that will serve as a baseline.

5.6 Summary and conclusions

Seismology-based methods have tremendous potential for use in concrete fracture monitoring due to the similarity of AE and earthquakes; in both cases, energy is suddenly released due to internal fracture processes in the form of a mechanical wave that propagates through and interacts with the medium. *b*-Value analysis, a qualitative approach, is fairly straightforward to implement and is already used for SHM applications. However, *b*-value analysis is limited in many ways as it can only provide a rough measure of the overall cracking processes, as the source location and mechanics are not estimated. In contrast, MTI, a quantitative approach, is currently only used in the laboratory as it requires a large number of sensors arranged in a network around the fracture source. The procedure is difficult to implement and requires experience to interpret. Additionally, the underlying assumptions are simplified and may not always accurately represent a complex material such as concrete. Also, the inversion procedure is sensitive to noise and does not always produce results that are reliable.

5.7 Future trends

Qualitative methods such as *b*-value analysis presented in Section 5.3 have not been fully explored and could likely be improved by, for example, scaling the attenuation relationship according to source−sensor distance. Another idea could be to use P-wave rather than maximum signal amplitudes and use the maximum frequency content-to-distance relationship to estimate the distance between signal and source (Schumacher, 2008). Quantitative *b*-value analysis could also be performed using the equivalent of the seismic moment in earthquake seismology, by correcting the P-wave spectral amplitude for distance and mechanism (using an average or median to describe the radiation pattern effect) for a multisensor network. The most notable opportunities to advance understanding of the presented quantitative seismology-based methods arguably lie in the area of numerical simulations. By modeling wave propagation in a complex nonhomogeneous concrete medium and combining these results with the observed data, both source location estimates and mechanisms can potentially be improved, see e.g. Kocur, Saenger, & Vogel (2010). Specifically, forward modeling of Green's functions for complex ray paths may improve current MTI methods markedly.

Table 5.3 Comparison of qualitative versus quantitative methods

	***b*-Value analysis (qualitative)**	**Moment tensor inversion (quantitative)**
Effort; required instruments	Small to medium; can theoretically be performed with a single sensor	High; requires sensor networks with at least eight sensors
Data acquisition	Extraction and storage of characteristic AE parameters	Storage of transient waveforms
Method of analysis	Simple statistical analysis of AE amplitudes based on cumulative amplitude−frequency distribution, typically per sensor	Series of inverse analyses involves the following steps: **1.** Accurate P-wave arrival-time picking and P-wave amplitude **2.** Estimation of source location using iterative nonlinear inverse method such as Geiger's method **3.** Estimation of moment tensor components using linear inversion approach, i.e., MTI **4.** Visualization using stereographs or so-called beach balls
Result	Qualitative, empirical correlations to reveal overall trends using large numbers of events	Quantitative spatial−temporal evolution of AE sources, inference of actual source mechanics for each individual event
Advantages	Simple forward computations, suitable for real-time visualization of changes in amplitude−frequency distribution, can cover a large area of the structure to allow for global monitoring, easy to interpret	Detailed result of location and fracture type of individual AE events
Disadvantages	Accuracy and reliability subject to changes in the boundary conditions (e.g., cracking), quality of the result difficult to judge since locations/fracture type are not known	Complicated inverse multistep computations, computationally expensive, simplistic assumptions (elastic homogeneous solid wave propagation) questionable after cracking occurs, can only cover a limited area of the structure, requires experience to interpret correctly
Applications	Structural in-service load testing, long-term structural health monitoring	Monitoring of fracture processes in the laboratory

Acknowledgements

The materials presented in this chapter stem from several research projects sponsored by the University of Delaware Research Foundation (UDRF) and the Center for Advanced Infrastructure and Transportation University Transportation Center (CAIT-UTC). Their support is greatly appreciated. The MTI code was developed during the pursuit of a part-time Ph.D. titled by Andersen (2001) while employed by the Council for Scientific and Industrial Research, Miningtek.

References

Abercombie, R. E. (1995). Earthquake locations using single-station deep borehole recordings: implications for microseismicity on the San Andreas fault in southern California. *Journal of Geophysical Research, 100*, 24,003−24,014.

Akaike, H. (1974). A new look at the statistical model identification. *Automatic Control, IEEE Transactions, 19*(6), 716−723.

Aki, K., & Richards, P. G. (1980). *Quantitative seismology*. San Francisco: Freeman.

Andersen, L. M. (2001). *A relative moment tensor inversion technique applied to seismicity induced by mining* (Ph.D. thesis). Johannesburg, South Africa: University of the Witwatersrand.

ASNT. (2005). *Nondestructive testing handbook—Volume 6—acoustic emission testing*. Columbus, OH: American Society for Nondestructive Testing (ASNT).

ASTM. (2014). *E1316−14: Standard Terminology for Nondestructive Examinations*. West Consohocken, PA.

Baranov, et al. (2007). Acoustic emission in friction. In B. J. Briscoe (Series Ed.), *Tribology and interface engineering series, No 53*. Elsevier.

Bazant, Z. P., & Lee, V. C. (1998). *Fracture Mechanics: Applications to Concrete*. Special Publ.SP-118. Detroit: Am. Concrete Inst.

Bonamy, D. (2009). Intermittency and roughening in the failure of brittle heterogeneous materials. *Journal of Physics D, 42*, 214014.

Carpinteri, A., Lacidogna, G., & Niccolini, G. (2006). Critical Behaviour in Concrete Structures and Damage Localization by Acoustic Emission. *Key Engineering Materials, 312*, 305−310.

Carpinteri, A., Lacidogna, G., & Puzzi, S. (2009). From criticality to final collapse: Evolution of the "b-value" from 1.5 to 1.0. *Chaos, Solitons & Fractals, 41*(2), 843−853.

Colombo, S., Main, I. G., & Forde, M. G. (2003). Assessing damage of reinforced concrete beam using "*b*-value" analysis of acoustic emission signals. *ASCE Journal of Materials in Civil Engineering, 15*(3), 280−286.

Cox, S. J. D., & Meredith, P. G. (1993). Microcrack Formation and Material Softening in Rock Measured by Monitoring Acoustic Emissions. *International Journal of Rock Mechanics and Mining Sciences & Geomechanics Abstracts, 30*(1), 11−24.

Dahm, T. (1996). Relative moment tensor inversion based on ray theory: theory and synthetic tests. *Geophysical Journal International, 124*(1), 245−257.

Dziewonski, A. M., & Gilbert, F. (1974). Temporal variation of the seismic moment tensor and the evidence for precursive compression for two deep earthquakes. *Nature, 247*, 185−188.

EN. (2000). *Non-destructive testing-Terminology-Part 9: Terms used in acoustic emission testing*. Brüssel, Belgium: European Committee for Standardization (CEN), 1330−1339.

Gutenberg, B., & Richter, C. F. (1949). *Seismicity of the Earth and Associated Phenomena*. Princeton: Princeton University Press.

Farhidzadeh, A., Salamone, S., et al. (2013). Acoustic emission monitoring of a reinforced concrete shear wall by *b*-value-based outlier analysis. *Structural Health Monitoring, 12*(1), 3−13.

Ge, M. (2003). Analysis of source location algorithms—part II: iterative methods. *Journal of Acoustic Emission, 21*, 29−51.

Geiger, L. (1912). Herdbestimmung bei Erdbeben aus den Ankunftzeiten. *Nachrichten von der Gesellschaft der Wissenschaften zu Göttingen, Mathematisch-Physikalische Klasse, 4*, 331349, 1910 (Translated to English by F.W.L. Peebles and A.H. Corey, "Probability method for the determination of earthquake epicenters from the arrival time only". Bulletin St. Louis University 8, 60−71(1912)).

Gibowicz, S. J., & Kijko, A. (1994). *An introduction to mining seismology*. San Diego: Academic Press.

Gilbert, F. (1970). Excitation of the normal modes of the earth by earthquake sources. *Geophysical Journal of the Royal Astronomical Society, 77*, 223−226.

Grosse, C. U., Reinhardt, H. W., & Dahm, T. (1997). Localization and classification of fracture types in concrete with quantitative acoustic emission measurement techniques. *NDT & E International, 30*(4), 223−230.

Grosse, C. U., & Schumacher, T. (2013). Anwendungen der Schallemissionsanalyse an Betonbauwerken. *Bautechnik, 90*(11), 721−731.

Hardy, H. R., Jr (1971). *Application of Acoustic Emission Techniques to Rock Mechanics Research*. Bal Harbor, FL: Symposium on Acoustic Emission at the ASTM Committee Meeting.

Higgins, D. D., & Bailey, J. E. (1976). Fracture measurements on cement paste. *Journal of Materials Science, 11*, 19952003.

Hillerborg, A., Modeer, M., & Peterson, P. E. (1976). Analysis of crack formation and crack growth by means of fracture mechanics and finite elements. *Cement and Concrete Research, 6*(6), 773781.

Jäger, J. C., & Cook, N. G. W. (1976). *Fundamentals of Rock Mechanics*. London, United Kingdom: Chapman and Hall (Halsted Press).

Kanamori, H., Mori, J., Heaton, T. H., Huttos, L. K., & Jones, J. M. (1993). Determination of earthquake energy release and M_L using TERRAscope. *Bulletin of the Seismological Society of America, 83*, 330−346.

Kaplan, M. F. (1961). Crack propagation and fracture of concrete. Journal of the American Concrete Institute. *Proceedings, 58*(11), 591−610.

Kijko, A., & Funk, C. W. (1995). The assessment of seismic hazard in mines. *Journal of South African Institute of Mining and Metallurgy*, 179−185.

Kocur, G. K., Saenger, E. H., & Vogel, T. (2010). Elastic wave propagation in a segmented X-ray computed tomography model of a concrete specimen. *Construction and Building Materials, 24*(12), 2393−2400.

Kurz, J. H., Finck, F., Grosse, C. U., & Reinhardt, H. W. (2006). Stress drop and stress redistribution in concrete quantified over time by the *b*-value analysis. *Structural Health Monitoring, 5*(1), 69−81.

Landis, E. N., & Shah, S. P. (1995). Frequency-dependent stress wave attenuation in cement-based materials. *ASCE Journal of Engineering Mechanics, 121*(6), 737−743.

Linzer, L., Mhamdi, L., & Schumacher, T. (2015). Application of a moment tensor inversion code developed for mining-induced seismicity to fracture monitoring of civil engineering materials. *Journal of Applied Geophysics, 112*, 256−267.

Linzer, L., Schumacher, T., & Mhamdi, L. (2013). The Application Of Moment Tensor Inversion Methods To Fracture Monitoring Of Civil Engineering Materials, 13th SAGA *Biennial Conference & Exhibition*. October 2013.

Lovejoy, S. C. (2006). *Development of acoustic emissions testing procedures applicable to conventionally reinforced concrete deck girder bridges subjected to diagonal tension cracking* (Ph.D. dissertation). Oregon State University.

McGarr, A. (1984). Some applications of seismic source mechanism studies to assessing underground hazard. In N. C. Gay, & E. H. Wainwright (Eds.), *Proceedings of the 1st International Congress on Rockbursts and Seismicity in Mines* (pp. 199−208). Johannesburg: SAIMM.

McLaskey, G., & Glaser, S. D. (2012). Acoustic emission sensor calibration for absolute source measurements. *Journal of Nondestructive Evaluation, 31*(2), 157−168.

Mhamdi, L., Schumacher, T., & Linzer, L. (2013). Development of Seismology-based Acoustic Emission Methods for Civil Infrastructure Applications. AIP Proceedings of Review of Progress in Quantitative Nondestructive Evaluation (QNDE) *Denver, CO, 1511*(1), 1363−1370.

Miller, R. K., Hill, E. v. K., & Moore, P. O. (2005). *Nondestructive Testing Handbook − Volume 6 − Acoustic Emission Testing, American*. Columbus, OH: Society for Nondestructive Testing (ASNT).

Mogi, K. (1962). *Study of elastic shocks caused by the fracture of heterogeneous materials and its relations to earthquake phenomena* (Vol. 40). Bulletin of the Earthquake Research Institute, University of Tokyo. p. 125.

Nuannin, P., Kulhanek, O., Persson, L., & Tillman, K. (2002). Forecasting of increasing induced seismicity in the Zinkgruvan mine, Sweden, by using temporal variations of *b*-values. *Acta Montana, Series A, 21*, 13−25.

Ohtsu, M. (1991). Simplified moment tensor analysis and unified decomposition of acoustic emission source: application to in situ hydrofracturing test. *Journal of the American Concrete Institute Proceedings, 58*(11), 591−610.

Ohtsu, M. (1996). The history and development of acoustic emission in concrete engineering. *Magazine of Concrete Research, 48*(177), 321−330.

Ohtsu, M., Okamoto, T., & Yuyama, S. (1998). Moment Tensor Analysis of Acoustie Emission for Cracking Mechanisms in Concrete. *ACI Structural Journal, 95*(2), 87−95.

Ohtsu, M., & Shigeishi, M. (2003). Virtual reality presentation of moment tensor analysis by SiGMA. *Journal of the Korean Society for Nondestructive Testing, 23*(3), 189−197.

Patton, H. (1980). Reference point equalization method for determining the source and path effects of surface waves. *Journal of Geophysical Research, 85*, 821−848.

Pollock, A. A. (1981). Acoustic emission amplitude distributions. *International Advances in Nondestructive Testing, 7*, 215−239.

Rao, M. V. M. S., & Lakshmi, K. J. P. (2005). Analysis of *b*-value and improved *b*-value of acoustic emissions accompanying rock fracture. *Current Science, 89*(9), 1577−1582.

Richardson, E., & Jordan, T. H. (2001). Some properties of gold-mine seismicity and implications for tectonic earthquakes. In *"Fifth international symposium on rockbursts and seismicity in mines" RaSIM5, 149−156*. Johannesburg: South African Institute of Mining and Metallurgy.

Rundle, J. B., Turcotte, D. L., Shcherbakov, R., Klein, W., & Sammis, C. (2003). Statistical Physics Approach to Understanding the Multiscale Dynamics of Earthquake Fault Systems. *Reviews of Geophysics, 41*(4), 5.1−5.30.

Schechinger, B. (2006). *SchallemissionsanalysezurÜberwachung der Schädigung von Stahlbeton*. InstitutfürBaustatik und Konstruktion. PhD Dissertation. Zurich, Switzerland: EidgenössischeTechnischeHochschule (ETH) Zürich.

Scholz, C. H. (1968). The frequency-magnitude relation of microfracturing in rock and its relation to earthquakes. *Bulletin of the Seismological Society of America, 58*(1), 399−415.

Schumacher, T. (2008). *Acoustic emission techniques applied to conventionally reinforced concrete bridge girders*. Final Report SPR 633. Salem, OR: Oregon Department of Transportation (ODOT).

Schumacher, T., Higgins, C. C., et al. (2010). Detection of studded tires using acoustic emission sensors mounted to highway bridges. *ASCE Journal of Transportation Engineering, 136*(5), 480−487.

Schumacher, T., Higgins, C., & Lovejoy, S. C. (2011). Estimating operating load conditions on reinforced concrete highway bridges with *b*-value analysis from acoustic emission monitoring. *Structural Health Monitoring, 10*(1), 17−32.

Schumacher, T., Higgins, C., & Lovejoy, S. C. (2013). Acoustic emission monitoring of conventionally reinforced concrete highway bridges under service conditions. In *International symposium on nondestructive testing of materials and structures.* Istanbul, Turkey: 847−853.

Schumacher, T., Straub, D., & Higgins, C. (2012). Toward a probabilistic acoustic emission source location algorithm: A Bayesian approach. *Journal of Sound and Vibration, 19*(10), 4233−4245.

Sellers, E. J., Kataka, M. O., & Linzer, L. M. (2003). Source parameters of acoustic emission events and scaling with mining-induced seismicity. *Journal of Geophysical Research, 108*(B9), 2418−2430.

Seth, S., & Wysession, M. (2002). *An Introduction to Seismology, Earthquakes, and Earth Structure*. UK: Blackwell, Oxford.

Shah, S. P., & Choi, S. (1999). Nondestructive Techniques for Studying Fracture Processes in Concrete. *International Journal of Fracture, 98*, 351−359.

Shiotani, T., & Ohtsu, M. (1998). Prediction of Slope Failure Based on AE Activity. Acoustic Emission: Standards and Technology Update, ASTM STP 1353 *American Society for Testing and Materials*, 156−171.

Shiotani, T., Yuyama, S., Li, Z. W., & Ohtsu, M. (2000). Quantitative evaluation of fracture processes in concrete by the use of improved b-value. In *Non-destructive testing in civil engineering 2000 (Seiken Symposium No. 26)* (pp. 293−302). Tokyo, Japan: Elsevier.

Spottiswoode, S. M., & McGarr, A. (1975). Source parameters of tremors in a deep-level gold mine. *Bulletin of the Seismological Society of America, 65*, 93−112.

Spottiswoode, S. M., Milev, A., Linzer, L. M., & Majiet, S. (2009). *Evaluation of the design criteria of regularly spaced dip pillars (RSDP) based on their in-situ performance*. Final SIMRAC report SIM040301. South Africa: Mine Health and Safety Council.

Stein, A., & Wysession, M. (2003). *An introduction to seismology, earthquakes and earth structure*. Oxford: Blackwell Publishing. p. 498.

Uomoto, T. (1987). Application of acoustic emission to the field of concrete engineering. *Journal of Acoustic Emission, 6*(3), 137−144.

Wiemer, S., & Wyss, M. (1997). Mapping the frequency-magnitude distribution in asperities: An improved technique to calculate recurrence times. *Journal of Geophysics Research, 102*, 15115−15128.

Weiss, J. (1997). The role of attenuation on acoustic emission amplitude distributions and *b*-values. *Bulletin of the Seismological Society of America, 87*(5), 1362−1367.

Yuyama, S., Li, Z. W., Ito, Y., & Arazoe, M. (1999). Quantitative analysis of fracture process in RC column foundation by moment tensor analysis of acoustic emission. *Construction and Building Materials, 13*(1−2), 87−97.

Zdenk, Z. P., & Oh, B. H. (1983). Crack band theory for fracture of concrete. *Materiaux et Construction, 16*(3), 155−177.

Acoustic emission monitoring and quantitative evaluation of damage in concrete beams under creep

6

J. Saliba[1,2], *A. Loukili*[1], *F. Grondin*[1]
[1]UNAM Université, École Centrale de Nantes, Nantes, France; [2]Université de Bordeaux, Bordeaux, France

6.1 Introduction

Concrete structures are susceptible to degradation due to delayed strains that have an impact on their safety margin and lifetime, especially when they are subjected to a high loading level.

Few studies have investigated the effects of creep loading history on failure mechanisms, including its influence on strength, stiffness, and fracture energy. Most of these studies have tried to quantify the effect of creep on the behavior of concrete mainly by measuring the residual strength (Carpinteri, Valente, Zhou, Ferrara, & Melchiorri, 1997; Cook & Haque, 1974; Denarié, Cécot, & Huet, 2006; Liniers, 1987; Omar, Loukili, Pijaudier-cabot, & Le Pape, 2009; Shah & Chandra, 1970).

Deformation and fracture of concrete are associated with very complicated progressive failure, and it is usually accepted that the failure process under a sustained load is associated with the development and growth of micro-cracking (Barpi & Valente, 2005; Bazant & Li, 1997; Rossi, Godart, Robert, Gervais, & Bruhat, 1994; Rossi, Tailhan, Le Maou, Gaillet, & Martin, 2012). Thus, understanding the behavior of concrete requires the detailed assessment of creep and the part of damage. Micro-cracking and damage localization in concrete beams cannot be investigated by the classical mechanical measurements. So, as a part of the investigation, the acoustic emission (AE) technique can be applied.

Nondestructive and instrumental investigation methods such as AE technique have been conducted widely over the last few years. This technique proves to be very effective, especially to check and measure micro-cracking that takes place inside a structure under mechanical loading, and it is particularly recommended for detecting and localizing cracks in concrete (Chen & Liu, 2004; Granger, Loukili, Pijaudier-Cabot, & Chanvillard, 2007; Landis & Shah, 1995; Otsuka & Date, 2000; Wu, Chen, & Yao, 2000).

Acoustic Emission (AE) and Related Non-destructive Evaluation (NDE) Techniques in the Fracture Mechanics of Concrete
http://dx.doi.org/10.1016/B978-1-78242-327-0.00006-4
Copyright © 2015 Elsevier Ltd. All rights reserved.

6.2 Creep behavior of concrete

6.2.1 Creep micro-mechanisms

Numerous contradictory theories have been put forward over the years to assess the creep behavior of concrete. Since no single mechanism can account for all the observed phenomena, several major real mechanisms can be distinguished, and it is commonly accepted that a combination of these mechanisms act together. Several theories have been suggested: viscous flow (Glanville & Thomas, 1939), plastic flow (Bernal & Megaw, 1935), seepage of gel water (Ghosh, 1973), consolidation (Bazant & Prasannan, 1989), micro-pre-stress of creep sites in cement gel microstructure (Bazant & Li, 1997), bond breakage in slip and nonlinear deformation, and micro-cracking (Carrasquillo, Slate, & Nilson, 1981; Ngab, Slate, & Nilson, 1981; Rossi et al., 1994). Usually, creep mechanisms are associated with the hydrated cement paste and can be considered as material properties. Micro-cracking is an apparent creep mechanism that can also contribute to the observed deformation and is responsible for the permanent deformation.

Creep has important effects on the stresses and deflections of the concrete structure. For low load levels, it is assumed that linear viscoelasticity takes place, and the instantaneous mechanical behavior of concrete remains elastic. However, for high load levels, micro-cracks, initiated by the local stress, develop and interact with the viscoelasticity (Mazzotti & Savoia, 2002); deviation of the linearity of the mechanical response may occur and nonlinear creep occurs (Bazant & Li, 1997; Freudenthalt & Roll, 1958; Masuero, 1995; Mazzotti & Savoia, 2002). In fact, micro-cracking may initiate at the moment of load application and begin to grow to form a time-dependent crack path (Bazant & Gettu, 1992; Meyers, Slate, & Winter, 1969).

Creep deformations under tension present similarities and differences in comparison to creep under compression (Atrushi, 2003; Bissonnette, Pigeon, & Vaysburd, 2007). Three main mechanisms were recognized for tensile creep (Bissonnette et al., 2007; Garas, 2009): water seepage, viscous shear, and micro-cracking. The study of creep in tension has shown different effects on the behavior of concrete with some contradiction at times. On one hand, creep may relax internal tensile stresses generated by restrained shrinkage and thermal dilation at early ages by increasing the deformation capacity to the rupture and, consequently, reducing the risk of potential cracking in concrete (Altoubat & Lange, 2001; Bissonnette & Pigeon, 2000). However, the principal mechanism of tensile creep is due to micro-crack development, which could be responsible for the decrease of the residual strength and the modification of concrete properties (Cook & Haque, 1974; Rossi et al., 1994).

6.2.2 Limitations of the classical creep and fracture measurements

The purpose of this section is to investigate the effect of basic creep on the residual capacity of concrete specimens and the fracture energy.

Table 6.1 Concrete mixture proportions

Constituent	Dosage (Kg/m^3)
Gravel: G5/12.5 mm	936.0
Sand: 0/5 mm	780.0
Cement: CEMII 42.5	350.0
Water	219.5
Superplasticizer	1.9

Source: Saliba et al. (2014).

Concrete specimens were mixed with Portland cement CPA-CEMII 42.5, crushed limestone aggregate distributed in fine sand with a maximum size of 5 mm, and crushed gravel of size 5−12.5 mm. A superplasticizer agent has been added for workability. Table 6.1 shows the mix quantities of constituent materials. This mixture is characterized by a water-to-cement (*W/C*) ratio of 0.56 and a slump of 70 mm. The proportioning of the cement paste, sand, and coarse aggregates were kept constant throughout the program. Concrete beams of size 800 × 200 × 100 mm^3 ($l \times h \times b$) were prepared with an effective span (S) equal to 600 mm and a notch-to-depth ratio of 0.2 ($a_0 = \mathrm{h}/5$).

Concrete beams are submitted to bending creep tests with a high level of sustained load. The bending creep tests are performed on frames placed in a climate-controlled chamber at 50% RH and a temperature of 20 °C. The displacement is measured at mid-span. Creep develops quickly in the first days of loading (primary creep) and then stabilizes (secondary creep) (Figure 6.1). The larger the applied stress, the more important are all the kinetics and the magnitude of creep displacement.

Then, the beams subjected to creep are removed from the creep frames after four months and are immediately subjected to three-point bending loading up to failure under closed loop crack mouth opening displacement (CMOD) control with a constant loading rate of 0.3 μm/s. The fracture test employs a load-controlled universal testing machine as per RILEM-TMC 50 recommendations (RILEM, 1985), based on Hillerborg's method (Hillerborg, 1985).

Figure 6.2 shows the curves of the load-CMOD for the creep beams and comparative beams with the same age and free of loading for four months. The load-CMOD variations are linear up to about 80% of the ultimate load (phase 1), followed by a nonlinear variation up to the peak load (phase 2). A stable failure is then observed, and the post-peak response seems to be very gradual. The fracture properties (fracture energy, flexural strength…) of concrete are then calculated. The results show a slight increase in energy that may be explained by the strengthening effect due to basic creep in the compression zone (Rao & Prasad, 2002; Shah & Chandra, 1970; Zhou, Barn, Lydon, College, & Iyf, 1995).

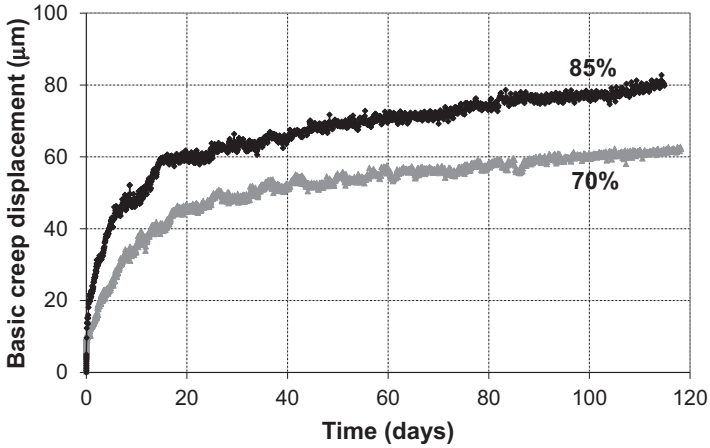

Figure 6.1 Basic creep displacement of notched beams.

Considering the measurement uncertainties, the results do not distinctly show the influence of creep on the fracture behavior due to the small difference between comparative and creep specimens. This small difference was also observed by Hansen (1991), who reported that the fracture energy is independent of the time duration of the sustained load for three-month-old concrete specimens. The Hillerborg method seems to be not fine enough to assess the influence of the creep load on the fracture of concrete.

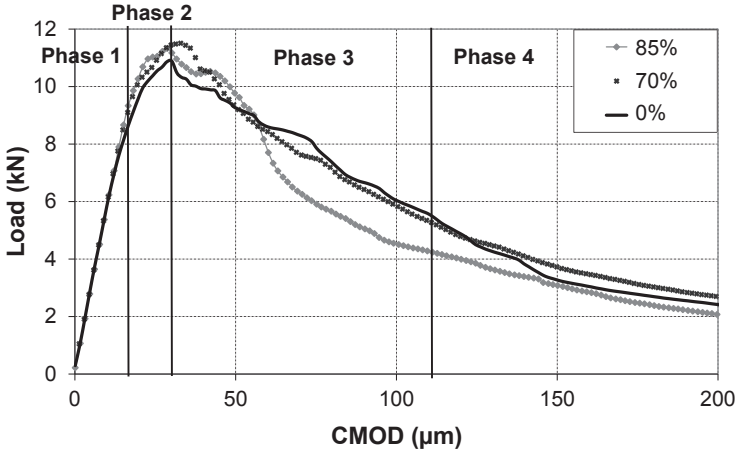

Figure 6.2 Load−CMOD curves for comparative and creep beams.

6.3 Application of the acoustic emission (AE) technique to discriminate the creep effect on the cracking behavior

6.3.1 Localization of AE events in concrete

The AE system is comprised of an eight-channel AE Win system, a general-purpose interface bus (2 PCI-DISP4), and a PC for data storage analysis. Piezoelectric transducers (resonant frequency of 150 KHz) were used to convert the mechanical waves to electrical signals. The detected signals were amplified with a 40-dB gain differential amplifier. In order to overcome the background noise, the signal detection threshold was set at a value of about 35 dB (value adjusted before every test), slightly above the measured background noise. The acquisition system was calibrated before each test using a pencil lead break procedure HSU-NIELSEN (Norme NF EN 1330). The effective velocity and the attenuation of acoustic waves were also calculated. For this analysis, the effective velocity was assumed to be a constant for the analysis of AE source locations even though there may be some variability depending on the wave propagation path. The effective velocity was assumed to be 3800 m/s. In order to eliminate mechanical and electromagnetic disturbances, a low-pass filter with a cut-off frequency of 20 KHz and a high-pass filter with a cut-off frequency of 400 KHz were used. Signal descriptors such as rise time, counts, energy, duration, amplitude, average frequency, and counts to peak were captured and calculated by AE Win system. Each waveform was digitized and stored.

During the formation of a crack, energy is emitted as an elastic wave and propagates from the crack location to the AE transducers at the specimen surface (Figure 6.3). The locations of the AE sources of each event are evaluated based on the arrival times of the first wave at each transducer and their respective velocity in the concrete specimen. On the surface of the beam, four piezoelectric transducers are placed in a rectangular position (120×120 mm^2) around the expected location of the fracture process zone (FPZ) to minimize errors in the AE event localization program (Figure 6.3). Once the arrival time is picked, the least-square method is used to estimate the event location. A measurable event has a minimum of three well-defined arrival times.

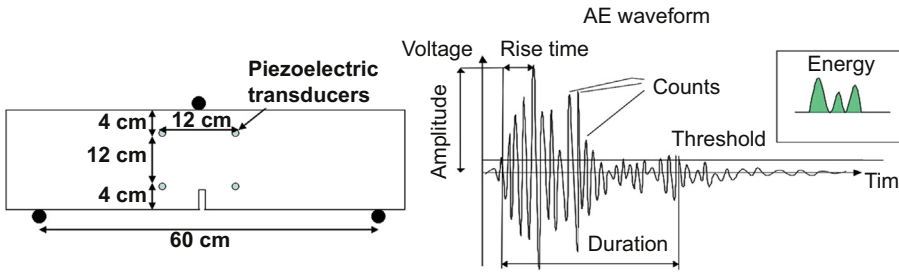

Figure 6.3 Position of the piezoelectric transducers on the beam (left) and an AE waveform (right).

The location resolution is estimated to be ± 5 mm. This accuracy depends on many conditions such as the transducer arrangement, the covering of the herd sphere, the homogeneity of concrete, the coupling of the transducers, and the variation in wave propagation velocity that may arise based on the number of aggregate crossings over the path of wave propagation, and so on. The relevant method is recommended by RILEM TC212-ACD (RILEM, 2010).

The locations of the AE sources are analyzed in the four stages of the fracture test (elastic stage, precritical crack growth, critical crack growth, crack bridging) (Van Mier, 2008). The cumulated locations of acoustic events are shown in Figure 6.4(a)–(d) for comparative and creep specimens. Each plotted point indicates a detected AE source. The damage accumulation is observed over a window as a function of the position x and y centered at the notch, with a width of 300 mm and covering the beam depth.

The AE events are evenly distributed throughout the zone of maximum tensile stress in the specimen, and the AE sources are localized in a band describing the way of the propagation of the crack. The comparison between comparative and creep specimens shows many differences. More events are recorded with creep specimens. The AE activity, proportional to the density of micro-cracking, shows a more intense localization of micro-cracks and, thus, a clearer active damage zone.

In the first stage, the AE activity is more important for comparative specimen indicating an early crack initiation in the pre-peak region (Figure 6.4(a)). This behavior is correlated to the shape of the load–CMOD curve. In fact, the linear elastic phase of creep beams is more important than comparative beams where the nonlinear behavior begins at a low loading rate. A recent study on the size effect (Alam, Loukili, & Grondin, 2012) showed that a crack initiates at 50% in the pre-peak regime for small beams and then continues to grow gradually, while a crack initiates just before the peak load for larger beams. The same behavior is observed here with creep specimens, where the crack length is obviously delayed (Figure 6.4(b)). Thus, the behavior of creep specimens seems to be close to that of specimen of larger size that have more brittle behavior.

6.3.2 Correlation of load–CMOD curve and AE parameters

AE hits provide an indication of the number of burst emissions or events and other wave characteristics, such as the amplitude and the energy (Figures 6.5 and 6.6). During the initial loading stage, corresponding essentially to the linear portion of the load–CMOD curve (pre-peak), the AE activity is weak, and few events are located. Micro-cracks nucleate in a somewhat random pattern in the zone of the maximum tensile stress. In addition, the amplitude and the energy of the waves released at this stage are weak, and thus, micro-cracks occurring early in the loading cycle could be attributed to primarily matrix–aggregate interface cracks.

The second set of event locations corresponds to the pre-peak nonlinear region as the load reaches about 80% of the maximal strength. The AE activity becomes more intense, indicating the formation of micro-crack bands. In this stage, damage starts to localize around the notch tip forming the FPZ (Landis & Shah, 1995; Li & Shah,

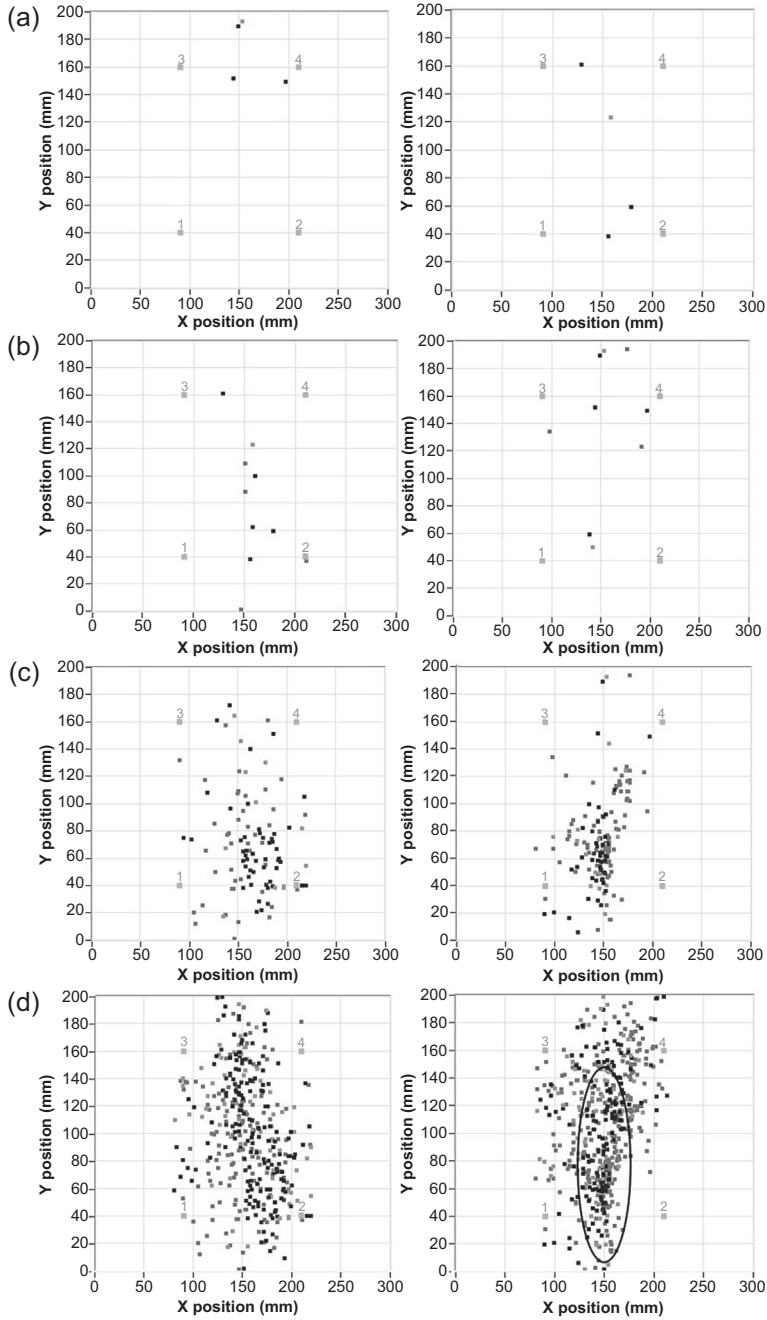

Figure 6.4 Maps of the AE sources located at four stages of the loading for aging specimen (left) and creep specimen (right): (a) 0−80% of the peak load, (b) 80−100% of the peak load, (c) 100−40% of the peak load in the post-peak region, (d) total localization map.

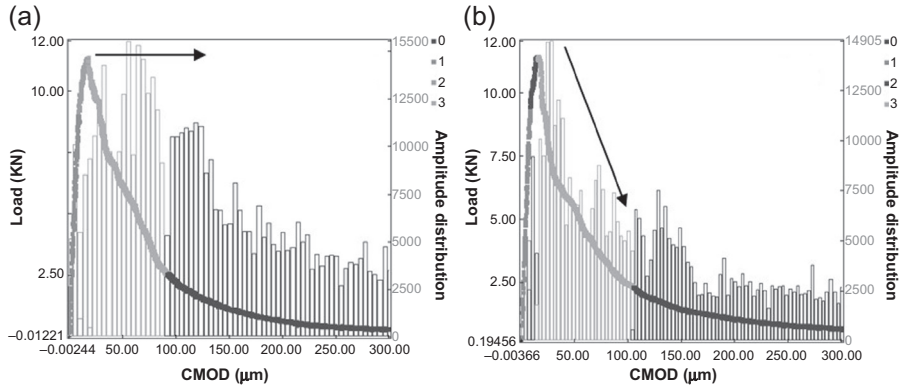

Figure 6.5 Correlation of load−CMOD curve with AE amplitude distribution for aging (a) and creep beams (b) during the four phases.
Source: Saliba et al. (2012).

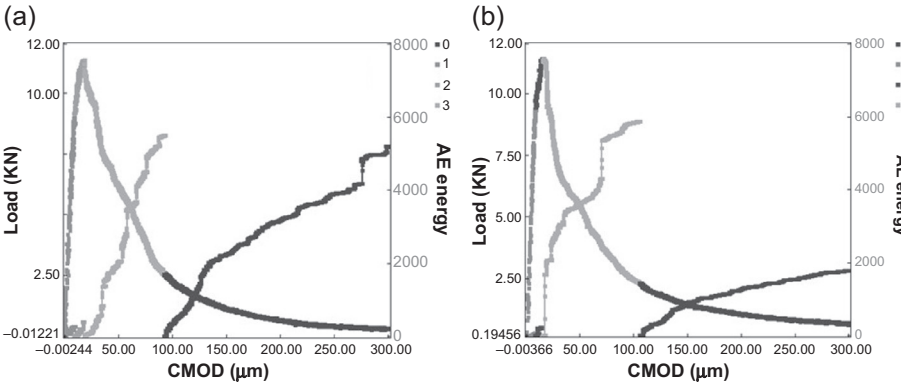

Figure 6.6 Correlation of load−CMOD curve with AE energy rate for aging (a) and creep beams (b) during the four phases.
Source: Saliba et al. (2012).

1994). As the load approaches the peak, a higher energy is released, indicating that there is matrix cracking (Landis, 1999).

After the peak load, the AE activity increases rapidly in a third phase. This increase is associated with the high surface corresponding to cracks that develop when the external load exceeds the ultimate strength (Kim & Weiss, 2003). In fact, in the beginning, micro-cracks start to develop at the surface of the concrete, and at this point, micro-cracks coalesce into an area around the location of the critical macro-cracking until visible unstable cracking appears. As can be seen in Figure 6.4, the locations of the AE sources increase with time, and the area becomes wider and spreads away from the notch tip. At this stage, concrete damage increases gradually with a constant AE rate.

The amplitude distribution versus CMOD curve shows that there exists a plateau in comparative specimens and that the number of AEs remains approximately constant during the third phase, with no obvious occurrence of AE peak distribution (Figure 6.5). Whereas, the amplitude distribution for creep specimens peaks in the region of 80−90% of the maximum load in the descending branch of load−CMOD, and then it decreases brutally, indicating a more brittle behavior for concrete beam subjected to creep. Thus, creep influences the AE characteristics and changes the distribution of hits occurring in the descending branch of the load−CMOD curves, which shift to the latter with comparative specimens.

Energy rate jumps are observable at certain point (Figure 6.6). These discrete jumps in the energy release rate may be explained by an aggregate acting to arrest cracks before they propagate across the specimen, requiring a greater driving force to propagate across the specimen (Kim & Weiss, 2003).

The distinguishing characteristic that separates the initial post-peak and terminal post-peak region is the slope of the cumulative event count plot. In the terminal post-peak region, the AE activity rate decreases. This is probably due to the existence of the fracture surface inside the FPZ and the decrease of stress (Hadjab, Thimus, & Chabaat, 2007). AE events are generated as a consequence of different toughening mechanisms through the crack faces on micro- and meso-levels, such as friction and bridging (Shah & Ouyang, 1994). The rate of the absolute AE energy decreases in the fourth phase (Figure 6.6). However, some AE hits present high amplitude and energy toward the end, indicating different toughening mechanisms.

6.3.3 Calculation of the FPZ width by an AE-based method

The FPZ surrounding the crack tip is one of the principal mechanisms in the fracture of quasi-brittle materials, and presently is considered the hottest topic in the field of concrete fracture mechanics. This zone is characterized by complex micro-structural features in concrete in the vicinity of a macro-crack front, such as frictional interlock between tortuous cracked surfaces and discontinuous fractures of unbroken aggregate bridging and other inelastic, irreversible material changes that dissipate energy (Shah & Choi, 1999). This energy absorption during crack growth manifests itself in the nonlinear stress−strain behavior and the strain softening post-peak behavior. Landis and Baillon (2002) and Wu et al. (2000) suggest that the energy dissipated by fracture is proportional to the energy measured by AE technique, whereas the energy dissipated by toughening mechanisms do not produce a proportional response.

The size of the FPZ can be significant and depends on many parameters upon the material's microstructure: grain size, rate of loading, dimensions of the specimen (Otsuka & Date, 2000), and other parameters such as notch depths (Zhang & Wu, 1999).

The approach used to measure the crack band width consists of dividing the specimen into an array of rectangular elements and counting the AE events located within each element (Haidar, Pijaudier-Cabot, Dubé, & Loukili, 2005). The fineness of the grid (2×2 cm^2) is chosen to be large enough to give a sufficient number of events per element and not too small compared to the accuracy of the AE localization method.

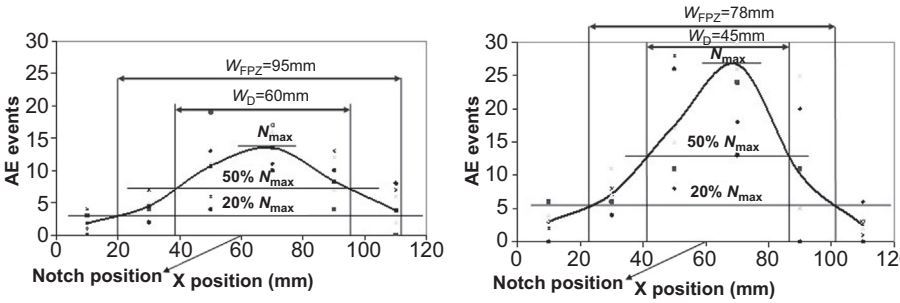

Figure 6.7 Evolution of cumulative events per grid: comparative specimen (left) and creep specimen (right).
Source: Saliba et al. (2012).

The cumulative number of events over the entire record during the experiment is plotted as a function of its horizontal position x for various vertical positions y over the depth of the specimen at the final load step. The average curve is then presented in a continued line. The horizontal straight line, which intersects the vertical axis at the value of 20% of the maximum number of events on the average curve (N_{max}), is plotted in the same graph (Figure 6.7). The crack band width was defined as the length of the segment of this horizontal straight line that intersects the average distribution of AE events. The FPZ could be divided into two areas (Hadjab et al., 2007):

1. The first area corresponds to a zone of confidence of events in which the number of AE events have higher values related to the damage of the material in front of the macro-crack.
2. The second area represents the lower percentage of AE events corresponding to lower damage.

The width of the damage zone is determined by drawing a line at 50% of N_{max} (Rossi, Robert, Gervais, & Bruhat, 1990). The value of the FPZ is about 95 and 78 mm and the width of the damage zone is about 60 and 45 mm for comparative and creep specimens, respectively. This difference can also be seen in Figure 6.4 where AE events are located in a smaller region in creep specimens. Based on these figures, the propagation of the FPZ can also be measured forward according to the loading stages (Otsuka & Date, 2000). This decrease of the FPZ is consistent with the results obtained by Omar (Omar et al., 2009) that show the same decrease in the size of the FPZ obtained from the size effect law and the characteristic length fitted before and after creep and, again, a more brittle behavior in the specimen.

There are several reasons for this discrepancy: on one hand, the change in the microstructure of the material under creep due to the creation of micro-cracking and defects (Rossi et al., 1994), and on the other hand, the consolidation of the cement paste in the compression zone during the creep test. The first phenomenon is more significant in the tensile zone of the beam where tensile creep is largely a result of time-dependent micro-cracking (Cook, 1972). As tests have been made without mass exchange, those micro-cracks may be due to the adsorption of internal water into the

tips of preexisting or load-induced cracks, and thus more intense localization of micro-cracks in concrete creep beams.

But what is the reason for this brittleness after creep? And how do micro-cracks develop in the microstructure during creep?

6.4 Assessment of damage mechanisms occurring under creep

6.4.1 Localization of AE events in concrete during creep

In order to have more information on the AE activity, eight piezoelectric transducers are used to convert the mechanical waves to electrical signals and are placed in a 3-D parallelepiped position on both sides of the specimen around the expected location of the FPZ. Figure 6.8 shows the localization map of the AE sources in a concrete beam during a basic creep period and followed by a desiccation creep period. The cumulated locations of acoustic events detected throughout the test are observed over a window as a function of the position x and y, centered at the notch with a width of 200 mm and covering the beam depth, and as a function of the position y and z.

During basic creep, events are arbitrarily distributed and diffused along the length (x, y) and the depth (y, z) of the specimen (Figure 6.8(a)). During desiccation, the number of AE events increases with a higher rate and more energetic events, especially at the surfaces (Figure 6.8(b)). Those events are highly dependent on desiccation. In fact, the nonuniform desiccation (humidity gradient) induces a nonuniform shrinkage in the specimen and, thus, presents structural consequences (Bazant & Gettu, 1992; Bisschop & Van Mier, 2002). Then, events begin to localize at the front of the notch in the zone of the maximum tensile stress. As the average stress along the ligament surface is lower than the stress in front of the crack, micro-cracks relax the stress in front of the FPZ by the creation of new crack surfaces. Then, events follow a conical progress before the total failure where there is an emission of high amplitude and energetic signals (Figure 6.8(c)). Those results allow for the understanding of the influence of creep on the brittleness of concrete observed during the failure of beams subjected to creep (Saliba, Loukili, Grondin, & Regoin, 2012). Note here that the relative kinetics of acoustic waves does not present an important variation during the test.

6.4.2 Correlation between creep displacement and AE parameters

The correlation between creep displacement and the characteristics of AE signals collected during creep is shown in Figure 6.9. The AE activity is important during primary creep with the emission of high amplitude signals and then decreases and stabilizes during secondary creep. At this moment, when the beam is subjected to desiccation, the number of AE hits increases quickly with the emission of high amplitude signals, then it decreases progressively in correlation with shrinkage. The

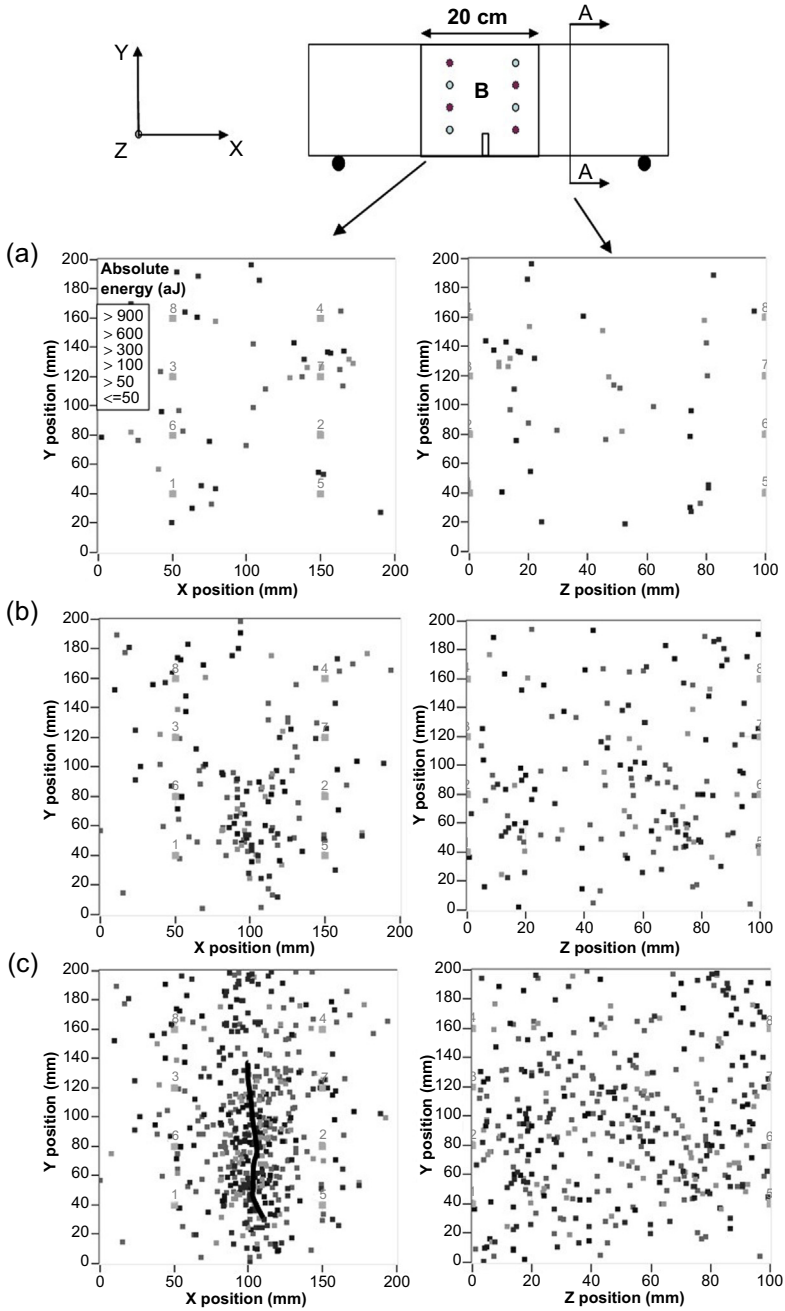

Figure 6.8 Damage localization during (a) basic creep, (b) desiccation creep, and (c) at the rupture in the planes A and B.
Source: Saliba et al. (2014).

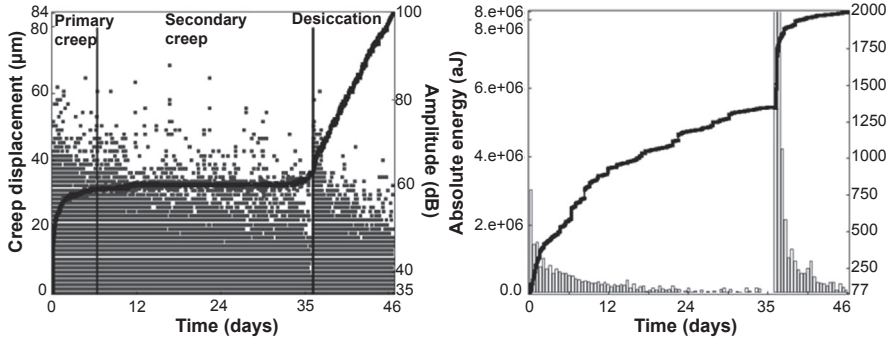

Figure 6.9 Correlation between creep displacement and AE hits amplitude (left); correlation between the cumulated AE energy and the distribution of the AE hits during creep test (right). *Source*: Saliba et al. (2014).

cumulated AE energy follows the same evolution and gives information on the crack initiation that progresses until the failure. Thus, it could be related to the fracture energy measured on a global scale. This finding strengthens the assumption that the acoustic events recorded during creep are related to the creation of micro-cracks or, in other terms, the damage occurring inside the material under creep.

6.4.3 Multivariable data clustering of AE signals

The quantitative understanding of the physical processes and the micro-structural phenomena that control the fracture behavior on the macroscopic scale is poor. During the last few years, quantitative evaluation of fracture processes in concrete consisted of evaluating the different modes of failure and stress fields based on moment tensors (Finck, Yamanouchi, Reinhardt, & Grosse, 2003; Grosse & Finck, 2006; Ohtsu, Kaminaga, & Munwam, 1999) and some AE indices as the average frequency and the RA value, defined as the rise time over the amplitude (Aggelis, 2011). It then appears necessary to take the analysis further to obtain information about the physical mechanisms, the origin of the AE signatures. For this, a multivariable analysis of the recorded acoustic signals is proposed to discriminate the damage mechanisms in the material according to the typical AE signals and their apparition chronology.

For the classification process of the monitored AE data under creep, the unsupervised method K-means associated with a principal component analysis (PCA) and the dendrogram are proposed (Kostopoulos, Loutas, Kontsos, Sotiriadis, & Pappas, 2003). The K-means method allows obtaining an unsupervised classification in n class representative of the n damage mechanisms in the case of multidimensional data. The PCA method is achieved in order to improve the visualization of the classification results by reducing the dimension of the data (Oja, 1989). In the unsupervised method, each signal can be associated with a pattern composed of multiple relevant features extracted from the random AE waveforms (amplitude, energy, rising time, average

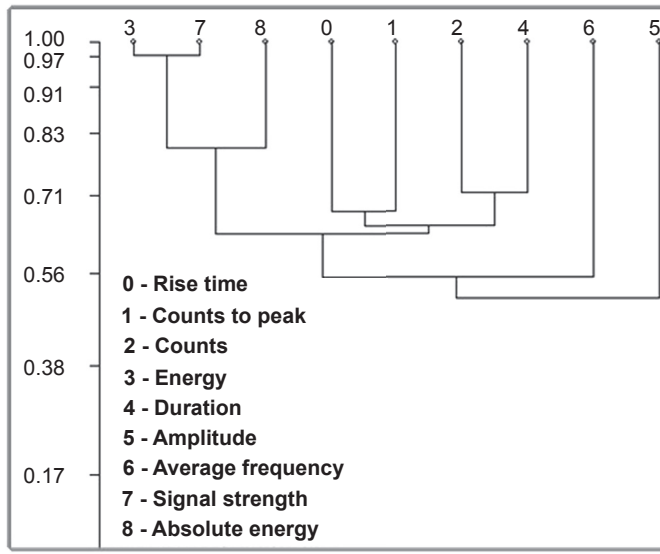

Figure 6.10 Correlation dendrogram of AE features.
Source: Saliba et al. (2014).

frequency, etc.). Those parameters can be correlated and, consequently, redundant. It is then necessary to choose those descriptors wisely. The parameters were classified hierarchically with the dendrogram (Figure 6.10), which exhibits the correlation level among the AE features. The descriptors used are the energy, the absolute energy, the amplitude, the rise time, the counts, the counts to peak, the average frequency, and the duration of the signals. The descriptors are normalized in the interval of $[-1; 1]$ to impose an equivalent weight factor to each AE component.

The results of the K-means method for a correlation level set to 0.9 are presented in Figure 6.11 in 2-D as a function of the first and second principal components that represent the most important variance of AE parameters. Two clusters are distinguished for basic creep and three for desiccation creep. The clusters are well separated and discriminated.

In the case of basic creep, the first cluster corresponds to signals of weak energy, whereas the second cluster corresponds to signals of higher energy (Figure 6.12). For desiccation creep, the same behavior is observed for clusters 1 and 2, and the additional cluster 3 is characterized by signals of very weak energy. The chronological apparition of these clusters shows that the first is the most distinguished damage mechanism during basic creep and involves much more numerous AE hits than the second class (Figure 6.13). During desiccation creep, the same trend is observed for the first two clusters, and the AE hits distribution of the third cluster appears to be the most important, mainly at the beginning of desiccation, and it decreases with time. In addition, the number of AE hits for clusters 1 and 2 increases in desiccation in comparison with basic creep.

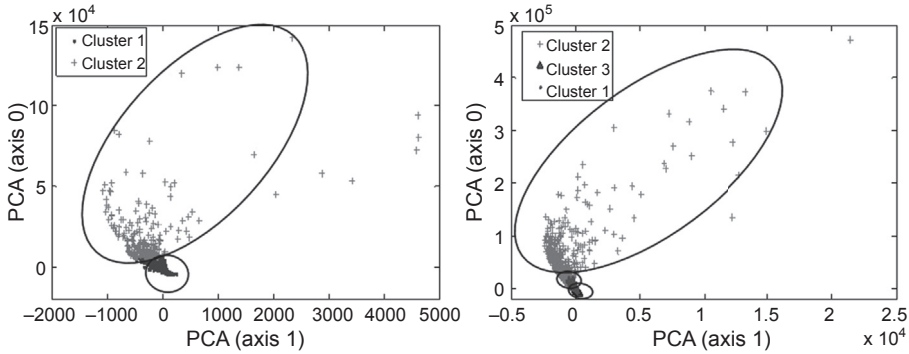

Figure 6.11 Visualization of the PAC clusters for basic (left) and desiccation creep (right). *Source*: Saliba et al. (2014).

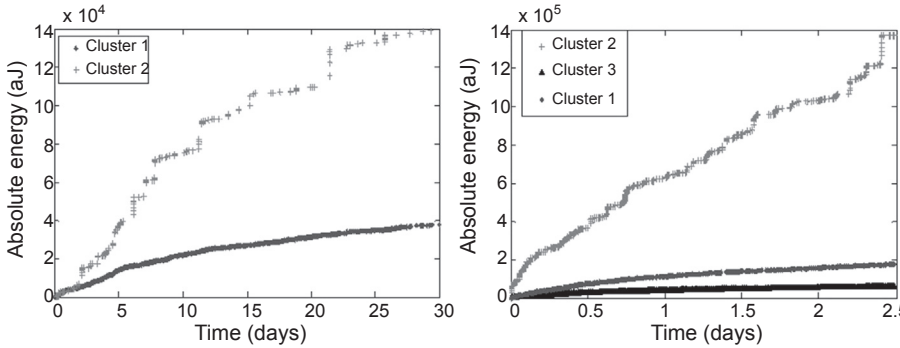

Figure 6.12 Cumulated energy for each cluster during basic (left) and desiccation creep (right). *Source*: Saliba et al. (2014).

The number of hits by amplitude recorded is averaged to create an experimental distribution of the AE hits amplitude for each cluster and is fitted with a statistical Laplace−Gauss model:

$$f_{(x)} = \frac{1}{\sigma\sqrt{2\pi}} e^{-\frac{1}{2}\left(\frac{x-m}{\sigma}\right)^2} \tag{6.1}$$

where $f_{(x)}$ represents the statistical variation of the population, σ the population standard deviation, which corresponds to the full width at half maximum, x the studied parameter, and m the population mean (mode).

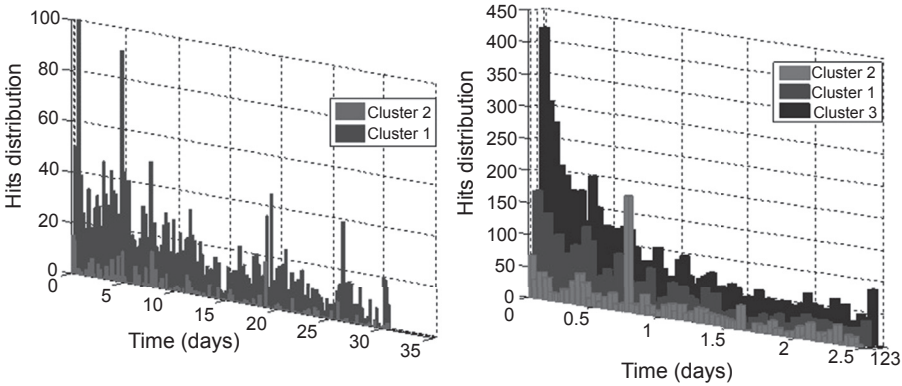

Figure 6.13 Apparition Chronology of the clusters during basic (left) and desiccation creep (right).
Source: Saliba et al. (2014).

Figure 6.14 shows the experimental distribution and the corresponding statistical law of the AE hits amplitude for each class. The mode of the AE hits amplitude distribution for the first cluster is 42 dB, and the range is between 36 and 47 dB. It can be associated with micro-cracking at the matrix−aggregate interface (Rossi, Robert, Gervais, & Bruhat, 1989). For the second class, the mode is 50 dB, the range is

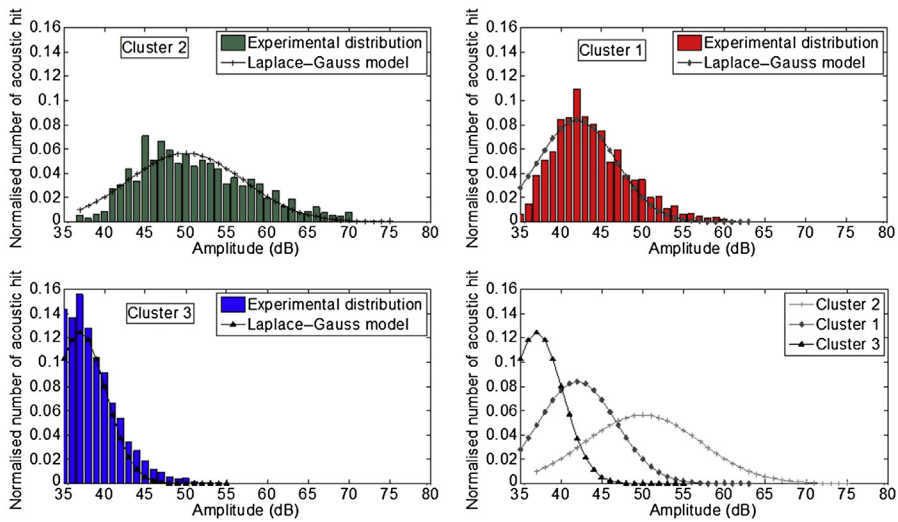

Figure 6.14 Experimental and statistical AE hits amplitude distributions for each cluster.
Source: Saliba et al. (2014).

between 42 and 59 dB, and it can be associated with micro-cracking in the matrix (Rossi et al., 1989). For the third cluster, the mode is 37 dB and the range is between 35 and 41 dB. Based on the variation of the AE parameters, this cluster could correspond to signals due to drying as liquid transfer in concrete (Chotard, Quet, Ersen, & Smith, 2006; Chotard, Smith, & Quet, 2007) and cavitation (Lura, Couch, Jensen, & Weiss, 2009). Note that the differences between ranges of amplitude of classes obtained here could be different for other specimen geometries and recording system parameters. The ranges have to be considered as relative differences.

6.4.4 Effects of desiccation creep on AE activity

The use of the AE method shows that it is possible to identify the most critical damage mechanisms leading to the final failure of concrete. In order to study the damage evolution during the three creep phases at the micro-structural level and, more particularly, tertiary creep, the AE technique can also be used during desiccation creep tests. The possibility of assessing the time to failure of the tested beams from AE is shown. Figure 6.15 presents the evolution of the AE activity during the desiccation creep test at 70%. The AE activity is followed by the three distinct phases of creep corresponding to the evolution of creep displacement into three regimes: primary creep, secondary creep, and tertiary creep. Those phases generate different signals covering different ranges of amplitude and corresponding to different damage mechanisms.

The AE activity is important during primary creep with AE hits of high amplitude and an important emission of AE energy (Figure 6.15). The rate decreases in correlation with the rate of creep displacement. During this phase, the events are arbitrarily distributed, especially in the tension zone (Figure 6.16(a)), and may correspond to the initiation and the development of micro-cracks inside the material as other physical

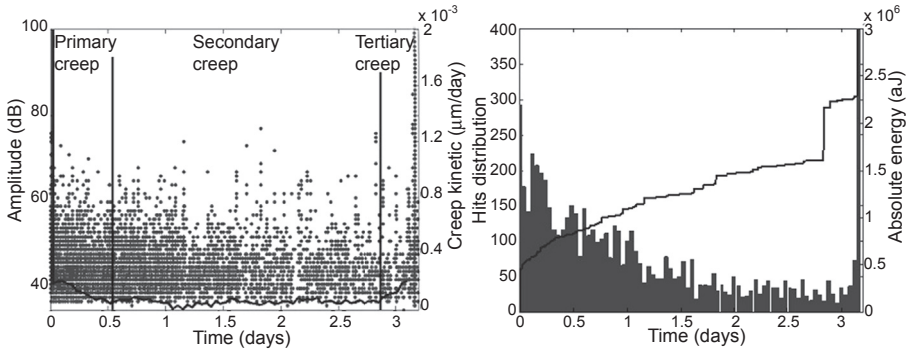

Figure 6.15 Correlation between the creep kinetic and the AE hits amplitude (left); correlation between the cumulated AE energy and the distribution of the AE hits (right).
Source: Saliba et al. (2014).

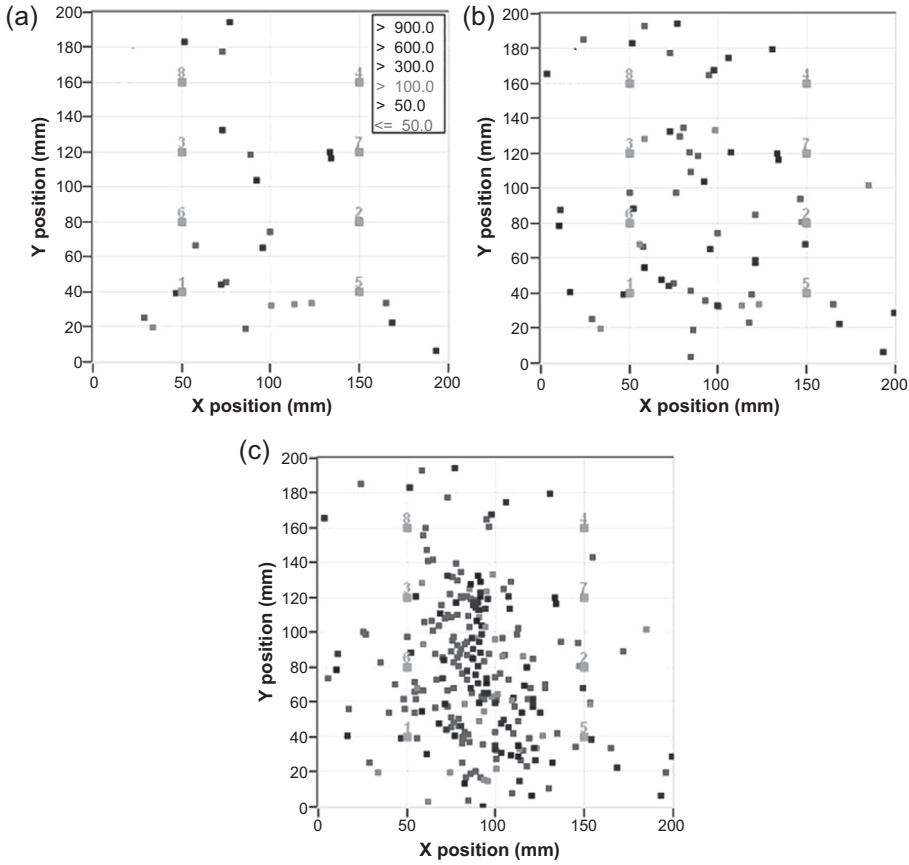

Figure 6.16 Localization of AE events during the (a) primary, (b) secondary, and (c) tertiary desiccation creep test loaded at 70%.
Source: Saliba et al. (2014).

mechanisms responsible for creep as water and stress redistribution in the beams and, consequently, micro-cracking.

During secondary creep, the rate of the AE activity is quasi-constant with a stable evolution of AE energy (Figure 6.15). The number of events continues to increase with different energetic value near the notch (Figure 6.16(b)). This phase corresponds to the apparition of a new damage mechanism due to the extension and the propagation of micro-cracking. Stresses are also generated by the deformation incompatibility between the aggregate and the cement paste (Idiart, López, & Carol, 2011; Saliba, Loukili, Grondin, & Regoin, 2014). This could be seen on the localization map, which presents events of different energy corresponding to different damage mechanisms as micro-cracks at the interface between the matrix and aggregate and into the matrix (Saliba, Grondin, Matallah, Loukili, & Boussa, 2012).

During the last phase, creep evolves toward the tertiary creep regime where the strain rate accelerates up to failure. The AE activity increases quickly with the emission of very energetic signals. This phase corresponds to the coalescence and the fast propagation of micro-cracks, generating a localized crack and leading to the failure of the specimen in the third day. The amplitude of the AE signals in this phase covers different ranges and sometimes reaches 100 dB at the failure, where the events begin to concentrate in the cracking zone to finally create a macroscopic crack (Figure 6.16(c)).

The stress concentration and redistribution are responsible for the failure and depend highly on the rate of loading and the loading condition. The rate of stress modifies the crack development and causes a slow and stable increase of micro-cracks until the unstable condition is reached during tertiary creep. This structural damage can be correlated to the evolution of micro-cracks or hits by relating the rate of the cumulated number of AE hits (N) and the number obtained at the end of the test (N_{max}), corresponding to the total failure where the scalar damage value is equal to 1 (Carpinteri, Lacidogna, & Pugno, 2007):

$$D_{EA} = \frac{N}{N_{max}} \tag{6.2}$$

where $N_{max} = 3425$ and $N_{max} = 5900$ for the beams loaded at 85% and 70%, respectively. Figure 6.17 shows the evolution of the damage coefficient during flexural creep tests at 70% and 85%. The rate of damage measured for the creep at 85% is more important in correlation with the rate of loading and the kinetics of creep displacement. Before the failure, creep displacement increases with an exponential function, and residual lifetime duration can then be estimated. This damage accumulation evolves as a bathtub-shaped curve and can be described using the Weibull

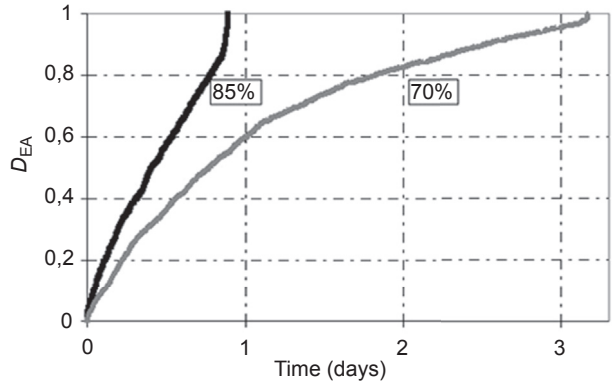

Figure 6.17 Evolution of the damage coefficient during desiccation creep.
Source: Saliba et al. (2014).

function (Verstrynge, Schueremans, Van Gemert, & Wevers, 2009). This suggests a method to predict the rupture by following the AE activity during creep and allows estimating the degree of concrete deterioration at an early stage of the deformation before the macro-crack formation.

6.5 Conclusions

AE analysis yields a wealth of information about the fracture process and helps in the understanding of micro-cracking and its role in mechanical behavior. The AE technique could be used to observe localization phenomena in concrete specimens. The evolution of the FPZ is clearly observed from the AE source location maps. The characteristics of the AE waves show a good correlation with the tension-softening properties. The decrease of the amplitude distribution after the peak load and the decrease of the width of the FPZ zone indicate a more fragile behavior for creep specimens.

Quantitative analysis of the AE data and characteristics of individual micro-cracks can be associated with two clusters for basic creep and three clusters for desiccation creep. The state of damage increases with the rate of loading, and the AE method gives sufficient data to predict the nonlinear creep and the failure of concrete.

The possibility of combining the multivariable data clustering with the moment tensor is an interesting research topic to study in the future. In addition, the simulation of AE activities at a micro- or a meso-level can be a helpful numerical tool to explain and to clarify the associated failure mechanisms.

References

Aggelis, D. G. (2011). Classification of cracking mode in concrete by acoustic emission parameters. *Mechanics Research Communications, 38*(3), 153−157. http://dx.doi.org/10.1016/j.mechrescom.2011.03.007.

Alam, S. Y., Loukili, A., & Grondin, F. (2012). Monitoring size effect on crack opening in concrete by digital image correlation. *European Journal of Environmental and Civil Engineering, 16*(7), 818−836.

Altoubat, S. A., & Lange, D. A. (2001). Creep, shrinkage and cracking of restrained concrete at early age. *ACI Materials Journal, 98*(4), 323−331.

Atrushi., D.S., (2003). *Tensile and compressive creep of early age concrete: testing and Modelling Science and Technology* (Ph.D. thesis). Norway: The Norwegian University of Science and Technology Trondheim.

Barpi, F., & Valente, S. (2005). Lifetime evaluation of concrete structures under sustained post-peak loading. *Engineering Fracture Mechanics, 72*(16), 2427−2443. http://dx.doi.org/10.1016/j.engfracmech.2005.03.010.

Bazant, Z. P., & Gettu, R. (1992). Rate effect and load relaxation in static fracture of concrete. *ACI Materials Journal, 89*(5), 456−468.

Bazant, Z. P., & Li, Y. (1997). Cohesive crack with rate-dependent opening and viscoelasticity: I. mathematical model and scaling. *International Journal of Fracture, 86*, 247−265.

Bazant, Z. P., & Prasannan, S. (1989). Solidification theory for concrete creep. I: formulation. *Journal of Engineering Mechanics, 115*(8), 1691−1703.

Bernal, J. D., & Megaw, H. D. (1935). The function of hydrogen in intermolecular forces. *Proceeding of the Royal Society, A151*, 384.

Bisschop, J., & Van Mier, J. G. M. (2002). How to study drying shrinkage microcracking in cement-based materials using optical and scanning electron microscopy? *Cement and Concrete Research, 32*(2), 279−287.

Bissonnette, B., & Pigeon, M. (2000). Le comportement viscoélastique du béton en traction et la compatibilité déformationnelle des réparations. *Materials and Structures, 33*, 108−118.

Bissonnette, Pigeon, M., & Vaysburd, A. M. (2007). Tensile creep of concrete: study of its sensitivity to basic parameters. *ACI Materials Journal, 104*(4), 360−368.

Carpinteri, A., Lacidogna, G., & Pugno, N. (2007). Structural damage diagnosis and life-time assessment by acoustic emission monitoring. *Engineering Fracture Mechanics, 74*(1−2), 273−289. http://dx.doi.org/10.1016/j.engfracmech.2006.01.036.

Carpinteri, A., Valente, S., Zhou, F., Ferrara, G., & Melchiorri, G. (1997). Tensile and flexural creep rupture tests on partially-damaged concrete specimens. *Materials and Structures, 30*(5), 269−276.

Carrasquillo, R. L., Slate, F. O., & Nilson, A. H. (1981). Microcracking and behavior of high strength concrete subjected to short-term loading. *ACI Journal, 78*(3), 179−186.

Chen, B., & Liu, J. (2004). Effect of aggregate on the fracture behavior of high strength concrete. *Construction and Building Materials, 18*(8), 585−590. http://dx.doi.org/10.1016/j.conbuildmat.2004.04.013.

Chotard, T., Quet, A., Ersen, A., & Smith, A. (2006). Application of the acoustic emission technique to characterise liquid transfer in a porous ceramic during drying. *Journal of the European Ceramic Society, 26*(7), 1075−1084. http://dx.doi.org/10.1016/j.jeurceramsoc.2005.01.048.

Chotard, T., Smith, A., & Quet, A. (2007). Characterisation of liquid transfer processes and water adsorption mechanism on a porous ceramic by acoustic emission means. *Journal of the European Ceramic Society, 27*(2−3), 457−462. http://dx.doi.org/10.1016/j.jeurceramsoc.2006.04.171.

Cook, B. D. J. (1972). Some aspects of the mechanism of tensile creep. *ACI Journal, 69*, 645−649.

Cook, D. J., & Haque, M. N. (1974). The tensile creep and fracture of desiccated concrete and mortar on water sorption. *Materials and Structures, 7*(3), 191−196.

Denarié, E., Cécot, C., & Huet, C. (2006). Characterization of creep and crack growth interactions in the fracture behavior of concrete. *Cement and Concrete Research, 36*(3), 571−575. http://dx.doi.org/10.1016/j.cemconres.2005.11.011.

Finck, F., Yamanouchi, M., Reinhardt, H., & Grosse, C. U. (2003). Evaluation of mode I failure of concrete in a splitting test using acoustic emission technique. *International Journal of Fracture, 124*, 139−152.

Freudenthalt, A. M., & Roll, F. (1958). Creep and creep recovery of concrete under high compressive stress. *Journal of the American Concrete Institute, 29*(12), 1111−1142.

Garas. V.Y. (2009). *Multi-scale investigation of tensile creep of ultra-high performance concrete for bridge applications* (Ph.D. thesis). School of Civil and Environmental Engineering, Georgia Institute of Technology.

Ghosh, R. S. (1973). A hypothesis on mechanism of maturing creep of concrete. *Matériaux et Constructions, 6*(31), 23−27.

Glanville, W. H., & Thomas, F. G. (1939). Further investigation on the creep or flow of concrete under load. In *Building Research Technical Paper, Department of Scientific and Industrial Research 21*.

Granger, S., Loukili, A., Pijaudier-Cabot, G., & Chanvillard, G. (2007). Experimental characterization of the self-healing of cracks in an ultra high performance cementitious material: mechanical tests and acoustic emission analysis. *Cement and Concrete Research, 37*(4), 519−527. http://dx.doi.org/10.1016/j.cemconres.2006.12.005.

Grosse, C. U., & Finck, F. (2006). Quantitative evaluation of fracture processes in concrete using signal-based acoustic emission techniques. *Cement and Concrete Composites, 28*(4), 330−336. http://dx.doi.org/10.1016/j.cemconcomp.2006.02.006.

Hadjab, H. S., Thimus, J., & Chabaat, M. (2007). The use of acoustic emission to investigate fracture process zone in notched concrete beams. *Current Science, 93*(5), 648−653.

Haidar, K., Pijaudier-Cabot, G., Dubé, J. F., & Loukili, A. (2005). Correlations between the internal length, the fracture process zone and size effect in mortar and model materials. *Materials and Structures, 38*, 201−210. http://dx.doi.org/10.1617/14053.

Hansen, E. A. (1991). Influence of sustained load on the fracture energy and the fracture zone of concrete. In J. G. M. van Mier, & A. Bakker (Eds.), *Rock and ceramics* (pp. 829−838). UK: E&FN Spon.

Hillerborg, A. (1985). The theoretical basis of a method to determine the fracture energy *Gf* of concrete. *Materials and Structures, 18*(106), 291−296.

Idiart, A. E., López, C. M., & Carol, I. (2011). Chemo-mechanical analysis of concrete cracking and degradation due to external sulfate attack: a meso-scale model. *Cement and Concrete Composites, 33*(3), 411−423. http://dx.doi.org/10.1016/j.cemconcomp.2010.12.001.

Kim, B., & Weiss, W. J. (2003). Using acoustic emission to quantify damage in restrained fiber-reinforced cement mortars. *Cement and Concrete Research, 33*(2), 207−214.

Kostopoulos, V., Loutas, T., Kontsos, A., Sotiriadis, G., & Pappas, Y. (2003). On the identification of the failure mechanisms in oxide/oxide composites using acoustic emission. *NDT & E International, 36*(8), 571−580. http://dx.doi.org/10.1016/S0963-8695(03)00068-9.

Landis, E. N. (1999). Micro−macro fracture relationships and acoustic emissions in concrete. *Construction and Building Materials, 13*, 65−72.

Landis, E. N., & Baillon, L. (2002). Experiments to relate acoustic emission energy to fracture energy of concrete. *Journal Engineering Mechanics, 128*(6), 698−702.

Landis, E. N., & Shah, S. P. (1995). The influence of microcracking on the mechanical behavior of cement based materials. *Cement Based Materials, 2*, 105−118.

Li, Z. J., & Shah, S. P. (1994). Localization of microcracking in concrete under uniaxial tension. *ACI Materials Jounal, 91*(4), 372−381. http://dx.doi.org/10.14359/4052.

Liniers, A. D. (1987). Microcracking of concrete under compression and its influence on tensile strength. *Materials and Structures, 20*(2), 111−116. http://dx.doi.org/10.1007/BF02472746.

Lura, P., Couch, J., Jensen, O. M., & Weiss, J. (2009). Early-age acoustic emission measurements in hydrating cement paste: evidence for cavitation during solidification due to self-desiccation. *Cement and Concrete Research, 39*(10), 861−867. http://dx.doi.org/10.1016/j.cemconres.2009.06.015.

Masuero, J. R. (1995). Crack growth initiation in concrete like materials in the presence of creep. In *SMiRT Conference, Stuttgart*, 156(1−2), pp. 209−218.

Mazzotti, C., & Savoia, M. (2002). Nonlinear creep, Poisson's ratio, and creep-damage interaction of concrete in compression. *ACI Materials Journal, 99*(5), 450−457.

Meyers, B. L., Slate, F. O., & Winter, G. (1969). Relationship between time-dependent deformation and microcracking of plain concrete. *ACI Materials Journal, 66*(1), 60−68.

Ngab, A. S., Slate, F. O., & Nilson, A. H. (1981). Microcracking and time-dependent strains in high strength concrete. *ACI Materials Journal, 11*, 262−268.

Ohtsu, M., Kaminaga, Y., & Munwam, M. C. (1999). Experimental and numerical crack analysis of mixed-mode failure in concrete by acoustic emission and boundary element method. *Construction and Building Materials, 13*, 57−64.

Oja, E. (1989). Neural networks, principal components, and subspaces. *International Journal of Neural Systems, 1*, 61−68.

Omar, M., Loukili, A., Pijaudier-cabot, G., & Le Pape, Y. (2009). Creep-damage coupled effects: experimental investigation on bending beams with various sizes. *Journal of Materials in Civil Engineering, 21*(2), 65−72.

Otsuka, K., & Date, H. (2000). Fracture process zone in concrete tension specimen. *Engineering Fracture Mechanics, 65*(2−3), 111−131.

Rao, G. A., & Prasad, B. K. R. (2002). Fracture energy and softening behavior of high-strength concrete. *Cement and Concrete Research, 32*, 247−252.

RILEM 50-FMC Recommendation. (1985). Determination of fracture energy of mortar and concrete by means of three-point bend test on notched beams. *Materials and Structures, 18*, 285−290.

RILEM TC212-ACD. (2010). Recommendation of RILEM TC 212-ACD : acoustic emission and related NDE techniques for crack detection and damage evaluation in concrete. *Materials and Structures, 43*, 1187−1189. http://dx.doi.org/10.1617/s11527-010-9638-0.

Rossi, P., Godart, N., Robert, J. L., Gervais, J. P., & Bruhat, D. (1994). Investigation of the basic creep of concrete by acoustic emission. *Materials and Structures, 27*, 510−514.

Rossi, P., Robert, J. L., Gervais, J. P., & Bruhat, D. (1989). Identification of the physical mechanisms underlying acoustic emissions during the cracking of concrete. *Materials and Structures, 22*, 194−198.

Rossi, P., Robert, J. L., Gervais, J. P., & Bruhat, D. (1990). The use of acoustic emission in fracture mechanics applied to concrete. *Engineering Fracture Mechanics, 35*, 751−763.

Rossi, P., Tailhan, J.-L., Le Maou, F., Gaillet, L., & Martin, E. (2012). Basic creep behavior of concretes investigation of the physical mechanisms by using acoustic emission. *Cement and Concrete Research, 42*(1), 61−73. http://dx.doi.org/10.1016/j.cemconres.2011.07.011.

Saliba, J., Grondin, F., Matallah, M., Loukili, A., & Boussa, H. (2012). Relevance of a meso-scopic modeling for the coupling between creep and damage in concrete. *Mechanics of Time-Dependent Materials, 17*(3), 481−499. http://dx.doi.org/10.1007/s11043-012-9199-4.

Saliba, J., Loukili, A., Grondin, F., & Regoin, J.-P. (2012). Experimental study of creep-damage coupling in concrete by acoustic emission technique. *Materials and Structures, 45*(9), 1389−1401. http://dx.doi.org/10.1617/s11527-012-9840-3.

Saliba, J., Loukili, A., Grondin, F., & Regoin, J.-P. (2014). Identification of damage mechanisms in concrete under high level creep by the acoustic emission technique. *Materials and Structures, 47*(6), 1041−1053. http://dx.doi.org/10.1617/s11527-013-0113-6.

Shah, S. P., & Chandra, S. (1970). Fracture of concrete subjected to cyclic and sustained loading. *ACI Materials Journal, 67*(10), 816−827.

Shah, S. P., & Choi, S. (1999). Nondestructive techniques for studying fracture processes in concrete. *International Journal of Fracture, 98*, 351−359.

Shah, S. P., & Ouyang, C. (1994). Fracture mechanics for failure of concrete. *Annual Review of Materials Science, 24*, 293−320.

Van Mier, J. G. M. (2008). Framework for a generalized four-stage fracture model of cement-based materials. *Engineering Fracture Mechanics, 75*(18), 5072−5086. http://dx.doi.org/10.1016/j.engfracmech.2008.07.011.

Verstrynge, E., Schueremans, L., Van Gemert, D., & Wevers, M. (2009). Monitoring and predicting masonry's creep failure with the acoustic emission technique. *NDT & E International, 42*(6), 518−523. http://dx.doi.org/10.1016/j.ndteint.2009.03.001.

Wu, K., Chen, B., & Yao, W. (2000). Study on the AE characteristics of fracture process of mortar, concrete and steel-fiber-reinforced concrete beams. *Cement and Concrete Research, 30*, 1495−1500.

Zhang, D., & Wu, K. (1999). Fracture process zone of notched three-point-bending concrete beams. *Cement and Concrete Research, 29*, 1887−1892.

Zhou, F.P., Barn, B.I.G., Lydon, F.D., College, W., & Iyf, C.F. (1995). Fracture properties of high strength concrete with varying silica fume content and aggregates. *School of Engineering, Division of Civil Engineering*, *25*(3), 543−552.

Laboratory investigations on concrete fracture using acoustic emission techniques

7

R. Vidya Sagar[1], *B.K. Raghu Prasad*[1], *R.K. Singh*[2]
[1]Indian Institute of Science, Bangalore, India; [2]Bhabha Atomic Research Centre, Mumbai, India

7.1 Introduction

Fracture mechanics has been applied to the study of load carrying capacity of a structure with initial cracks and is based on principles governing the propagation of cracks. In general, the field of fracture mechanics is concerned with the quantitative description of the mechanical state of a deformable body containing a crack or cracks, with a view toward characterizing and measuring the resistance of materials to crack growth (Bazant & Planas, 1998; Karihaloo, 1995; van Mier, 1997, 2013; Shah, Swartz, & Ouyang, 1995). Concrete is a heterogeneous material and cracks in it are cohesive in nature. As a result, the fracture process zone (FPZ) ahead of the crack tip retards the crack growth. The FPZ is the a cause for softening behavior in concrete.

Previously, researchers attempted to apply linear elastic fracture mechanics (LEFM) principles to concrete. The deviations from the laws of LEFM have been found to be more responsible for the transitional behavior of concrete with different sizes of test specimens. Applications of LEFM to concrete were initiated by Neville in 1959, Kaplan in 1961, and Kesler et al. in 1972. Then, it was concluded that LEFM was not valid for cementitious materials such as concrete because of the existence of an FPZ in front of the crack tip. Due to this fact, several researchers developed nonlinear fracture mechanics (NLFM) approaches to characterize FPZ. Starting with the fictitious crack model (FCM) by Hillerborg, Modeer, and Peterson (1976), the crack band model, the two-parameter model, the effective crack model, and the size effect model are known to be noteworthy developments in concrete fracture mechanics (Bazant & Planas, 1998; Karihaloo, 1995).

LEFM requires a single fracture parameter like critical stress intensity factor to characterize the failure of concrete, whereas NLFM models need more than one experimentally determined fracture parameter to characterize failure of concrete structures. Current codes of practice require to incorporate (1) strain softening associated with the post-cracking behavior, (2) the non-simultaneous failure due to propagating cracks, as in the punching shear failure of slab sand, and (3) the influence of the size of a structure upon its shear capacity (Karihaloo, 1995).

Acoustic Emission (AE) and Related Non-destructive Evaluation (NDE) Techniques in the Fracture Mechanics of Concrete
http://dx.doi.org/10.1016/B978-1-78242-327-0.00007-6
Copyright © 2015 Elsevier Ltd. All rights reserved.

Another important concept in fracture mechanics of concrete is the size effect. Laboratory experiments represent reality where full-scale structures are subjected to specific loading conditions. Because the real sizes of these structures generally exceed the maximum sizes in experiments, laboratory experiments are often scaled versions of the actual structures.

The size effect is associated with the variation of material parameters with the material. The well known size effect is generally explained by Weibull's hypothesis, but more specifically by Bazant's size effect law particularly for quasibrittle materials. With increasing the size of the structure, the tensile strength decreases. This is because the number of weak spots could increase with an increase in the material volume. Insight into the physical mechanisms underlying the size effect is essential to extrapolate experimental findings at laboratory scale. Consequently, the size effect is an important issue of fracture mechanics of concrete (Bazant & Pfeiffer, 1987; Karihaloo, 1995; Shah et al., 1995).

In relation to the size effect, the fracture energy as well as other NLFM parameters are to be defined by their values extrapolated to a specimen of large size. In a large specimen, the FPZ occupies a small fraction of the specimen volume. Hence, nearly all portions of the specimen could be in the elastic state. According to LEFM, it is known that the near-tip asymptotic field of displacements and stresses are identical, regardless of the specimen (or structure) geometry. Therefore, the FPZ must dissipate the same energy and have the same length and width. The energy release rate required for crack growth is reported (Karihaloo, 1995).

On the basis of these findings in fracture mechanics of concrete, applications of acoustic emission (AE) techniques to study the fracture process in concrete are discussed.

7.2 Acoustic emission (AE) studies in concrete

AE techniques have been applied to study the fracture process in concrete structures (Behnia, Chai, & Shiotani, 2014; Grosse & Ohtsu, 2008; Maji, Ouyang, & Shah, 1990; Mindess, 1990; Rossi, Robert, Gervais, & Bruhat, 1990; Vidya Sagar & Raghu Prasad, 2012). Generally, researchers and engineers use two different approaches related to AE techniques. One is a parameter-based technique, and the other is a signal-based AE technique. In the former technique, by using *b*-value analysis, magnitudes of crack's width are determined (Colombo, Main, & Forde, 2003). In the latter, AE techniques are advantageous to locate cracks in real time and to test the whole structure at once. By using the moment tensor analysis, orientations of propagating cracks are analyzed (Ohtsu & Ono, 1984; Ohtsu, 1987a, 1987b, 1988; Ohtsu, Shigeishi, Yuyama, & Okamoto, 1991).

So far, in the case of monitoring large concrete structures, it is usually not possible to use signal-based techniques (Grosse, Reinhardt, & Finck, 2003). In contrast, parameters such as peak amplitude, duration, frequency, phase, rise time, decay time, frequency spectra, and polarity signal parameters are useful for better characterization of the source of AE event (Behnia et al., 2014; Grosse & Ohtsu, 2008; Nor, Ibrahim, Bunnori, & Saman, 2013; Ohtsu, 1996).

The classification of cracks in concrete structures is a topical issue associated with AE parameter analysis and has been applied to AE signals emitted at different modes of fracture (mode-I, mode-II and mode-III) (Aggelis, 2011; Aldahdooh & Bunnori, 2013; Farhidzadeh, Salamone, & Singla, 2013; Nor et al., 2013; Shahidan, Pulin, Bunnori, & Holford, 2013). Such AE indices like the average frequency (AF) and the rise angle (RA) are employed to classify tensile cracking and shear cracking. Ohno and Ohtsu (2010) have compared the crack classification in reinforced concrete (RC) beams based on AE parameters with results of the moment tensor analysis.

7.3 AE energy release during fracture process in concrete

AE energy is the total elastic energy released by an AE event. The strain energy released is related to the energy of the signal received at the AE sensor, which is actually affected by attenuation due to heterogeneity of the material, coupling medium used, and the distance from the source (Harris & Bell, 1977; Landis & Baillon, 2002; Miller, Moore, & Hill, 2005; Vidya Sagar & Raghu Prasad, 2009a).

AE energy is defined as follows:

$$E_i = \int_{t_0}^{t_1} V_i^2(t)\mathrm{d}t \tag{7.1}$$

where V_i is the voltage transient of an i^{th} channel, t_0 is the starting time of the voltage transient record, and t_1 is the ending time of the voltage transient record. The energy is often given in the form of energy count. Here, the energy counts correspond to MARSE (measured area of the rectified signal envelop) and are presented as the values of absolute energy in joules. AE energy was found to be useful as a parameter to monitor concrete beams and to provide information about the structural condition (Colombo, Forde, Main, & Shigeishi, 2005; Colombo, Forde, Main, Halliday, & Shigeishi, 2005). By using AE energy, a parameter called a relaxation ratio (ratio of average energy during unloading phase to the average energy during loading phase) was defined to assess the damage state of concrete structures. Thus, it was concluded that AE energy can be used to assess the state of damage in concrete structures (Colombo, Forde, Main, Shigeishi, et al., 2005; Colombo, Forde, Main, Halliday, 2005; Grosse & Ohtsu, 2008; Landis & Baillon, 2002; NDIS 2421). Also, it was realized that a relationship between AE energy and fracture energy of concrete can be used to tune the damage mechanics models related to concrete (Landis & Baillon, 2002; Loland, 1989; Vidya Sagar & Raghu Prasad, 2009a).

7.4 Finite element analysis of concrete fracture and comparison with AE testing

Earlier, numerical models related to fracture process in concrete were developed at the meso-scale, by assuming that aggregates are spherical in shape (Lilliu, 2003;

van Mier, 1997, 2013; Schlangen, 1993; Schlangen & Garboczi, 1996, 1997). Recently, researchers attempted to model the aggregates as they are by using a computed tomography (CT-scan) technique (Man & van Mier, 2008).

Elsewhere, the lattice model was developed using the finite element method to simulate a wide range of experiments related to concrete fracture. But, the comparison between numerical and experimental results has usually been limited to the load–displacement diagram and to the macroscopic crack pattern (van Mier, 1997, 2013). A comparison with AE measurements is a major interest because it would allow a better understanding of the capability of the lattice model in predicting the formation of micro-cracks, both in the pre-peak and in the post-peak regime. Vidya Sagar, Raghu Prasad, and Karihaloo (2010) studied the applicability of the lattice model to concrete fracture by using AE testing. Notched three-point bend specimens (TPB) were tested, measuring the crack mouth opening displacement (CMOD). The entire fracture process was simulated using a regular triangular two-dimensional (2-D) lattice network of beam elements over the expected FPZ width. The beam specimen was discretized by a coarse, triangular finite element mesh. The discrete grain structure of the concrete was generated assuming the grains to be spherical. The load versus CMOD plots simulated agreed reasonably well with the experimental results.

During the experiments, AE events were monitored using an eight-channel AE system. AE transducers (sensors) used were of the resonant type with the highest sensitivity at 50-kHz frequency. It was found that cumulative AE hits were correlated well with the cumulative fractured lattice elements as shown in Table 7.1, both in the pre-peak and in the post-peak regimes. By applying AE measurement, it was concluded that the lattice model technique is eminently effective for the study of fracture process in concrete, which has hitherto only been presumed (Vidya Sagar et al., 2010). It was found that the trend in the cumulative fractured beam elements in the lattice fracture simulation physically reflects that of recorded AE hits, as shown in Figure 7.1(a) and (b).

7.5 Applications and results

7.5.1 Use of AE amplitude to compute b-value and Ib-value for monitoring the fracture process in concrete

AE amplitude is an important AE parameter and b-value is an important index to study the fracture process in concrete structures. The b-value is computed from AE amplitude distribution by a well-known method used in seismology (Colombo et al., 2003; Ohtsu, 1996; Rao & Prasanna Lakshmi, 2005; Vidya Sagar, Raghu Prasad, & Shantha Kumar, 2012a; Vidya Sagar & Raghu Prasad, 2012; Vidya Sagar & Rao, 2014). In the case of the AE method, the Gutenberg–Richter relationship between the maximum amplitude and AE events is given by the following:

$$\log_{10} N = a - b\left(\frac{A_{\mathrm{dB}}}{20}\right) \tag{7.2}$$

Table 7.1 Record of AE parameter and fractured lattice elements at different times and load levels

	Time (s)									
	Pre-peak zone		Post-peak zone							
	75	**93.7**	**154**	**299**	**475**	**601**	**912**	**1192**	**1219**	**1433**
Load (kN)	3.88	5.56	6.74	4.63	2.51	1.88	1.0	0.478	0.45	0.281
AE hits	18	48	183	908	1823	2197	2783	3000	3024	3160
Fractured lattice elements	167	879	984	1054	1136	1137	1145	1148	***	***

Vidya Sagar, R., Raghu Prasad, B. K., & Karihaloo, B. L. (2010). Verification of the applicability of lattice model to concrete fracture by AE study. *International Journal of Fracture*, *161*(2), 121−129.

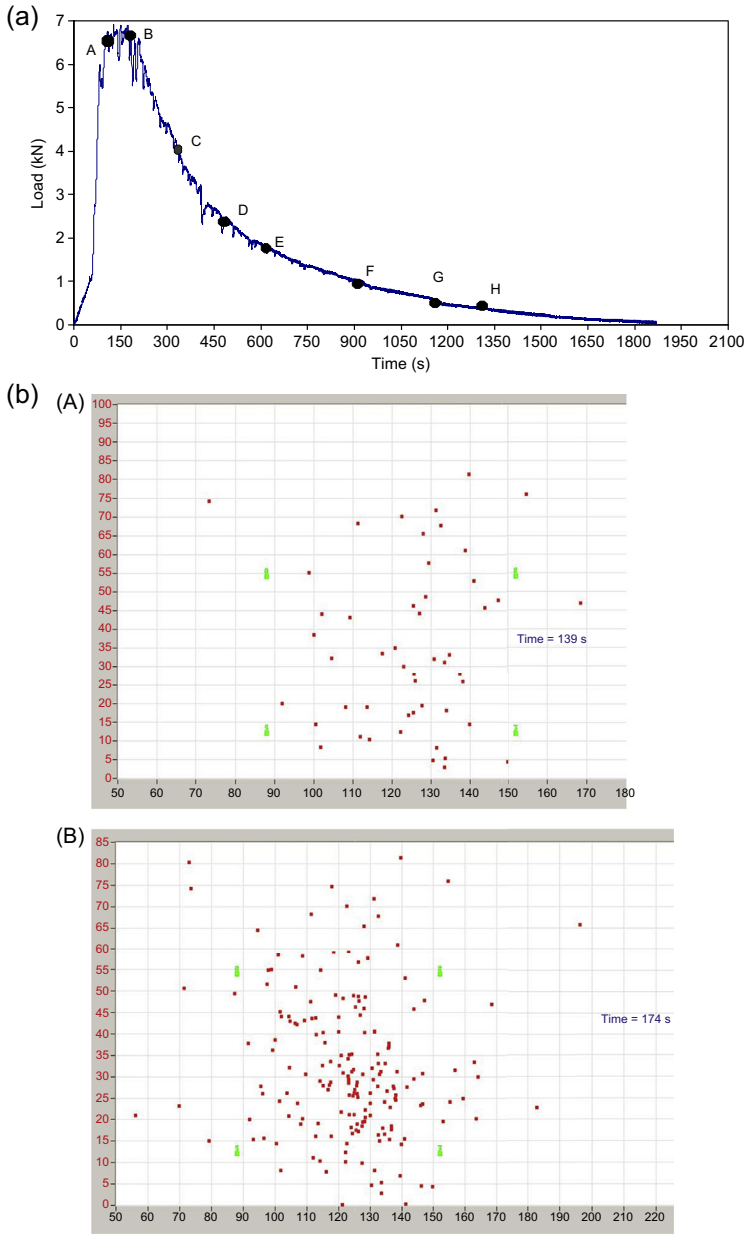

Figure 7.1 (a) A typical recorded load time diagram. (b) The AE source locations in TPB specimen tested at time, *t*: (A) 139 s, (B) 174 s, (C) 300 s, (D) 475 s, (E) 600 s, (F) 912 s, (G) 1192 s, and (H) 1219 s (*X*-axis represents the span and *Y*-axis represents the depth of the TPB specimen tested).
Vidya Sagar, R., Raghu Prasad, B. K., & Karihaloo, B. L. (2010). Verification of the applicability of lattice model to concrete fracture by AE study. *International Journal of Fracture*, *161*(2), 121−129.

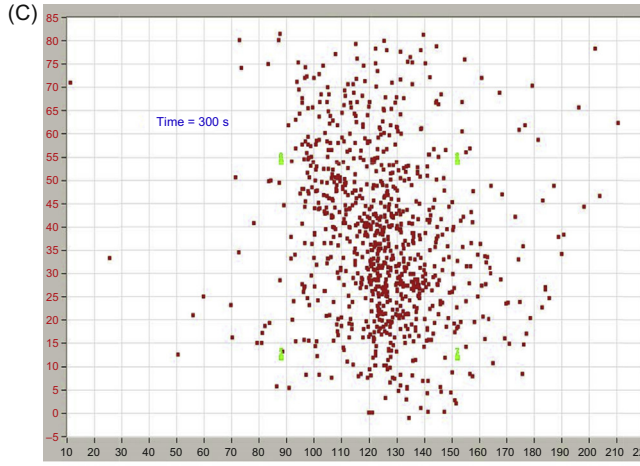

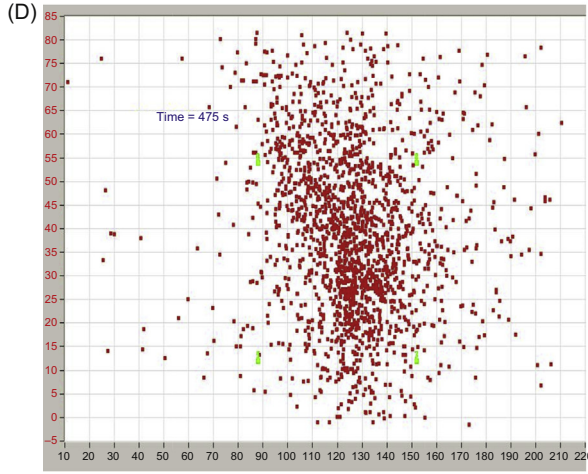

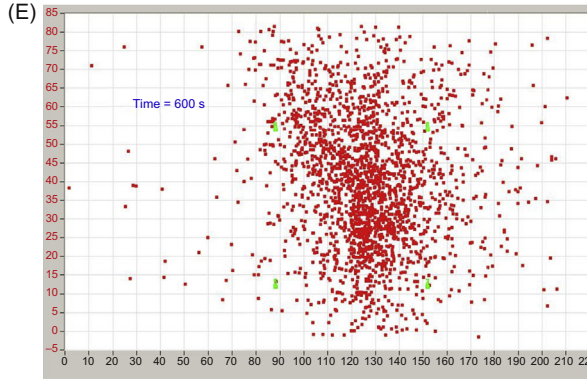

Figure 7.1 Continued.

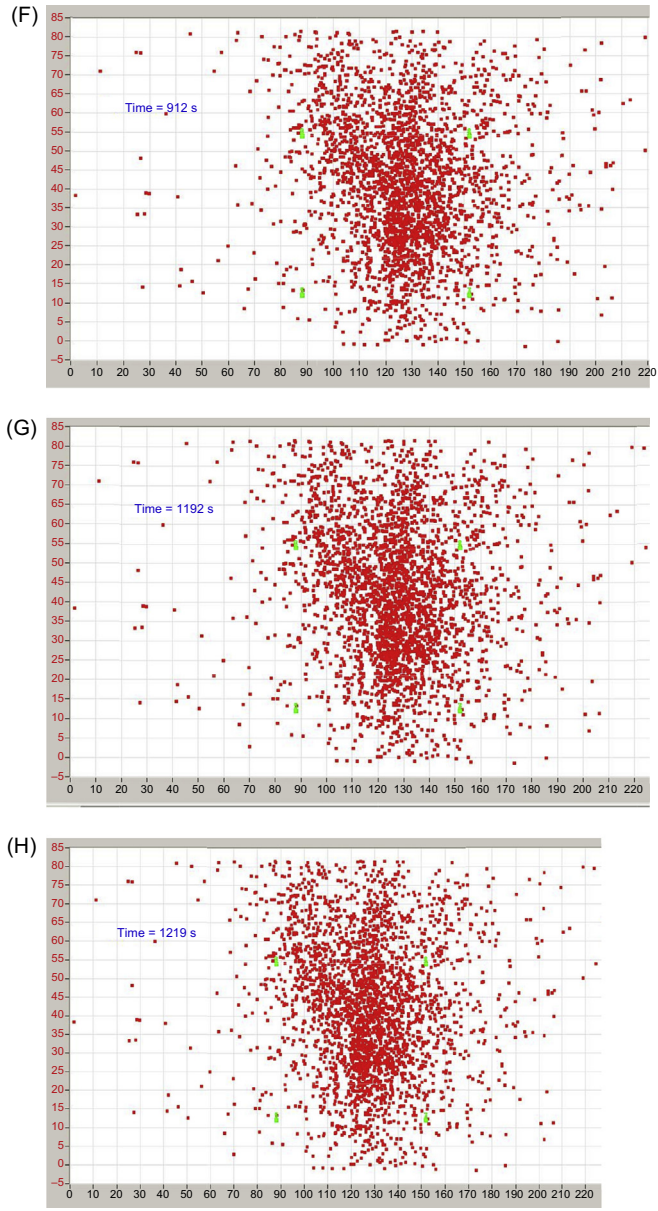

Figure 7.1 Continued.

where A_{dB} is the peak amplitude of AE events (or hits) in decibels, b is the b-value, and $N(M)$ is the number of AE hits (or events) of magnitude $\geq M$. Several studies related to the diagnosis of damaged concrete structures and masonry buildings based on the b-value analysis have been carried out (Carpinteri & Lacidogna, 2003, 2006a, 2006b, 2007; Carpinteri, Invernizzi, & Lacidogna, 2005; Carpinteri, Lacidogna, & Pugno,

2007; Carpinteri, Lacidogna, & Puzzi, 2008; Ohtsu, 1987a). Vidya Sagar, Raghu Prasad, and Shantha Kumar (2012b) and Vidya Sagar and Rao (2014) attempted to relate the *b*-values with strains in steel and concrete. Colombo et al. concluded that the larger *b*-value indicates the occurrence of microscopic cracks more predominantly, and the smaller *b*-value indicates the occurrence of macro-cracking (Colombo et al., 2003). Figure 7.2 shows variations of the *b*-values under sinusoidal loading in a RC beam subjected to incremental cyclic loading. A sudden drop in the *b*-value is observed at the peak load of cyclic loading applied on RC beams. This could result from localization of micro-cracks (Vidya Sagar & Rao, 2014).

The high rate of loading could accelerate the damage accumulation of micro-cracks that is accompanied by the release of AE events. Normally, fluctuations in the *b*-values are emphasized when the rate of loading is high. From Figure 7.3, it is observed that the *b*-values vary, depending on the loading rates (Vidya Sagar & Rao, 2014). In case the loading rate is higher, the faster crack development leads to sudden fluctuations and a drop in the *b*-value. Because the material behaves relatively more brittle at higher loading rates (or in higher strain rates), the *b*-values become lower on average.

The *b*-value analysis is useful in evaluating the damage level (minor, intermediate, or heavy) in RC structures *in situ* and is applicable to estimate the present operating conditions. A sudden drop in the *b*-value occurs due to the formation of a new crack or the propagation of existing cracks.

In addition to the conventional *b*-value, an improved *b*-value (I*b*-value) is proposed as suitable for AE applications to concrete fracture. The I*b*-value is obtained from a statistical slope of the peak amplitude distribution of AE signals (Aggelis, Shiotani, Momoki, & Hirama, 2009; Grosse & Ohtsu, 2008; Rao & Prasanna Lakshmi, 2005; Shiotani, Fujii, Aoki, & Amou, 1994; Shiotani, Yuyama, Li, & Ohtsu, 2000, 2001).

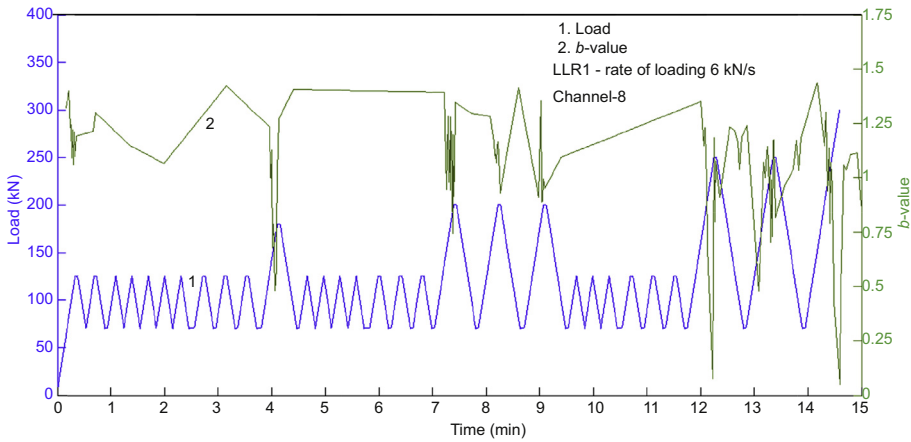

Figure 7.2 Variation of *b*-value with load.
Vidya Sagar, R., & Rao, M. V. M. S. (2014). An experimental study on loading rate effect on acoustic emission based *b*-values related to reinforced concrete fracture. *Construction and Building Materials*, *70*, 460–472. http://dx.doi.org/10.1016/j.conbuildmat.2014.07.076.

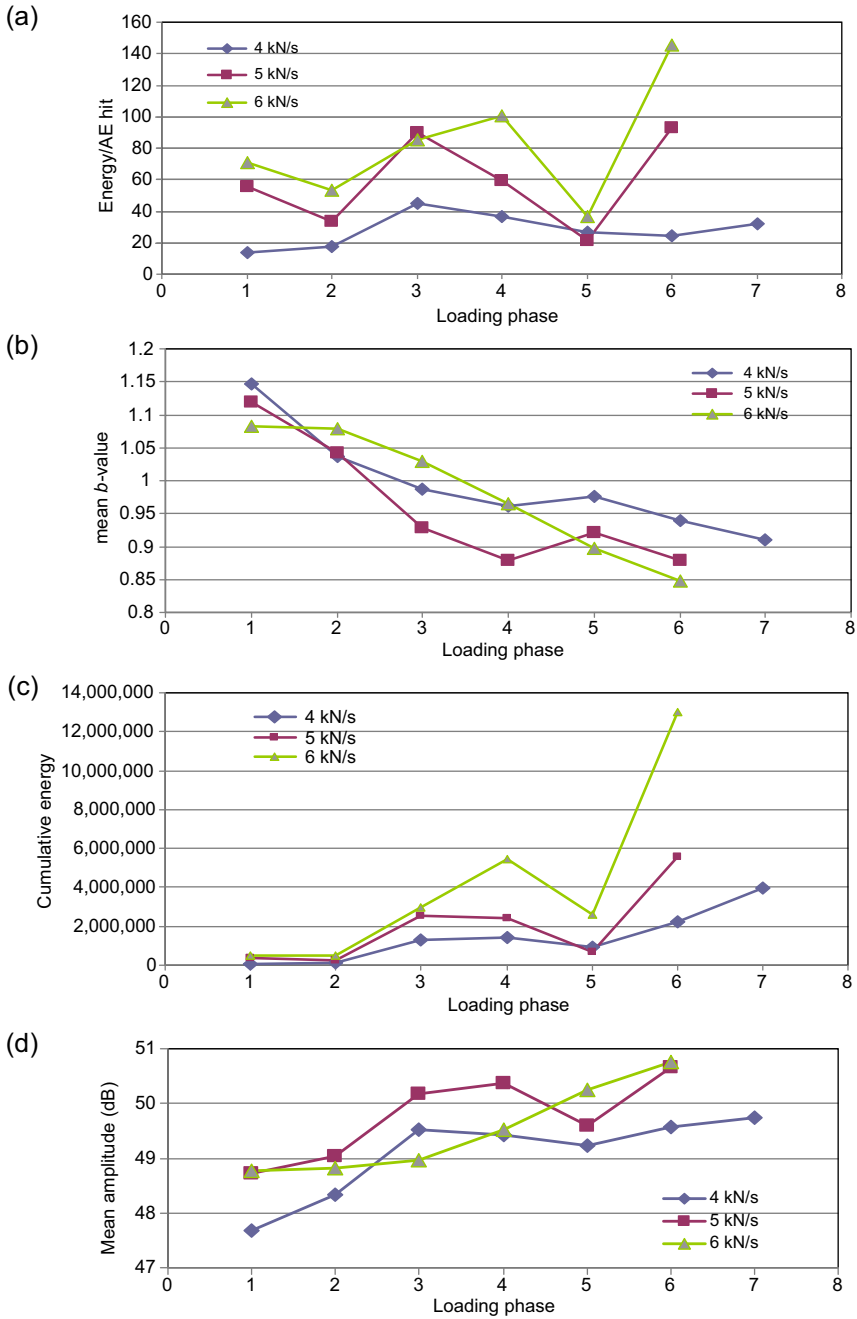

Figure 7.3 (a) Variation of energy per hit, (b) mean *b*-value, (c) cumulative energy, and (d) mean amplitude with the loading phase.
Vidya Sagar, R., & Rao, M. V. M. S. (2014). An experimental study on loading rate effect on acoustic emission based *b*-values related to reinforced concrete fracture. *Construction and Building Materials*, *70*, 460−472. http://dx.doi.org/10.1016/j.conbuildmat.2014.07.076.

In the computation, the statistical values of amplitude distribution of AE are considered because AE amplitudes vary with time:

$$Ib = \frac{\log_{10}N(\mu - \alpha_1\sigma) - \log_{10}N(\mu + \alpha_2\sigma)}{(\alpha_1 + \alpha_2)\sigma} \tag{7.3}$$

where μ is the mean amplitude, σ is the standard deviation, and α_1 and α_2 are user-defined constants. Shiotani et al. (2000) studied the I*b*-value to quantify the damage in concrete piers due to an earthquake. The I*b*-values were computed for AE events located within a pier (Shiotani et al., 2001). The I*b*-value is known to be unaffected by the monitoring conditions, and it uniquely varies depending on the damage level. Aggelis et al. implemented I*b*-value analysis to study the fracture process in RC structures (Aggelis et al., 2009).

7.5.2 Use of AE hit rate in assessing nucleation of crack growth

The parameter AE hit is used to study the nucleation phases of micro-cracking in concrete structures. Yoon et al. carried out AE monitoring in RC beams subjected to corrosion of the steel reinforcement, and it was observed that AE counts (hits) decrease with the increase in the degree of corrosion (Yoon, Weiss, & Shah, 2000). Vidya Sagar, Raghu Prasad, Rashmi V Prasad, and Rao (2013) applied AE hit rate to investigate nucleation of micro-cracks and macro-cracks in cement concrete and mortar. AE activity increases steadily and slowly due to the formation of micro-cracks. Variation in recorded AE hits was observed under cyclic loading applied to RC beams with different percentages of reinforcement (Ohtsu, Uchida, Okamoto, & Yuyama, 2002).

Earlier researchers concluded that AE hit rate might not be a satisfactory measure of damage because the conditions for increase in AE activity should be considered. Ohtsu et al. observed in an under-reinforced beam that AE hit rate increased exponentially due to sliding between reinforcement and concrete. In contrast, in an over-reinforced beam, AE hit rate remained constant until final failure (Ohtsu et al., 2002).

7.5.3 Use of AE testing to measure the FPZ size in concrete

The concept of the FPZ was introduced to enunciate the softening behavior of concrete. A relation between the area of the FPZ and aggregate size was studied, taking into account the size of the specimens (Hadjab, Thimus, & Chabaat, 2007; Izumi, Mihashi, & Nomura, 1986; Lysak, 1996; Maji & Shah, 1988; Mihashi, Nomura, & Niseki, 1991; Otsuka & Date, 2000; Vidya Sagar & Raghu Prasad, 2009b). It has been observed that the width of the FPZ increases with an increase in the size of aggregate. In addition, the length of the FPZ decreases with an increase in the aggregate size (Maji & Shah, 1988; Mihashi et al., 1991; Otsuka & Date, 2000; Izumi et al., 1986). AE testing has also been applied to study the effect of aggregate on the fracture behavior of high-strength concrete and high-performance concrete (Chen & Liu, 2004a, 2004b, 2007; Lysak, 1996).

For specimens with an identical size of the maximum aggregate, the length of the FPZ increased with the increase in the specimen size. It was also observed that many AE events had low energy and higher energy events localized around the notch tip. The zone of AE events, which included more than 95% of the total energy, was considered as the FPZ (Otsuka & Date, 2000). Vidya Sagar and Raghu Prasad (2009b) carried out studies to estimate the size of the FPZ in three-point bend specimens of high-strength concrete. It was observed that a few AE events with high energy occurred in a number and were concentrated near the crack tip, as shown in Figure 7.4. Vidya Sagar and Raghu Prasad (2009b) tested three-point bend specimens of dimensions as shown in Table 7.2, and in the same Table 7.2, measured maximum loads, cumulative AE energy, calculated fracture energy, and nominal strength are given. Table 7.3 shows AE data and the recorded AE energy for the specimens of different depths. The distribution of AE energy in different sizes of the specimens is shown in Figure 7.5. In Figure 7.4, E indicates AE energy and CL indicates the specific class according to the released energy level. The area of AE events around 93% of the total energy can be considered the FPZ in TPB concrete specimens (Otsuka & Date, 2000; Vidya Sagar & Raghu Prasad, 2009b).

7.5.4 Experiments to relate AE energy and fracture energy of concrete

It is known that AE activity is correlated with a rapid release of strain energy in a material. Thus, the relation between AE energy and fracture energy of concrete could be useful to develop a laboratory tool in order to study the damage in concrete structures under controlled conditions. In damage mechanics in concrete, it is required to define the crack density. But, crack density is considered to be a difficult property to quantify. In this respect, AE has the potential to provide information on the crack density. The relation between AE energy released and fracture energy of concrete has been studied (Landis & Baillon, 2002; Raghu Prasad & Vidya Sagar, 2008; Vidya Sagar & Raghu Prasad, 2009a). Figure 7.6 shows the variation of AE energy released under loading. It is clearly observed that AE energy release starts right after reaching the peak load (Vidya Sagar, 2010). Figure 7.7 shows the plots of cumulative AE energy versus the fracture energy (RILEM 50-FMC) in concrete and cement mortar. The scatter is more apparent in concrete than mortar, as shown in Figure 7.7. AE energy is a localized phenomenon, whereas the fracture energy is globally estimated. In the case that the wavelength is shorter than the size of aggregate, propagated AE waves of high-frequency components easily attenuate due to internal deflections of the waves, which is called scattering. Since scattering absorbs AE energy, AE energy estimated could decrease. Scattering of AE waves strongly depends on the heterogeneity of concrete and, thus, on the size distributions of inclusions and aggregate. Regarding damage models, there is a large class of concrete performance models based on the principles of continuum damage mechanics, which are often associated with parameters such as the crack density. It is promising that AE techniques have the potential to

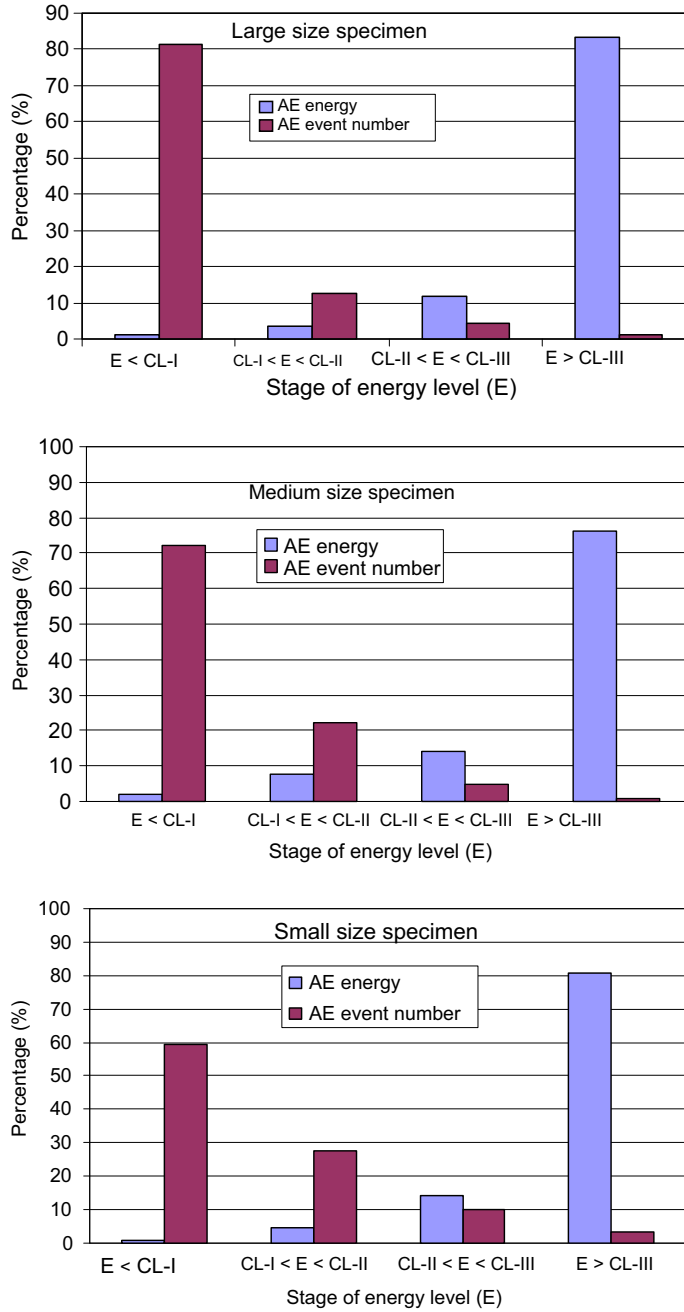

Figure 7.4 Distribution of AE energy in large size (depth = 320 mm), medium size (depth = 160 mm), and small size (depth = 80 mm) three-point bend concrete specimens. Vidya Sagar, R., & Raghu Prasad, B. K. (2011). *Construction and Building Materials*, *25*, 2349−2357.

Table 7.2 Measured maximum loads, cumulative AE energy, calculated fracture energy, and nominal strength

Specimen	$\frac{a_0}{d}$	Depth, mm	Load, N	Average load, P_{max}	W_F, N−m	Fracture energy, N/m	Average fracture energy	Nominal strength, N/mm^2	Cumulative AE energy (relative units)	Average cumulative AE energy (relative units)
FSN_1a	0.15	80	7063.203	6700.08	0.9827	180.60	167.76	1.10362	317.47	219.5
FSN_1b	0.15	80	6902.066		0.9116	167.50		1.07844	128.99	
FSN_1c	0.15	80	6134.983		0.8451	155.20		0.95859	212.86	
FSN_2a	0.30	80	4182.867	4183.42	0.5865	130.90	140.27	0.65357	72.31	102.5
FSN_2b	0.30	80	4662.920		0.7716	172.20		0.72858	88.04	
FSN_2c	0.30	80	3704.490		0.5274	117.70		0.57875	147.37	
FSN_3a	0.50	80	2422.101	2048.91	0.3198	99.90	81.47	0.37845	76.44	42.6
FSN_3b	0.50	80	1770.840		0.2528	79.00		0.27669	16.84	
FSN_3c	0.50	80	1953.791		0.2099	65.50		0.30527	36.57	
FMN_1a	0.15	160	8891.110	10,173.04	1.4194	130.40	129.44	0.69030	270.43	201.5
FMN_1b	0.15	160	11,144.000		1.4538	133.60		0.86521	180.54	
FMN_1c	0.15	160	10,484.023		1.3525	124.30		0.81397	153.85	
FMN_2a	0.30	160	7583.544	7030.752	1.1548	128.80	109.34	0.58878	186.09	117.4
FMN_2b	0.30	160	6594.897		0.8093	90.32		0.51202	73.2	
FMN_2c	0.30	160	6913.815		0.9759	108.90		0.53678	92.1	
FMN_3a	0.50	160	4194.616	4266.79	0.6719	104.90	101.25	0.32566	91.05	79.5
FMN_3b	0.50	160	****		****	****		****	***	
FMN_3c	0.50	160	4338.969		0.6251	97.60		0.33687	67.12	
FLN_1a	0.15	320	19,316.385	20,698.26	2.5687	118.00	133.7	0.75454	647.2	410.34
FLN_1b	0.15	320	23,646.961		2.7637	127.00		0.92368	416.6	
FLN_1c	0.15	320	19,131.463		3.3986	156.10		0.74732	168.05	
FLN_2a	0.30	320	10,942.259	12,332.07	2.2183	123.70	122.67	0.42743	232.6	209.5
FLN_2b	0.30	320	13,438.215		2.1848	121.90		0.52493	114.6	
FLN_2c	0.30	320	12,615.742		2.1941	122.40		0.49280	283.5	
FLN_3a	0.50	320	8335.520	8369.65	1.5273	119.32	141.04	0.32560	242.4	225.5
FLN_3b	0.50	320	7627.186		1.7266	134.80		0.29793	189.41	
FLN_3c	0.50	320	9146.245		2.1639	169.00		0.35727	244.6	

Raghu Prasad, B. K., & Vidya Sagar, R. (2008). Relationship between AE energy and fracture energy of plain concrete beams-experimental study. *Journal of Materials in Civil Engineering*, *20*(3), 212−220.

Table 7.3 AE emissions data and the recorded AE energy for the specimens of different depths

AE energy (volt^2-μs)	AE events occurred		AE energy (volt^2-μs)		Remarks
	Number	%	Total AE energy	%	
For large size specimens 960 mm × 320 mm × 80 mm					Class-I = 10,000 volt^2-μs Class-II = 100,000 volt^2-μs Class-III = 10,00,000 volt^2-μs
Total	6049	100	7.04E8	100	
Under class-I	4929	81.48	8.24E6	1.17	
Above class-I	1120	18.51	6.96E8	98.87	
Above class-II	351	5.80	6.70E8	95.17	
Above class-III	83	1.37	5.87E8	83.38	
For medium size specimens 480 mm × 160 mm × 80 mm					
Total	5342	100	4.96E8	100	
Under class-I	3846	72	9.42E6	1.9	
Above class-I	1496	28	4.87E8	98.1	
Above class-II	306	5.73	4.5E8	90.7	
Above class-III	57	1.07	3.79E8	76.4	
For smaller size specimens 240 mm × 80 mm × 80 mm					
Total	1156	100	2.43E8	100	
Under class-I	685	59.26	1.86E6	0.77	
Above class-I	471	40.74	2.41E8	99.23	
Above class-II	154	13.32	2.3E8	94.67	
Above class-III	38	3.29	1.96E8	80.67	

provide information on the crack density that could be useful for the continuum damage models in concrete.

7.5.5 Size-independent specific fracture energy of concrete and AE energy

Duan, Hu, and Wittmann (2001) studied the boundary effect on concrete fractures induced by non-constant fracture energy distribution. The study concluded that the fracture energy of concrete is independent of size. Ramachandra Murthy, Karihaloo, Iyer, and Raghu Prasad (2013) studied the size-independent fracture energy of concrete based on the boundary effect.

AE technique has been applied to the study of crack extension during the fracture process. Muralidhara, Raghu Prasad, Karihaloo, and Singh (2011) observed that the generation of AE events under loading follows approximately a tri-linear distribution, a reminiscent analogy of R-curve in a finite size specimen. Initially, the number of AE events increases almost linearly, reaching an extended plateau as the number of events remains nearly constant, and eventually, the number reduces as the crack approaches a stress-free boundary of the specimen.

7.5.6 Detection and assessment of damage in concrete using AE testing

Ohtsu and Watanabe (2001) introduced the rate process analysis to quantitatively evaluate the change of AE activity in the structure due to damage (Ohtsu & Watanabe, 2001; Ohtsu, 1992). For a concrete specimen containing a large number of microcracks, AE occurrence is expected under loading. On the contrary, AE activity in a well-compacted and adequately cured concrete is stable and low up to final failure (Grosse & Ohtsu, 2008).

In the rate process theory, a probability function of AE occurrence from stress level V (%) to $V + \mathrm{d}V$ (%) was represented as a hyperbolic function to devise the occurrence of AE activity under loading (Ohtsu, 1992). A relationship between the number of total AE events, N, and stress level, V (%), is proposed as follows:

$$N = CV^{a} \exp^{(bv)} \tag{7.4}$$

where a and b are empirical coefficients and C is the integration constant (Loland, 1989; Ohtsu, 1992; Ohtsu & Watanabe, 2001).

Researchers studied damage mechanisms by interpreting AE signals (Carpinteri et al., 2007). Carpinteri and Lacidogna (2003) employed AE testing to assess the damage in a historical masonry building, Casa Capello, located in Italy. It was observed that by correlating the evolution of cracks with the cumulative AE events, crack growth underwent a progressive deceleration (Carpinteri et al., 2005). Yuyama et al. conducted AE monitoring on an aged dock under mobile loading (Yuyama, Okomoto, Shigeishi, & Ohtsu, 1993). Three levels of loading applied were

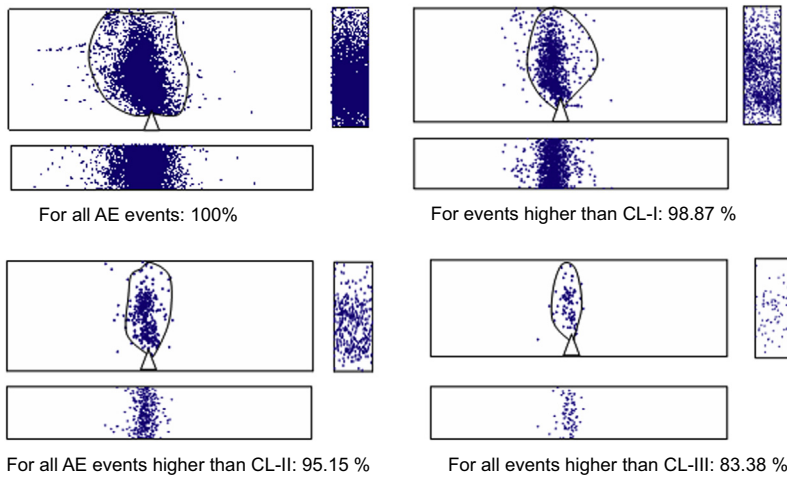

Figure 7.5 Diagrams of AE source locations represented by four energy stages (depth = 320 mm; $a_0/d = 0.15$).
Vidya Sagar, R., & Raghu Prasad, B. K. (2009b). An experimental study on fracture process zone in HSC three-point bend beam specimen using an acoustic emission method. *Journal of Structural Engineering (SERC, Chennai, India)*, *36*(1), 59−69.

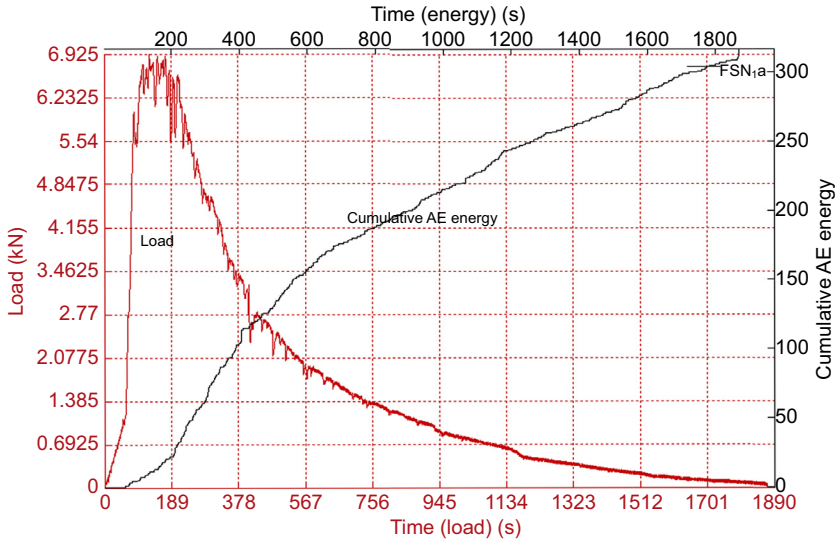

Figure 7.6 Variation of AE energy with time and load during concrete fracture.
Vidya Sagar, R., Raghu Prasad, B. K., & Karihaloo, B. L. (2010). Verification of the applicability of lattice model to concrete fracture by AE study. *International Journal of Fracture*, *161*(2), 121−129.

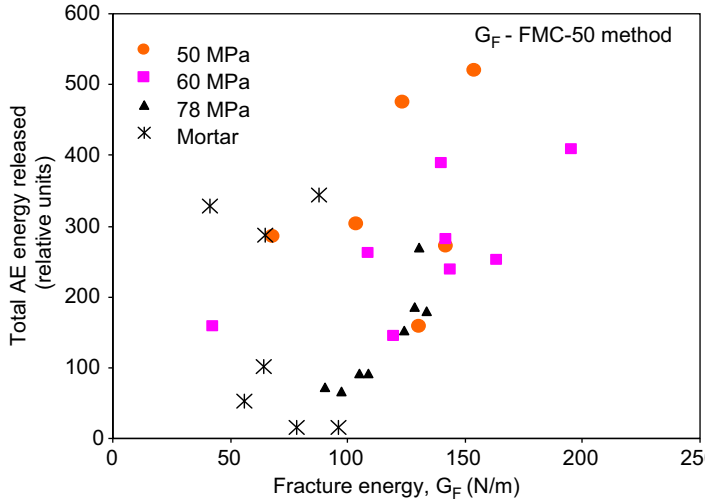

Figure 7.7 Variation of total AE energy release versus fracture energy by FMC-50 method. RILEM Committee 50-FMC. (1985). Determination of the fracture energy of mortar and concrete by means of three-point bend tests on notched beams. *Materials and Structures*, *18*, 285−290. Vidya Sagar, R., & Raghu Prasad, B. K. (2009a). AE energy release during the fracture of HSC beams. *Magazine of Concrete Research*, *61*(6), 419−435.

zero-load of an empty truck, half-load bearing capacity of the truck, and full-load bearing capacity of the truck. During the first cycles, fewer AE hits were observed during loading and unloading. In the second cycle, the Kaiser effect was observed during the loading phase and in the unloading phase. During the third cycle, no Kaiser effect was observed during loading and unloading phases. Vidya Sagar, Raghu Prasad, and Singh (2015) studied the Kaiser effect as a measure of damage in RC beams. It was observed that RC beams made with high-strength concrete tested under incremental, cyclic loading showed the Kaiser effect before the ultimate failure (Vidya Sagar et al., 2015).

7.6 Conclusions

This chapter recapitulates laboratory investigations done by various researchers on concrete fracture using AE monitoring techniques. Research in the field of AE testing of concrete structures is undergoing a drastic improvement due to an increasing need for analysis and renovation of concrete structures. Various research works have led to the realization of several practical applications of AE testing. In relation to such research activities, RILEM technical committee: TC 212-ACD (AE and Related NDE Techniques for crack detection and damage evaluation in concrete) was established and a recommendation (Ohtsu, 2010) was published to assess the damage of concrete structures. There is surely a need to develop a more generalized method to interpret the recorded AE data. The

information given in this chapter may help toward making AE technology a field of widespread application for fracture monitoring of concrete structures.

References

Aggelis, D. G. (2011). Classification of cracking mode in concrete by acoustic emission parameters. *Mechanics Research Communications, 38*, 153−157.

Aggelis, D. G., Shiotani, T., Momoki, S., & Hirama, A. (November−December 2009). Acoustic emission and ultrasound for damage characterization of concrete elements. *ACI Materials Journal, 106*(6), 1−6. http://dx.doi.org/10.1016/10.14359/51663333.

Aldahdooh, M. A. A., & Bunnori, M. N. (2013). Crack classification in reinforced concrete beams with varying thickness by means of acoustic emission signal features. *Construction and Building Materials, 45*, 282−288.

Bazant, Z. P., & Pfeiffer, P. A. (1987). Determination of fracture energy from size effect and brittleness number. *ACI Materials Journal, 84*(6), 463−480.

Bazant, Z. P., & Planas, J. (1998). *Fracture and size effect in concrete and other quasi brittle materials*. Boca Raton, FL: CRC Press.

Behnia, A., Chai, H. K., & Shiotani, T. (2014). Advanced structural health monitoring of concrete structures with the aid of acoustic emission. *Construction and Building Materials, 65*, 282−302.

Carpinteri, A., Invernizzi, S., & Lacidogna, G. (2005). In-situ damage assessment and nonlinear modeling of an historical masonry tower. *Engineering Structures, 27*, 387−395.

Carpinteri, A., & Lacidogna, G. (2003). Damage diagnostic in concrete and masonry structures by acoustic emission technique. *Facta Universitatis, 3*, 755−764.

Carpinteri, A., & Lacidogna, G. (2006a). Damage monitoring of a historical masonry building by the acoustic emission technique. *Materials and Structures, 39*, 161−167.

Carpinteri, A., & Lacidogna, G. (2006b). Structural monitoring and integrity assessment of medieval towers. *Journal of Structural Engineering, 132*, 1681−1690.

Carpinteri, A., & Lacidogna, G. (2007). Damage evaluation of three masonry towers by acoustic emission. *Engineering Structures, 29*, 1569−1579.

Carpinteri, A., Lacidogna, G., & Pugno, N. (2007). Structural damage diagnosis and life-time assessment by acoustic emission monitoring. *Engineering Fracture Mechanics, 74*, 273−289.

Carpinteri, A., Lacidogna, G., & Puzzi, S. (2008). Prediction of cracking evolution in full scale structures by the *b*-value analysis and Yule statistics. *Physical Mesomechanics, 11*(5−6), 260−271.

Chen, B., & Liu, J. (2004a). Effect of aggregate on the fracture behavior of high strength concrete. *Construction and Building Materials, 18*, 585−590.

Chen, B., & Liu, J. (2004b). Experimental study on AE characteristics three-point-bending concrete beam. *Cement and Concrete Research, 34*, 391−397.

Chen, B., & Liu, J. (2007). Investigation of effects of aggregate size on the fracture behavior of high performance concrete by acoustic emission. *Construction and Building Materials, 21*, 1696−1701.

Colombo, S., Forde, M. C., Main, I. G., Halliday, J., & Shigeishi, M. (2005). AE energy analysis on concrete bridge beams. *RILEM Materials and Structures, 38*, 851−856.

Colombo, S., Forde, M. C., Main, I. G., & Shigeishi, M. (2005). Predicting the ultimate bending capacity of concrete beams from the "relaxation ratio" analysis of AE signals. *Construction and Building Materials, 19*, 746−754.

Colombo, S., Main, I. G., & Forde, M. C. (2003). Assessing damage of reinforced concrete beam using *b*-value analysis of acoustic emission signals. *Journal of Materials in Civil Engineering, 5*(6), 280−286.

Duan, K., Hu, X. Z., & Wittmann, F. H. (2001). Boundary effect on concrete fracture induced by non-constant fracture energy distribution, in fracture mechanics of concrete structures. In R. De Borst, J. Mazars, G. Pijaudier-Cabot, & J. G. M. Van Mier (Eds.), *Proceedings FRAMCOS-4* (pp. 49−55). Rotterdam: A.A. Balkema Publishers.

Farhidzadeh, A., Salamone, S., & Singla, P. (2013). A probabilistic approach for damage identification and crack mode classification in reinforced concrete structures. *Journal of Intelligent Material Systems and Structures*. http://dx.doi.org/10.1016/10.1177/1045389X13484101.

Grosse, C. U., & Ohtsu, M. (2008). *Acoustic emission testing*. Berlin Heidelberg: Springer-Verlag.

Grosse, C. U., Reinhardt, W. H., & Finck, F. (May/June 2003). Signal based acoustic emission techniques in civil engineering. *Journal of Materials in Civil Engineering*, 274−279.

Hadjab, H. S., Thimus, J.-F., & Chabaat, M. (2007). The use of acoustic emission to investigate fracture process zone in notched concrete beams. *Current Science, 93*(5), 648−653.

Harris, D. O., & Bell, R. (1977). The measurement and significance of energy in acoustic emission testing. *Experimental Mechanics, 17*, 347−353.

Hillerborg, A., Modeer, M., & Peterson, P. E. (1976). Analysis of crack formation and crack growth in concrete by means of fracture mechanics and finite elements. *Cement and Concrete Research, 6*, 773−782.

Izumi, M., Mihashi, H., & Nomura, N. (1986). In F. H. Wittmann (Ed.), *Acoustic emission technique to evaluate fracture mechanics parameters of concrete, fracture toughness and fracture energy of concrete* (pp. 259−268). Amsterdam: Elsevier Science Publishers.

Karihaloo, B. L. (1995). *Fracture mechanics and structural concrete*. London: Longman Scientific & Technical.

Landis, E. N., & Baillon, L. (2002). Experiments to relate acoustic emission energy to fracture energy of concrete. *Journal of Engineering Mechanics, 128*, 698−702.

Lilliu, G. (2003). *3D analysis of fracture process in concrete* (Ph D. thesis). Micro lab: TU Delft.

Loland, K. E. (1989). Continuous damage model for load-response estimation of concrete. *Cement and Concrete Research, 10*, 395−402.

Lysak, M. V. (1996). Development of the theory of acoustic emission by propagating cracks in terms of fracture mechanics. *Engineering Fracture Mechanics, 55*, 443−452.

Maji, A. K., Ouyang, C., & Shah, S. P. (1990). Fracture mechanism of quasi-brittle materials based on acoustic emission. *Journal of Materials Research, 5*, 206−217.

Maji, A. K., & Shah, S. P. (1988). Process zone and acoustic emission measurement in concrete. *Experimental Mechanics, 3*, 27−33.

Man, H. K., & van Mier. (2008). Size effect on strength and fracture energy for numerical concrete with realistic aggregate shapes. *International Journal of Fracture, 154*, 61−72.

van Mier, J. G. M. (1997). *Fracture process of concrete, assessment of material parameters for fracture models*. Boca Rotan, FL: CRC Press.

van Mier, J. G. M. (2013). *Concrete fracture—a multi scale approach*. Boca Rotan, FL: CRC Press.

Mihashi, H., Nomura, N., & Niseki, S. (1991). Influence of aggregate size on fracture process zone of concrete detected with three dimensional acoustic emission techniques. *Cement and Concrete Research, 21*, 737−744.

Miller, R. K., Moore, P. O., & Hill, E.v. K. (2005). *Acoustic emission testing, non-destructive testing handbook* (Vol. 6). Columbus, OH: American Society for Non-Destructive Testing.

Mindess, S. (1990). Acoustic emission. In V. M. Malhotra, & N. Carino (Eds.), *Handbook on nondestructive testing of concrete*. Boca Raton, FL: CRC Press.

Muralidhara, S., Raghu Prasad, B. K., Karihaloo, B. L., & Singh, R. K. (2011). Size-independent fracture energy in plain concrete beams using tri-linear model. *Construction and Building Materials, 25*(7), 3051−3058.

Nor, M. N., Ibrahim, A., Bunnori, M. N., & Saman, M. H. (2013). Acoustic emission signal for fatigue crack classification on reinforced concrete beam. *Construction and Building Materials, 49*, 583−590.

Ohno, K., & Ohtsu, M. (2010). Crack classification in concrete based on acoustic emission. *Construction and Building Materials, 24*(12), 2339−2346.

Ohtsu, M. (1987a). Acoustic emission characteristics in concrete and diagnostic applications. *Journal of Acoustic Emission, 6*(2), 99−108.

Ohtsu, M. (1987b). Mathematical theory of acoustic emission and moment tensor solution. *Journal of the Society of Materials Science, 36*(408), 1025−1031.

Ohtsu, M. (1988). Diagnostics of cracks in concrete based on acoustic emission. *Nondestructive Testing, ACI, SP-112*, 63−82.

Ohtsu, M. (1992). Rate process analysis of acoustic emission activity in core test of concrete. *Concrete Library JSCE, 20*, 143−153.

Ohtsu, M. (1996). The history and development of acoustic emission in concrete engineering. *Magazine of Concrete Research, 48*(147), 321−330.

Ohtsu, M. (2010). RILEM recommendation: test method for damage qualification of reinforced concrete beams by AE. *Materials and Structures, 43*, 1183−1186.

Ohtsu, M., & Ono, K. (1984). A generalized theory of acoustic emission and Green's functions in a half space. *Journal of Acoustic Emission, 3*(1), 124−133.

Ohtsu, M., Shigeishi, M., Yuyama, S., & Okamoto, T. (1991). SiGMA procedure for AE moment tensor analysis. *JNDI, 42*(10), 570−575.

Ohtsu, M., Uchida, M., Okamoto, T., & Yuyama, S. (2002). Damage assessment of reinforced concrete beams qualified by AE. *ACI Structural Journal, 99*(4), 411−417.

Ohtsu, M., & Watanabe, H. (2001). Quantitative damage estimation of concrete by AE. *Construction and Building Materials, 15*(5−6), 217−224.

Otsuka, K., & Date, H. (2000). Fracture process zone in concrete tension specimen. *Engineering Fracture Mechanics, 65*, 111−131.

Raghu Prasad, B. K., & Vidya Sagar, R. (2008). Relationship between AE energy and fracture energy of plain concrete beams-experimental study. *Journal of Materials in Civil Engineering, 20*(3), 212−220.

Ramachandra Murthy, A., Karihaloo, B. L., Iyer, N. R., & Raghu Prasad, B. K. (2013). Determination of size-independent specific fracture energy of concrete mixes by two methods. *Cement and Concrete Research, 50*, 19−25.

Rao, M. V. M. S., & Prasanna Lakshmi, K. J. (2005). Analysis of *b*-value and improved *b*-value of acoustic emissions accompanying rock fracture. *Current Science, 89*, 1577−1582.

RILEM Committee 50-FMC. (1985). Determination of the fracture energy of mortar and concrete by means of three-point bend tests on notched beams. *Materials and Structures, 18*, 285−290.

Rossi, P., Robert, J. L., Gervais, J. P., & Bruhat, D. (1990). The use of acoustic emission in fracture mechanics applied to concrete. *Engineering Fracture Mechanics, 35*, 751−763.

Schlangen, E. (1993). *Experimental and numerical analysis of fracture process in concrete* (Ph.D. thesis). The Netherlands: Delft University of Technology.

Schlangen, E., & Garboczi, J. (1996). New method for simulating fracture using an elastically uniform random geometry lattice. *International Journal of Engineering Science, 34*(10), 1131−1144.

Schlangen, E., & Garboczi, E. J. (1997). Fracture simulations of concrete using lattice models: computational aspects. *Engineering Fracture Mechanics, 57*(2/3), 319−332.

Shahidan, S., Pulin, R., Bunnori, M. N., & Holford, K. M. (2013). Damage classification in reinforced concrete beam by acoustic emission signal analysis. *Construction and Building Materials, 45*, 78−86.

Shah, S. P., Swartz, S. E., & Ouyang, C. (1995). *Fracture mechanics of concrete — applications of fracture mechanics to concrete, rock and other quasibrittle materials*. Chichestor: John Wiley & Sons.

Shiotani, T., Fujii, K., Aoki, T., & Amou, K. (1994). Evaluation of progressive failure using AE sources and improved *b*-value on slope model tests. *Progress in Acoustic Emission VII, 7*, 529−534.

Shiotani, T., Yuyama, S., Li, Z. W., & Ohtsu, M. (2000). In T. Uohoto (Ed.), *Quantitative evaluation of fracture process in concrete by the use of improved b-value. 5th Int. Symposium on non-destructive testing in civil engineering* (pp. 293−302). Amsterdam: Elsevier Science.

Shiotani, T., Yuyama, S., Li, Z. W., & Ohtsu, M. (2001). Application of the AE improved *b*-value to qualitative evaluation of fracture process in concrete materials. *Journal of Acoustic Emission, 19*, 118−132.

Vidya Sagar, R. (2010). *Fracture mechanics of concrete—experimental and numerical studies*. Dudweiler Landstr. 99, 66123 Saarbruecken, Germany: VDM-VerlagDr Muller Aktiengesellschaft & Co.KG, ISBN 978-3-639-23724-5.

Vidya Sagar, R., & Rao, M. V. M. S. (2014). An experimental study on loading rate effect on acoustic emission based *b*-values related to reinforced concrete fracture. *Construction and Building Materials, 70*, 460−472. http://dx.doi.org/10.1016/j.conbuildmat.2014.07.076.

Vidya Sagar, R., & Raghu Prasad, B. K. (2009a). AE energy release during the fracture of HSC beams. *Magazine of Concrete Research, 61*(6), 419−435.

Vidya Sagar, R., & Raghu Prasad, B. K. (2009b). An experimental study on fracture process zone in HSC three point bend beam specimen using acoustic emission method. *Journal of Structural Engineering (SERC, Chennai, India), 36*(1), 59−69.

Vidya Sagar, R., & Raghu Prasad, B. K. (2012). A review of recent development in parametric based acoustic emission techniques applied to concrete structures. *Nondestructive Testing and Evaluation, 1*, 47−68.

Vidya Sagar, R., Raghu Prasad, B. K., & Karihaloo, B. L. (2010). Verification of the applicability of lattice model to concrete fracture by AE study. *International Journal of Fracture, 161*(2), 121−129.

Vidya Sagar, R., Raghu Prasad, B. K., & Shantha Kumar, S. (2012a). An experimental study on cracking evolution in concrete and cement mortar by the *b*-value analysis of acoustic emission technique. *Cement and Concrete Research, 42*(8), 1094−1104.

Vidya Sagar, R., Raghu Prasad, B. K., & Shantha Kumar, S. (December 2012b). Comparison of *b*-values with strains in steel and concrete of RC beam for damage evaluation. *Proceedings in Bridge Engineering, 125*(BE4), 233−244. http://dx.doi.org/10.1016/tbe800038. Revised.pdf (12).

Vidya Sagar, R., Raghu Prasad, B. K., Rashmi V. Prasad, & Rao, M. V. M. S. (2013). Micro-cracking and fracture behavior of cement concrete and mortar: a comparative study using AE technique. *Experimental mechanics, 53*(7), 1161−1175.

Vidya Sagar, R., Raghu Prasad, B. K., & Singh, R. K. (2015). Kaiser effect observation in reinforced concrete structures and its use for damage assessment. *Archives of Civil and Mechanical Engineering, 15*(2), 548−557. http://dx.doi.org/10.1016/j.acme.2014.05.004. Elsevier.

Yoon, D. J., Weiss, W., & Shah, S. P. (2000). Assessing damage in corroded reinforced concrete using acoustic emission. *Journal of Engineering Mechanics, 26*(3), 273−283.

Yuyama, S., Okamoto, T., Shigeishi, M., & Ohtsu, M. (1993). Some application of moment tensor analysis for concrete specimen. *Proceedings of the 9th National Conference on AE JSNDI*, 121−129.

Monitoring of crack propagation in reinforced concrete beams using embedded piezoelectric transducers

8

C. Dumoulin, G. Karaiskos, A. Deraemaeker
Université Libre de Bruxelles (ULB), Brussels, Belgium

8.1 Introduction

In the field of automated structural health monitoring (SHM), the trend is to use very large sensor networks relying on dynamic signatures of structures that are either generated by the ambiance or by the monitoring system itself (Deraemaeker & Worden, 2010). Ambient excitation is suitable for the low frequency range corresponding to the first vibration modes of the structure that are not very sensitive to local damage. Local information can be carried by higher frequency waves that must be generated by the monitoring system itself. Indeed, shorter wavelengths imply stronger interactions with the local defects and make possible their detection. Piezoelectric (lead zirconate titanate) transducers (PZT) can be used as both actuators and sensors in a wide frequency band. Their small size and low cost make them ideal candidates for active sensing. The ultrasonic pulse velocity method (UPV) is currently one of the most widely used techniques for nondestructive testing (NDT) of concrete. It is an established technique described in different national norms, among which is the European norm (EN 12,504-4), and is used in many commercial systems. The technique is based on a pitch-catch configuration using external transducers. It consists of exciting the emitter by a short pulse signal and measuring the time of flight of the wave from the emitter to the receiver.

The use of large external probes requires skilled manpower that not only prevents using this technique for online monitoring, but it also strongly limits the measurement areas when the structure is in service. The application of this technique is additionally restricted by the need for flat surfaces and coupling agents, which strongly reduce the efficiency of the transducers. When in service, the accessible surfaces of the structure only allow ultrasonic measurements that are either through the thickness or semidirect or indirect, which makes the interpretation uncertain and difficult (Figure 8.1(a)).

Since 2000, some researchers have studied the possibility of replacing the large external probes with small and low-cost piezoelectric transducers embedded in the structure (Figure 8.1(a)). This enables them to overcome many drawbacks of external transducers that have been mentioned above. No coupling agent is needed because the

Acoustic Emission (AE) and Related Non-destructive Evaluation (NDE) Techniques in the Fracture Mechanics of Concrete
http://dx.doi.org/10.1016/B978-1-78242-327-0.00008-8
Copyright © 2015 Elsevier Ltd. All rights reserved.

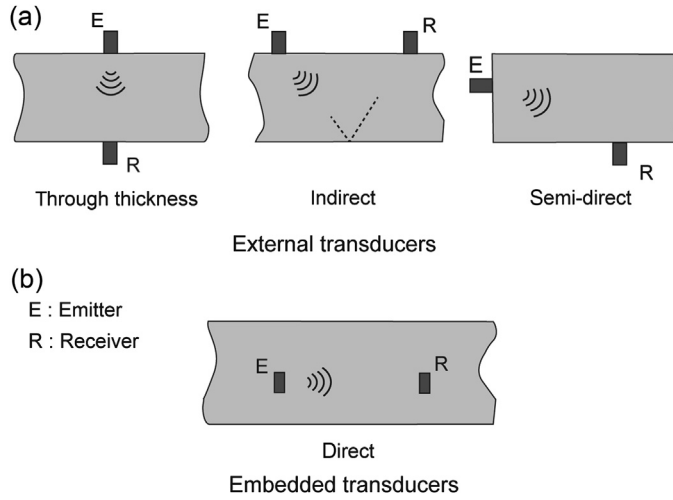

Figure 8.1 Wave propagation in ultrasonic pulse velocity method. (a) Using external transducers: the method is limited to through thickness or indirect wave propagation. (b) Using embedded transducers: the method enables one to overcome most of the drawbacks of external probes.

transducer has a direct contact with the structure, which improves its efficiency. The configuration of the transmitter–receiver paths is also much more flexible. The use of such transducers also adds flexibility in the choice of their position and enhances their integration in the overall design of the structure.

These transducers are known as smart aggregates (SMAGs) because their size is of the same order of magnitude as the average size of aggregates in concrete (around 1 cm) (Gu, Song, Dhonde, Mo, & Yan, 2006). The first section of this chapter is dedicated to a brief review of different types of SMAGs and their applications, and it details the design and the manufacturing process of the SMAGs used in the present study.

The second part of this chapter deals with the development of a specific indicator for damage monitoring in concrete. The third section illustrates the application of this indicator in the case of a three-point bending test performed on a reinforced concrete (RC) beam in which a pair of SMAGs has been cast.

8.2 Embedded transducers for ultrasonic testing of concrete

Embedded piezoelectric transducers are made of PZT, which is a piezoceramic material polarized so it is able to generate a certain voltage when a strain is applied on the material, and conversely, in a large frequency range. These phenomena are respectively called direct piezoelectric effect and inverse piezoelectric effect. This kind of material is perfectly suited for generating or measuring mechanical waves. Two

main approaches of design of embedded piezoelectric transducers can be reported. Both approaches comply with the need for maximising the transmitted energy from the transducer to the tested specimen, which is known as acoustic impedance matching. The first type of transducer is made of a thin PZT patch surrounded by several coating layers. These transducers were first produced by researchers at the University of Houston and are mostly designed for compression waves (P-waves) (Song, Gu, & Mo, 2007). They have been used to monitor the mechanical properties of concrete at an early age (Dumoulin, Karaiskos, Carette, Staquet, & Deraemaeker, 2012) and to detect damage in concrete structures (Dumoulin, Karaiskos, & Deraemaeker, 2013; Song, Gu, & Mo, 2008). The application of such type of transducers has also been recently explored for monitoring water seepage in marine constructions (Liu, Huang, Zou, Teng, & Li, 2013). Other embedded transducers have also been designed to simultaneously generate P-waves and S-waves (Li, Qin, & Huang, 2009). The second type of piezoelectric transducers is made of cement-based piezoelectric ceramic composite material. The piezoelectric material is, therefore, fixed in a matrix of cement. This enable the production of transducers that better match the acoustic impedance of concrete and, consequently are more effective, but they are also much more difficult to manufacture. The composite can be achieved either by means of particles of piezoelectric material scattered in the cement matrix (0-3 composite), multiple PZT plates (2-2 composite) or PZT rods (1-3 composite) (Cheng, Xu, Lu, Huang, & Jiang, 2010; Dong & Li, 2005). Figure 8.2 illustrates these different types of composite transducers. Such a type of transducers has been used for assessing hydration properties of concrete (Qin & Li, 2008), acoustic emission detection (Qin, Peng, Ren, & Li, 2009) and damage monitoring (Lu, Li, & Liao, 2010).

The transducers used in the present study are of the first category of embedded transducers (multiple coating layers). They have been designed in the civil engineering laboratory at ULB-BATir. A thin PZT patch of 0.2 mm is surrounded by several coating layers. The coating materials are imposed by multi-physics constraints. These are both mechanical criteria (mechanical strength or impedance matching) and electric criteria, which are the electrical coupling between transducers (mainly in presence of water at an early age) and a proper shielding against the electromagnetic interferences. Many efforts in the manufacturing process have allowed for significantly enhancing

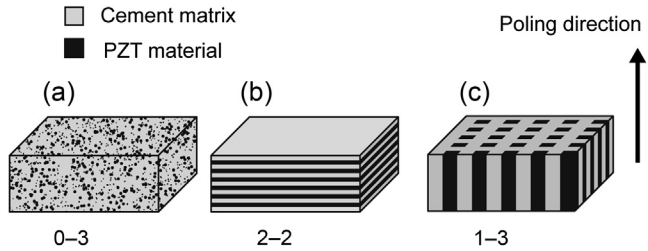

Figure 8.2 Illustration of different types of cement-based composite piezoelectric transducers. (a) Scattered piezoelectric material in the cement matrix (0-3 composite). (b) PZT plates (2-2 composite). (c) PZT RODS (1-3 composite).

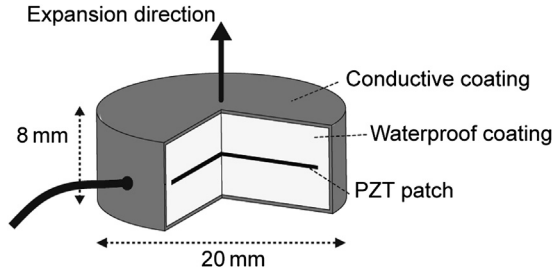

Figure 8.3 Smart aggregate transducer, details of different layers.

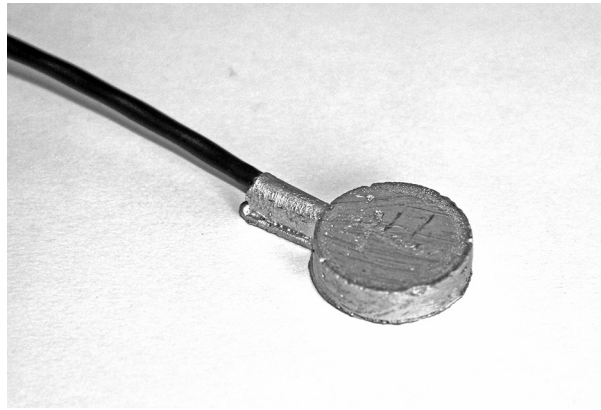

Figure 8.4 Smart aggregate transducer manufactured at ULB-BATir.

these parameters since the first produced SMAGs (Dumoulin et al. 2012). Figure 8.3 shows the different material layers used during the manufacturing of the SMAGs used in this study. The dimensions of the PZT patches are 12 × 12 mm in width, and the dimension of the SMAG with the coating layers is about 2 cm in diameter and 0.8 cm in thickness (Figure 8.4).

8.3 Extraction of a damage indicator from ultrasonic waves

When a wave is propagating in heterogeneous media such as concrete, it is strongly scattered and absorbed by the medium. This strongly depends on the frequency of the transmitted wave (Planès & Larose, 2013). At low frequencies (up to 20 kHz), the magnitude of the corresponding wavelengths is greater than the macroscopic size of the structure. The waves only excite the first vibration modes of the structure and are consequently weakly affected by local damage. The frequency range between 20 and 150 kHz is often called the single scattering regime because the

waves are only affected by the bigger aggregates or defaults in the concrete structure. In this regime, the ballistic wave (direct wave) still reaches first the receiver and can be easily distinguished from the scattered wave that arrives later. Above 150 kHz the wave interacts with numerous heterogeneities before reaching the receiver. This defines the multiple scattering regime where the ballistic wave progressively disappears in favor of the multiple scattered waves (Tourin, Fink, & Derode, 2000). Above 1 MHz, the wave suffers both from multiple wave scattering and absorption.

In many commercial systems, the state of the concrete is estimated from the time of flight of ultrasonic waves from the emitter to the receiver. Researchers have also demonstrated that the wave amplitude is slightly more sensitive to damage than the propagation velocity (Selleck, Landis, Peterson, Shah, & Achenbach, 1998; Shokouhi, Zoëga, Wiggenhauser, & Fischer, 2012). In multiple scattering regimes, the ultrasonic wave follows random paths. This behavior can be compared to the Brownian motion of a particle (Tourin et al., 2000). With this assumption, one can use the diffusion equation that, therefore, describes the average intensity of the wave in space and time. Some authors have investigated the influence of damage on the diffusion coefficient and dissipation rate that describe the equation of diffusion (Deroo, Kim, Qu, Sabra, & Jacobs, 2010). A multiple scattered wave can also be seen as the superposition of the initial wave packet with random amplitudes and delays. Consequently, the effect of a global velocity change in the medium, which can be due to damage, is to stretch the original signal. This enables one to detect very weak changes in the time of reception. This method is known as coda-wave interferometry (CWI) (Planès & Larose, 2013). It has been used to estimate the acoustoelastic parameters of concrete (Larose & Hall, 2009) and their evolution with damage (Schurr, Kim, Sabra, & Jacobs, 2011; Shokouhi, Zoëga, & Wiggenhauser, 2010).

Experiments have shown that the appearance of damage mainly impacts two parameters of the transmitted wave: the time of flight of the wave and its amplitude. This confirms observations reported in previous studies (Popovics & Popovics, 1989; Suaris & Fernando, 1987). Nevertheless, the evaluation of these two parameters can lead to scattered results, which are consequently unsuitable. Indeed, as the amplitude of the received signal decreases, the signal to noise ratio (SNR) can be too weak to properly estimate these values. In this study, it is suggested to define a damage indicator by assessing the evolution of the first half period of the early wave (Figure 8.5). Indeed, the first part of the received signal must match the shortest wave paths from the emitter. Then, the first half period is mainly affected by the mechanical properties of the concrete in the area between the emitter and the receiver (Dumoulin et al. 2013; Karaiskos, Flawinne, Sener, & Deraemaeker, 2013).

All measured signals are compared to a reference measurement, which corresponds to the average of a high number of recordings carried out before any load has been applied on the structure. This reference signal is called the healthy signal. By contrast, other measurements are called the damaged signals. The damage index is defined as the root mean square deviation (RMSD) value between the healthy signal and a damaged signal computed in the time window corresponding to the first half period

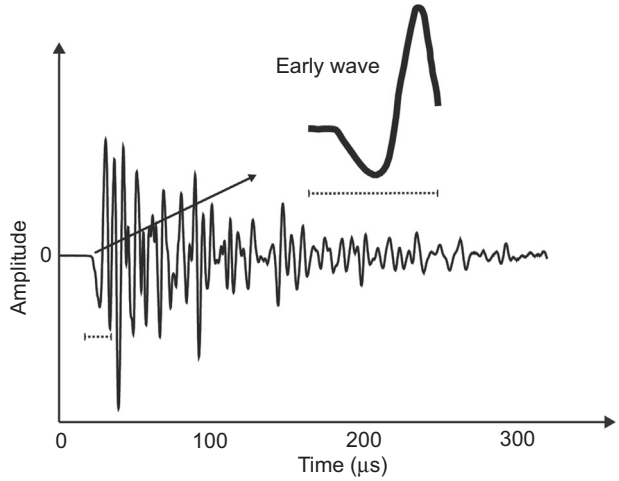

Figure 8.5 Illustration of the early wave of a typical recorded signal on the receiver. The emitter is excited by a short pulse signal.

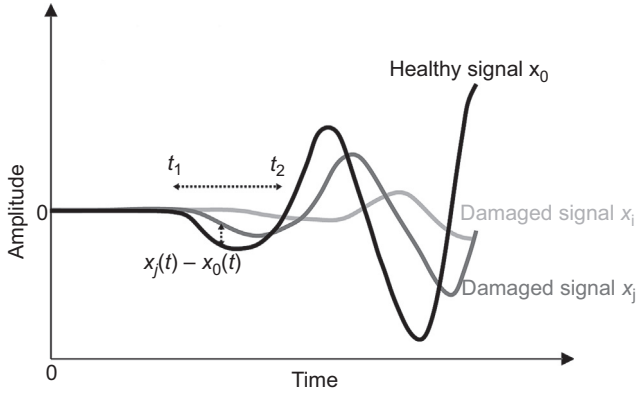

Figure 8.6 Definition of the time window, t_1 is the time of reception of the healthy signal, $t_2 - t_1$ corresponds to the duration of the first half period of the healthy signal.

of the healthy signal (Figure 8.6). The definition of the damage index is given in Eqn (8.1).

$$I_j = \sqrt{\frac{\int_{t_1}^{t_2} \left(x_j(t) - x_0(t)\right)^2 \mathrm{d}t}{\int_{t_1}^{t_2} x_0^2(t) \mathrm{d}t}} \tag{8.1}$$

where $x_j(t)$ and $x_0(t)$ are respectively the damaged signal j and the original undamaged signal; t_1 and t_2 correspond to the limits of the first half period of the healthy signal.

It can be seen that this definition of the damage index enables one to take into account the decrease of both the velocity and the amplitude without explicitly evaluating their values. This indicator is equal to one and saturates when the amplitude of the damage signal is either too weak or arrives later than the first half period of the healthy signal. Because it saturates quickly, the damage index is suited to detect a weak damage appearance but is not designed to monitor the evolution of higher damage, as will be shown in Section 8.4.

8.4 Application to crack monitoring in a reinforced concrete beam

8.4.1 Description of the test setup

The current section is aimed at illustrating the use of the damage index for a real size experiment. For this purpose, a three-point bending test on a reinforced concrete beam seems appropriate since the appearance of damage in such a test is easy to control and has the great advantage of being well localised. Theoretically, the main crack must first appear exactly on the center of the beam. In practice, the heterogeneity of concrete implies that the crack is rarely initiated exactly at the center. That is an undesirable effect for this test. A good practice consists in making a notch which locally reduces the strength of the beam and leads to a stress concentration ensuring the crack initiation at the right location. The main characteristics of the beam are given in Table 8.1, where the concrete properties have been characterized by specific mechanical tests on specimens poured at the same time as the beam and disposed in similar environmental conditions.

The experimental setup is summarised in Figure 8.7. The emitter is excited by a high-voltage pulse and generates a wave that propagates through the structure. The receiver measures the strains and generates an electrical signal, which is first amplified by an analog preamplifier and then recorded by the DAQ system. This system is based on the FreshCon system, which is a commercial system designed at the University of Stuttgart for assessing both the P-wave and S-wave velocity of concrete at a very early age. In this study, the specific molds and transducers of the system have been replaced by the smart aggregates, and the postprocessing is implemented in MATLAB. The duration of each excitation pulse is 10 μs at a voltage of 800 V, and the transmitted signal is recorded at a sampling rate of 10 MHz. It has been observed that this pulse

Table 8.1 RC beam properties and mechanical properties of concrete

Length × width × height	1470 × 140 × 190 mm
Bottom/top reinforcement bars	2 × 12 mm diameter/2 × 6 mm diameter
Compressive strength/tensile strength	57.1/2.86 MPa
Young's modulus	33 GPa

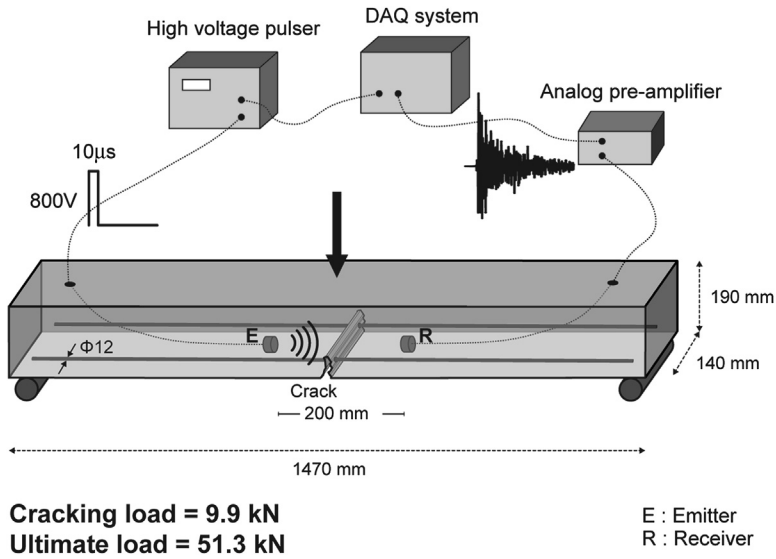

Figure 8.7 Illustration of the experimental setup. The test consists of a three-point bending test. Excitation signal is a high-voltage short pulse sent to the emitter (E), and the transmitted wave is caught by the receiver (R).

width is optimal for the current application. During the loading, the ultrasonic measurement rate has been set at one measurement every 10 s, which corresponds to the maximum rate for the system that is strongly restricted by the rise time of the high-voltage pulser. With the load increase, cracks or micro-cracks modify the internal structure of the specimen and, therefore, the wave paths and, consequently, the received signals. A high-quality camera focused on the area of the notch where the crack is assumed to first appear has been placed in front of the beam. The frame rate of the camera has been synchronised with the ultrasonic measurement rate so that each measured signal at each damage state corresponds to one picture. It is then possible to match the ultrasonic response signal with a visual detection of cracks.

8.4.2 Loading and monitoring procedure

The three-point bending test was performed on a 200 kN hydraulic jack bending testing machine (see Figure 8.8) in two different phases. The first loading phase was aimed at initiating the crack at the center of the beam by successive small loading steps (±1 kN) with a slow rate (±1 kN/min). This phase is summarized on Figure 8.9(a). This loading procedure has allowed detection of the exact moment of the crack initiation. The beam was unloaded slightly after the crack was observed. Figure 8.9(b) illustrates the loading procedure of the second phase. The beam was loaded close to the maximum acceptable load. The successive loading steps are greater and faster than in the first phase. During this phase, LVDT extensometers were used to estimate the crack width. Indeed, the use of such a sensor requires knowing the exact location of the cracks, which was, of course, not possible during the first phase.

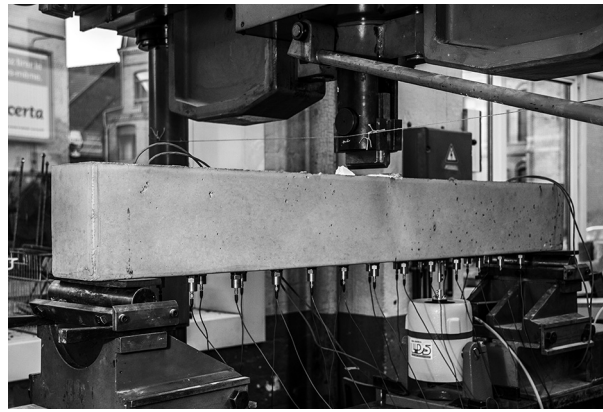

Figure 8.8 Experimental setup. The three-point bending test has been performed on a 200 kN hydraulic jack bending testing machine.

8.4.3 Visual inspection

The main idea of taking high-quality pictures at regular intervals (10 s) is to detect and follow the initiation and the propagation of cracks by analysing these pictures and, afterward, to join these pictures to ultrasonic measurements. Several numerical filters were applied on the pictures in order to detect very thin cracks (Figure 8.10b). Since the processing tools tend to increase the width of the crack, the processed pictures cannot be used for evaluating crack width. Nevertheless, this can be made by digital image correlation (DIC) techniques, which are certainly a better tool to follow the crack initiation (Mauroux, Benboudjema, Turcry, Aït-Mokhtar, & Deves, 2012). Such a technique could be used in this study but was not available at the time of the test.

The results of the visual inspection are exposed hereafter. Before 10 kN, no crack appeared around the notch. At 10 kN, the first micro-cracks appear, and the crack is totally formed under a load of 14 kN, and the crack width is around 0.1 mm (see Figure 8.10b). Thin cracks have also appeared outside of the area of interest but are not detected by the monitoring system, as the damage index is only impacted by modifications in the structure or the microstructure in the area between the SMAGs.

8.4.4 Results of the damage indicator

Figure 8.10 shows the evolution of the damage index and three related pictures corresponding to different states of the crack opening process. The evolution of the index can be divided into three different phases. In the first phase, the indicator is practically steady and equal to the baseline value. This baseline value of the damage index is due to small differences and the noise that necessarily differentiates each signal from the reference average signal, even if this signal is not impacted by damage. The loading range between 5 and 15 kN defines the second phase. This corresponds to the interval

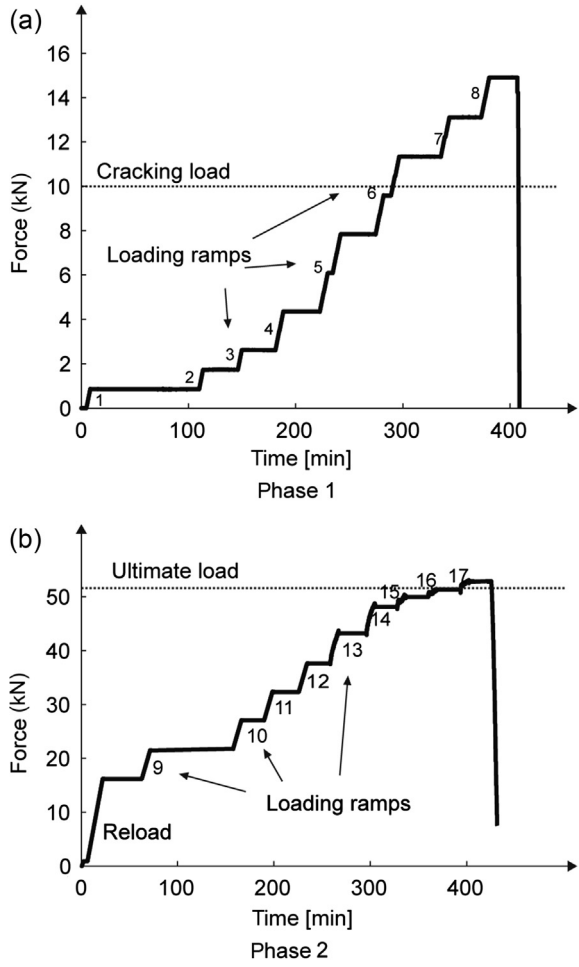

Figure 8.9 Loading procedure in two phases. (a) Phase 1: the beam is loaded up to the crack initiation (15 kN). (b) The beam is loaded up to the failure (±50 kN).

in which the damage index increases continuously from the baseline value to a value of one, which is the upper possible limit of the damage index. This phase also perfectly matches the evolution of the crack appearance as it has been visually observed. Indeed, at 5 kN, no crack has been observed (Figure 8.10a), and at 14 kN, the crack is totally opened. In the third phase, the indicator saturates and does not evolve anymore, although the crack width is still growing (Figure 8.10c). There is, therefore, a very good correlation between the observations and the evolution of the damage index defined in this study. The damage index appears to be an excellent indicator for detecting crack appearance but is not suited for following the evolution of the crack or estimating the size of the damage.

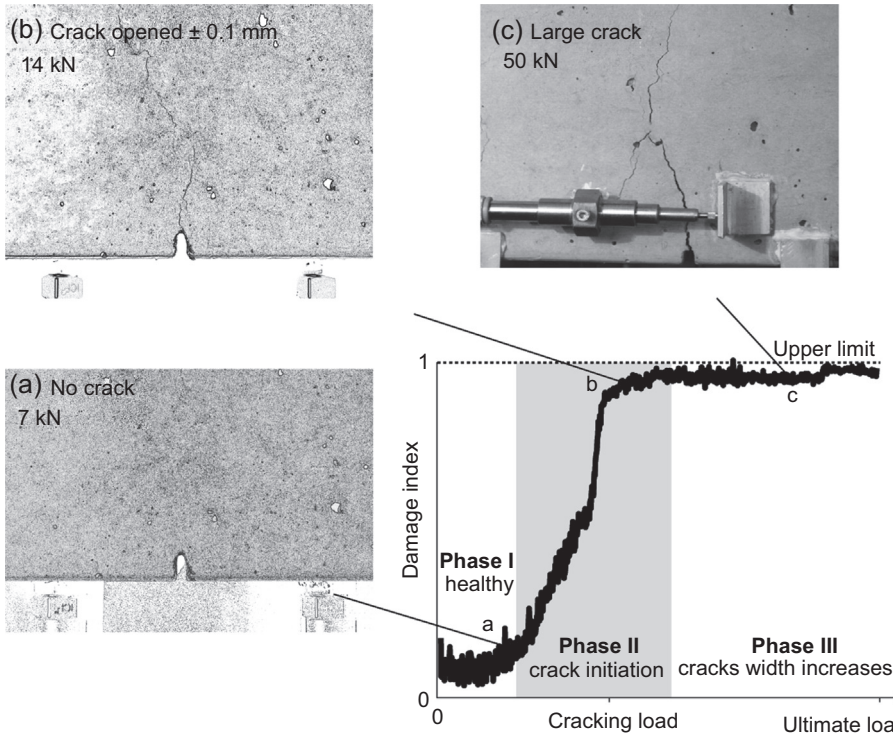

Figure 8.10 The evolution of the damage index is strongly correlated with the visual observations. (a) Numerically processed picture: no crack observed in the area between the transducers. The damage indicator starts to grow. (b) Numerically processed picture: the crack in the center of the beam is fully initiated. The damage indicator reaches the upper limit. (c) The crack becomes very large, and the damage indicator is steady.

8.5 Conclusion

An efficient damage indicator has been developed in this study. It has allowed detecting the appearance of cracks in a reinforced concrete beam using embedded piezoelectric transducers. The method is based on the principle of ultrasonic pulse velocity testing, without explicitly computing the time of flight of the ultrasonic wave. Indeed, in the framework of damage monitoring, it has been observed that the assessment of the time of propagation can lead to scattered results with a wide margin of error, which makes them unusable or at least very difficult to interpret. The damage indicator suggested in the current study also takes into account the decrease of the amplitude of the early received wave. The application of this indicator on a reinforced concrete beam has demonstrated that this indicator is very sensitive to small changes in the structure. It has allowed detecting the start of the cracking process before the cracks have been visually observed.

The damage indicator has not been designed for monitoring the evolution of the damage or for giving quantitative information related to the magnitude of the damage.

It also does not provide information about the location of modifications in the structure. More complex signal processing strategies will, therefore, be studied in further researches in order to address these important challenges.

The use of embedded transducers brings in the structure heterogeneities, which are of the same order of magnitude as the largest aggregates of the concrete. This leads to an important issue concerning the potential influence of these transducers on the strength of the structure. Nevertheless, it has appeared that they do not seem to affect the mechanical behavior of the structure.

The appearance of cracks or micro-cracks in concrete can be a very fast phenomenon. The current monitoring device only allows a measurement rate of one measurement every 10 s. This requires that the loading procedure must be very slow to give the opportunity to follow each step of deterioration of concrete during the test. It has been observed that the wave generated by a short pulse excitation signal is totally attenuated after 5 ms. This implies that the number of measurements can reach a much higher measurement rate.

8.6 Future trends

One of the main limits of the current method is the use of high-voltage pulser, limiting both the measurement rate due to the important rising time of the device and making the method difficult to set up in large structures because of the high cost of such instruments. The current trend is to use a large sensor network in order to monitor in real time different parts of the structure. It is obvious that the different parts of a structure do not need to be interrogated simultaneously. A cost-effective solution is to use switching devices that enable successive interrogation of the different pairs of transducers embedded in the structure using a reduced number of data acquisition boards. The current technology of high scan rate switches requires low-voltage applications. All this leads us to the conclusion that it is necessary to develop alternative systems based on low-voltage excitation signals and fast data acquisition.

For this purpose, many efforts must be made in the design of the transducers in order to improve their efficiency. This can only be achieved through a multi-physics approach. Indeed, both the mechanical constraints, such as the acoustic impedance matching, and the electromagnetic aspects must be taken into consideration. This requires a high level of technical expertise both in the analysis and manufacturing processes. Further developments in embedded piezoelectric transducers should include transducers that operate with S-Waves in addition to those working with P-Waves.

Further studies should also focus on the development of more complex signal processing strategies. A very promising method to locate the appearance of cracks using piezoelectric transducers is time reversal nonlinear elastic wave spectroscopy (Le Bas, Ulrich, Anderson, Guyer, & Johnson, 2011).

An accurate method for long-term structural health monitoring should be able to differentiate modifications in the measurement from environmental effects such as temperature or load variation from those due to damage. This implies the development of a multivariate damage vector in order to filter out environmental variations using statistical correlations (Deraemaeker & Worden, 2014; Kullaa, 2008).

Computed tomography (CT) is widely used in many research fields. It consists of X-ray scans in order to obtain a complete 3-D model of a specimen. This technology can be very beneficial in the scope of SHM using piezoelectric transducers. A likely future application is to compare ultrasonic measurements with the real geometry of the structure. This can help to better understand the wave propagation in heterogeneous media such as concrete and, therefore, to develop more powerful monitoring methods. The 3-D models can also be used as the geometry for numerical simulations. This can lead to a significant improvement in current models of wave propagation in complex media and fracture mechanics of concrete.

8.7 Sources of further information and advice

Clear explanations of the most widely used nondestructive testing methods for concrete assessment are provided in Malhotra and Carino (2003). The book deals with pulse velocity techniques but also with the surface hardness test method, penetration resistance, pullout, or magnetic and electrical methods. More comments and advice on *in situ* nondestructive testing can be found in Bungey, Millard, and Grantham (2006).

Many sources are focused on ultrasonic wave propagation and design of ultrasonic transducers. Information concerning the fundamentals of piezoelectricity, piezoelectric materials for ultrasonic transducers, and design and fabrication methods of piezoelectric transducers can be found in both Safari (2008) and Vives (2008). The latter book describes models for different types of piezoelectric transducers such as resonant sensors or broadband sensors. That book is specifically dedicated to present applications of piezoelectric transducers in various fields such as nondestructive testing or medical imaging.

Fracture mechanics of concrete is one of the key elements to set up new experiments and to deeply analyze and interpret results. A very interesting book regarding this important topic is *Fracture processes of concrete: assessment of material parameters for fracture models* (Van Mier, 1997).

References

Bungey, J., Millard, S., & Grantham, M. (2006). In J. Bungey, S. Millard, & M. Grantham (Eds.), *Testing of concrete in structures* (4th ed.). CRC Press [Hardcover].

Cheng, X., Xu, D., Lu, L., Huang, S., & Jiang, M. (May 2010). Performance investigation of 1-3 piezoelectric ceramic−cement composite. *Materials Chemistry and Physics, 121*(1−2), 63−69. http://dx.doi.org/10.1016/j.matchemphys.2009.12.045.

Deraemaeker, A., & Worden, K. (2010). CISM Lecture Notes. *New trends in vibration based structural health monitoring* (vol. 520). Springer.

Deraemaeker, A., & Worden, K. (2014). On the use of the mahalanobis squared-distance to filter out environmental effects in structural health monitoring. In *The second international conference on structural nonlinear dynamics and diagnosis (CSNDD'2014), 4. Agadir, Morocco.*

Deroo, F., Kim, J.-Y., Qu, J., Sabra, K., & Jacobs, L. J. (June 2010). Detection of damage in concrete using diffuse ultrasound. *The Journal of the Acoustical Society of America, 127*(6), 3315−3318. http://dx.doi.org/10.1121/1.3409480.

Dong, B., & Li, Z. (July 2005). Cement-based piezoelectric ceramic smart composites. *Composites Science and Technology, 65*(9), 1363−1371. http://dx.doi.org/10.1016/j.compscitech.2004.12.006.

Dumoulin, C., Karaiskos, G., Carette, J., Staquet, S., & Deraemaeker, A. (April 1, 2012). Monitoring of the ultrasonic P-wave velocity in early-age concrete with embedded piezoelectric transducers. *Smart Materials and Structures, 21*(4), 4. http://dx.doi.org/10.1088/0964-1726/21/4/047001.

Dumoulin, C., Karaiskos, G., & Deraemaeker, A. (2013). Monitoring of crack propagation in reinforced concrete beams using embedded piezoelectric transducers. In *VIII international conference on fracture mechanics of concrete and concrete structures FraMCos-8* (pp. 1717−1725). Toledo.

Gu, H., Song, G., Dhonde, H., Mo, Y. L., & Yan, S. (2006). Concrete early-age strength monitoring using embedded piezoelectric transducers. *Smart Materials and Structures, 15*(6), 1837−1845. http://dx.doi.org/10.1088/0964-1726/15/6/038.

Karaiskos, G., Flawinne, S., Sener, J.-Y., & Deraemaeker, A. (2013). Design and validation of embedded piezoelectric transducers for damage detection applications in concrete structures. In *10th international conference on damage assessment of structures* (pp. 1−7). Dublin.

Kullaa, J. (September 22, 2008). Eliminating environmental or operational influences in structural health monitoring using the missing data analysis. *Journal of Intelligent Material Systems and Structures, 20*(11), 1381−1390. http://dx.doi.org/10.1177/1045389X08096050.

Larose, E., & Hall, S. (April 2009). Monitoring stress related velocity variation in concrete with a $2 \times 10(-5)$ relative resolution using diffuse ultrasound. *The Journal of the Acoustical Society of America, 125*(4), 1853−1856. http://dx.doi.org/10.1121/1.3079771.

Le Bas, P. Y., Ulrich, T. J., Anderson, B. E., Guyer, R.a, & Johnson, P.a (October 2011). Probing the interior of a solid volume with time reversal and nonlinear elastic wave spectroscopy. *The Journal of the Acoustical Society of America, 130*(4), EL258−63. http://dx.doi.org/10.1121/1.3638926.

Li, Z., Qin, L., & Huang, S. (November 2009). Embedded piezo-transducer in concrete for property diagnosis. *Journal of Materials in Civil Engineering*, 643−647.

Liu, T., Huang, Y., Zou, D., Teng, J., & Li, B. (2013). Exploratory study on water seepage monitoring of Concrete structures using piezoceramic based smart aggregates. *Smart Materials and Structures, 22*(6), 65002.

Lu, Y., Li, Z., & Liao, W.-I. (December 23, 2010). Damage monitoring of reinforced concrete frames under seismic loading using cement-based piezoelectric sensor. *Materials and Structures, 44*(7), 1273−1285. http://dx.doi.org/10.1617/s11527-010-9699-0.

Malhotra, V. M., & Carino, N. J. (Eds.). (2003). *Handbook on nondestructive testing of concrete* (2nd ed.). CRC Press.

Mauroux, T., Benboudjema, F., Turcry, P., Aït-Mokhtar, A., & Deves, O. (July 2012). Study of cracking due to drying in coating mortars by digital image correlation. *Cement and Concrete Research, 42*(7), 1014−1023. http://dx.doi.org/10.1016/j.cemconres.2012.04.002.

Planès, T., & Larose, E. (November 2013). A review of ultrasonic coda wave interferometry in concrete. *Cement and Concrete Research, 53*, 248−255. http://dx.doi.org/10.1016/j.cemconres.2013.07.009.

Popovics, S., & Popovics, J. S. (1989). Effect of stresses on the ultrasonic pulse velocity in concrete. In *2nd international RILEM symposium on advances in concrete through science and engineering* (pp. 15−23).

Qin, L., & Li, Z. (October 1, 2008). Monitoring of cement hydration using embedded piezoelectric transducers. *Smart Materials and Structures, 17*(5), 055005. http://dx.doi.org/10.1088/0964-1726/17/5/055005.

Qin, L., Peng, Y., Ren, H., & Li, Z. (2009). Application of cement-based piezoelectric composites in acoustic emission detection for Concrete. In *Second international conference on smart materials and nanotechnology in engineering, 7493* (pp. 1−9). Spie. http://dx.doi.org/10.1117/12.842045.

Safari, A. (2008). In A. Safari, & E. K. Akdoğan (Eds.), *Piezoelectric and acoustic materials for transducer applications*. Boston, MA, USA: Springer. http://dx.doi.org/10.1007/978-0-387-76540-2.

Schurr, D. P., Kim, J.-Y., Sabra, K. G., & Jacobs, L. J. (December 2011). Damage detection in concrete using coda wave interferometry. *NDT & E International, 44*(8), 728−735. http://dx.doi.org/10.1016/j.ndteint.2011.07.009.

Selleck, S. F., Landis, E. N., Peterson, M. L., Shah, S. P., & Achenbach, J. D. (1998). Ultrasonic investigation of concrete with distributed damage. *ACI Materials Journal, 95*(1), 27−36.

Shokouhi, P., Zoëga, A., & Wiggenhauser, H. (2010). Nondestructive investigation of stress-induced damage in concrete. *Advances in Civil Engineering, 2010*, 1−9. http://dx.doi.org/10.1155/2010/740189.

Shokouhi, P., Zoëga, A., Wiggenhauser, H., & Fischer, G. (February 2012). Surface wave velocity-stress relationship in uniaxially loaded concrete. *ACI Materials Journal*, 141−148.

Song, G., Gu, H., & Mo, Y. L. (2007). Concrete structural health monitoring using embedded piezoceramic transducers. *Smart Materials and Structures, 16*, 959−968. http://dx.doi.org/10.1088/0964-1726/16/4/003.

Song, G., Gu, H., & Mo, Y.-L. (June 1, 2008). Smart aggregates: multi-functional sensors for concrete Structures—a tutorial and a review. *Smart Materials and Structures, 17*(3), 033001. http://dx.doi.org/10.1088/0964-1726/17/3/033001.

Suaris, W., & Fernando, V. (1987). Detection of crack growth in concrete from ultrasonic intensity measurements. *Materials and Structures, 20*, 214−220.

Tourin, A., Fink, M., & Derode, A. (October 2000). Multiple scattering of sound. *Waves in Random Media, 10*(4), R31−R60. http://dx.doi.org/10.1088/0959-7174/10/4/201.

Van Mier, J. G. M. (1997). *Fracture processes of concrete: assessment of material parameters for fracture models*. Boca Raton: CRC Press.

Vives, A. A. (2008). In A. A. Vives (Ed.), *Piezoelectric transducers and applications*. Berlin, Heidelberg: Springer Berlin Heidelberg. http://dx.doi.org/10.1007/978-3-540-77508-9.

Quantitative estimation of rebar corrosion in reinforced concrete by thermography

9

H. Oshita
Chuo University, Tokyo, Japan

9.1 Introduction

In concrete structures, the corrosion of reinforcing steel bar (rebar) is well known to not only initiate cracks due to the expansion of corrosion products, but also decrease the ultimate strength of the concrete with the decrease in the effective cross-section of rebar. Moreover, the delamination in cover concrete could lead to a remarkable decline in the durability and the ultimate strength as a result of the accelerated degradation with the exposure of rebar to the atmosphere. Consequently, it is very important to quantitatively estimate characteristics of the corrosion of rebar in RC structures. The most accurate technique currently available for the estimation of the corrosion is to remove the rebar and measure it visually. It is, however, realistically difficult to take out rebar from existing structures, and thus, nondestructive evaluation (NDE) techniques have been applied.

NDE techniques that are currently applied to the estimation of rebar corrosion are the half-cell potential method (ASTM, 2001) and the polarization resistance method (ASTM, 2009). The former can judge the activity of the corrosion from the electric potentials measured at the concrete surface and estimate the possibility for corrosion. The latter measures the resistance between rebar and the reference bar and estimates the rate of the corrosion reaction. It is known that both methods are marginally successful to predict the characteristic of rebar corrosion, and there exists one problem in that damage is inevitably exerted by chipping covered concrete to set the electrode directly in the rebar. That is, it seems that any NDE techniques currently available could not predict the corrosion degree or the thickness of the corrosion products in rebar accurately. Hence, quantitative NDE techniques, which can estimate the effective cross-section of rebar damaged by the corrosion, have to be developed.

As follows, one promising NDE technique that applies thermography is presented. The corrosion of rebar is estimated from the temperature history at the concrete surface, which varies due to heat conduction from the reinforcement heated by electromagnetic induction.

Acoustic Emission (AE) and Related Non-destructive Evaluation (NDE) Techniques in the Fracture Mechanics of Concrete
http://dx.doi.org/10.1016/B978-1-78242-327-0.00009-X
Copyright © 2015 Elsevier Ltd. All rights reserved.

9.2 Outline of the proposed technique

An evaluation technique for the characteristics of rebar corrosion in concrete structures was developed under conditions of no destruction and no contact at the surface of the concrete. Based on the characteristics of rebar with high heat conduction and easy magnetization, heat applied to rebar by electromagnetic induction heating is diffused to the surface of the concrete. When the corrosion product exists on the rebar surface, the temperature on the surface of the concrete over rebar could becomes lower than that of nonexistence of the corrosion product. Thus, the temperature on the surface of the concrete is dependent on the thickness and distribution of the corrosion products. The thermal characteristics of the corrosion product are similar to those of air, as the specific heat is relatively large, and the thermal conductivity is inversely small. This is because the corrosion product of steel bar mainly contains the components of hematite and, according to X-ray analysis, has many pores inside (Oshita, Horie, Nagasaka, Taniguchi, & Yoshikawa, 2009). The effect of the corrosion product is illustrated in Figure 9.1. Since heat conduction is prevented by a layer of the corrosion product, the temperature at the concrete surface over non-corroded rebar (case a in the figure) is very different from that of corroded rebar (case b).

9.2.1 *Electromagnetic induction for heating*

For noncontact heating, electromagnetic induction is applied. By charging a high-frequency electric current on an electromagnetic induction coil, an alternating field is generated around the coil, and thus, an eddy current is driven in a steel bar located in that field. As a result, the rebar is heated. In the case of a circular coil, an electromagnetic induction generates an alternating magnetic field concentrically, as shown in Figure 9.2. At the center and the edge of the coil, the magnetic flux density becomes smaller than that in between. Therefore, for a rebar set in the alternating magnetic field,

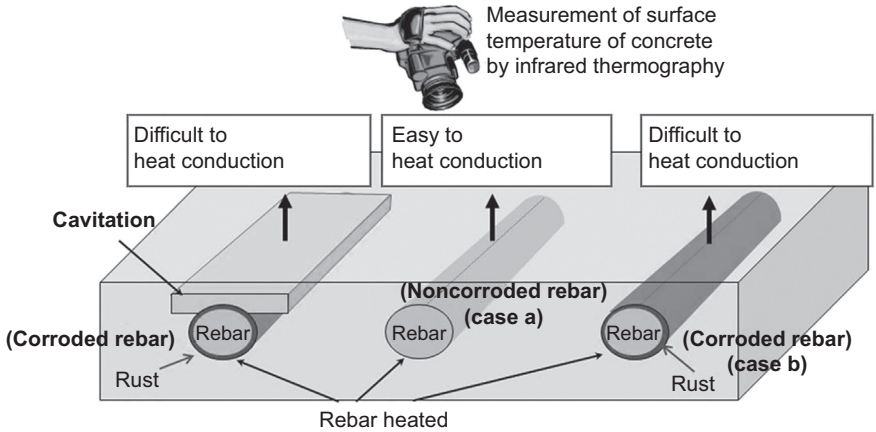

Figure 9.1 Proposed technique.

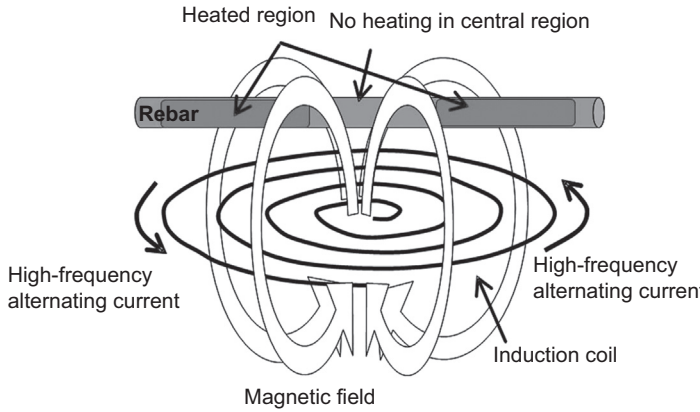

Figure 9.2 Magnetic field and heated region by electromagnetic induction.

nonuniform heating areas are generated, as the temperature around the center and the edge of the coil becomes lower while that of the other region becomes higher.

In the proposed procedure, it is very important to heat a rebar uniformly in the longitudinal direction. To this end, various experiments for the characteristics of heating were performed in which the coils were investigated on the shape and size of steel tube for the coil and the diameter of steel tube. We found that a rectangular coil, shown in Figure 9.3, has one of the most suitable shapes for heating the rebar uniformly so that no heating gradients exist in the range of 60 × 300 mm, as shown in Figure 9.4. The electromagnetic induction coil developed is equipped with a copper pipe of 10-mm diameter, inside which cooling is performed with water to reduce the heat of

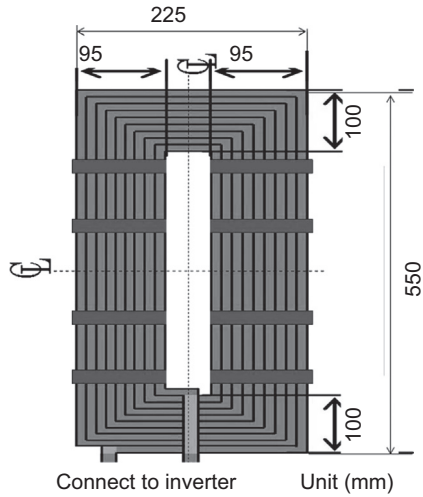

Figure 9.3 Outline of coil shape.

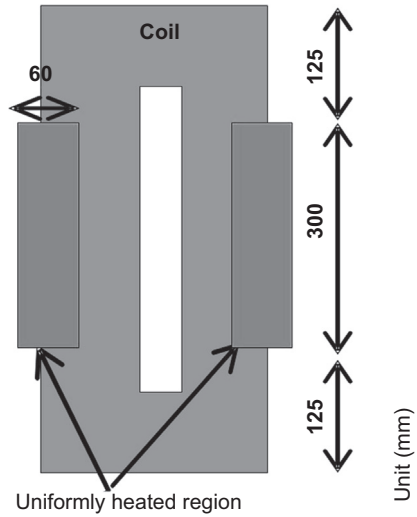

Figure 9.4 Uniformly heated region.

Table 9.1 Maximum temperature applied to reinforcement

Diameter	Maximum
16 mm	35 °C
19 mm	24 °C
25 mm	20 °C

the coil due to radiofrequency current. The coil temperature becomes about 30 °C at the time of radiofrequency current charge, even if cooling is performed. Therefore, it is necessary to set styrene foam of about 10 mm in thickness as an insulator at the concrete surface when heating is conducted.

The temperature induced in rebar by heating has to be controlled, so as not to make a crack in the concrete due to thermal stress. Thus, thermal stress analysis was conducted, and the results are summarized in Table 9.1. Further, the specification of the electromagnetic induction heating apparatus is shown in Table 9.2.

9.2.2 Heat conduction through corrosion product

The thermal properties of partially corroded rebar are studied by electromagnetic induction heating. As shown in Figure 9.5(a), the central section of 100 mm is corroded in the axial direction, and the other regions that are not corroded are tested. The average rate of the corrosion was about 0.7% by weight, and the thickness of the corrosion product was about 0.041 mm. The rate of the corrosion is defined as the mass

Table 9.2 Characteristics of electromagnetic induction heating

Input	3φ AC200/220V50/60Hz
Input power	26 KVA
Output voltage	1000 V_{max}
Output current	230 A_{max}
Electric power	20 kW
Frequency	10 ~ 40 kHz
Cooling method	Water-cooling

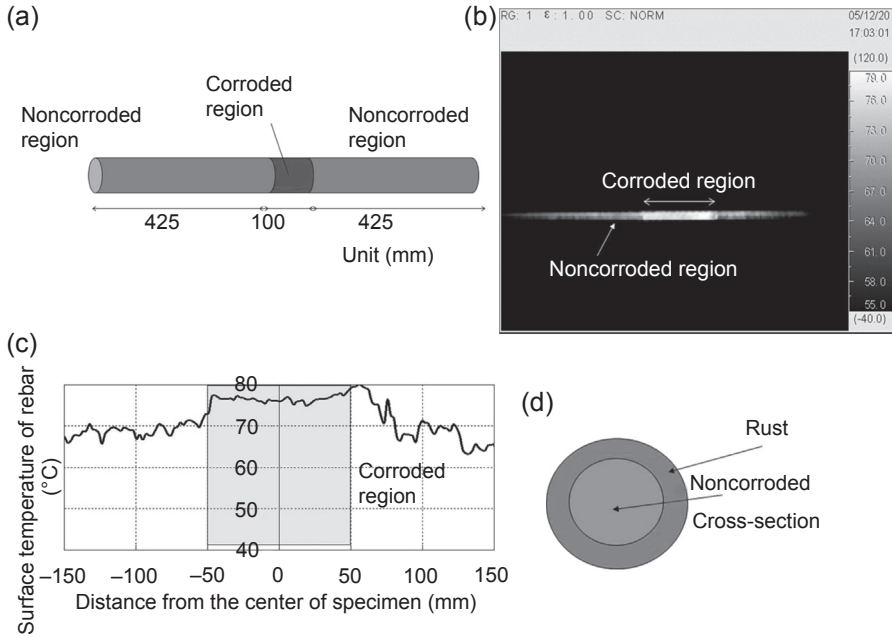

Figure 9.5 Temperature of corroded rebar: (a) corrosion property, (b) thermograph, (c) distribution of surface temperature of rebar, and (d) cross-section of corroded region.

ratio of the corrosion product to the noncorroded rebar. The corrosion product was removed by soaking the corroded rebar in citric acid di-ammonium solution of 10% concentration at a temperature of 20 °C for 24 h. The thickness of the corrosion product was calculated from the rate of the corrosion and the density of steel and rust given in Table 9.3. The rebar was heated at the uniform heating region of the coil shown in Figure 9.4. The coil was arranged so the axis of rebar was identical to the axial direction in the uniform heating region of the coil. An electric current was

Table 9.3 Material properties

Reinforcement	Thermal conductivity	51.3	W/m °C
	Density	7850	kg/m^3
	Specific heat capacity	0.470	kJ/kg °C
Rust	Thermal conductivity	0.07	W/m °C
	Density	5300	kg/m^3
	Specific heat capacity	1.20	kJ/kg °C

Table 9.4 Experimental conditions of rebar

Diameter	**D16 (SD295A)**
Length of corroded region	100 mm
Corrosion ratio	0.7%
Thickness of rust	0.04 mm
Heating time	120 s
Coil power	4.0 kW
Space between rebars and coil	40 mm

charged into the coil for a fixed time, and the temperature at the surface of the rebar was measured by infrared thermography from the start of heating to 10 min elapsed as heating was terminated. Details of the experimental conditions are shown in Table 9.4. Here, the rebar was corroded by a galvanic corrosion test.

A thermal image of the rebar at the end of heating is shown in Figure 9.5(b). The temperature in the corroded region is clearly higher than that of the noncorroded region. According to the temperature distribution in the axial direction at the surface of the rebar, the difference in the temperature between the corroded and noncorroded region is around 7−10 °C, as denoted in Figure 9.5(c). The difference of temperature results from the thermal properties of the corrosion product with a high specific heat and small heat conductivity, compared with those of steel as shown in Table 9.3. This implies that rusting of the corrosion product, shown in a cross-section in Figure 9.5(d), could store heat inside, which was diffused from the noncorroded region, and consequently, restrain heat conduction to the outside. In contrast, after heat conduction to the atmosphere is activated, the temperature in the noncorrosion region becomes lower because the specific heat of the noncorroded region is small compared with that of the corroded region.

Note that the distribution of temperature at the concrete surface is different depending on the presence of rust, as shown in Figure 9.6. Heat stored in the rebar could diffuse toward the concrete surface. In the case of corroded rebar in Figure 9.6(b), heat stored in the rebar becomes difficult to diffuse to the concrete compared in the

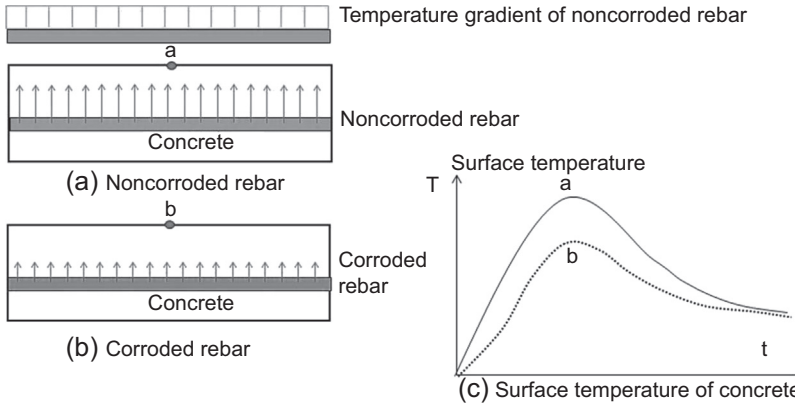

Figure 9.6 (a–c) Difference in surface temperature of concrete due to the presence of a corroded region.

case of noncorroded rebar in Figure 9.6(a) due to accumulated heat in the corrosion product, thus preventing conduction of the heat to the outside. Therefore, in the measurement of infrared thermography, the temperature at the concrete surface seems to become lower compared with the case of noncorroded rebar in Figure 9.6(c).

9.2.3 Heat conductivity of the corrosion product

Heat conductivity of the corrosion product was measured by laser flash. Ferric oxide was scraped off the corroded rebar, and then a sample was formed by pulverizing the corrosion product and molding it into a pellet of 10-mm diameter and 2-mm height. The pellet was calcinated for 24 h at 500–900 °C. It is ideal to measure the sample directly, without crushing, for measuring the heat conductivity of the corrosion product. But, the pellet samples were tested because the corrosion product was very brittle and uneven on the rebar surface.

The result shows that the heat conductivity is highly dependent on porosity, as illustrated in Figure 9.7. Since the porosity of the corrosion product was estimated as 50.5% in this research, the heat conductivity was determined to be 0.70 W/m °C. Further, porosity of the corrosion product was calculated from the differences in the density of corroded product, including the pores, for which the volume and mass were measured using Archimedes' principle and an electronic balance.

Akiyama, Takahashi, and Yagi (1991) and Akiyama, Ohta, Takahashi, Waseda, and Yagi (1992) have pointed out that the heat conductivity of ferric oxide (hematite) also depends on the amount of bound water. It has been reported that bound water perfectly removed by calcinations is about 10 times as much heat conductivity, compared with a non-calcinated sample having about 10% bound water. In this research, the heat conductivity of the corrosion product was 0.07 W/m °C, which is one-tenth of a calcinated ferric oxide sample because the main component of the corrosion product is hematite of noncalcination according to X-ray analysis (Akiyama, Takahashi, and Yagi, 1989).

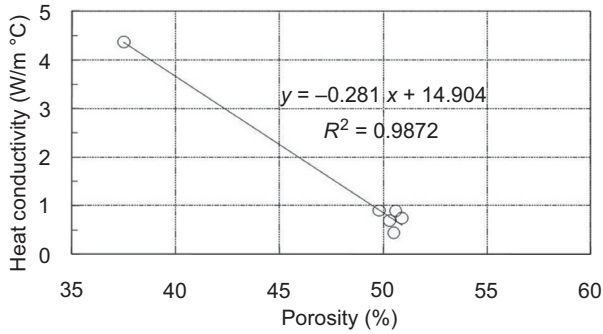

Figure 9.7 Heat conductivity and porosity of ferric oxide.

9.3 Temperature at surface of concrete related to corrosion properties of rebar

9.3.1 Experimental outline

A cubic concrete specimen with a height of 250 mm and length and width of 450 mm is shown in Figure 9.8. Two rebars with the diameter of 16 mm are arranged with a 200-mm interval of 30, 50, and 70 mm cover thicknesses. One is noncorroded, and another is corroded, where uniform corrosion was confirmed along the axial direction. By charging an electric current into a coil for a fixed time, the temperature of rebar was controlled by electromagnetic induction heating, and then the coil was removed. The maximum temperature of the rebar has to be prescribed to prevent cracking from thermal stress. Prescribed values for three types of rebar are shown in Table 9.1. Here, the region of uniformly heated rebar is 300 mm, as shown in Figure 9.8, due to the restrictions of coil size. Both the lengths of the coil and the specimen are 450 mm, but extended regions of the rebar outside the concrete specimen were actually heated due to the formation of the magnetic field.

In the measurement, the temperature on the surface of the concrete was measured by infrared thermography. Initially, the surface temperature was measured before installing the electromagnetic induction coil. Then, the temperature was measured for 90 min at every 5-seconds after the end of electromagnetic induction heating.

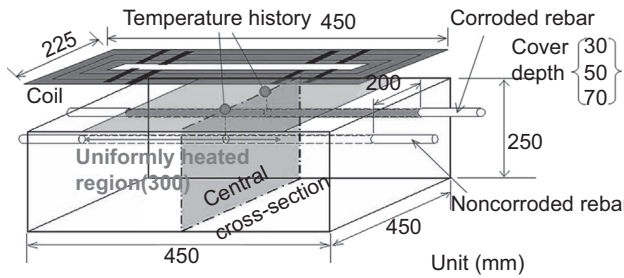

Figure 9.8 Dimensions of specimen.

Table 9.5 Experimental conditions of three specimens

Specimens	K30-C0.66	K50-C0.82	K70-C0.70
Heating time (s)	320	540	780
Coil power (kW)	2.0	6.0	6.0
Raised temperature of reinforcement (°C)	14.7	27.9	15.9
Average corrosion ratio (%)	0.66	0.82	0.70
Average thickness of rust (mm)	0.04	0.05	0.05
External temperature (°C)	23.7	21.2	21.8

Experimental parameters were the cover depth of concrete, the length of the corroded area, and the rate of corrosion. Details of all specimens are listed in Table 9.5. Thus, the specimen's name is classified with the cover depth as K30 and the rate of corrosion as C0.66. The electric powers applied are also shown in Table 9.5.

9.3.2 Thermal characteristics of rebar in concrete

Figure 9.9 shows the distribution of temperature on the surface of the rebars for three cover thicknesses (30 mm: K30, 50 mm: K50, and 70 mm: K70). Here the rate of corrosion in the rebars is appended as K30-C0.66, for which the rate is 0.66%. As seen, the temperature of the corroded rebar is lower than that of the noncorroded rebar. This thermal behavior is opposite to that exhibited while exposing the rebar to air. These differences are caused by the corrosion product restraining the diffusion of heat to concrete from the noncorroded cross-section of the reinforcing bar, as shown in Figure 9.10.

9.3.3 Thermal characteristics at the surface of concrete

Figure 9.11 shows thermal images at the concrete surface for three cover thicknesses at 180 s after heating. In these figures, a rectangular white line shows the concrete specimen. It is clearly found that the temperature at the location over the corroded rebar is lower than that of the noncorroded rebar, although the difference decreases with an increase in cover thickness. The temperature history and temperature distribution at the concrete surface over the rebars are shown in Figure 9.12 at the middle point of the rebar and in Figure 9.13 along the rebars, respectively. The temperature over the corroded rebar is 0.5−0.9 °C lower than that over the noncorroded rebar.

Osada and Yamada (2004) pointed out that the threshold value to judge the presence of a cavitation in concrete by an infrared thermography method would be 0.5 °C. Hence, the threshold to classify corroded and noncorroded rebars could be reasonably set at the same value. Based on the heat conduction mechanisms, the judgment whether a rebar is corroded or not can be made by the relative difference of the temperature at the concrete's surface over the rebar.

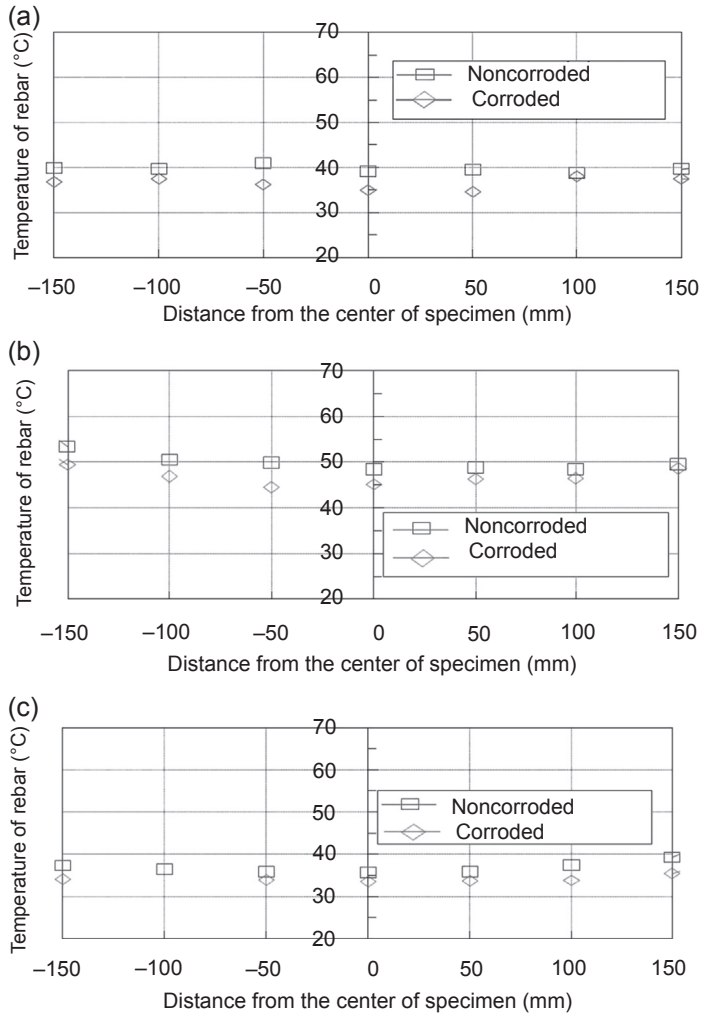

Figure 9.9 Temperature distribution of rebar embedded in concrete: (a) specimen K30-C0.66, (b) specimen K50-C0.82, and (c) specimen K70-C0.70.

9.3.4 Thermal characteristics of a concrete surface due to corrosion-induced cracks

The influence of corrosion-induced cracks (generated in the cover concrete due to the volume expansion of corrosion products) on the temperature of the concrete surface will now be compared with the surface temperature over noncorroded rebar.

Figure 9.14 shows the following aspects of a tested specimen: the distribution of crack widths after corrosion, the rate of the corrosion by the galvanic method, and the thermal image of the concrete surface by electromagnetic induction heating. Note

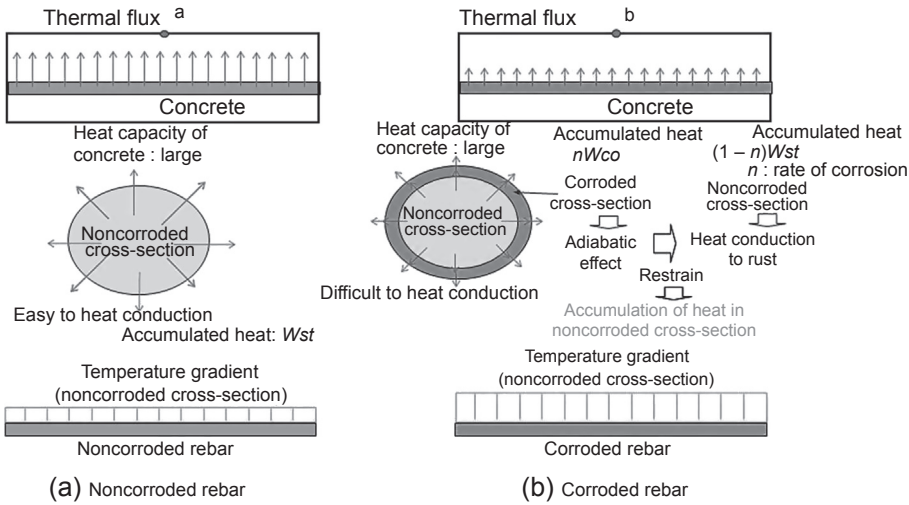

Figure 9.10 (a,b) Surface temperature properties of concrete due to the presence of corroded rebar.

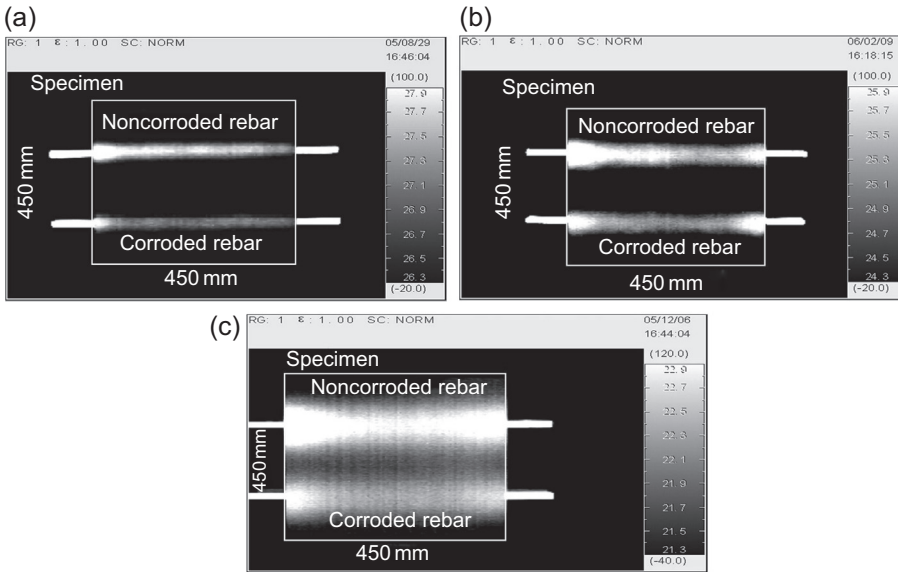

Figure 9.11 Thermograph of surface of concrete. (a) Specimen K30-C0.66 (180 s after the end of heating). (b) Specimen K50-C0.82 (180 s after the end of heating). (c) Specimen K70-C0.70 (180 s after the end of heating).

that locations of cracks and their widths are not explicitly correlated with the rate of corrosion at the rebar. According to Figure 9.14(c), the rate of the corrosion of the rebar is higher in the regions of 100−400 mm and 700−750 mm in length than other regions. However, the region with wider crack widths is observed at

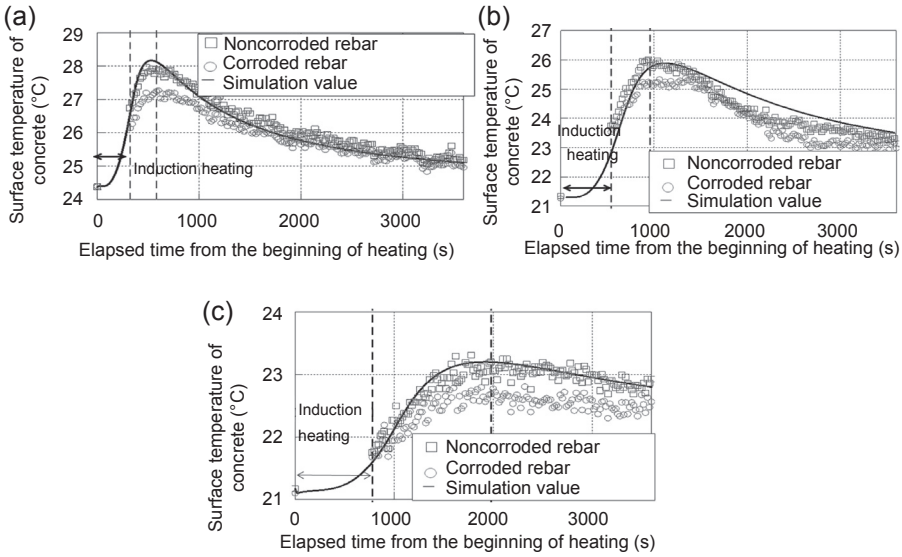

Figure 9.12 Temperature history of the concrete surface: (a) specimen K30-C0.66, (b) specimen K50-C0.82, and (c) specimen K70-C0.70.

only 100−400 mm in length (Figure 9.14(b)). Results suggest that corrosion-induced cracks are not directly correlated with the rate of the corrosion but instead with structural details: the quality of concrete, environmental condition, etc. The thermal image at the concrete surface is shown in Figure 9.14(d). In this case, only the central regions of three rebars were heated. It was observed that the temperature was lower in the regions with high corrosion rates (Figure 9.14(c)) and is higher in the regions with low corrosion rates, in spite of the presence of corrosion-induced cracks. Compared to other regions, the temperature at the concrete surface is lower both in the regions of corrosion-induced cracks (100−400 mm) and the absence of cracks (700−800 mm). Therefore, we conclude that the main effect on the thermal property at the concrete surface is not the presence of cracks but the rate of corrosion. Namely, although it could also depend on atmospheric temperature and wind velocity, an application of the proposed technique is promising. However, cracks nucleated with large widths might be another case.

9.4 Surface temperature property of reinforced concrete (RC) with partially corroded rebar

In the previous section, the proposed technique was applied to the specimens with the rebar corroded uniformly in the axial direction. However, the partial corrosion often occurs due to macro-cell corrosion mechanisms in RC structures. Therefore, the case of an RC specimen with partially corroded rebars is discussed in relation to the length of the corrosion, the rate of corrosion, and the cover depth.

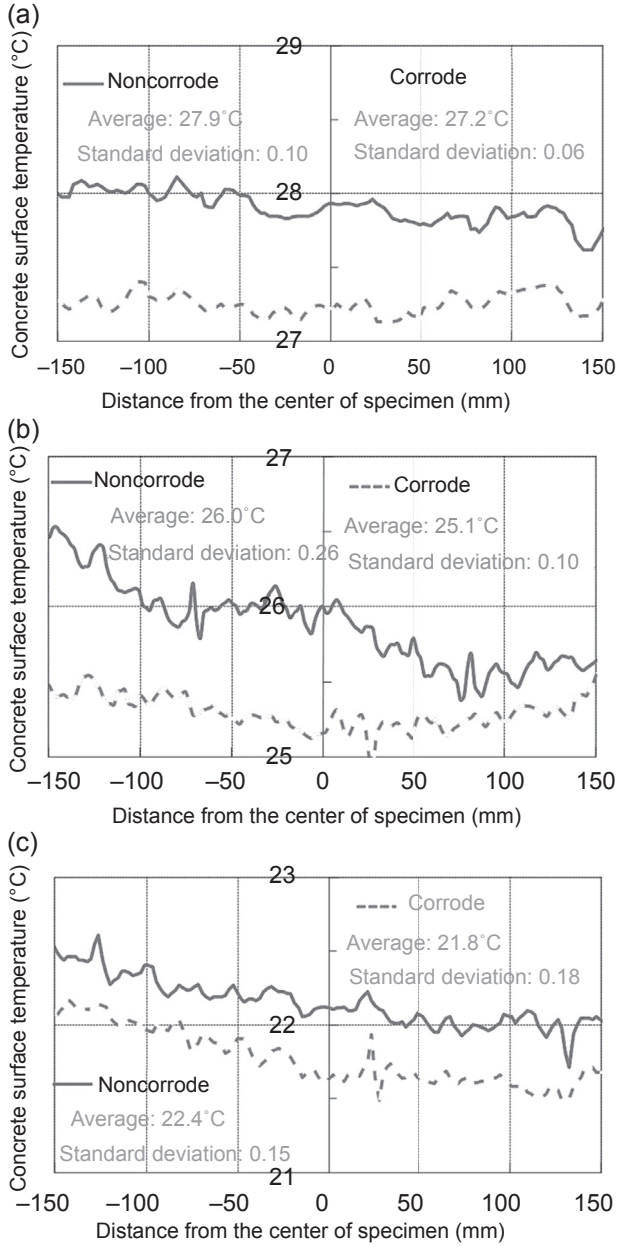

Figure 9.13 Distribution of temperature when the surface temperature of concrete reaches maximum: (a) specimen K30-C0.66, (b) specimen K50-C0.82, and (c) specimen K70-C0.70.

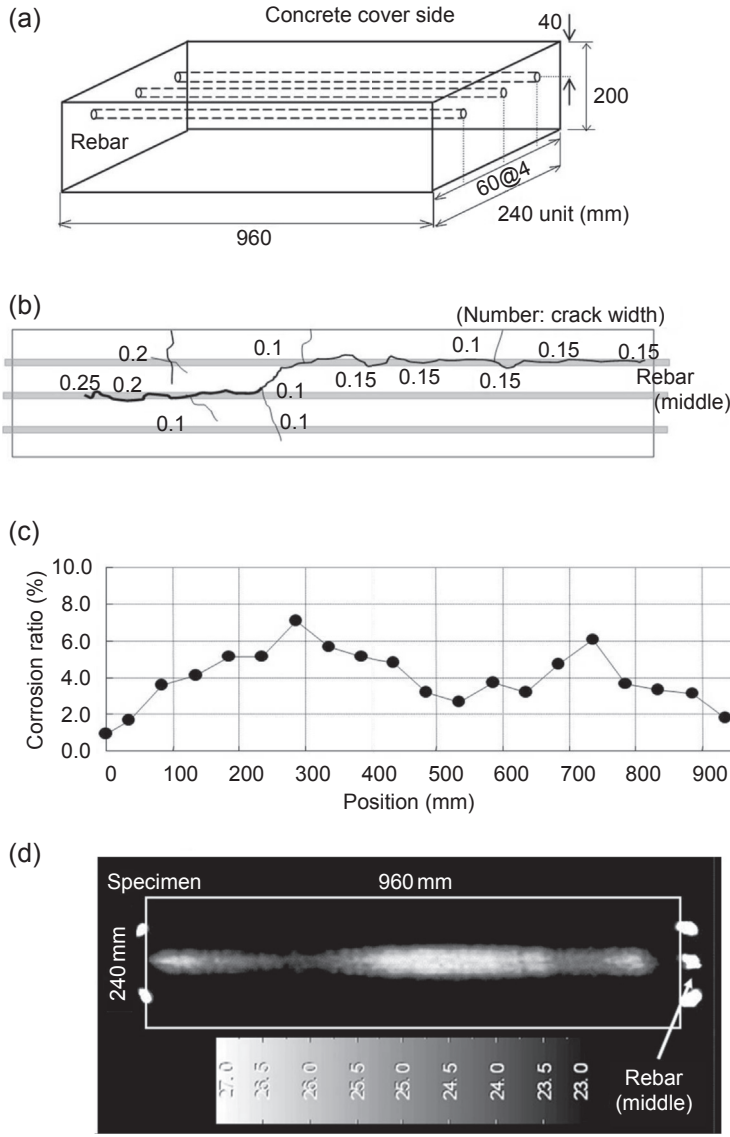

Figure 9.14 Corrosion behavior and corrosion ratio versus surface temperature of concrete: (a) dimension of specimen, (b) corrosion crack in concrete cover, (c) distribution of corrosion ratio (middle rebar), and (d) surface temperature of concrete.

9.4.1 Experimental outline

A cubic concrete specimen has the following dimensions: height of 180 mm, width of 500 mm, and length of 550 mm. As shown in Figure 9.15, a reinforcing steel bar with the diameter of 16 mm is arranged in two cases where the corroded regions are 100 and

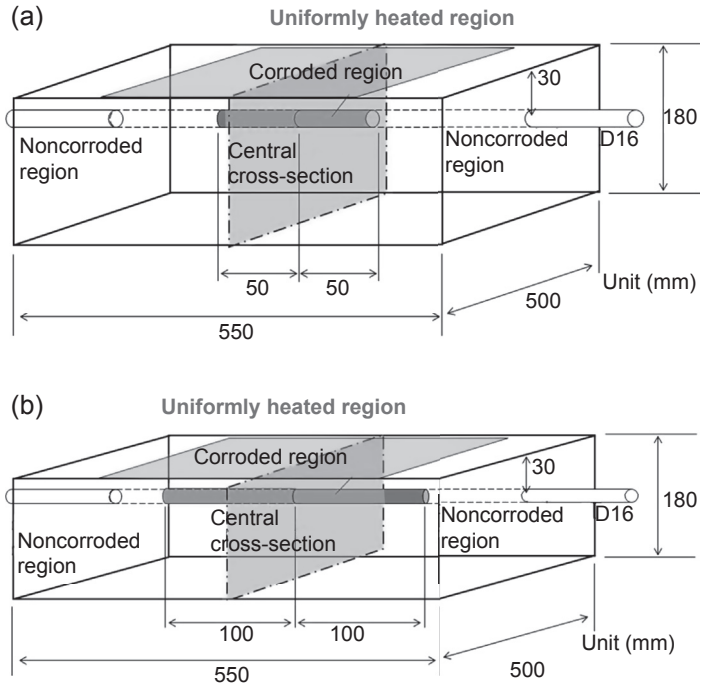

Figure 9.15 Dimensions of concrete specimen: (a) length of corroded region is 100 mm, (b) length of corroded region is 200 mm.

200 mm around the central section in the axial direction of rebar. Experimental parameters are the cover depth of concrete, the length of the corroded area, and the rate of corrosion. Details of all specimens are listed in Table 9.6. Thus, the specimen's name is classified with the cover depth as N30, the length of corroded region as R200, and the rate of corrosion as C3.5. The heating technique and the temperature control of the rebar are identical to those in the preceding section, and the electric powers applied are also shown in Table 9.6. Further, unheated regions around the edge of the specimen seem to exist due to the restrictions of the coil size (uniform heating area length is 300 mm). The specimen's length is 550 mm, which is larger than that of the coil.

9.4.2 Thermal characteristics of a concrete surface (cover depth 30 mm)

Figures 9.16 and 9.17 show thermal images of the concrete surface and the temperature distributions over the rebars of specimens N30-R200-C3.5 and N30-R100-C0.73. These results are obtained at 180 s after electromagnetic induction heating. The presence of the corrosion product on the rebar can be confirmed by the thermal image and the distribution of temperature. As can be seen in each specimen,

Table 9.6 Experimental conditions

Specimens	N30-R200-C3.5	N30-R100-C0.73	N50-R200-C4.1	N50-R100-C8.3	N50-R100-C0.4A	N50-R100-C0.4B
Concrete cover (mm)	30	30	50	50	50	
Length of corroded region (mm)	200	100	200	100	100	
Corrosion ratio (%)	3.5	0.73	4.1	8.3	0.40	
Average thickness of rust (mm)	0.19	0.04	0.23	0.47	0.02	
Coil power (kW)	4.0	4.0	10.0	10.0	10.0	
Heating time (s)	240	240	300	300	300	550
Raised temperature of rebar (°C)	22.5	22.6	28.9	31.7	27.9	45.3
External temperature (°C)	23.7	16.7	22.1	18.3	19.4	16.9

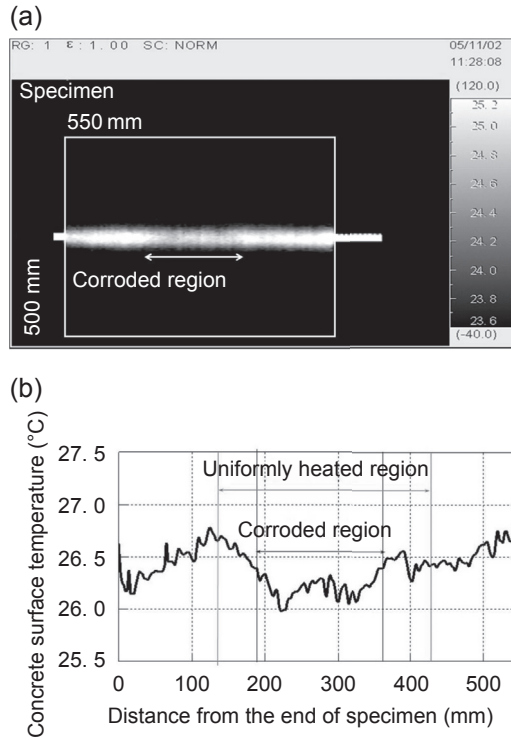

Figure 9.16 Temperature property of N30-R200-C3.45: (a) thermograph (180 s after the end of heating), and (b) distribution of surface temperature of concrete.

the temperature at the concrete surface over the corroded region is lower than that over the noncorroded region.

The difference between corroded and noncorroded regions must be conspicuous in the case that the corroded region is wide because the heat conduction from the noncorroded region is minor and the temperature at the surface is not affected much, as shown in Figure 9.18(a). In contrast, in the case that the corroded region is narrow, the gradient of temperature becomes so steep in the axial direction of the rebar that the temperature at the surface could be affected by the noncorroded region, as shown in Figure 9.18(b). As a result, the presence of the corrosion in rebar might be difficult to identify. Therefore, when estimating the partially corroded rebar from the temperature at the concrete surface, it is desirable to compare the temperatures, as there is little mutual influence between noncorroded and corroded rebars. The temperature should become lower at the corroded region, whereas it becomes higher at the noncorroded region of rebar. The judgment of the presence of the corrosion product could be made by the comparison of both temperatures.

From these results, we find that the difference between the minimum value of the temperature at the concrete surface over the corroded region and the maximum temperature over the noncorroded region is 0.5−0.7 °C. So, the difference is

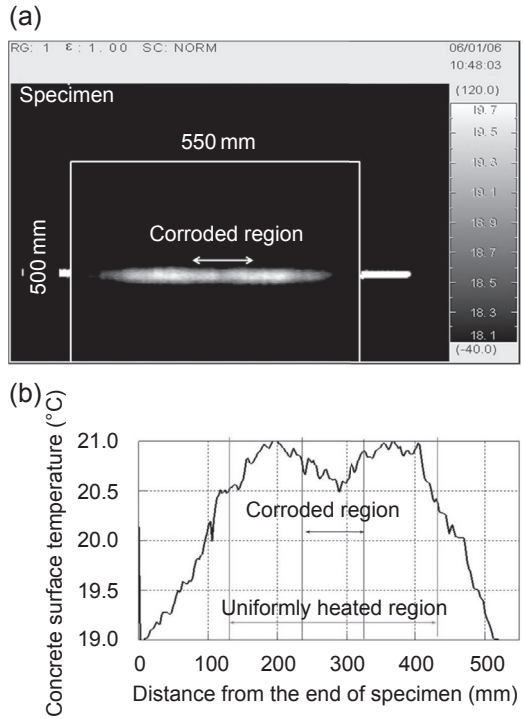

Figure 9.17 Temperature property of N30-R100-C0.73: (a) thermograph (180 s after the end of heating), and (b) distribution of surface temperature of concrete.

higher than 0.5 °C (the threshold for the judgment of the presence of the corrosion product in Figures 9.16(b) and 9.17(b)). As mentioned, the proposed technique can estimate the corrosion of rebar where the rate is relatively small, such as 0.73%.

9.4.3 Thermal characteristics of a concrete surface (cover depth 50 mm)

Figures 9.19–9.21 show thermal images of the concrete surface and the temperature distributions over the rebars of specimens N50-R200-C4.1, N50-R100-C8.3, and N50-R100-C0.40A. Results are obtained at 600 s after the electromagnetic induction heating.

From specimen N50-R200-C4.1 shown in Figure 9.19(a) and (b), the presence of the corrosion product on the reinforced bar is confirmed. Comparing specimen N50-R200-C4.1 with specimen N30-R200-C3.5 in Figure 9.16, where the corrosion rate is almost the same, the presence of the corrosion product is not completely clear with the increase of the cover thickness. In the case that the cover concrete is deeper, the heat is readily conducted from the noncorroded region and spreads in the cover

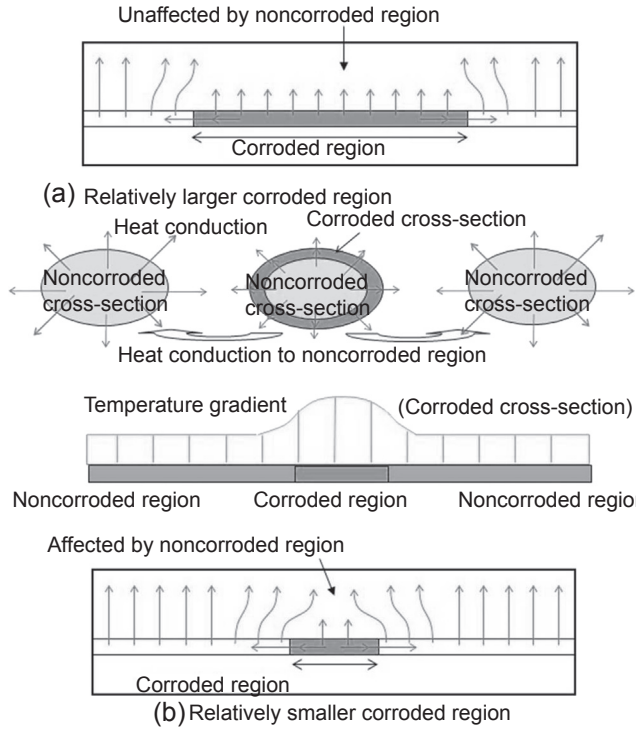

Figure 9.18 (a,b) Different temperature characteristics due to different corroded regions.

concrete, as shown in Figure 9.22. The difference between the minimum value of the temperature at the corroded region and the maximum value at the noncorroded region is about 0.5 °C, which is in good agreement with the limited threshold shown in Figure 9.19(b).

In specimen N50-R100-C8.3, for which the corrosion length is shorter than that of specimen N50-R200-C4.1, the presence of the corrosion product is confirmed in Figure 9.20(a). The difference between the minimum value of the temperature at the corroded region and the maximum at the noncorroded range, shown in Figure 9.20(b), is about 0.5 °C. Again, the limited threshold for the judgment of the presence of the corrosion product is obtained. Namely, for specimens with 50-mm cover depth, it is possible to estimate the corrosion of the rebar in the case of a relatively high corrosion rate, around 8.3%. On the other hand, for specimen N50-R100-C0.4A, which has the relatively lower corrosion rate, the presence of the corrosion product is not clearly confirmed, as observed in Figures 9.21(a) and 9.21(b) where the duration of electromagnetic induction heating is 300 s, as indicated in Table 9.6. However, in the case that the duration of electromagnetic induction heating is 550 s (specimen N50-R100-C0.4B in Figure 9.23), the presence of the corrosion product seems to be identified, and the difference in the temperature at the concrete surface between the corroded and noncorroded region is higher than the 0.5 °C limit

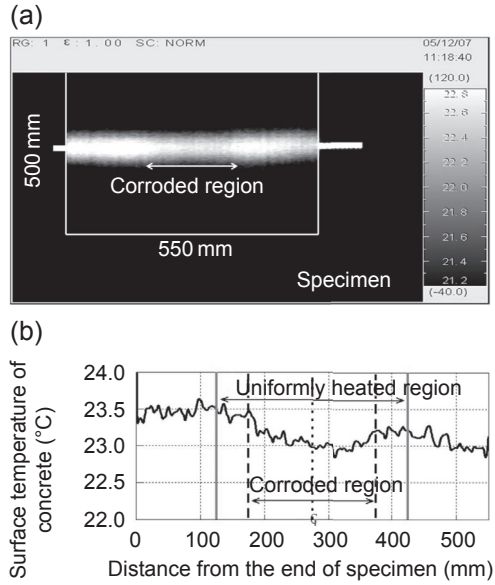

Figure 9.19 Temperature property of N50-R200-C4.1: (a) thermograph (600 s after the end of heating), and (b) distribution of surface temperature of concrete.

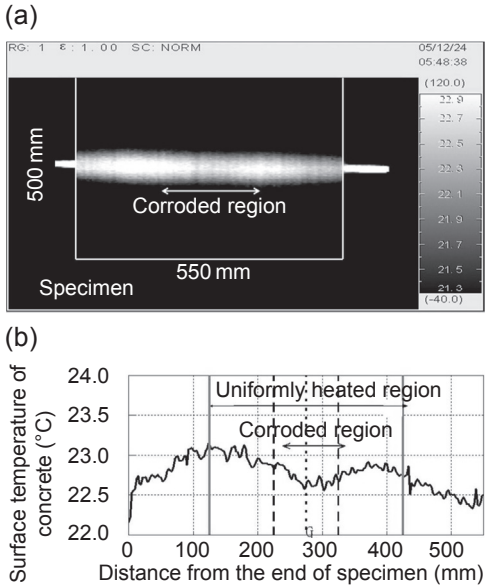

Figure 9.20 Temperature property of N50-R100-C8.3: (a) thermograph (600 s after the end of heating), and (b) distribution of surface temperature of concrete.

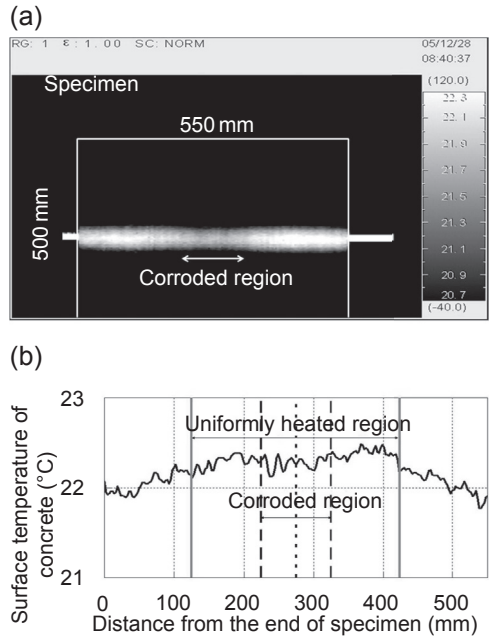

Figure 9.21 Temperature property of N50-R100-0.40A: (a) thermograph (600 s after the end of heating), and (b) distribution of surface temperature of concrete.

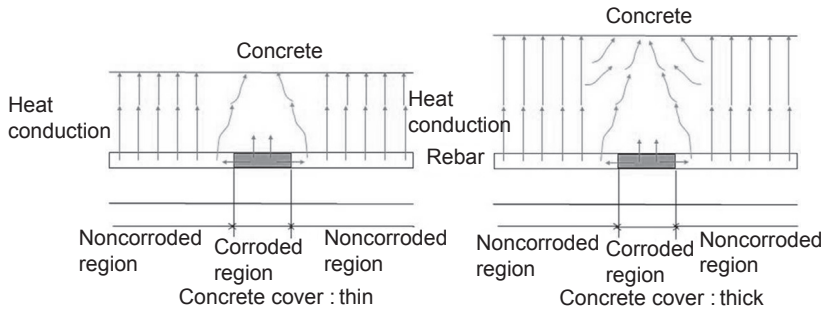

Figure 9.22 Influence of concrete cover on heat dissipation.

threshold. Consequently, for the specimen with a relatively small corrosion rate, it is possible to estimate the corrosion of rebar by the proposed technique that uses electromagnetic induction heating.

9.5 Predictive model for the corrosion rate

In the previous section, the presence of the corrosion product on the rebar was confirmed by relative comparison of the temperature at the concrete surface

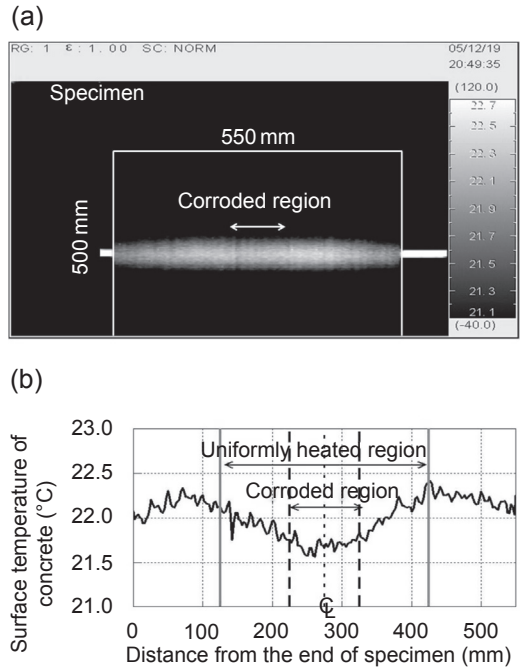

Figure 9.23 Temperature property of N50-R100-C0.40B: (a) thermograph (600 s after the end of heating), and (b) distribution of surface temperature of concrete.

between the corroded and noncorroded regions. Primarily, not a relative evaluation, but an absolute evaluation for the corrosion of rebar is to be performed from the thermal image of the concrete surface located over the rebar. The rate of corrosion of a reinforcing bar is greatly dependent on characteristics of the temperature at the concrete surface such as the maximum temperature and the rate of temperature rise.

As mentioned previously, the presence of a corrosion product causes a decrease in the maximum temperature at the concrete surface, and the decreasing value corresponds to the rate of the corrosion. Hence, the rate of the corrosion will be predicted by the comparison between the value measured in a corroded RC structure and the prescribed value (noncorroded bar).

9.5.1 Temperature at the concrete surface over noncorroded rebar due to electromagnetic induction heating

To predict the rate of the corrosion of rebar, information on surface temperature $T_{\max}$ of concrete, in which noncorroded rebar is arranged, is essential. One empirical estimation is given as follows (Yazaki, Imai, & Oshita, 2012):

$$T_{\max} = a + c\{-0.0023(a-b) - 0.0395\} + 3.075 \tag{9.1}$$

where the variables a, b, and c are the initial temperature, the atmospheric temperature, and the cover depth, respectively.

The corrosion product at the surface of rebar restrains heat conduction from the noncorroded section inside steel to concrete, and thus, the restrained heat is dependent on the rate of the corrosion, as shown in Figure 9.10. In conclusion, the rate of the corrosion is able to be estimated, if the restrained heat is obtained from the difference between the temperature at the surface over corroded rebar and that of noncorroded rebar.

9.5.2 Heat restrained by the corrosion product

In the case of noncorroded rebar, as shown in Figure 9.10(a), all of the heat due to electromagnetic heating is stored inside steel as W_{st}, which could influence the temperature at the concrete surface. In the case of corroded rebar, the stored heat should be related to the rate of the corrosion, n, because the corrosion product is a nonmagnetic material. In addition, the corrosion product restrains the heat conducted from the noncorroded steel inside rebar to concrete. As a result, the heat W_{co} that influences the temperature at the concrete surface can be expressed as follows:

$$W_{co} = (1-n)W_{st} + nW'_{co} \tag{9.2}$$

where W'_{co} is the heat conducted to concrete from the corrosion product. It can be expressed as the difference between the heat conducted from the noncorroded section and the heat accumulated in the corrosion product. Here, heat is assumed to be dependent on the rate of the heat capacity between the corrosion product and steel and is expressed as follows:

$$W'_{co} = W_{st}\frac{C_{st}}{C_{co}} \tag{9.3}$$

where C_{st} and C_{co} are the heat capacity of steel and the corrosion product, respectively.

The heat, $lossW$, is restrained from conduction to concrete by the corrosion product and can be expressed as follows:

$$lossW = W_{st} - W_{co} \tag{9.4}$$

Equation (9.4) is normalized by the stored heat, W_{st}, through electromagnetic heating. Then, we obtain the following:

$$RlossW = \frac{W_{st} - W_{co}}{W_{st}} \tag{9.5}$$

Finally, substituting Eqns (9.3) and (9.4) into Eqn (9.5), we derive the following:

$$RlossW = n\frac{C_{co} - C_{st}}{C_{co}} \tag{9.6}$$

9.5.3 Decreasing rate of concrete surface temperature due to the presence of corrosion product

The decreasing rate, RT, of the temperature at the concrete surface due to the presence of the corrosion product is expressed as follows:

$$RT = \frac{\Delta T_{st} - \Delta T}{\Delta T} \tag{9.7}$$

where ΔT_{st} and ΔT are the increase in the temperature at the concrete surface over the noncorroded rebar and the corroded rebar, respectively.

For a body constituted by the same material, Eqn (9.6) is equivalent to Eqn (9.7). In contrast, for a composite body constituted of concrete and steel, the thermal properties are so different that this effect has to be taken into account. The heat capacity per unit volume of the body can be expressed by the product of the specific heat and the density (Oshita et al., 2009). Thus, the ratio of the heat capacity, h, between concrete and steel is expressed as follows:

$$h = \frac{C_{st} \cdot \rho_{st}}{C_{con} \cdot \rho_{con}} \tag{9.8}$$

where C_{con} is the specific heat, and ρ_{st} and ρ_{con} are the densities of concrete and steel, respectively.

Taking the heat-conducting region in concrete into account, Eqn (9.8) becomes the following equation:

$$h' = \frac{C_{st} \cdot \rho_{st} \cdot S_{st}}{C_{con} \cdot \rho_{con} \cdot S_{con}} \tag{9.9}$$

where S_{st} and S_{con} are the cross-sectional areas of steel and concrete, respectively.

Multiplying Eqn (9.9) by Eqn (9.7), the decreasing ratio of the temperature at the concrete surface, RT_{rc}, can be expressed by taking into account the difference of the heat property between concrete and steel:

$$RT_{rc} = \frac{\Delta T_{st} - \Delta T}{\Delta T} \cdot \frac{C_{st} \cdot \rho_{st} \cdot S_{st}}{C_{con} \cdot \rho_{con} \cdot S_{con}} \tag{9.10}$$

9.5.4 Estimation of the corrosion rate

Because Eqn (9.10) is associated with Eqn (9.6), the relation of both equations is derived as follows:

$$n \frac{C_{co} - C_{st}}{C_{co}} = \alpha \frac{\Delta T_{st} - \Delta T}{\Delta T} \cdot \frac{C_{st} \cdot \rho_{st} \cdot S_{st}}{C_{con} \cdot \rho_{con} \cdot S_{con}} \tag{9.11}$$

Finally, the corrosion rate of rebar can be expressed as:

$$n = \alpha \frac{\Delta T_{st} - \Delta T}{\Delta T} \cdot \frac{C_{st} \cdot \rho_{st} \cdot S_{st}}{C_{con} \cdot \rho_{con} \cdot S_{con}} \cdot \frac{C_{co}}{C_{co} - C_{st}} \tag{9.12}$$

where the coefficient α defines the diffusive distribution of heat and gives the following equation (Yazaki et al., 2012):

$$\alpha = 0.0164c - 0.1 \tag{9.13}$$

where c is the cover depth.

9.6 Applicability of the proposed model

The applicability of the proposed model is examined in comparison with experimental results. Estimated values of the corrosion rate in the measurements at the concrete surface are shown in Figure 9.24. The solid and blank symbols show the cases of full-length corrosion (Section 9.3) and partial corrosion (Section 9.4), respectively. For full-length corrosion and for partial corrosion with a relatively small corrosion rate, the proposed model shows a good agreement with the measured values. However, for partial corrosion with a relatively large corrosion rate, the estimated values are fairly small compared to the measured values. As illustrated in Figure 9.18, the heat could conduct from the noncorroded region of the rebar to concrete over the corroded region. Therefore, the concrete temperature is measured higher than estimated, even with the same corrosion rate, as the heat restrained by the corrosion product is small.

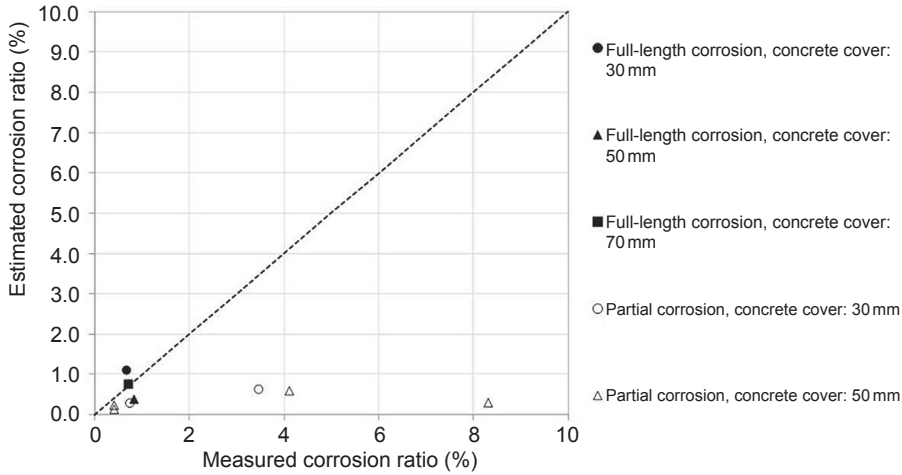

Figure 9.24 Prediction for corrosion rate.

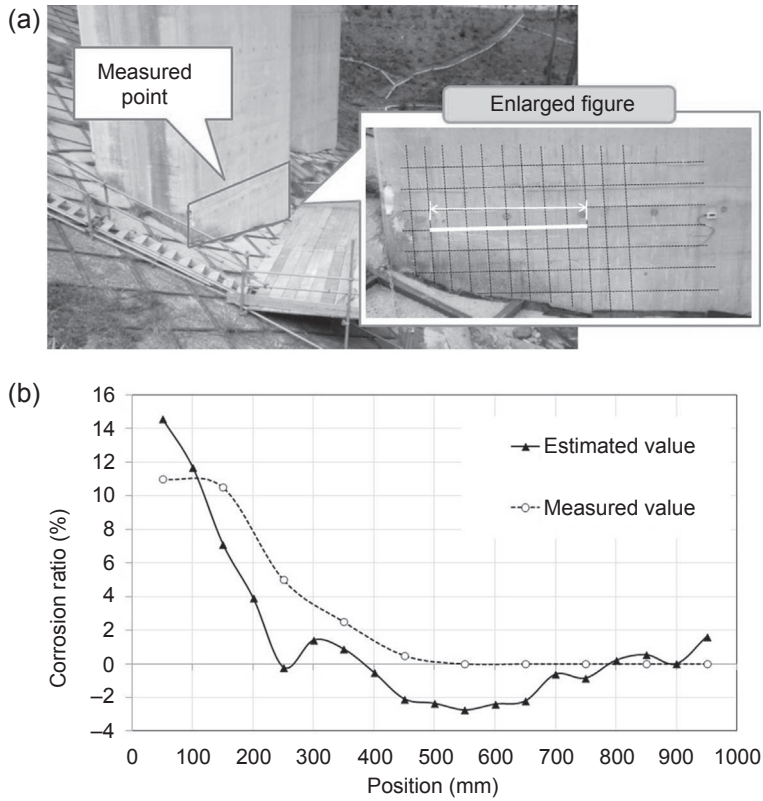

Figure 9.25 Existing RC structure: (a) panoramic view, and (b) prediction for corrosion rate.

An example of on-site measurement is shown in Figure 9.25. A bridge pier of RC structure has been deteriorated by the corrosion of rebars. A picture of the site is given in Figure 9.25(a), and the estimated values of the corrosion rate in the direction of the axis of rebars are compared with the measured values in Figure 9.25(b). The pier was deteriorated in the wide range by salt attack. The distribution of the corrosion rate estimated by the proposed model is in reasonable agreement with that measured.

9.7 Concluding remarks

One promising NDE technique, which can quantitatively estimate the corrosion rate of rebar in RC structures, is presented. The technique is based on the temperature history at the concrete surface, which could change due to the heat conduction from the rebar stored from electromagnetic induction heating.

The temperature at the concrete surface over the rebar increases uniformly due to the heat conduction from the rebar in the case where the heat is applied and stored by electromagnetic heating. If corrosion product exists on the rebar, the temperature

at the concrete surface just over the corroded region of rebar becomes lower than that of the noncorroded region by the effect of the thermal property of the corrosion product.

A model to predict the rate of the corrosion of rebar was presented on the basis of the temperature at the concrete surface. It can be seen that the proposed model has applicability for full-length corrosion of rebar.

9.8 Future trends

The model to predict the rate of the corrosion of rebar has to be improved to allow estimation in the case of partial corrosion. Moreover, the measurement accuracy of the proposed technique has to be improved to enable applying it to many sites where the corrosion of the rebar occurs by salt attack, carbonation, etc. Finally, suggestions for new NDE techniques are expected.

References

Akiyama, T., Takahashi, R., & Yagi, J. (1991). Heat transfer simulation on drying processes of nonfired pellets containing combined water in the moving bed reactor. *ISIJ International, 31*, 24−31.

Akiyama, T., Ohta, H., Takahashi, R., Waseda, Y., & Yagi, J. (1992). Measurement and modeling of thermal conductivity for dense iron oxide and porous iron ore agglomerates in stepwise reduction. *ISIJ International, 32*(7), 829−837.

Akiyama, T., Takahashi, R., & Yagi, J. (1989). Exergy evaluation on the pellets production and direct reduction processes for the fired and nonfired pellets. *ISIJ International, 29*, 447−454.

ASTM C876. (2001). *Standard test method for half-cell potentials of uncoated reinforcing steel in concrete*. Annual Book of ASTM Standards, 452−457.

ASTM G59. (2009). *Standard test method for conducting potentiodynamic polarization resistance measurements*. Annual Book of ASTM Standards.

Osada, F., Yamada, Y., Mushiake, N., & Akamatsu, I. (2004). Development of inspecting method for a defect inside of concrete railway viaduct using thermal image. *Journal of Material, Concrete Structures and Pavement, Japan Society of Civil Engineers, 5−63*(760), 121−133.

Oshita, H., Horie, H., Nagasaka, S., Taniguchi, O., & Yoshikawa, S. (2009). Nondestructive evaluation of corrosion in reinforced concrete by thermal behavior on concrete surface due to electro-magnetic heating. *Journal of Material, Concrete Structures and Pavements (V), Japan Society of Civil Engineers, 65*(1), 76−92.

Yazaki, S., Imai, T., & Oshita, H. (2012). Study on diagnosis nondestructive method of rebar corrosion based on the surface temperature of concrete, the 4th NDI symposium of concrete structure. *Japan Society for Non-Destructive Inspection, 4*, 411−416.

Estimation of concrete strength by the contrast X-ray method

10

M. Takeda, K. Otsuka
Tohoku Gakuin University, Tagajo, Miyagi, Japan

10.1 Introduction

A method for estimating the strength of concrete by the contrast X-ray method, is under development (Takeda & Otsuka, 2012, 2006a; Otsuka & Takeda, 2003). In this method, drilled cores are sliced to 10-mm-thick discs, impregnated with a contrast medium specially developed for concrete, and subjected to radiography to detect fine cracks and voids in concrete. The relationship between the concrete strength and the quantified values of detected cracks and voids (hereafter referred to as transmission dose difference, TDD) is obtained and is applied to estimate the strength of concrete. Originally, the method was applicable only to areas that allow a destructive testing, as it was initially considered necessary to use cores 100 mm in diameter. However, recent experiments have demonstrated that comparable results can be obtained by a semi-destructive testing using small-diameter cores.

Accordingly, the contrast X-ray method is presented with a combination of destructive and nondestructive testing. Thus, the following section describes characteristics of the contrast X-ray method and methods for imaging and determining cracks and voids. Then, the results of the tests are discussed. The relationship between TDD and the concrete strength is derived. The effect of the diameter of cores drilled for semi-destructive testing is discussed, and the state of cracking in concrete structures affected by alkali−silica reaction (ASR) is presented. Possible developments of this technique are discussed as well.

10.2 The contrast X-ray method

Contrast X-ray imaging is a method whereby voids in concrete, such as micro-cracks and early defects, can be detected by impregnating sliced concrete with a contrast medium for concrete. The technique was originally developed by our laboratory. Specifically, 10-mm slices of cores are placed in a container filled with a contrast medium to impregnate the slices, as shown in Figure 10.1. These are removed from the container 60 min later, wiped with a rubber tool to remove the extra medium on the surfaces, and subjected to radiography (see Figure 10.2).

Acoustic Emission (AE) and Related Non-destructive Evaluation (NDE) Techniques in the Fracture Mechanics of Concrete
http://dx.doi.org/10.1016/B978-1-78242-327-0.00010-6
Copyright © 2015 Elsevier Ltd. All rights reserved.

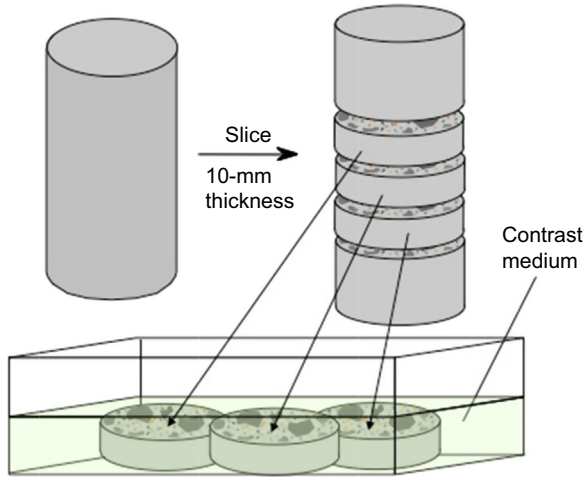

Figure 10.1 Cutting and impregnating method.
Takeda & Otsuka (2012).

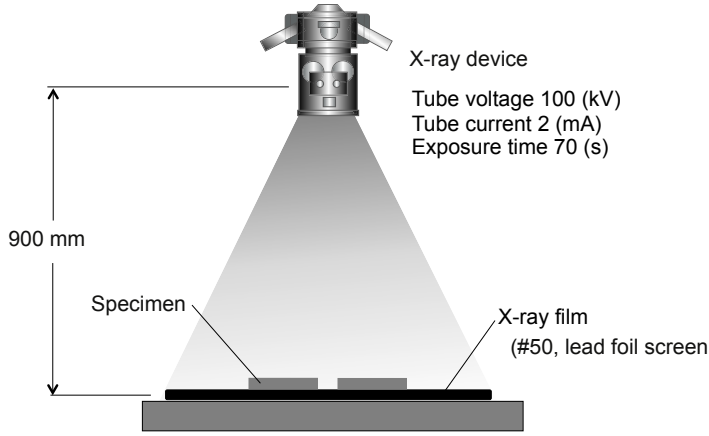

Figure 10.2 Contrast X-ray method.
Takeda & Otsuka (2006a).

Figure 10.3 shows examples of X-ray images (on X-ray film) before and after impregnation with a contrast medium. These specimens were prepared from concrete beams of dimensions 100 × 100 × 400 mm with the initial strength of 48 N/mm^2 and air content of 3%. These were subjected to freezing and thawing tests specified in ASTM C 666 to reduce the relative dynamic modulus up to 40%. The X-ray images before immersion with a contrast medium only show aggregate and large voids, while numerous voids and fine cracks can be clearly observed from the images after

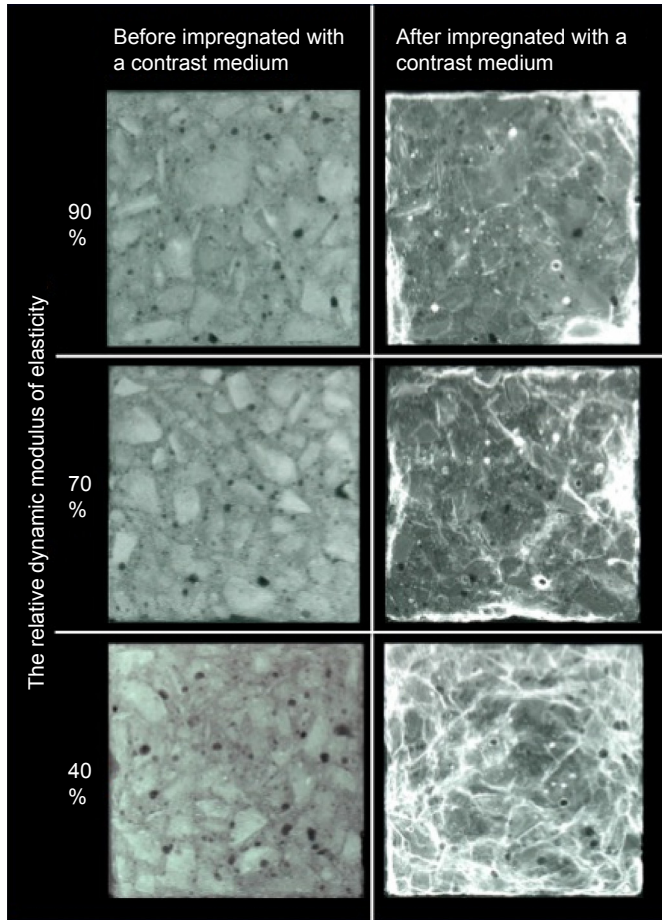

Figure 10.3 Typical X-ray images of specimens with relative dynamic moduli reduced to 90%, 60%, and 40% taken before and after impregnation with the contrast medium for 60 min. Mitsuhiro Takeda & Koji Otsuka (May 23−28, 2010). Detection of cracks in concrete and evaluation of freeze−thaw resistance using contrast X-ray. In *7th International Conference on Fracture Mechanics of Concrete and Concrete Structures & Post-Conference Workshops, Jeju, Korea* (pp. 1129−1135).

immersion. It is confirmed that the contrast X-ray method enables one to detect fine cracks and voids within concrete.

This visualization seems sufficient for qualitative observation of cracking but insufficient for quantitative evaluation. For this reason, it is improved by transferring the images to a PC, using an image intensifier, and processing them for quantification of the amount of cracks and voids.

Figure 10.4 shows the method of taking X-ray images. Specimens are set up under the conditions given in Table 10.1 before and after impregnation with a contrast medium. The X-ray images are processed on a PC via an image intensifier. The gray scale of the obtained images is determined by the number of X-ray photons passing through specimens and reaching the detector (transmission dose). In other words, the X-ray transmission dose increases with air voids and cracks because a low absorption coefficient increases. When an X-ray film is used as the detector, these areas look black. Conversely, the gray scale tends to be more transparent at areas of material with a high absorption coefficient as a contrast medium. In the case of concrete with many voids, where the medium penetrates as the example shown in Figure 10.3, the X-ray film before impregnation becomes darker, and after impregnation it becomes whiter (when an image intensifier is used as the detector, the gray scale is reversed). Air voids and fine cracks in concrete could be quantified by determining the difference

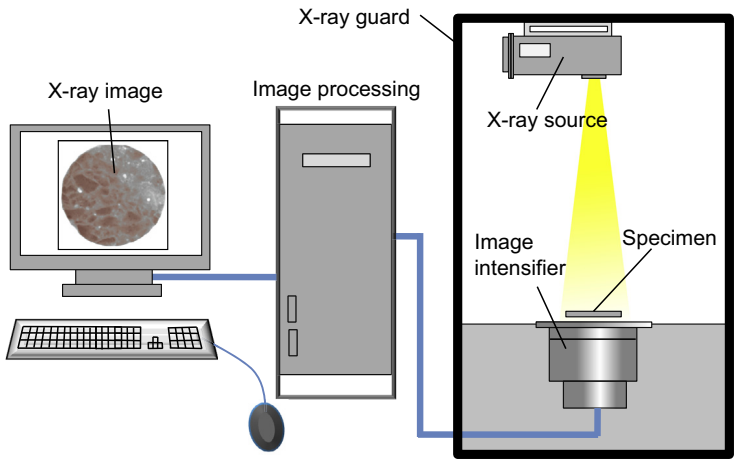

Figure 10.4 State of taking X-ray method.
Takeda & Otsuka (2012).

Table 10.1 Conditions of contrast X-ray method

X-ray source (Toshiba I-311)	Tube voltage	50 (kV)
	Tube current	100 (mA)
	Focus dimensions	0.1 × 0.1 (mm)
	Focal distance	515 (mm)
Image intensifier	Toshiba 6-inch I/I	6 (inch)

Mitsuhiro Takeda & Koji Otsuka (2012). Development and application of a method of evaluating properties of concrete by contrast radiography. *Journal of Materials Concrete Structures and Pavements*, *68*(3), 146−156.

between the transmission doses before and after impregnation of concrete with a contrast medium (TDD).

For determining TDD, it is necessary to determine the X-ray transmission dose. The density of the transmission images is determined by the X-ray transmission dose on the image intensifier, and thus, it is expressed in terms of standard optical density after transferring onto a PC, as follows:

$$D = \log(1/T),$$

where D is the standard optical density and T is the transmissivity.

Note that the central circles 80, 50, and 20 mm in diameter were selected in the experiments of specimens 100, 70, and 40 mm, respectively, as the areas of measurement in consideration of the effect of core drilling.

10.3 Test results

10.3.1 Concrete strength versus TDD relationship

With a variety of mixture proportions, cylindrical concrete specimens of 100-mm diameter and 200-mm height were made and then subjected to the contrast X-ray test to determine the relationship between TDD and the concrete strength.

These mixes consisted of ordinary Portland cement, high-early-strength Portland cement, and cement replaced 50% by blast-furnace slag. Coarse aggregate was crushed stone with the maximum size of 20 mm, saturated surface-dry (SSD) density of 2.66 g/cm^3, and water absorption of 2.12%. Two kinds of fine aggregate were sand A with an SSD density of 2.62 g/cm^3 and water absorption of 1.89%, and sand B with an SSD density of 2.36 g/cm^3 and water absorption of 5.10%. An air-entraining admixture (alkyl ether-type anionic surfactant) was used as a chemical admixture. To simulate deteriorated conditions, the water−cement ratios (*W/C*) and air content ranged between 40% and 90% and 2% and 7%, respectively. Concrete specimens were cured either in water or in air. In the case of water curing, specimens were de-molded 1 day after cast and immersed in a curing tank at 20 °C for 28 days. For air curing, specimens were left in air in a thermo-hygrostatic room at 20 °C and 60% RH for 28 days after cast. Three specimens for the compressive strength and three for the contrast X-ray test were fabricated for each of 39 types, of which strengths eventually range from 9.3 to 54.9 N/mm^2. The number of specimens is 234 in total.

For the contrast X-ray method, three specimens were cut into discs 10 mm in thickness using a wet diamond cutter and kept in a thermo-hygrostatic room at 20 °C and 60% RH for 24 h before tests. Only three mid-height discs were used to minimize the effect of bleeding after placing, and the averages of the measurement results of nine discs were analyzed.

Figure 10.5 shows the relationship between the strength and TDD obtained from the 39 types of concrete specimens. This figure reveals that the compressive strength

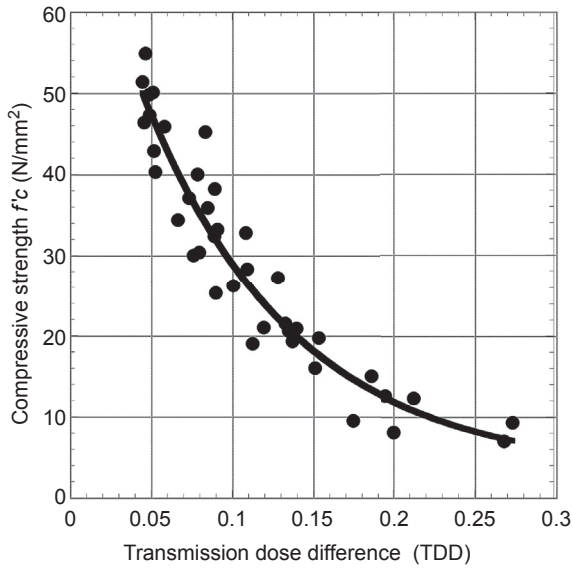

Figure 10.5 Relationship between *f'c* and transmission dose difference (TDD). Mitsuhiro Takeda & Koji Otsuka (May 23−28, 2010). Detection of cracks in concrete and evaluation of freeze−thaw resistance using contrast X-ray. *In 7th International Conference on Fracture Mechanics of Concrete and Concrete Structures & Post-Conference Workshops, Jeju, Korea* (pp. 1129−1135).

tends to decrease as the TDD value increases. Though the results of air-cured specimens tend to be plotted slightly above the regression curve, no appreciable differences are observed among the cement types, water absorptions of fine aggregate, and air contents. The fact that the correlation coefficient was 0.954 suggests that the materials, mixture proportions, and curing conditions have no appreciable effect on this relationship. Note that the amount of voids is defined as being equal to the TDD values here. A strong correlation is known to exist between the amount of voids and the concrete strength as proposed by A. N. Talbot, known as the principle of cement−void ratio. Also, the relationship between the strength and TDD presents a strong correlation. The concept that TDD determined by the contrast X-ray imaging is equivalent to the amount of voids in concrete is, therefore, confirmed.

10.3.2 Effect of core size on the strength estimation

It is necessary to consider the effect of core sizes when drilling concrete cores at the jobsite to estimate the strength by the contrast X-ray method. Since the present test intends to estimate the void distribution for determination of the strength of concrete *in situ*, wall-shaped specimens were fabricated, and cores of different sizes (100, 70, and 40 mm) were drilled from the same levels and subjected to contrast X-ray imaging to examine the distribution of voids (TDD) from the surface inward. The effect of core sizes on the strength estimation was directly examined by the compression test. For 40-mm cores, two samples were drilled at the same level, and the averaged value was taken into account to minimize the scatter.

Table 10.2 Mixture proportion of concrete

G_{max} (mm)	Slump (cm)	*W/C* (%)	Air (%)	s/a (%)	Concrete composition (Kg/m^3)				
					W	C	S	G	Ad.
20	15	60	5.5	44	180	300	725	975	0.17

W, water, C, cement, S, sand, G, gravel.
Mitsuhiro Takeda & Koji Otsuka (May 23–28, 2010). Detection of cracks in concrete and evaluation of freeze–thaw resistance using contrast X-ray. In *7th International Conference on Fracture Mechanics of Concrete and Concrete Structures & Post-Conference Workshops, Jeju, Korea* (pp. 1129–1135).

Table 10.2 gives the mixture proportion of concrete used for the tests. Concrete was placed in a wall-shaped wooden formwork of dimensions measuring 600 × 300 × 1400 mm and cured by retaining the formwork for 1 week, with water ponding on the top surface. After removal from the formworks, the specimens were exposed to air outdoors. The 28-day strength of the cylinder specimens (100-mm diameter and 200-mm height) prepared was 28 N/mm^2. Figure 10.6 shows the specimen size and the drilling core position.

Figure 10.7 shows the distribution of void amount (TDD) determined in 100-mm cores drilled with the depths of 150, 715, and 1280 mm from the placement surface. The TDD values are large, representing low strength, only in the surface area (from the surface to the depth around 10 mm), whereas the TDD values are nearly constant at 20 mm and deeper. The large TDD values near the surface could be attributed to

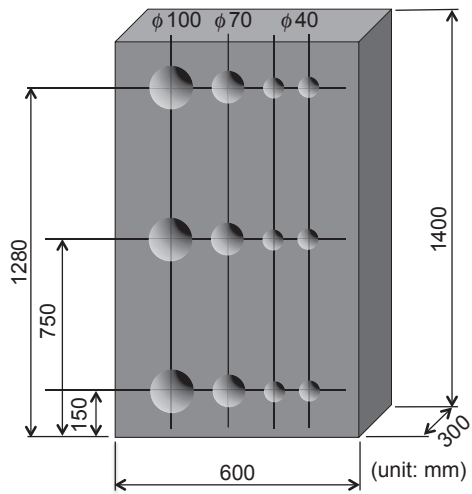

Figure 10.6 Specimen size and the drilling core position.
Mitsuhiro Takeda & Koji Otsuka (May 23–28, 2010). Detection of cracks in concrete and evaluation of freeze–thaw resistance using contrast X-ray. In *7th International Conference on Fracture Mechanics of Concrete and Concrete Structures & Post-Conference Workshops, Jeju, Korea* (pp. 1129–1135).

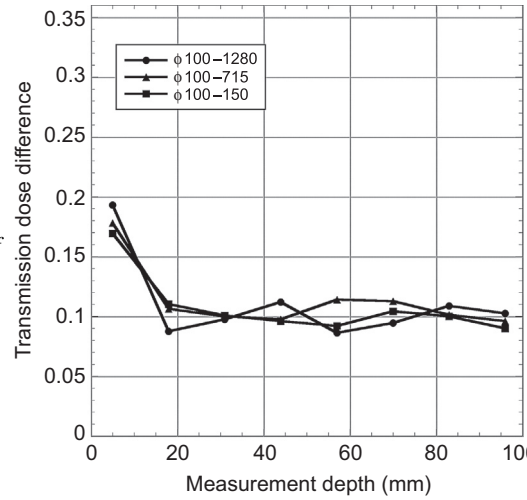

Figure 10.7 Relationship between transmission dose difference and measurement depth (100-mm core). Mitsuhiro Takeda & Koji Otsuka (May 23−28, 2010). Detection of cracks in concrete and evaluation of freeze−thaw resistance using contrast X-ray. In *7th International Conference on Fracture Mechanics of Concrete and Concrete Structures & Post-Conference Workshops, Jeju, Korea* (pp. 1129−1135).

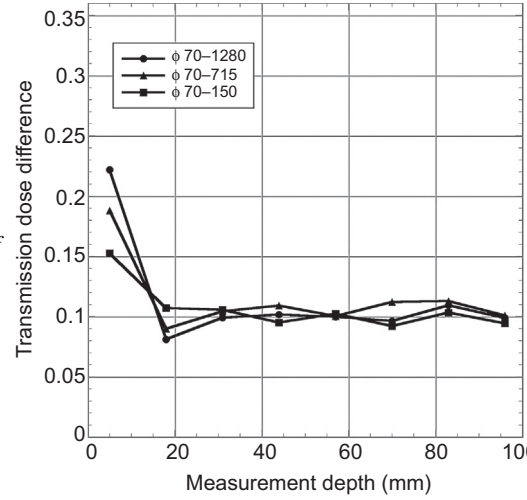

Figure 10.8 Relationship between transmission dose difference and measurement depth (70-mm core). Mitsuhiro Takeda & Koji Otsuka (May 23−28, 2010). Detection of cracks in concrete and evaluation of freeze−thaw resistance using contrast X-ray. In *7th International Conference on Fracture Mechanics of Concrete and Concrete Structures & Post-Conference Workshops, Jeju, Korea* (pp. 1129−1135).

the effect of bleeding along the formwork. The larger the *W/C* ratios, the larger the TDD values, as observed at the higher placement level. Therefore, the strength at 20 mm deeper inward is constant with little scatter. The concrete strength estimated from the average TDD was 28.5 N/mm^2, excluding the surficial core data at the depth of 10 mm.

Figures 10.8 and 10.9 show the distribution of TDD by the contrast X-ray method in 70- and 40-mm cores drilled at the positions of 150, 715, and 1280 mm from the surface. In the case of 70-mm cores, the scatter of TDD of the surface layer is larger than

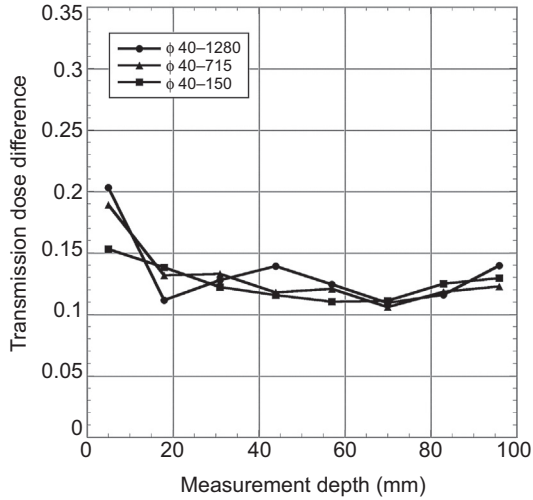

Figure 10.9 Relationship between transmission dose difference and measurement depth (40 mm core, result of using the wall-shaped specimen).
Mitsuhiro Takeda & Koji Otsuka (May 23−28, 2010). Detection of cracks in concrete and evaluation of freeze−thaw resistance using contrast X-ray. In *7th International Conference on Fracture Mechanics of Concrete and Concrete Structures & Post-Conference Workshops, Jeju, Korea* (pp. 1129−1135).

that of 100-mm cores, but the trend of constant values is the same as that of 100-mm cores. In the case of 40-mm cores, however, the TDD values at the deep areas tend to be 1.22 times larger than those of 100- and 70-mm cores. Although the scatter was taken into account by averaging two cores, results are scattered widely. This may be because small-diameter cores are more sensitive to voids and early defects present or absent in each core, resulting in larger differences from one core to another. It is known that concrete placed at the deeper level becomes denser due to the gravity effect, which is clearly observed in Figures 10.7−10.9.

Accordingly, when determining the void distribution by the contrast X-ray method using 40 mm cores, the void amounts tend to be evaluated as being greater than the case of using 70 and 100 mm cores. However, all three sizes of cores accurately represent the state of void distribution within each core. As to strength estimation, the strength of concrete can be determined from the TDD-strength relationship when using 70 and 100 mm cores. When cores 40 mm in diameter are used, the strength can be accurately estimated by multiplying the results by 1.22.

10.3.3 Void properties of ASR-deteriorated concrete

Numerous concrete structures are damaged by ASR in Japan. In most cases, ASR is suspected after map cracks or cracks along the reinforcement become visible at the surfaces of concrete structures. After detailed investigation, the judgment of ASR is eventually made. In the case that cracking due to ASR is recognized at an early stage,

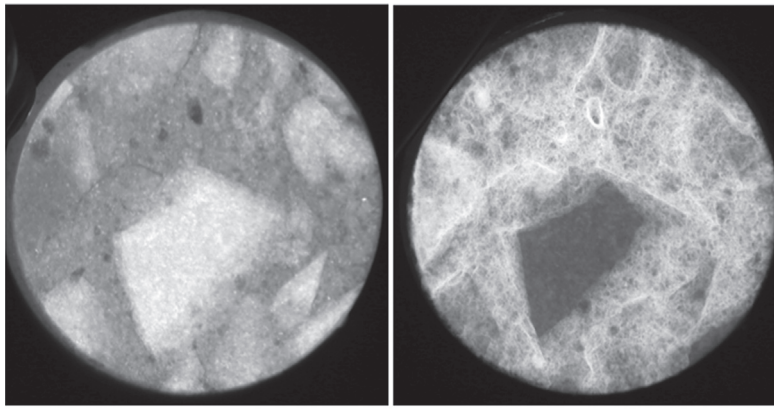

Figure 10.10 Cracks in alkali−silica reaction-deteriorated concrete.
Mitsuhiro Takeda & Koji Otsuka (May 23−28, 2010). Detection of cracks in concrete and evaluation of freeze−thaw resistance using contrast X-ray. In *7th International Conference on Fracture Mechanics of Concrete and Concrete Structures & Post-Conference Workshops, Jeju, Korea* (pp. 1129−1135).

several measures to suppress the crack propagation should be attempted before cracking becomes detrimental. To this end, cores are usually taken out of ASR-deteriorated concrete structures. Thus, the contrast X-ray method is available for examining the TDD values.

Structural members from which cores in 40-mm diameter were drilled from three different piers of a bridge that had been judged as being ASR-deteriorated through detailed investigation.

Figure 10.10 shows transfer images (X-ray films) of ASR-deteriorated concrete before and after impregnation with a contrast medium. Numerous fine cracks are found to occur near aggregate particles on the image after impregnation, whereas they are not recognized on the image before impregnation.

Figure 10.11 shows the relationship between the TDD values determined by the contrast X-ray method and the depths from the surface in cores drilled from three bridge piers. For comparison, one datum from a structure unaffected by ASR is shown. It is clearly observed that the TDD values in two piers are extremely large and even larger than those at the surface layer. In the other pier, the TDD values at the surface layer are larger than those at deeper areas as observed in Figures 10.6−10.8. This pier is exposed to rainwater, where water supply from the surface layers may have caused expansion particularly near the surfaces.

The TDD profiles of concrete, in which ASR begins to occur, tend to vary significantly in a zigzag manner, which may allow early detection of ASR. Note that strength estimation of ASR-deteriorated concrete by the contrast X-ray was not applicable because of the extremely large scatters of the TDD values. This issue requires further investigation.

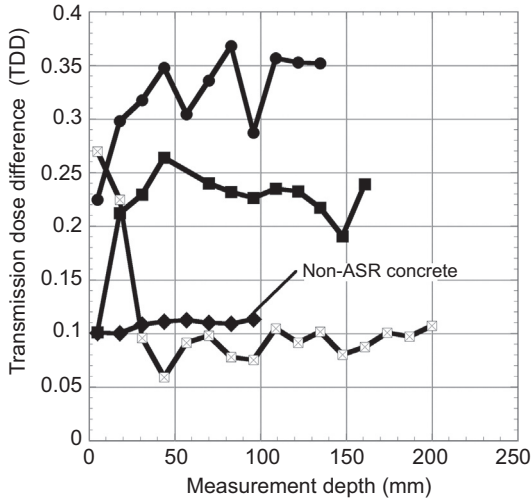

Figure 10.11 Relationship between transmission dose difference and measurement depth (40-mm core, result of using the structure which degraded by ASR).

10.4 Conclusions

The contrast X-ray method is presented and is proven to be applicable to small-diameter cores. The following results are summarized from tests of the semi-destructive method:

1. The void distribution and the strength of concrete can be estimated by the contrast X-ray method using 10-mm slices of drilled cores. The deterioration profile can, therefore, be examined in the depth direction from the surface.
2. By the contrast X-ray method, the strength can be estimated based on the relationship between the strength and the determined TDD values when using 70-mm or 100-mm cores. When the core size is 40 mm, the test values tend to be lower, but the strength can be estimated by multiplying the test values by a correction factor of 1.22.
3. Investigation into ASR-deteriorated concrete shows that the void properties are widely varied along the depth from the surface when compared with sound concrete. This characteristic suggests the possibility of detecting ASR at an early stage by the contrast X-ray method.

10.5 Future trends

The contrast X-ray method is a technique of visual and quantitative evaluation based on images obtained by X-ray transmission imaging of concrete impregnated with a contrast medium. It is possible to detect the state of cracking inside concrete with X-rays by injecting a contrast medium into cracks. In the case of thicker members, an X-ray apparatus with higher energy and longer exposure time is necessary.

As discussed here, the application of the contrast X-ray method is promising as a semi-destructive method in order to estimate the concrete strength and to determine the deterioration depth by slicing small-diameter cores drilled on site and taking contrast X-ray images in a laboratory.

This method is also available for characterizing deterioration phenomena due to liquids (e.g., freezing and thawing action), as concrete is impregnated with a liquid referred to as a contrast medium and then cracks and voids filled with this liquid are quantified. It is already known that the TDD values are well correlated with the relative dynamic modulus and scaling of concrete deteriorated by freezing and thawing (Takeda & Otsuka, 2006b). It is, therefore, considered possible to evaluate the resistance of concrete to frost damage by determining the TDD values.

Future development may include three-dimensional observation of the void structure in small-diameter concrete cores impregnated with a contrast medium, instead of sliced cores, using a computed tomography. In addition, this method is applicable to evaluation of not only deteriorated concrete but also newly built concrete. Quality of concrete widely varies, depending on mixing, transportation, placing, and curing. Currently, it is regarded as being acceptable if the strength and air content requirements are satisfied. These are readily estimated by the present method. If the durability of a newly built concrete structure poses a problem based on the evaluation of the initial properties, testing on small-diameter cores has become feasible.

References

Otsuka, K., & Takeda, M. (2003). Detection of fine cracks by X-ray technique using contrast medium in concrete. *Concrete Library International, 42*, 121−136, 12.

Takeda, M., & Otsuka, K. (2006a). Estimation of concrete strength by X-Ray technique with contrast medium. *Journal of Materials, Concrete Structures and Pavements, 62*(2), 376−384.

Takeda, M., & Otsuka, K. (2006b). Quantification of concrete degradation and evaluation of freeze-thaw resistance using X-Ray technique with contrast medium. *Journal of Japan Society of Civil Engineers, Ser. E, 62*(3), 728−738.

Takeda, M., & Otsuka, K. (2012). Development and application of a method of evaluating properties of concrete by contrast radiography. *Journal of Materials, Concrete Structures and Pavements, 68*(3), 146−156.

Low-level acoustic emission (AE) in the long-term monitoring of concrete

11

P. Ziehl, M. ElBatanouny
University of South Carolina, Columbia, SC, USA

11.1 Introduction

Acoustic emission (AE) is the term used to define transient stress waves emitted from the sudden release of energy due to a deformation in the monitored material, such as crack formation or growth (ASTM E1316 2013; Pollock, 1986; Ziehl, 2008). As a passive piezoelectric sensing technique, which does not need excitation or human intervention after the sensors are connected to the data acquisition system, AE is suitable for real-time long-term monitoring of structures. AE sensors are very sensitive (in the kHz), which enables them to detect active cracks long before they are visible (micro-cracks).

Reinforced concrete (RC) structures are widely used in the construction of infrastructure including buildings, highway bridges, hydraulic structures, and nuclear power plants. However, concrete is susceptible to different material degradation mechanisms due to its heterogeneous nature, including corrosion of reinforcement, sulfate attack, alkali−aggregate reaction (AAR), freeze−thaw cycling, leaching, radiation, elevated temperatures, salt crystallization, and microbiological attack (Clifton, 1991). Additionally, under service loading conditions, concrete structures are usually designed as cracked sections due to the low-tensile strength of concrete. Most of the aforementioned degradation mechanisms, such as corrosion and AAR, take years to progress and are associated with formation of micro-cracks. The sensitivity of AE can be used to monitor the progression of these degradation mechanisms that will create AE activity with low-amplitude and level, referred to here as low-level AE.

11.2 Damage mechanisms for which low-level acoustic emission (AE) is needed

Low-level AE generates from formation of micro-cracks within concrete structures. These cracks can form as a result of material degradation mechanisms or load-induced damage. This section provides examples of degradation mechanisms that produce low-level AE.

11.2.1 Alkali−silica reaction

Alkali−silica reaction (ASR) is a material degradation mechanism that occurs in concrete structures. ASR is a chemical reaction occurring between the reactive siliceous

Acoustic Emission (AE) and Related Non-destructive Evaluation (NDE) Techniques in the Fracture Mechanics of Concrete
http://dx.doi.org/10.1016/B978-1-78242-327-0.00011-8
Copyright © 2015 Elsevier Ltd. All rights reserved.

aggregate particles and hydroxyl ions of the pore solution in hardened concrete (Saouma, Perotti, & Shimpo, 2007). The reaction product is a gelatinous material that swells when moisture is absorbed and can cause expansion and cracking in concrete structures. The reactive silica is normally an amorphous material (lack of long-range order at the atomic level), such as chert and acidic volcanic glass, or a material whose original ordered molecular structure has been destroyed, such as strained quartz. The high concentration of hydroxyls (high pH value) typically found in the pore solution of Portland cement concrete is a result of, and is maintained by, the release of alkali ions (potassium and sodium) from the hydration of Portland cement. The product gel is also amorphous and normally contains silicon, alkalis, calcium, and water. Three conditions must be present for deleterious ASR to occur: (1) high hydroxyl ion concentration in the pore solution of the concrete, usually due to the high alkali content of Portland cement; (2) reactive siliceous aggregate; and (3) available moisture (Stark, Morgan, & Okamoto, 1993).

ASR is a localized reaction. The degree of reaction and the extent of subsequent deterioration may vary from location to location in the same concrete structure, depending on the localized composition of the pore solution, characteristics of each reactive aggregate particle, and the configuration of the structure. The composition and quality (permeability) of the concrete are generally the controlling factors for determining the likely severity of ASR. ASR also depends on many external factors such as relative humidity, temperature, drying and wetting, freezing and thawing, and restraint of the structure.

The expansion of the gel from ASR generates pressure within the concrete and produces micro-cracking when the tensile strength of the concrete is exceeded, which results in low-level AE. Water can infiltrate into the concrete through the cracks and cause additional gel expansion, which could lead to more cracking and potentially spalling of the concrete (Figure 11.1).

The continued development of cracks due to ASR undermines the structural integrity of the concrete. Specifically, the cracks provide a path to the steel reinforcement, which can lead to corrosion and strength loss of the concrete elements. In extreme cases, the expansion due to ASR could lead to yielding of the steel reinforcement and limit

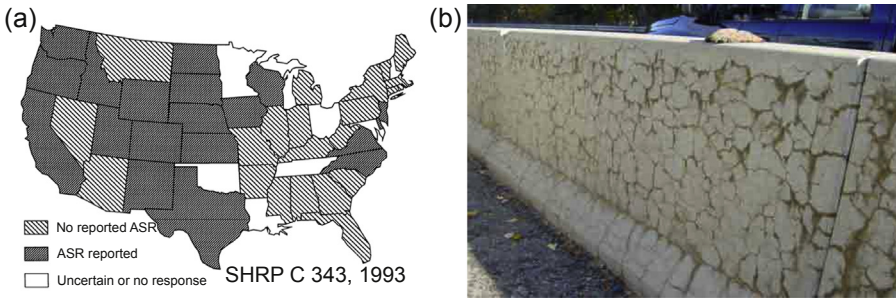

Figure 11.1 (a) Map of states with ASR degradation (Stark et al., 1993), and (b) example of ASR-induced cracks (NRC IN 2011-20).

the performance of the structure. ASR is currently affecting several structures across the United States, as shown in Figure 11.1, and Canada, especially British Columbia. Washington State Department of Transportation indicates that they have more than 150 structures that may be affected by ASR, while British Columbia, Canada, may have more than 125 structures affected with ASR (Shrimer, 2005). A concrete structure at the Seabrook Nuclear Power Plant was also found to be affected by ASR in 2010 (NRC IN 2011-20).

11.2.2 Corrosion of reinforcement

Corrosion of reinforcement is the main degradation mechanism in RC structures, especially in coastal areas or areas where de-icing salts are used (ElBatanouny, Mangual, Ziehl, & Matta, 2010). The alkalinity of concrete, where a pH of ~13 may be found, protects steel by passivation through a resistant oxide film that surrounds the reinforcement. Corrosion of the steel reinforcement may occur at pH levels of 11 and lower. In the presence of chlorides, the pH may reach a value of 8, creating the worst case scenario for corrosion (Austin, Lyons, & Ing, 2004). Corrosion is an irreversible process; the degree of damage and cost of maintenance increase with time, which may ultimately lead to replacement of corroded parts.

The main problem with chloride-induced corrosion is that not only the mechanical strength of the steel reinforcement is reduced, but also the corrosion product exerts stress into the concrete structure, producing cracks that deteriorate the steel–concrete bond, which directly affects serviceability performance. When a rebar starts to corrode, a gradual decrease of its diameter is produced, together with the generation of an oxide of higher volume than that of steel. The unit volume of the final corrosion product $Fe(OH)_3 \cdot 3H_2O$ is as large as six and a half times the original Fe volume (Li, Li, Zdunek, Landis, & Shah, 1998). This expansion exerts pressure on the surrounding material, leading to micro-cracks that generate low-level AE. Eventually, surface longitudinal and transverse cracks will form, which may lead to concrete spalling as shown in Figure 11.2. The steel reinforcement bond is also weakened due to the high porosity of the corrosive product around the steel. In addition, corrosion decreases the cross-sectional area of the steel strands, minimizing their ductility and increasing stress concentrations at the reinforcement interface (Yoon, Weiss, & Shah, 2000).

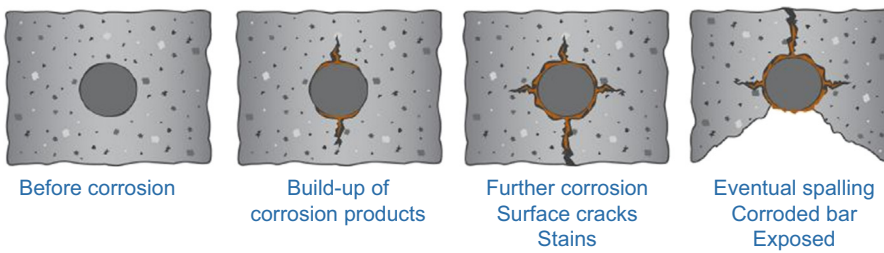

Figure 11.2 Corrosion process in concrete (http://concrete-forum.com/).

11.2.3 Corrosion of pre-stressing strands

Corrosion-induced degradation affects the durability of pre-stressed concrete (PC) structures in much the same way: it (1) reduces the cross-section of the pre-stressed reinforcement, thereby, decreasing the load-bearing capacity and (2) degrades the integrity of the surrounding concrete (Jaffer & Hansson, 2009). The longitudinal cracks created along the reinforcement after the expansive product is formed may affect the load-bearing capacity of the components undergoing this distress, resulting in a decrease of service life of the structure (ElBatanouny et al., 2010).

Awareness of the potential for corrosion damage in PC and post-tensioned concrete (PT) has increased due to sudden failures of a number of highway bridges, including the St. Stefano bridge in Italy (Darmawan & Stewart, 2007), the Lakeview Drive Bridge in Pennsylvania (Harries, 2006), a pedestrian bridge in Concord, NC (Sly, 2001), and the Ynys-y-Gwas Bridge, UK, in 1985 (Trejo, Pillai, Hueste, & Reinschmidt, 2009). The high level of stress in pre-stressing strands makes the corrosion concern more significant in such systems. Stress corrosion cracking may take place in the pre-stressed strands due to this high level of stress, about $0.54\,f_{pu}$ (147 ksi) in post-tensioned (Naaman, 2004) and $0.75\,f_{pu}$ (202.5 ksi) in PC. The manufacturing process and the geometrical shape of the strands also make them more susceptible to crevice corrosion, a localized corrosion type that can decrease the capacity of the strands significantly in a short time period. Major differences exist between the different types of structural concrete, namely passively reinforced, pre-stressed, and post-tensioned. Yet, it is customary to view corrosion phases in all reinforcement types as similar because they lie in similar environments. However, the causes of corrosion and the resulting damage will differ due to differences in geometry and manufacturing processes between passive rebars and pre-stressing strands. Additionally, corrosion initiation in pre-stressing strands happens at a lower chloride concentration as compared to steel rebars (Moser, Singh, Kahn, & Kurtis, 2011).

11.2.4 Load testing prior to visible cracking

Load tests are widely used to evaluate the condition of aging for in-service structures and sometimes for new structures. The low-tensile strength of concrete materials makes it susceptible to cracking under service loads when passive reinforcements are used. For PC and PT structures, the pre-stressing force inhibits the formation of cracks under service loads, for instance, Class U PC (ACI 318, 2011). Therefore, loading the structure to service load levels will lead to growth in the cracks already formed during the load history of RC structures, while in PC structures, micro-cracks may form. In either case, loading the structure up to service loads will result in low-level AE.

11.2.5 Analysis of damage due to seismic events

Seismic events are usually resisted by pile foundations in highway bridges, whereas columns and/or shear walls typically resist lateral loads in buildings. For both systems, the primary load is axial compression load due to the dead load of the structure in

addition to the live load. Therefore, under primary service loads, cracking is not expected, and no AE waves should generate. During seismic events, cracks may generate in the structure if the tensile strength of the concrete is exceeded, which will generate AE waves. Although severe cracking may occur, the duration of seismic events, typically less than 1 min, qualifies AE activity from seismic events as low-level AE. The use of AE damage detection algorithms in such cases will be extremely beneficial in determining the condition of monitored structures after a seismic event.

11.3 Damage mechanisms for which low-level AE is not appropriate

11.3.1 Load testing beyond visible cracking

Current available load test methods, such as the monotonic load test method proposed by ACI 318 (2011) and the cyclic load test (CLT) method proposed by ACI 437 (2012), require loading the structure between 80% and 90% of its nominal capacity. The high load level during such tests will often cause very significant visual cracking in the structure. In such cases, AE activity cannot be considered as low-level AE because a vast amount of high-amplitude AE hits will generate during the opening and growth of visual cracks. Figure 11.3 shows results of a load test on a medium-scale PC beam before and after visual cracks. As can be seen, most of the AE activity before visual cracking is between 60 and 75 dB and has low signal strength, whereas after visual cracking, the number of hits with amplitude exceeding 75 dB increases significantly along with the signal strength of AE hits.

11.3.2 Bridges in service with severe degradation

In-service bridges with severe degradation are not appropriate for low-level AE monitoring. The superstructure in bridges is loaded under fatigue, due to the continuous

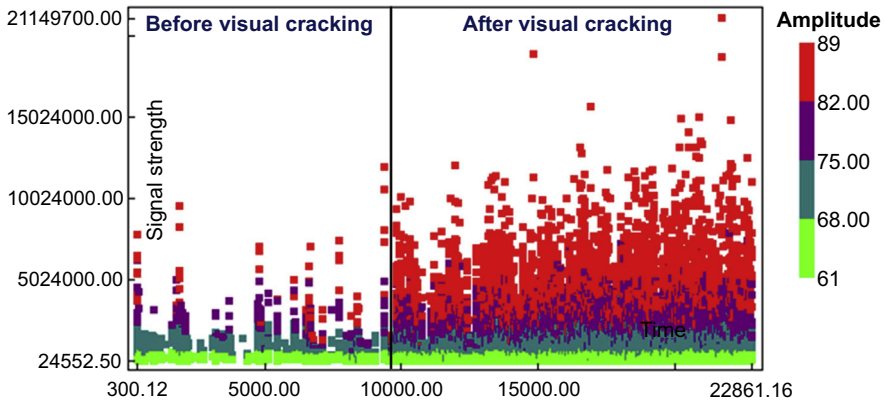

Figure 11.3 AE activity before and after visual cracking.

passage of cars and trucks. Therefore, existing cracks will grow when the structure is being loaded while friction between cracked surfaces will occur when the structure is unloading. This will generate high AE activity during both phases, loading and unloading, making it difficult to classify the data as low-level AE.

11.4 Separation of noise from data of interest

While the AE technique provides several advantages for real-time remote monitoring of in-service massive concrete structures with a minimal number of sensors, filtering techniques to differentiate genuine AE data from wave reflections and noise are a significant challenge. The sensitivity of the method makes it vulnerable to collecting data from mechanical noise, wave reflections (especially in small-scale structures or laboratory specimens), as well as environmental containments, such as rain, hail, or sand. Electrical noise can also generate non-genuine AE data; however, this type of noise can easily be reduced by checking the electrical connections.

The effect of wave reflections and background noise on the AE data can be minimized by setting up AE filters, which effectively reject signals having noise characteristics. Front-end filters are generally used for this purpose by setting values for peak definition time, hit definition time, and hit lockout time. If noise remains in the recorded signals, postprocessing tools for noise discrimination are used to clean the recorded signals. These filters can be produced using single parameters, such as amplitude, peak frequency, or frequency centroid, or by using the relationship between two parameters, such as rise time and amplitude. One of the common filters for postprocessing uses the relationship between the duration and amplitude of the AE signals. This filter is referred to as duration−amplitude (D−A) filter, and a variant of this approach is the Swansong II filter (ElBatanouny, Larosche, et al., 2014; Tinkey, Fowler, & Klingner, 2002). The limits of these types of filter are set through visual inspection of AE waveforms. Table 11.1 shows an example of filters developed during laboratory load tests of concrete beams. A demonstration of the effectiveness of previously developed filtering techniques is shown in the source location, Figure 11.4.

Table 11.1 Data rejection limits for AE filters

D−A filter		R−A filter	
Amplitude (dB)	**Duration (μs)**	**Amplitude (dB)**	**Rise time (μs)**
60−67	>2000	60−67	>300
68−75	>4000	68−75	>450
76−83	>6000	76−83	>600
84−91	>8000	84−91	>750
92−100	>10,000	92−100	>900

Source: ElBatanouny, Ziehl, et al. (2014)

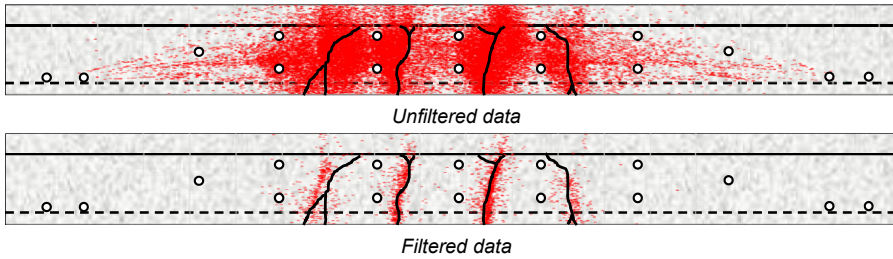

Figure 11.4 Source location using AE data during a load test (Abdelrahman, ElBatanouny, & Ziehl, 2014).

11.5 Special considerations for wireless sensing

AE systems have been steadily developing over the past decades to become affordable and deployable. Currently, a self-powered wireless AE system is commercially available through Mistras Group, Inc. These advantages make AE suitable for remote/real-time/rapid inspection of massive structures using a minimal number of sensors. The node has the ability to collect data from parametric inputs and four AE sensors, which enables source location capability. The node reduces the data transferred wirelessly by sending the waveform parameters without including the waveforms. The waveforms are saved on an SD card that is attached to the node for more detailed signal processing. This data reduction technique enables the system to process and send data wirelessly in real time and reduces the possibility of data loss due to insufficient buffer.

The wireless node has significant advantages. However, the capacity of data collection of the wireless system is less than that of wired systems. While this inhibits the ability of wireless systems to be used when high data collection capacity is needed, this makes wireless AE systems particularly suitable for low-level AE. The main consideration with using wireless systems is the application of AE-based damage evaluation mechanisms that were primarily developed based on the use of wired AE systems.

11.6 Case studies

11.6.1 Alkali–silica reaction

The ability of AE to detect ASR degradation was recently investigated in two studies (ElBatanouny, Jones, & Ziehl, 2014; Pour-Ghaz, Spragg, Castro, & Weiss, 2012). Pour-Ghaz et al. (2012) investigated the ability of AE to detect ASR earlier than conventional standardized methods such as length change tests. A number of mortar specimens having a cylindrical shape were created with different diameters. Reactive fine aggregates, with a 0.1% expansion after 3 days when tested using ASTM C1260 (2007), were used. The specimens were immersed in a NaOH solution according to ASTM C1260 at a temperature of 38 ± 1 °C. The top and bottom surfaces were sealed

with water-resistant epoxy to ensure moisture and ion ingress through the sides. The length change (expansion) of the specimens was measured along with continuous AE measurements using broadband sensors. Since the specimens were completely immersed, a stainless-steel wave guide was attached to the specimens and the AE sensors attached to it. The test setup is shown in Figure 11.5.

The AE and length change results with respect to time for one specimen are shown in Figure 11.5. Results showed the ability of AE to detect micro-cracks forming in the aggregate early in the reaction (first 5 days) as indicated by cumulative AE energy. This was hypothesized since little to no matrix cracking was observed during this period as indicated by limited optical microscopy results. Note that at 5 days, no expansion was observed. The cumulative AE energy had a sharp increase at around 11 days in the test, which was accompanied by an increase in the expansion of the specimen. This limited study demonstrates the potential for linking AE results to expansion resulting from ASR. After around 20 days in the reaction (0.06% expansion) a decrease in the rate of AE data was observed. This was not formally investigated but may be attributed to cracking and deposition of ASR gel at the interface between the waveguides and the specimen that leads to loss of contact among other potential factors.

The results of this study demonstrate the ability of AE to detect micro-cracks forming as a result of ASR. However, the use of steel waveguides may have affected the AE results. Because the ASR is expansive, gaps may form between the waveguides and the surrounding mortar material as the reaction progresses. Even if gaps do not exist, the pressure between the waveguides and the surrounding material will change as the surrounding material cracks, thereby affecting the AE signals transferred to the waveguides. Additionally, the use of waveguides causes unwanted complications in drilling and tapping, setting, etc., for *in situ* evaluation of field structures.

ElBatanouny, Jones, et al. (2014) reported the results of an experimental test including 12 specimens with dimensions of $3 \times 3 \times 11.25$ inches according to ASTM C1293 in addition to three control specimens. To accelerate the ASR, reactive

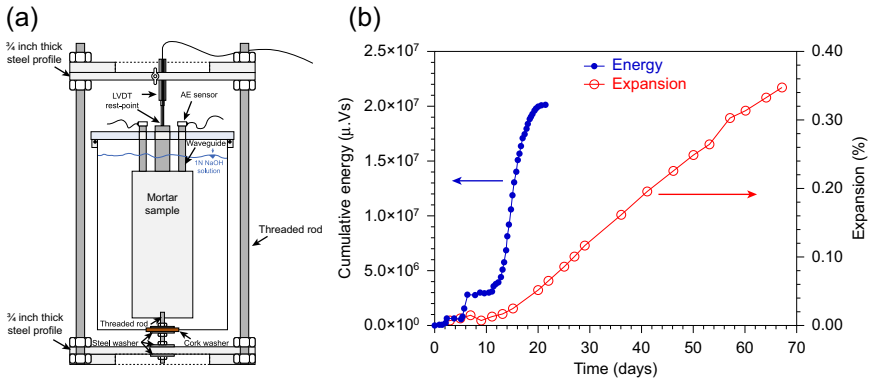

Figure 11.5 (a) Test setup, and (b) AE and length change results of ASR test (Pour-Ghaz et al., 2012).

Figure 11.6 Test setup. Controlled temperature chamber (left) and specimens placed in 100% relative humidity buckets (right) (ElBatanouny, Jones, et al., 2014).

aggregate (Knife River) from Cheyenne, Wyoming, was used to prepare the specimens. The alkalinity concentration of the concrete was increased by adding 5% $Na_2O_{(Eq)}$ to the mix. The specimens were then placed in a controlled environment of 100% relative humidity and temperature of 100 ± 2 °F, as shown in Figure 11.6.

Resonant AE sensors (R6i) with a 40-dB preamplifier were used to monitor the specimens with an amplitude threshold of 40 dB. The length change was measured at discrete time intervals, and the damage in the specimens was assessed using petrographic analysis. AE results from the control specimens were used as a baseline to develop data filters. The small scale of the specimens promotes noise as a result of wave reflections. Therefore, a D−A filter was developed for the specific case of ASR, as shown in Table 11.2.

The results of this study showed that the rate of AE activity, CSS, can be related to the rate of ASR expansion, as shown in Figure 11.7. Similar results were obtained from the remainder of the specimens. In addition, the absolute value of the CSS increased with the increase of the length change percentage. However, the use of absolute value as an indicator of damage is not favorable in AE-based techniques as this value may change with different specimen sizes and different sensor types. Therefore, methods based on changes in the rate of AE activity are preferred.

Table 11.2 Data rejection limits for D−A filter

Rejection limits		Rejection limits	
Amplitude (dB)	**Duration (μs)**	**Amplitude (dB)**	**Duration (μs)**
40−44	400	61−65	1000
45−48	500	66−70	1500
47−52	600	71−75	2500
53−56	700	76−80	3500
57−60	800	81−95	5000

Source: ElBatanouny, Jones, et al. (2014)

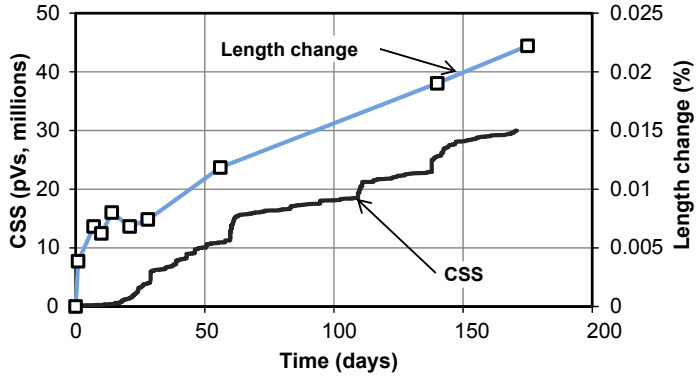

Figure 11.7 CSS and length change percentage with respect to time.

The intensity analysis (IA) method was used to classify the damage associated with ASR distress. This method was proposed by Fowler, Blessing, Conlisk, and Swanson (1989) to assess damage in fiber-reinforced polymer vessels and tanks. Recently, the use of the method was extended to material degradation mechanisms in concrete structures such as corrosion; this is further discussed in the following section. The method assesses the intensity of AE activity by calculating two parameters (using signal strength) historic index, and severity. Historic index, $H(t)$, measures the change in the slope of the CSS in historic approach, while severity, S_r, is the average signal strength of the largest 50 hits. Historic index and severity can be calculated using Eqn (11.1) and Eqn (11.2) where N is the number of hits up to a time (t), S_{oi} is the signal strength of the i-th event, and K is an empirically derived factor that varies with the number of hits. In this study, the value of K was selected to be (1) N/A if $N \leq 50$, (2) $K = N-30$ if $51 \leq N \leq 200$, (3) $K = 0.85N$ if $201 \leq N \leq 500$, and (4) $K = N - 75$ if $N \geq 501$ (ElBatanouny, Jones, et al., 2014).

$$H(t) = \frac{N}{N-K} \frac{\sum_{i=K+1}^{N} S_{oi}}{\sum_{i=1}^{N} S_{oi}} \tag{11.1}$$

$$S_r = \frac{1}{50} \sum_{i=1}^{i=50} S_{oi} \tag{11.2}$$

The two parameters are then plotted in a chart with severity on the y-axis and historic index on the x-axis. As damage increases, the values of both parameters increase, and data points plot in the top-right corner of the chart. Empirical damage limits are then placed to classify damage. Using the results of this study, AE data were related to length change measurements, exposure duration, and petrographic analysis, so that damage was classified into three zones, as shown in Figure 11.8. The maximum damage obtained was rated as moderate damage as length change percentage was approximately half the limit proposed by ASTM C 1293. Future studies should focus on further development of the limits of such damage classification methods and to calibrate these

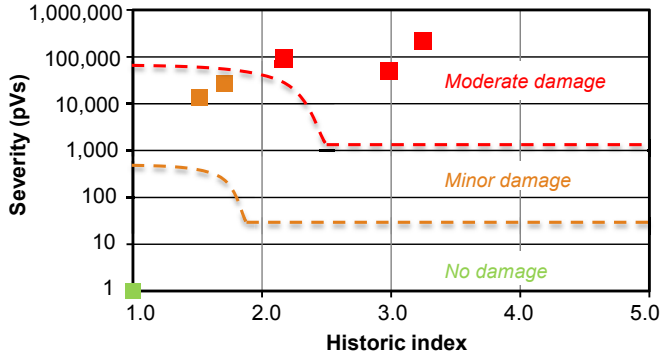

Figure 11.8 Intensity analysis chart for ASR damage. (Special thanks are extended to Mr Carl Larosche and Dr Derek Cong of WJE Austin, TX, for their technical support and help with petrographic examination.)

limits for field structures. Such efforts will yield a standard method for ASR detection based on AE data similar to the AE-based standard for damage detection in vessels and tanks which utilize IA (ASTM E1067, 2011).

11.6.2 Corrosion of pre-stressing strands

Corrosion detection using AE has been studied since the 1980s (Weng, Dunn, Hartt, & Brown, 1982). Literature shows that AE can be correlated with the corrosion rate through the detection of two mechanisms: (1) accumulation of chlorides and breakdown of the passive film (Perrin, Gaillet, Tessier, & Idrissi, 2010; Prateepasen & Jirarungsatian, 2011) and (2) the micro-cracking of the concrete that occurs due to the expansive nature of the corrosion products (ElBatanouny, Mangual, Ziehl, & Matta, 2011). The extreme sensitivity of AE enables it to detect the corrosion process early, which gives it a unique advantage when compared to existing corrosion detection methods such as visual inspection and electrochemical measurements.

The early efforts that were made to investigate corrosion detection using AE focused on passively reinforced concrete as opposed to PC. These studies reported that AE can detect corrosion initiation prior to standard electrochemical measurements and can also measure the change in the rate of corrosion activity using AE parameters such as number of AE hits and/or events (Idrissi & Limam, 2003; Li et al., 1998; Zdunek, Prine, Li, Landis, & Shah, 1995). Other researchers also investigated the use of AE condition assessment methods such as simplified Green's functions for moment tensor analysis and *b*-value for corrosion assessment (Farid Uddin, Numata, Shimasaki, Shigeishi, & Ohtsu, 2004; Ohtsu & Tomoda, 2008).

Recently, an extensive research study was conducted at the University of South Carolina to investigate the ability of AE in early detection and classification of corrosion damage in PC structures. Mangual, ElBatanouny, Ziehl, and Matta (2013a,b) provides an overview of the capabilities of AE sensing toward effectively detecting damage due to corrosion in pristine and cracked concrete specimens

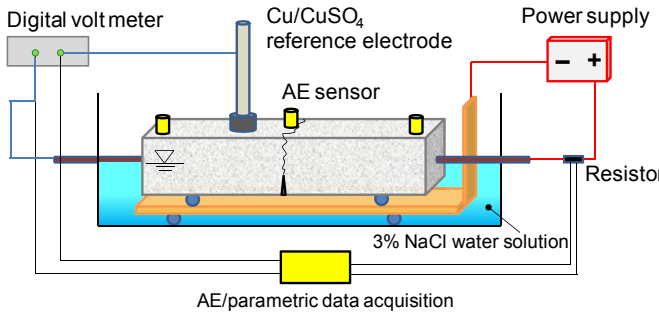

Figure 11.9 Schematic of the accelerated corrosion setup (Mangual et al., 2013a).

reinforced with an embedded one-half-inch diameter pre-stressing strand, where the dimensions of each specimen were 4.5 × 4.5 × 20 in. Corrosion damage was accelerated by impressing current and forming a galvanic cell, as shown in Figure 11.9. Fluctuations in current, half-cell potential, corrosion rate, and AE data were compared to assess the capability of AE toward detecting the onset of corrosion and its progression.

The results showed that stresses induced by volume expansion resulted in dense AE activity that was correlated to the onset of corrosion and nucleation of cracks. Comparing AE data with electrochemical half-cell potential measurements showed that the cumulative signal strength relates well with potential variations. It also allowed discrimination between different corrosion stages. The magnitude of the slope in the cumulative signal strength (CSS) versus time curve was able to portray the de-passivation process and the onset of corrosion as corroborated by half-cell potential. This shows that AE is capable of detecting and discriminating between early corrosion stages while mimicking the behavior of resistivity changes in the concrete. Source location based on AE data enabled the accurate detection of events as a result of passivity breakdown along the reinforcement and debonding.

The use of IA based on AE data proved to be effective in relating the steel section loss with the significance of the damage. Two IA evaluation charts were proposed for pre-cracked and pristine specimens and presented in Figure 11.10. For pre-cracked specimens, the chart divides the corrosion damage into four categories as follows: (1) no damage: at this level, the steel is still in the passive condition and no corrosion damage occurred; (2) de-passivation: at this level, corrosion has just initiated with sectional mass loss less than 15%; (3) cracking: refers to the level at which cracks due to corrosion started to form, and the sectional mass loss is less than 21%; and (4) severe damage: more cracks form and the sectional mass loss exceeds 21%. For pristine specimens, specimens in which de-passivation was absent were found in region A of the IA grading chart, whereas de-passivated specimens were in the B region. This enables the development of AE into a damage quantification tool for maintenance prioritization because significant damage (such as macro-cracking and spalling) is not required for detection (Mangual et al., 2013a,b).

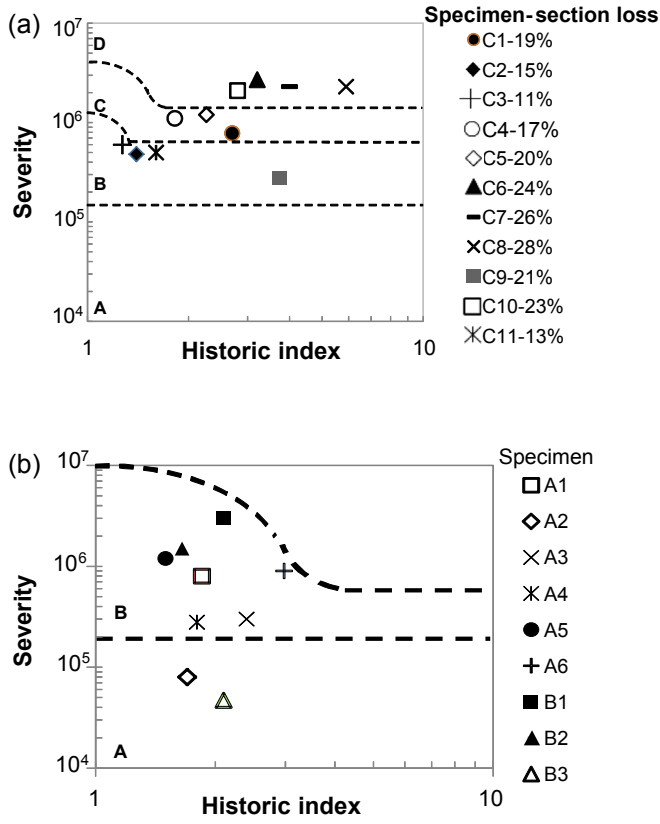

Figure 11.10 AE-based corrosion classification charts for (a) pre-cracked specimens and (b) pristine specimens (Mangual et al., 2013a,b).

The validity of the chart was examined using results from a long-term corrosion test conducted on specimens with different scale and exposure conditions (ElBatanouny, Mangual, Ziehl, & Matta, 2014). The same AE filters were also used in both studies, as shown in Table 11.3. AE IA showed that AE can enable the detection and classification of corrosion damage (ElBatanouny, Mangual, et al., 2014). Given the use of the same chart and limits for both small- and medium-scale specimens, the method proves to be independent of specimen size and duration of exposure. Future efforts should focus on validating the limits of this chart and investigating the feasibility of using this method in field structures.

11.6.3 Load testing

Numerous studies were conducted to utilize AE in damage quantification during load tests of RC and PC structures (Abdelrahman, 2013). This resulted in the development of a number of AE-based condition assessment methods including IA (ElBatanouny,

Table 11.3 AE duration–amplitude data filter

Filter type	Rejection limits		Rejection limits		Rejection limits	
	Amplitude, dB	Duration, μs	Amplitude, dB	Duration, μs	Amplitude, dB	Duration, μs
Duration–Amplitude	40–42	>400	50–52	>1500	60–65	>4500
	42–44	>600	52–54	>2000	65–70	>6500
	44–46	>800	54–56	>2500	70–75	>7500
	46–48	>1000	56–58	>3000	75–80	>9000
	48–50	>1200	58–60	>3500	90–100	>10,000

Source: ElBatanouny, Mangual, et al. (2014)

Ziehl, et al., 2014; Golaski, Gebski, & Ono, 2002; Tinkey et al., 2002), calm and load ratios (Ohtsu, Uchida, Okamoto, & Yuyama, 2002), peak cumulative signal strength ratio (Ridge & Ziehl, 2006), relaxation ratio (Colombo, Forde, Main, & Shigeishi, 2005), *b*-value analysis (Shiotani, Ohtsu, & Ikeda, 2001), index of damage, and modified index of damage (Abdelrahman et al., 2014; Benavent-Climent, Gallego, & Vico, 2011). However, most of the developed techniques can only classify damage if cracking has occurred, such as relaxation ratio and *b*-value, which can classify in terms of micro- and macro-cracking (ElBatanouny, Ziehl, et al., 2014); therefore, these are not suitable for low-level AE.

On the other hand, IA, calm and load ratios, and modified index of damage are based on plotting a chart that can classify damage into different regions based on empirical limits. Therefore, even if the load level was limited to service-level loads, these methods will provide insight regarding the degree of damage in the tested structures. For example, ElBatanouny, Ziehl, et al. (2014) developed an AE IA condition assessment chart that classifies damage into two regions: within design criteria and failed design criteria, as shown in Figure 11.11. This chart was developed during cyclic load testing, confirming with the ACI 437 (2012) protocol, of medium-scale PC beams while monitoring the specimens with AE. The chart with the same limits was tested on pristine (uncracked), pre-cracked, and heavily cracked PC specimens. In all cases, the chart assessed the condition of the specimens properly with a perfect agreement to a predetermined definition of damage, except for pre-cracked specimens, which had an error of 6%.

It is noted that the chart is promising for quantifying existing damage. This is shown in the results of the heavily cracked specimen. As shown in Figure 11.11, all the data points from the first cycle indicated the specimen had failed the design criteria; unlike the CLT deviation from linearity (CLT) acceptance criteria that showed the specimen passed the test in the first three load sets. This result is confirmed by the specimen's

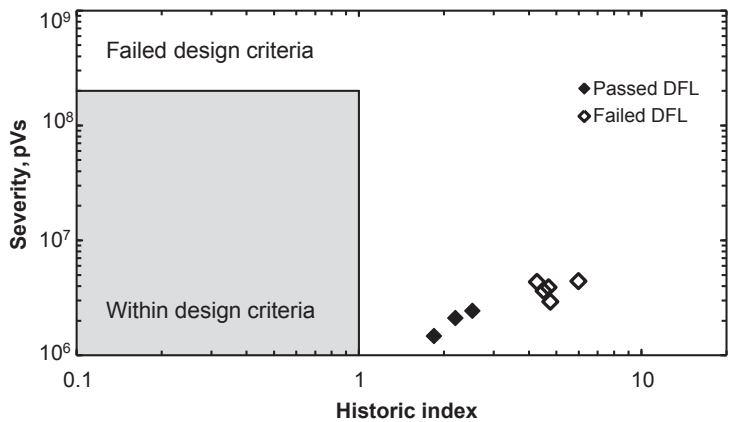

Figure 11.11 Intensity analysis condition assessment chart compared to CLT DFL index, heavily cracked specimen (ElBatanouny, Ziehl, et al., 2014).

load history as it was previously loaded to 80% of its capacity and had visible cracks before the test was conducted. Even though the specimen was pre-stressed, no camber was observed prior to specimen testing, which confirms the degree of damage in the specimen (ElBatanouny, Ziehl, et al., 2014). Therefore, after proper calibration of the chart's limits, this method can be used to quantify damage in field structures by testing the member under service loads and determining the damage level from the chart.

11.6.4 Seismic evaluation

As discussed in the previous section, the AE method has been used for damage quantification during cyclic load tests. The paramount difference between cyclic load tests and seismic events is in the affected system, bridge foundations, and the duration of loading. Larosche (2013) reported the results of cyclic load tests and seismic loading on full-scale pile-bent cap specimens representative of the current practice in the state of South Carolina. The test program included eight full-scale specimens with a single precast pre-stressed pile connected to a representative portion of a cast-in-place bent cap. These specimens were subjected to cyclic pile displacements ranging from 0.1 to 8.0 inches to represent seismic loading. During testing, each specimen was monitored with four R6i AE sensors placed along the first 60 inches of the pile in the region of expected damage.

Based on data gathered through these tests, two damage evaluation models were developed. The first model results in an IA chart divided into five zones corresponding to differing levels of damage based on the yield and ultimate capacity of specimens. The second model results in a percentage of damage. This percentage is based on the ultimate capacity of the specimens. Each model is based on simple programmable calculations that may give users real-time information regarding damage occurring in similar elements.

Each of the two damage models were validated through a full-scale three-pile specimen subjected to multiple applications of a recorded earthquake displacement history. The displacement history was applied to the specimen at different amplifications simulating realistic seismic loading. The data gathered from this test show the ability of each model to accurately assess cumulative damage on a per channel basis. The results of IA for the three-pile specimen are shown in Figure 11.12. As seen in the figure, the method was able to classify damage in the specimen with 92% reliability. Only one sensor (15 in the chart) plotted in the region beyond yielding, whereas it should have plotted in the yielding zone (C in the chart). However, the region closest to the sensor was severely cracked during the application of the load that caused specimen yielding, which justifies the over-prediction of damage by this sensor. It is noted that units of millivolts second are used for severity. This chart may be suitable for field applications as it was developed from full-scale specimens. Implementation of this method in the field will provide bridge owners with necessary information after seismic events so that maintenance action can be taken.

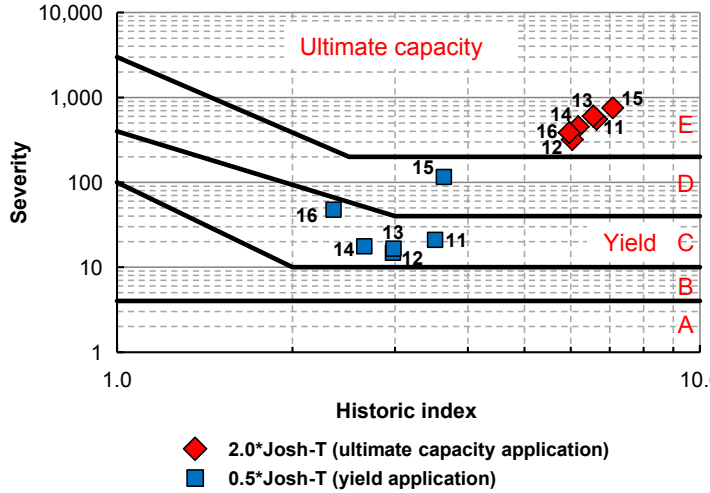

Figure 11.12 Intensity analysis chart for a three-pile specimen (Larosche, 2013).

11.7 Conclusions and recommendations

Case studies have been presented to illustrate the ability of AE to detect and quantify damage from mechanisms that generate low-level AE. These studies showed that simple AE algorithms were developed to classify damage from material degradation mechanisms, such as ASR and corrosion, as well as to evaluate damage during load testing and seismic events. Such algorithms may add in a wider implementation of the technique for purposes of condition assessment of concrete infrastructure systems. In addition, some case studies indicate that AE is more sensitive to ongoing damage than standard intrusive techniques, for example half-cell potential for the case of corrosion.

AE is a nonintrusive method that enables detection of damage locations. The availability of wireless AE equipment gives the method an advantage over most nondestructive evaluation techniques, especially for the case of large concrete structures. The high sensitivity of the method enables global assessment of the structure with a minimal number of sensors. Early detection of damage using AE may help in developing AE-based maintenance prioritization tools as significant visual damage is not required for detection.

A long-standing challenge with AE monitoring is the development of robust filters that can differentiate between genuine and non-genuine AE data. Some filtration algorithms are presented in this chapter. These algorithms should be verified and calibrated for specimens with different sizes as well as for field conditions. Future studies should verify and measure the reliability of the proposed AE damage classification algorithms. Further research should also be conducted to investigate the effect of uncertainties in AE data related to signal-to-sensor distance, wave speed, and signal attenuation.

References

Abdelrahman, M. (2013). *Assessment of damage in concrete structures using acoustic emission* (Master thesis). (p. 146). University of South Carolina.

Abdelrahman, M., ElBatanouny, M. K., & Ziehl, P. (2014). Acoustic emission based damage assessment method for prestressed concrete structures: modified index of damage. *Engineering Structures, 60*, 258−264.

American Concrete Institute (ACI). (2011). Building code requirements for structural concrete. In *ACI 318−011* (p. 503). Farmington Hills, MI: ACI Committee 318.

American Concrete Institute (ACI). (2012). Code requirements for load testing of existing concrete structures. In *ACI 437-12* (p. 34). Farmington Hills, MI: ACI Committee 437.

ASTM C1293. (2007). Standard test method for determination of length change of concrete due to alkali-silica reaction. *American Standard for Testing and Materials*, 1−7.

ASTM E1067/E1067M-11. (2011). Standard practice for acoustic emission examination of fiberglass reinforced plastic resin (FRP) tanks/vessels. *American Standard for Testing and Materials*, 1−15.

ASTM E1316-13c. (2013). Standard terminology for nondestructive examinations. *American Standard for Testing and Materials*, 1−38.

Austin, S., Lyons, R., & Ing, M. (2004). Electrochemical behavior of steel-reinforced concrete during accelerated corrosion testing. *Corrosion, 60*(2), 203−212.

Benavent-Climent, A., Gallego, A., & Vico, J. M. (2011). An acoustic emission energy index for damage evaluation of reinforced concrete slabs under seismic loads. *Structural Health Monitoring, 11*(1), 69−81.

Clifton, J. R. (1991). Predicting the remaining service life of concrete. In *NISTIR 4712*. Gaithersburg, Maryland: US Department of Commerce, National Institute of Standards and Technology.

Colombo, S., Forde, M., Main, I., & Shigeishi, M. (2005). Predicting the ultimate bending capacity of concrete beams from the 'relaxation ratio' analysis of AE signals. *Construction and Building Materials, 19*, 746−754.

Darmawan, M., & Stewart, M. (2007). Effect of pitting corrosion on capacity of prestressing wires. *Magazine of Concrete Research, 59*(2), 131−139.

ElBatanouny, M. K., Jones, M., & Ziehl, P. (2014). Assessment of alkali-silica-reaction using acoustic emission. In *2014 International Congress on Advances in Nuclear Power Plants (ICAPP), Charlotte, North Carolina, April 6−9*.

ElBatanouny, M. K., Larosche, A., Mazzoleni, P., Ziehl, P., Matta, F., & Zappa, M. (2014). Identification of cracking mechanisms in scaled FRP reinforced concrete beams using acoustic emission. *Experimental Mechanics, 54*(Issue 1), 69−82.

ElBatanouny, M., Mangual, J., Ziehl, P., & Matta, F. (2010). Detecting corrosion of steel prestressing strands using acoustic emission. In *Proc. annual conference of the prognostics and health management society (PHM society), paper #34, Portland, Oregon, October 10−14*.

ElBatanouny, M., Mangual, J., Ziehl, P., & Matta, F. (2011). Corrosion intensity classification in prestressed concrete using acoustic emission technique. In *Proc. American society for Nondestructive Testing (ASNT) fall conference and quality testing show 2011, Palm Springs, CA* (p. 8).

ElBatanouny, M. K., Mangual, J., Ziehl, P., & Matta, F. (2014). Early corrosion detection in prestressed concrete girders using acoustic emission. *Journal of Materials in Civil Engineering, 26*(3), 504−511.

ElBatanouny, M. K., Ziehl, P., Larosche, A., Mangual, J., Matta, F., & Nanni, A. (2014). Acoustic emission monitoring for assessment of prestressed concrete beams. *Construction and Building Materials, 58*, 46−53.

Farid Uddin, A. K. M., Numata, K., Shimasaki, J., Shigeishi, M., & Ohtsu, M. (2004). Mechanisms of crack propagation due to corrosion of reinforcement in concrete by AE-SiGMA and BEM. *Construction and Building Materials, 18*(3), 181−188.

Fowler, T., Blessing, J., Conlisk, P., & Swanson, T. L. (1989). The MONPAC system. *Journal of Acoustic Emission, 8*(3), 1−8.

Golaski, L., Gebski, P., & Ono, K. (2002). Diagnostics of reinforced concrete by acoustic emission. *Journal of Acoustic Emission, 20*, 83−98.

Harries, K. A. (2006). Full-scale testing program on de-commissioned girders from the lake view drive bridge. In *Report to the Pennsylvania Department of Transportation. FHWA-PA-2006-008-EMG001* (p. 147). University of Pittsburgh.

Idrissi, H., & Limam, A. (2003). Study and characterization by acoustic emission and electrochemical measurements of concrete deterioration caused by reinforcement steel corrosion. *NDT & E International, 36*(8), 563−569.

Jaffer, S., & Hansson, C. (2009). Chloride-induced corrosion products of steel in cracked-concrete subjected to different loading conditions. *Cement and Concrete Research, 39*, 116−125.

Larosche. A. K. (2013). *Behavior of prestressed pile to bent cap connections and damage evaluation with acoustic emission* (Doctoral dissertation). (pp. 207). University of South Carolina.

Li, Z., Li, F., Zdunek, A., Landis, E., & Shah, S. P. (1998). Application of acoustic emission technique to detection of reinforcing steel corrosion in concrete. *ACI Materials Journal, 95*(1), 68−76.

Mangual, J., ElBatanouny, M. K., Ziehl, P., & Matta, F. (2013a). Acoustic-emission-based characterization of corrosion damage in cracked concrete with prestressing strand. *ACI Materials Journal, 110*(1), 89−98.

Mangual, J., ElBatanouny, M. K., Ziehl, P., & Matta, F. (2013b). Corrosion damage quantification of prestressing strands using acoustic emission. *Journal of Materials in Civil Engineering, 25*(9), 1326−1334.

Moser, R. D., Singh, P. M., Kahn, L. F., & Kurtis, K. E. (2011). Chloride-induced corrosion of prestressing steels considering crevice effects and surface imperfections. *Corrosion, 67*(6), 1−14, 065001.

Naaman, A. E. (2004). *Prestressed concrete analysis and design* (2nd ed.). Ann Arbor, MI: Techno Press, 1072.

NRC IN 2011-20. (November 18 2011). *Concrete degradation by alkali-silica reaction*. Washington, DC: Nuclear Regulatory Commission (NRC).

Ohtsu, M., & Tomoda, Y. (March 2008). Phenomenological model of corrosion process in reinforced concrete identified by acoustic emission. *ACI Materials Journal, 105*(2), 194−199.

Ohtsu, M., Uchida, M., Okamoto, T., & Yuyama, S. (2002). Damage assessment of reinforced concrete beams qualified by acoustic emission. *ACI Structural Journal, 99*(4), 411−417.

Perrin, M., Gaillet, L., Tessier, C., & Idrissi, H. (2010). Hydrogen embrittlement of prestressing cables. *Corrosion Science, 52*, 1915−1926.

Pollock, A. A. (1986). Classical wave theory in practical AE testing. In *Progress in AE III, Proceedings of the 8th International AE Symposium, Japanese society for Nondestructive Testing* (pp. 708−721).

Pour-Ghaz, M., Spragg, R., Castro, J., & Weiss, J. (2012). Can acoustic emission be used to detect alkali silica reaction earlier than length change tests?. In *14th International conference on alkali aggregate reaction in concrete, May 20−25, Austin, TX*.

Prateepasen, A., & Jirarungsatian, C. (2011). Implementation of acoustic emission source recognition for corrosion severity prediction. *Corrosion, 67*(5), 11.

Ridge, A., & Ziehl, P. (2006). Evaluation of strengthened reinforced concrete beams: cyclic load test and acoustic emission methods. *ACI Structural Journal, 103*(6), 832−841.

Saouma, V. E., Perotti, L., & Shimpo, T. (2007). Stress analysis of concrete structures subjected to alkali-aggregate reactions. *ACI Structural Journal, 104*(5), 532−541.

Shiotani, T., Ohtsu, M., & Ikeda, K. (2001). Detection and evaluation of AE waves due to rock deformation. *Construction and Building Materials, 15*(5−6), 235−246.

Shrimer, F. H. (2005). *Progress in the evaluation of alkali-aggregate reaction in concrete construction in the Pacific Northwest, United States and Canada*. US Department of the Interior, US Geological Survey.

Sly, C. (2001). Walkway failure, an initial look at the Lowe's Motor Speedway pedestrian bridge collapse. *Practical Failure Analysis, 1*(2), 7−9.

Stark, D., Morgan, B., & Okamoto, P. (1993). *Eliminating or minimizing alkali-silica reactivity*. No. SHRP-C-343.

Tinkey, B. V., Fowler, T. J., & Klingner, R. E. (2002). *Nondestructive testing of prestressed bridge girders with distributed damage*. Research Report 1857-2, p. 106.

Trejo, D., Pillai, R. G., Hueste, M. B., & Reinschmidt, K. F. (2009). Parameters influencing corrosion and tension capacity of post-tensioning strands. *ACI Materials Journal, 106*(2), 144−153.

Weng, M. S., Dunn, S. E., Hartt, W. H., & Brown, R. P. (1982). Application of acoustic emission to detection of reinforcing steel corrosion in concrete. *Corrosion, 38*(1), 9−14.

Yoon, D., Weiss, W., & Shah, S. (2000). Assessing damage in corroded reinforced concrete using acoustic emission. *Journal of Engineering Mechanics, 126*(3), 273−283.

Zdunek, A. D., Prine, D. W., Li, Z., Landis, E., & Shah, S. (1995). Early detection of steel rebar corrosion by acoustic emission monitoring. In *Paper No. 547 presented at CORROSION95, the NACE International Annual Conference and Corrosion* (p. 9).

Ziehl, P. (2008). Applications of acoustic emission evaluation for civil infrastructure. In *SPIE Proc., SPIE Smart structures NDE, San Diego, CA* (p. 9).

Artificial neural network analysis of acoustic emission data during longtime corrosion monitoring of post-tensioned concrete structures

12

E. Proverbio, L. Calabrese
University of Messina, Messina, Italy

12.1 Introduction

Acoustic emission (AE) was widely used in studying corrosion phenomena and, in particular, stress corrosion cracking (SCC) since the early stage of the development of the technique (Newman & Sieradzki, 1983). More recently, AE technique was introduced into civil engineering for evaluating SCC of reinforcing cables in prestressed concrete structures (Ramadan, Gaillet, Tessier, & Idrissi, 2008a) as well as in the detection of corrosion of reinforcing bar and in the identification of the corrosion processes (Ohtsu & Tomado, 2007; Nair & Cai, 2010). However, more than the identification of the corrosion processes itself, the AE technique could show its greater potentialities in the detection of the highly acoustic emitting events caused by rebar corrosion, i.e. concrete cracking, concrete spalling and delamination. From this point of view, two different approaches are possible for damage evaluation: long-term monitoring or short-term testing. In the former case, continuous acoustic auscultation has to be performed to detect the effects of corrosion progression, which could be time-consuming, and it requires the immobilization of the whole AE equipment. In the latter case, corrosion-induced damaged can be detected by promoting crack propagation or crack rearrangement by momentary loading of the structure; the most damaged area will act as the greatest emitting source. Notwithstanding such potentialities, AE still has a limited diffusion in civil engineering as a consequence of some difficulties yet to be overcome in the field of data handling and analysis and, in particular, in finding reliable correlations between AE hit parameters and source typology. Pattern recognition techniques can be used with this aim (Speidel & Mattson, 1997); signal processing is performed at the waveform level, either by applying digital filtering, Fourier transforms or other processing such as wavelet transform, or by extracting AE features as a means to describe the shape and content of a detected AE waveform.

Acoustic Emission (AE) and Related Non-destructive Evaluation (NDE) Techniques in the Fracture Mechanics of Concrete
http://dx.doi.org/10.1016/B978-1-78242-327-0.00012-X
Copyright © 2015 Elsevier Ltd. All rights reserved.

A minimal knowledge of the main corrosion processes affecting post tensioned concrete (PTC) structure is, however, necessary in order to better understand the information gained during AE monitoring, some references are reported in the following paragraphs.

12.2 Corrosion mechanisms in post-tensioned concrete structures

Post-tensioning, as well as pre-stressing technology, is widely adopted in civil engineering, such as bridge engineering (Benaim, 2008; Hay, Cavaco, & Mustafa, 2009; Hewson, 2003), because it allows obtaining slender but high-performing structures. Although this technology is effective from a structural standpoint, it is particularly sensitive to corrosion damages depending on environmental conditions in which the structure operates. Indeed, several cases have been described in the literature of premature failures of structures due to localized attack such as corrosion fatigue and wear-corrosion, but mainly SCC (ACI, 2001; Salas, Schokker, West, Breen, & Kreger, 2005; West et al., 1999). This latter mechanism is more critical than previous ones because it induces premature and unexpected ruptures of the steel cables without a warning, affecting the mechanical integrity of the structure (Freyermuth, 1991).

On the other hand, deterioration in a pre-stressing strand or tendon is not always reflected by danger evidences visible on the concrete surface. Further, the effect of corrosion of pre-stressing steel is more dangerous than that of unstressed reinforcement. Strand, due to its high mechanical strength and metallurgical characteristics, is smaller in cross-section than conventional reinforcing steel and is proportionally more impaired by loss of section.

12.2.1 Unbounded single-strand tendons

Greased and sheathed type single-strand tendons commonly used in slabs are usually referred to as unbounded single-strand or monostrand tendons. The majority of this steel was used in buildings (including parking structures) and in slabs-on-grade. Although monostrand applications would be very limited in bridge substructures, they have been used for transverse post-tensioning in bridge decks and segmental box girders. Corrosion problems in monostrand tendons can be grouped into four areas:

1. Sheathing damage
2. Poor anchorage protection
3. System inadequacy
4. Structural aspects

A very comprehensive discussion of corrosion of monostrand tendons is provided by ACI/ASCE Committee 423 (ACI, 2014).

Inadequate anchorage protection can lead to multiple forms of corrosion problems in monostrand systems. Corrosion of the anchorage itself is a common problem.

Failure of the anchorage in an unbonded system obviously leads to loss of the tendon. Many corrosion problems in monostrand systems have been related to the system itself. Most of these problems occurred in older monostrand systems; new systems have eliminated many of the problems found in older systems. Another common source of monostrand corrosion problems has been the discontinuity of sheathing and grease on the strand immediately behind the anchorage.

Further corrosion problems can be a consequence of electrical contact between the monostrand tendon and other reinforcement. Such contact may indeed provide the opportunity for macro-cell corrosion with a large cathode (reinforcement) and a small anode (monostrand tendon) in a non-isolated system. Large cathode-to-anode areas can lead to high corrosion rates and severe corrosion damage. New electrically isolated systems allow prevention of this occurrence (Della Vedova & Elsener, 2006). Reinforcement congestion or reinforcement ties may furthermore lead to sheathing damage during post-tensioning of the monostrand.

12.2.2 Bonded post-tensioned tendons

This type of tendon is characterized by the presence in the duct of a cementitious matrix commonly referred to as grout, injected there after steel tensioning with a double aim: better stress redistribution and corrosion protection. Many corrosion problems have resulted, however, from various aspects of grouting because the effectiveness of the grout as corrosion protection is related both to material properties and to construction practices. The most common grout-related corrosion problems are attributed to incomplete grouting, that is, where the duct is not completely filled with grout. Common causes of incomplete grouting are construction difficulties, improper construction practices, blocked or damaged ducts and improper placement or usage of vents. The fresh properties of the grout may also affect the grouting process through insufficient or excessive fluidity and excessive bleed water, leading to entrapped air or the formation of bleed lenses. The severity of tendon corrosion is related to the extent of incomplete grouting and the availability of moisture, oxygen and chlorides (Thompson, Lankard, & Virmani, 1992).

Tendon corrosion may also occur in situations where the entire length of the tendon is well grouted.

The most common cause of corrosion in these situations has been sources of chlorides in the grout itself. Examples include seawater used as the mixing water or chloride containing admixtures. A combination of severe exposure conditions and low cover may lead to corrosion of the duct and subsequent penetration of moisture and chlorides from an external source.

The post-tensioning duct is a fundamental component for corrosion protection in post-tensioned structures. Duct materials range from galvanized steel to plastic with an increasing level of protection. Duct damaging, improper duct splicing and corroded ducts have been causes of tendon corrosion. Holes in the duct may allow concrete to enter the duct during casting, hindering tendon placement and tensioning and causing grouting faults. Damage or misalignment during construction or concrete placing may also lead to post-tensioning and grouting difficulties (West et al., 1999).

12.3 Monitoring of post-tensioned concrete structures by acoustic emission (AE)

It has been evidenced that SCC is the most critical corrosion mechanism affecting post-tensioned tendons. Note, however, that SCC phenomena evolve through complex and different mechanisms, where anodic metal dissolution and hydrogen embrittlement (HE) are not unique stages (Toribio & Lancha, 1998; Enos & Scully, 2002). Nevertheless, many mechanisms can be identified by AE (Alvarez, Lapitz, & Ruzzante, 2012; Yuyama, 1986). AE signals are generated mainly by crack initiation and growth due to metal dissolution or HE (Proverbio & Longo, 2007). Furthermore, the hydrogen evolution induced by cathodic reactions within the crack, the breakdown of thick surface-oxide films, the fracture or de-cohesion of phases (such as precipitates, second-phase particles and nonmetallic inclusions), twin or slip deformation in the plastic zone at the crack tip are all mechanisms that can produce detectable AE signals (Yuyama, Kishi, & Hisamatsu, 1983).

All these phenomena generate AE events characterized by specific waveforms. Therefore, the population of acoustic events can be heterogeneous, often making it difficult to interpret the data in order to correctly identify the damage mechanism of the structure.

Furthermore, in concrete structures, the determination of AE is influenced not only by the signal characteristics but also by the attenuation properties of the concrete itself (Aggelis, Shiotani, Philippidis, & Polyzos, 2008; Vogel & Koppel, 2003). It should indeed be noted that high-frequency acoustic waves are rapidly attenuated in concrete. In pre-stressed concrete elements, the attenuation of AE signals is relatively low (2−3 dB/m at 55 kHz), whereas in old concrete or concrete containing numerous small cracks or pores, severe attenuation (greater than 10 dB/m) strongly limits AE wave propagation (Golaski, Gebski, & Ono, 2002). It should also be considered that the attenuation of AE signals during their propagation leads to a homogenization of their characteristics. This phenomenon in post-tensioned concrete has also been due to the presence of cement grout around the strand that causes significant signal attenuation and also leakage into the rigid grout of AE waves originating in steel wires (Laguerre, Bouhelier, & Grimauld, 2004; Perrin, Gaillet, Tessier, & Idrissi, 2008a).

By considering the aforementioned effects, traditional AE analysis techniques are not sufficient to discriminate the different stages of damage in a corroding structure. The adoption of new statistical methods for data analysis is necessary to find out the significant parameters able to discriminate the different forms of damage. Pattern recognition techniques can be used with this aim (Anastasopoulos, 2007); signal processing is performed at the waveform level, either by applying digital filtering, Fourier transforms or other processing such as wavelet transform, or by extracting AE features as a mean to describe the shape and content of a detected AE waveform. However, waveform registration requires high data storage capacity and sophisticated equipment, whereas intensity analysis is based only on the evaluation of the main AE signal parameters such as energy, counts and amplitude without the need of the waveform record, and it is carried out by means of the cross-evaluation of different health indexes related to AE signal intensity and to loading condition (Proverbio, 2011).

12.4 Numerical modelling and experimental analysis

12.4.1 Clustering procedures for AE signals

When large datasets of AE signals have to be collected it is too costly, from a hardware point of view, to record all the raw AE signals (i.e. voltage versus time history for each sensor). More commonly, signals are reduced to a numbers of patterns describing the signal themselves. Such patterns can be divided into three main groups:

- Conventional patterns: amplitude, counts, duration, rise-time, energy. These patterns were calculated directly by the acquisition system from the input raw AE wave.
- Statistical patterns: In this second group statistical patterns derived from the previous ones such as historic index (HI) and severity (Golaski et al., 2002), the RA value, average and events frequency (JCSM-IIIB5706, 2003) and Ib values can be included.[1]
- Test variables: The last group included variables such as time, sensor identification and external variables such as loading condition. These patterns were strictly related to experimental set-up, acquisition and storing of the data.

A multistep analysis procedure can be then used with the aim to identify homogeneous clusters of AE signals to be related to specific damage conditions (e.g. tensile or shear cracks, micro-cracking or macro-cracking) on the basis of the adoption of a multivariable dataset. A hardware filtering of the data can be performed at the level of data recording in order to cut off low-amplitude noise by means of a high-pass filter (usually set in the range 30−42 dB, depending on test environmental noise).

Then, the procedure includes the following steps:

- Denoising clustering
- Univariate analysis
- Multivariate analysis
- Damage analysis

The scheme of clustering and damage analysis methodology is reported in Figure 12.1.

12.4.1.1 Denoising clustering

Four procedures with the purpose to reduce the redundancy of data and to remove the acquired spurious AE signals can be applied.

[1] The HI provides a measure of changes in signal strength during the test, while the severity index (SI) is the average signal strength of a number of events having the largest value of signal strength (Nair & Cai, 2010; Golaski et al., 2002). The RA value was defined as the ratio of waveform rise time to amplitude; average frequency combined with the ratio between counts and duration indicates the average wave frequency over one AE hit. Events frequency is the number of signals that were acquired for a range of events, calculated as described in Calabrese, Campanella, & Proverbio (2012). The Ib value is the slope of the log-linear plot of frequency versus amplitude of AE events. The Ib value improves calculation by selecting the amplitude limits of the linear range of the cumulative frequency distribution data of AE.

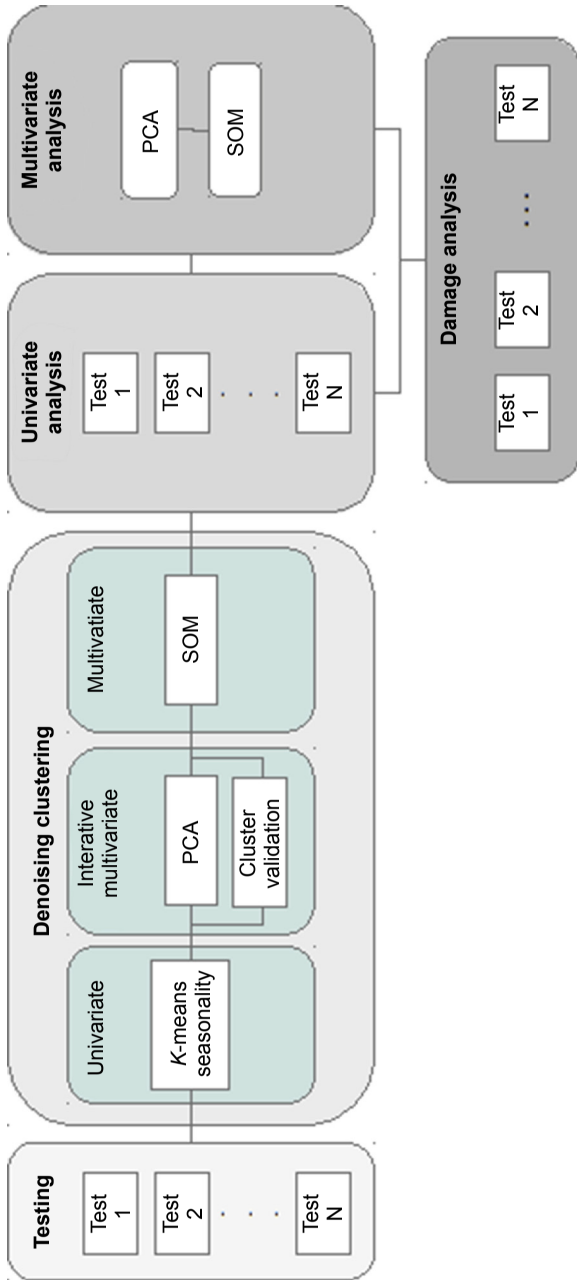

Figure 12.1 Scheme of the procedure for clustering and damage analysis of acoustic emission data.

1. By using a *k*-means and hierarchical clustering procedure the clusters related to environmental noise and characterized by uncorrelated significant amplitude events (not removed by hardware band pass filter) can be identified. Hierarchical clustering refers to the formation of a recursive clustering of the data points: a partition into two clusters, each of which is itself hierarchically clustered. A dendrogram, a bi-dimensional diagram that shows the subdivisions of clusters at each successive stage of analysis, was adopted here. The information can be then compared with a non-hierarchical clustering approach, *k*-means algorithm, to allow a most reliable identification of the cluster number, to identify the lack of homogeneity in the variables dispersion and to classify further noise events.
2. The denoised AE signals were still characterized by groups of correlated variables; to allow data comparison with different scales, logarithmic values had to be used instead of their natural values, and afterward, a normalization procedure had to be applied on the data matrix. This is a univariate denoising process, where by using a Cartesian or multidimensional plot of variables versus time, it is possible to identify a time-dependent periodicity of data that could be related to seasonality noising.
3. Afterward, a multivariate denoising process can be used to reduce the dimensionality of the data (e.g. by using principal component analysis, PCA). The PCA is a useful procedure to retain the nature of the original variables, but it reduces their number (Section 12.4.1.3). With multivariate data, it removes extraneous or redundant variables to simplify the subsequent multivariate analysis, which unproductively increases the dimensionality of the data. PCA, performed on the denoised data, could evidence the relevancies and interdependencies between variables favouring the possibility of finding important underlying patterns in the data. The criterion adopted in the variables reduction is connected to the evaluation of variance percentage. The results are then compared with the correlation matrix to verify interdependencies between the original variables in a correlation coefficient matrix. In the matrix, all the diagonal values have a value of one because all signals are perfectly correlated with themselves. Non-diagonal values close to one indicate that the corresponding variables are highly correlated; a threshold value of 0.80 was set here.
4. The remaining uncorrelated data can be finally processed by Kohonen's self-organizing map (SOM) algorithm (Section 12.4.1.3), which allows one to identify the characteristics of AE hits in specific clusters (e.g. high amplitude and low rise time, with high load conditions) and, therefore, allows one to evidence a relationship between AE signals and damage mode.

12.4.1.2 Univariate analysis

Univariate statistical analysis is used to identify any correlation between couples of variables and to obtain preliminary information about the effect of damage evolution of the structure on the acquired AE signal; the analysis is carried out with the description of a single variable and its attributes of the applicable unit analysis. This involves describing the way in which quantitative data tend to cluster around some relevant values. In order to define a common procedure to identify the different damage mechanisms, specific AE parameters (such as amplitude and duration) can, in fact, be used as AE discriminating factors. Sometimes, however, the analysis of a single parameter, or a combination of some of them, is not sufficient; consequently, a multivariate technique has to be used to evidence the hidden structure of complex datasets.

12.4.1.3 Multivariate analysis

Multivariate analysis is performed, at first, by means of PCA methodology. From a mathematical point of view, PCA is an orthogonal linear transformation that transforms the original statistical data by projecting them to a new set of coordinates in the order of decreasing variance (Chatfield & Collins, 1980; Hardle & Simar, 2007; Johnson, 2002). The algorithm projects, by a linear transformation, a p-dimensional data vector X into a new q-dimensional data vector Z, containing what is referred to as the data's principal components. Given the data $X_i = (x_{1i}, x_{2i},..., x_{pi})$ with $i = 1,\ldots,N$, the new data vector is $Z_i = (z_{1i}, z_{2i},\ldots, z_{qi})$, where z_1 is the linear combination of the original x_j ($j = 1,\ldots,p$) with maximal variance; z_2 is the linear combination which explains most of the remaining variance and so on, The new data vector, referred to as the principal component, is a linear combination of the original data and is both uncorrelated and orthogonal to all other principal components. The first principal component accounts for the maximum variance in the data; the second principal component accounts for the maximum of the remaining variance, and so on. PCA is widely used in statistics and neural computing with the purpose to reduce the number of significant variables and, consequently, to reduce the dimensionality of the dataset (Manson, Worden, Holford, & Pullin, 2001; Palakal, Pidaparti, Rebbapragada, & Jones, 2011). Furthermore, PCA is able to identify and classify hidden patterns in the data, favouring the understanding of the relationships between variables (Johnson, 2002; Kim, Kang, Yoon, & Choi, 2005). For a Gaussian distribution of the data, PCA maximizes the information transfer. In any case for a non-Gaussian distribution of data, the results can still be qualitatively interpreted. If it is for data reduction or exploratory purposes, then normality is not a strict requirement (Collins, Dasgupta, & Schapire, 2001). Since the PCA technique focuses only on second-order statistics, it can ensure the lack of correlation but not the requirement of statistical independence (Bindra, 2006).

Damage analysis can finally be completed by using self-organizing algorithms (Calabrese, Campanella, & Proverbio, 2013). SOM or Kohonen's map is a neural network used in the classification of complex multidimensional data (Kohonen, 1982). The algorithm could be unsupervised, requiring no user intervention. The SOM is indeed one of the most prominent artificial neural network models adhering to the unsupervised learning paradigm. The model consists of a number of neural processing elements, i.e. units. To each unit is assigned an n-dimensional weight vector m_i, $m_i \in R_m$. The training process of the SOM may be described in terms of input pattern presentation and weight vector adaptation. Each training iteration t starts with the random selection of one input pattern $x(t)$. This input pattern is presented to the SOM, and each unit determines its activation. Euclidean distance between the weight vector and the input pattern was used to calculate a unit's activation. In this particular case, the unit with the lowest activation is referred as the winner, c, of the training iteration, as given in Eqn (12.1):

$$c : m_c(t) = \min_i \|x(t) - m_i(t)\| \tag{12.1}$$

Subsequently, the weight vector of the winner as well as the weight vectors of selected units in the vicinity of the winner are adapted. This adaptation is implemented

as a gradual reduction of the difference between corresponding components of the input pattern and the weight vector, as shown in Eqn (12.2):

$$m_i(t+1) = m_i(t) + \alpha(t) * h_{ci}(t) * [x(t) - m_i(t)] \tag{12.2}$$

Geometrically speaking, the weight vectors of the adapted units are moved a bit towards the input pattern. The amount of weight vector movement is guided by a so-called learning rate, α, decreasing in time. The number of units that are affected by adaptation as well as the strength of adaptation is determined by a so-called neighbourhood function h_{ci}. This number of units decreases in time. Typically, the neighbourhood function is a unimodal function, which is symmetric around the location of the winner and monotonically decreasing with increasing distance from the winner. A Gaussian is used to model the neighbourhood function. At the beginning of training, a wide area of output space is subject to adaptation. The special width of units affected by adaptation is reduced gradually during the training process. Such a strategy allows the formation of large clusters at the beginning and a fine-grained input discrimination towards the end of the training process.

The training process of the SOM leads to a spatial arrangement of the input pattern such that similar inputs are ordered in a topological map (Kohonen, 1982; Godin, Huguet, Gaertner, & Salmon, 2004; Oja & Kaski, 1999). Training enables the convergence of the system towards a model clustering related with the internal nature of data.

The default training algorithm in SOM script is a batch algorithm; this is because it needs a much smaller number of iterations than the classic one, and each iteration uses numerous input data points. The whole training set is gone through at once, and only after this the map is updated with the net effect of all the samples. Actually, the updating is done by simply replacing the prototype vector with a weighted average over the samples (recorded data), where the weighting factors are the neighbourhood function values.

$$m_i(t+\Delta t) = \frac{\sum_{j=1}^{n} h_{ic(j)}(t) x_j}{\sum_{j=1}^{n} h_{ic(j)}(t)} \tag{12.3}$$

where $c(j)$ is the BMU of sample vector x_j, $h_{ic(j)}$ is the neighbourhood function (the weighting factor), and n is the number of sample vectors.

12.4.1.4 Damage analysis

With this approach, combining univariate and multivariate analysis information, a topological damage map can be identified; so, it could be possible to monitor the damage evolution of a real structure during time, detecting or preventing its final failure (Section 12.5.5).

By using this procedure, meaningful information on the interpretation of the acquired acoustic events can be provided. In fact, specific events clusters effectively discriminate different classes of SCC degradation phenomena. In particular, the detailed analysis of acoustic activity presented in terms of single variables (amplitude, duration and energy) is a limited approach.

12.5 Application, measurement and results

12.5.1 Experimental set-up

AE monitoring was performed on a post-tensioned concrete beam during a long-term hydrogen assisted stress corrosion cracking test (HASCC). The beam had a length of 6.30 m and a cross-section of $0.40 \times 0.25\ m^2$ (Figure 12.2(b) and (c)). It was made of a concrete mix with a characteristic strength Rck of 55 MPa and 430 kg/m^3 of ordinary Portland cement (OPC). The beam was reinforced with four 18-mm steel bars and pre-stressed with four post-tensioned 7-wire 6/10″ strands. Post-tensioning force induced a stress level on the strand of about 60% of the ultimate tensile strength (UTS), and of about 52% UTS due to losses for elastic shortening, creep and shrinkage in the concrete and relaxation in the steel. The tendon was completely grouted except for a small corrosion cell of 25 cm in length (Figure 12.2(a)) located at mid-span of the beam. The corrosive solution used was composed of 250 g/l of ammonium thiocyanate (NH_4CNS) in accordance with ISO 15630. The solution was kept at room temperature and with constant liquid recirculation from an external reservoir by a pump.

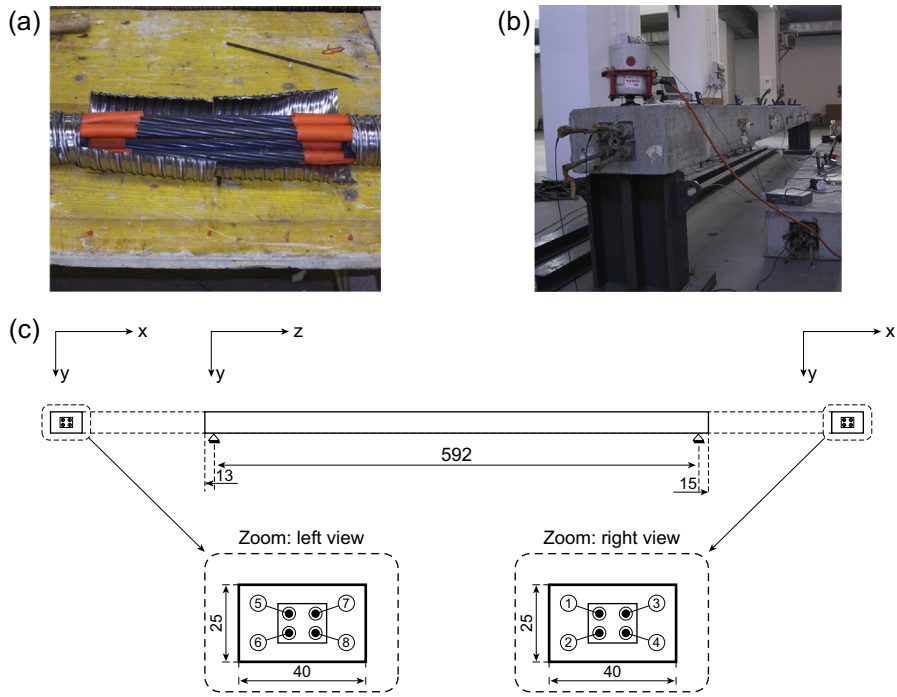

Figure 12.2 Details of the post-tensioned concrete beam used in the experimentation. Corrosion cell obtained in the metal duct (a), view of the experimental setup (b) and the scheme of the post-tensioned concrete beam setup used for the corrosion test. Circled numbers refer to AE sensor locations (c).

AE signals were recorded by a 10-channel Vallen AMSY-5 measurement system. A total of eight piezoelectric transducers were used for monitoring the pre-stressing steel (VS150-M type) working in a 100−450 kHz frequency range with resonance at 150 kHz. The sensors were positioned at the ends of the post-tensioned steel strands. Sensor location is evidenced in Figure 12.2(c). The AE acquisition covered a period of approximately 7 months with daily 24-h monitoring.

12.5.2 Clustering denoising

12.5.2.1 Univariate denoising process

Preliminarily, a traditional filtering method on population of data was applied. In particular, after a screening of distributions of all available variables, a high-pass filtering on duration (>10 μs) and counts (>2) was applied. The distribution of these data showed a great amount of events with low magnitude that could be related to background noise.

Afterward, in order to identify possible noise events due to seasonal effects, each variable was evaluated along daylight time (seasonality maps).

In Figure 12.3 the contour plots of rise time and events frequency (f_{EV}) parameters as a function of day and hours are represented. These graphs are usually used to represent equipotential curves. The different colour regions indicate a variable's magnitude (right-hand colour scale).

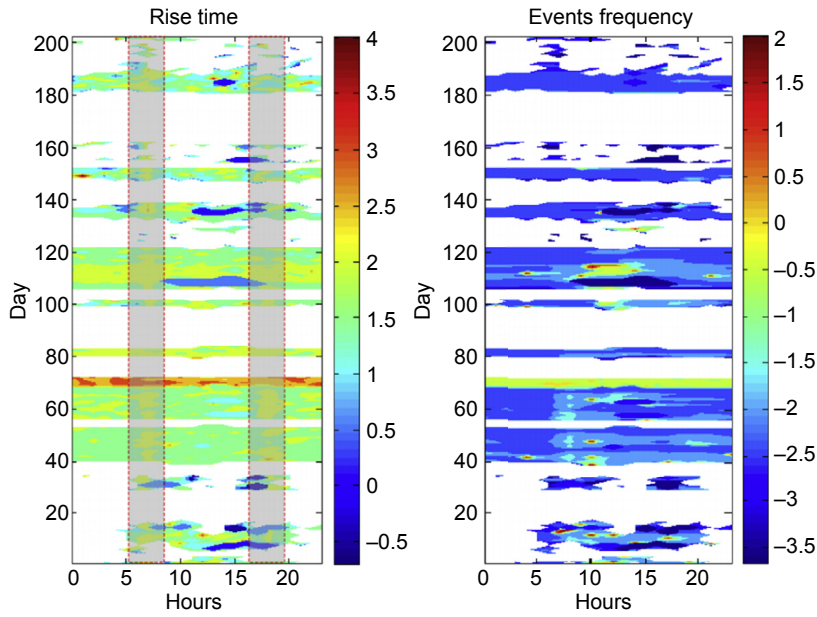

Figure 12.3 Distribution map of rise time and event frequency at different daylight times along time (colour bars on right on a logarithmic scale).

The distribution of rise time of recorded hits shows that relatively high values are periodically present in two different specific time spans in the range of 7 and 19 o'clock. These time events are probably related respectively with electromagnetic disturbances (e.g. switching off and on artificial lights). The first step of the noise filtering process was to remove all events present in this time sequence.

Furthermore, the seasonality map for event frequency showed how this variable was particularly sensitive to discern nighttime (combination of real events with electrical noises) and daytime events (sum of real events with electrical and external noises). High events frequency bands were detected during the daytime. The presence of AE swarms was identified as an indicator of events probably connected to disturbing noise (e.g. named activity in the laboratory).

The identification of spurious events can also be effected by the placement of a guard sensor, placed not in-build with the monitored concrete structure. In this way, the external noises that disturb the testing field can be discriminated by the sensor guard and removed from the population data.

Finally, in order to optimize the filtering process by PCA, in the reduced data matrix, all events were organized in independent sub-arrays, each consisting of events acquired by a specific sensor. In order to optimize the subsequent clustering procedure, the uncorrelated variables were identified by correlation matrix and PCA. This was done without losing significant information.

12.5.2.2 *Iterative multivariate denoising process*

Figure 12.4 shows, as a reference, the trend of the cluster validation[2] indexes for sensor 1 during the first filtering cycle. The optimal number of clusters, k, can be determined as a global/local maximum or minimum, or a significant knee in the cluster index trends, that indicate a better fitting with the data (Falasconi, Pardo, Vezzoli, & Sberveglieri, 2007). The optimal number of clusters, k, was identified as local maxima for Silhouette, Dunn, Krzanowski−Lai and Calinski−Harabasz index trends, and as local minima for Davies−Bouldin and Hartigan index trends. Six quality cluster indexes have been used because uncertain conclusions are reported about their performance in the literature. Depending on the application, their behaviour could vary considerably (Cardoso & Carvalho, 2009).

These validation indices allowed the evaluation of clustering quality in order to support the selection of a specific and valid partition structure in the unsupervised

[2] The prediction of the correct number of clusters is a fundamental problem in unsupervised classification data. Many clustering algorithms require the beforehand definition of the number of clusters. To overcome this problem, in the literature, various cluster validity indices can be proposed to assess the quality of a clustering partition by a cluster validation procedure (Batagelj, Bock, Ferligoj, & Iberna, 2006; Haldiki, Batistakis, & Vazirgiannis, 2001). This approach consists of running a clustering algorithm several times and obtaining different partitions. The clustering partition that optimizes a validity index is selected as the best partition. Thus, the main goal of a cluster validation technique is to identify the partition of clusters for which a measure of a quality is optimal. In this work, cluster validity techniques included the Silhouette method, Dunn's index, Davies-Bouldin index, Krzanowski−Lai index, Hartigan index and the Calinski−Harabasz index (Batagelj et al., 2006; Haldiki et al., 2001).

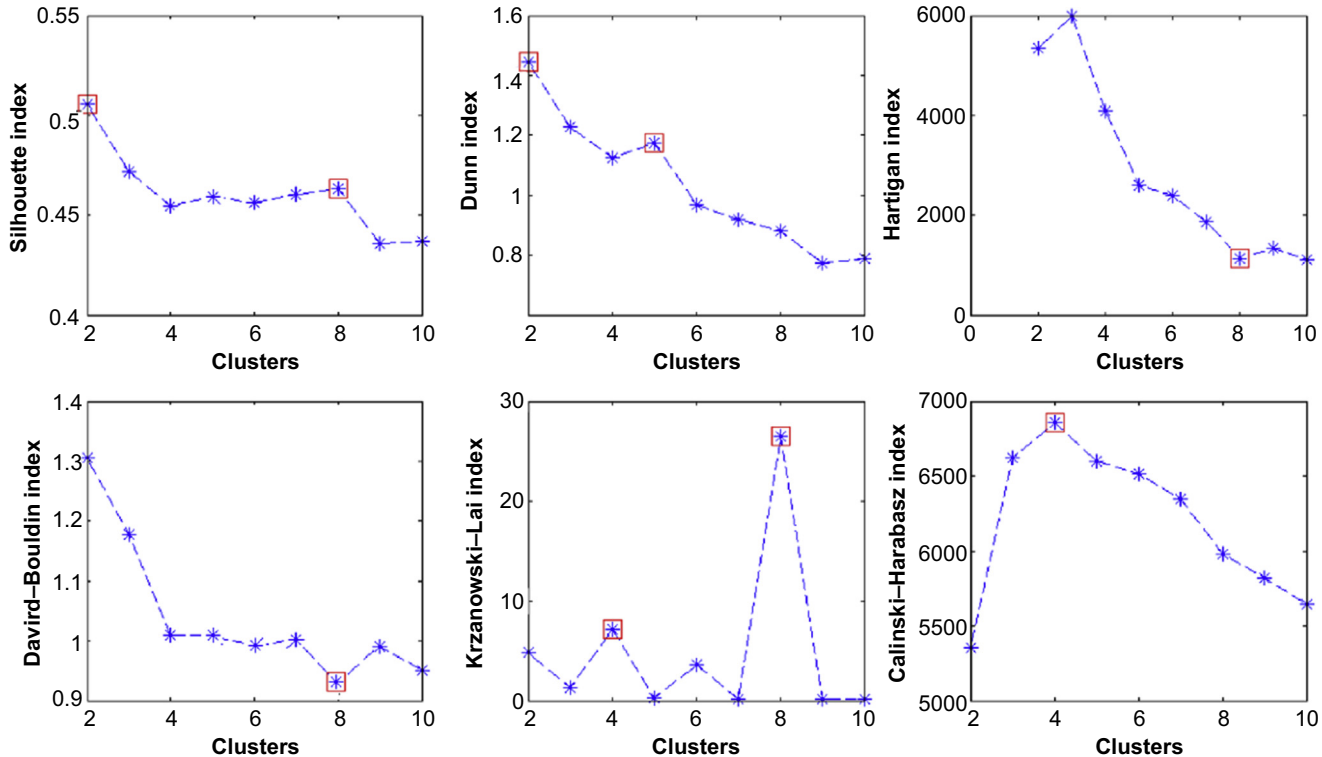

Figure 12.4 Cluster validation indexes (sensor 1; after first filtration cycle).

environment of the dataset, where the real events were still unknown or not identifiable. In this work, a general perspective regarding the valuable use of quality indices in the evaluation of AE events was offered. In the case shown in Figure 12.4, the proposed optimal number of clusters was eight.

The univariate denoising process used up to now was performed to remove clearly noisy clusters. Our aim was now to remove environmental noise where a high number of events was recorded during daylight time, and as a consequence, clusters including an extremely high number of daylight events (e.g. 95%) were removed.

A visual representation of the best clustering result is displayed in Figure 12.5, where the PCA score plot for a reference sensor was shown during the first filtration cycle with eight clusters (as identified by a previous cluster validation procedure). In the graph, the vertical axis represents the unrotated factor II (second principal component), and the horizontal axis represents the unrotated factor I (first principal component). The axes are labelled with 0 at the origin and extend outward to about ±0.5. The numbers on the axes represent the factor loadings. Cluster 6 was characterized by only about 3.2% of nightly events. And, because it was strictly correlated with the wave variables (duration, counts and energy), it was supposed that an external event influenced the data pattern, causing the acquisition of a noisy acoustical swarm.

This cluster was removed from the distribution of data. Then the iterative use of PCA and clustering validation techniques was performed until no more clusters including a high number of daylight events were observed. The data filtered in this way were finally used as input for Kohonen's SOM algorithm. This denoising procedure was performed for all channels.

By the iterative, multivariate denoising process, a further reduction of 60% of the data was obtained.

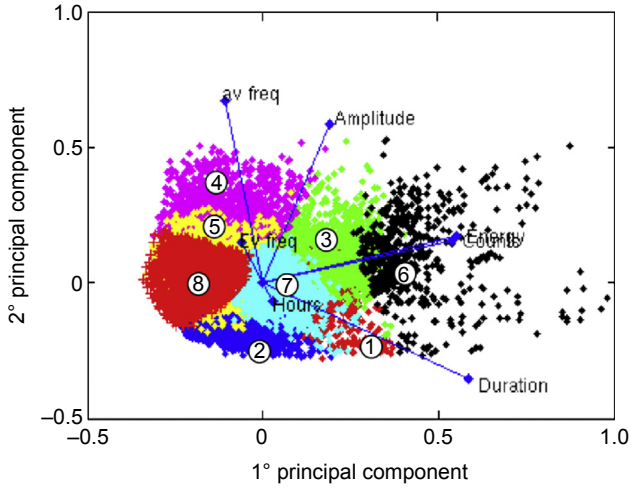

Figure 12.5 Bi-plot of clustered principal component analysis results (sensor 1; number of clusters eight; first filtration cycle).

12.5.2.3 SOM denoising process

An analogous denoising procedure can be applied for another multivariate clustering procedure (SOM). A graphical representation of the adopted effect of noise removal is reported in Figure 12.6. The figure shows trend evolutions of cumulative counts from all eight channels for the different denoising processes adopted. The original data, acquired during the entire duration of the test, showed different regions as apparently significant. These regions, characterized by letters A–D, were related to specific jumps in a monotonous trend of the curve and were induced by specific acoustic events, which could be related to degradation phenomena that took place in the pre-stressed beam or due to external disturbances.

The univariate denoising process removed a significant amount of data related mainly to zones A and C, highlighted in Figure 12.6. These clusters of removed events, acquired during the first days of testing, were characterized by very low counts and duration, as swarms of acoustic events characterized by high values of events frequency and identifiable mainly in the daylight period. This filtering criterion, however, did not provide information on other gaps (zones B and D) in the cumulative counts trend.

The application of the multivariate iterative method allowed us to optimize noise suppression from the data. Particularly, it was possible to discriminate spurious events in all zones. This process further reduced the number of useful data for the next steps.

The SOM denoising process allowed us to remove a lot of events in zone D, further refining the multivariate denoising process started by the iterative PCA procedure. Although the SOM denoising process offers a limited reduction of

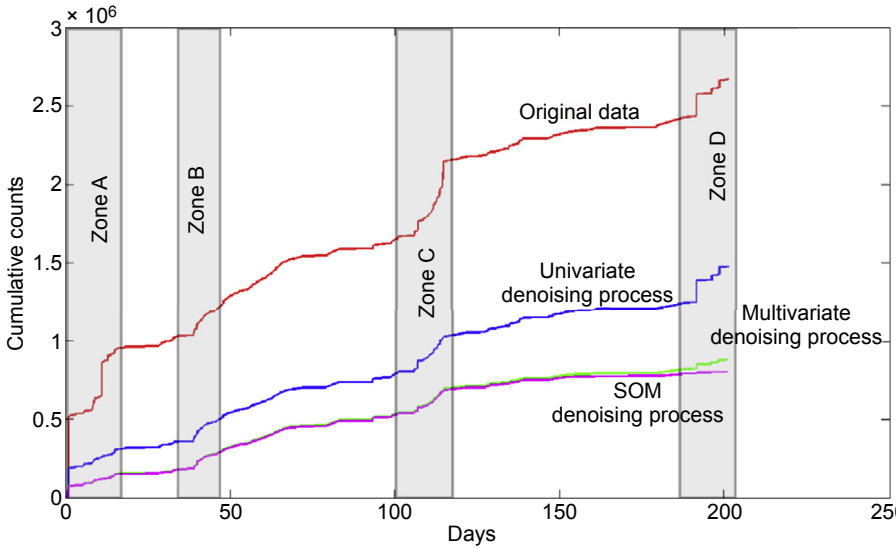

Figure 12.6 Cumulative counts for original and filtered data.

data, it was useful in the preliminary identification and classification of the damage state of the structure, visualizing low-dimensional views of high-dimensional data by topological maps.

After the denoising process, the cumulative counts were characterized by a cyclical gap-plateau trend. Zones A, B and C were equally relevant, and each one was followed by an energetically quiescent region where no relevant AEs were acquired. The gap of zone D disappeared after the robust data clustering. The significance of the change of the SOM curve in zone D is still under investigation, even if it is more likely the results of the best performance of the SOM algorithm in noise removal, as what is obtained in Zone A by the simple application of the univariate denoising process.

12.5.3 Univariate analysis

Figure 12.7 shows a plot of the cumulative number of hits versus acquisition time for residual denoised data, with the purpose to evidence the acoustic activity evolution during time. We can identify three relevant steps that could be related, indirectly, to specific damage evolution of the post-tensioned steel. Furthermore, by coring the beam at the end of the test, it was possible to evaluate the real corrosion damage of the strands.

Region I: During the early stages of the test there was a significant acoustic activity due to initial electrochemical interaction between the steel wires and the electrolytic solution. This period of activity is characterized by several sub-steps due to the activation and stabilization of different corrosive phenomena. At first, the acoustic activity is related to the homogenization and stabilization of reactions at the metal surface in

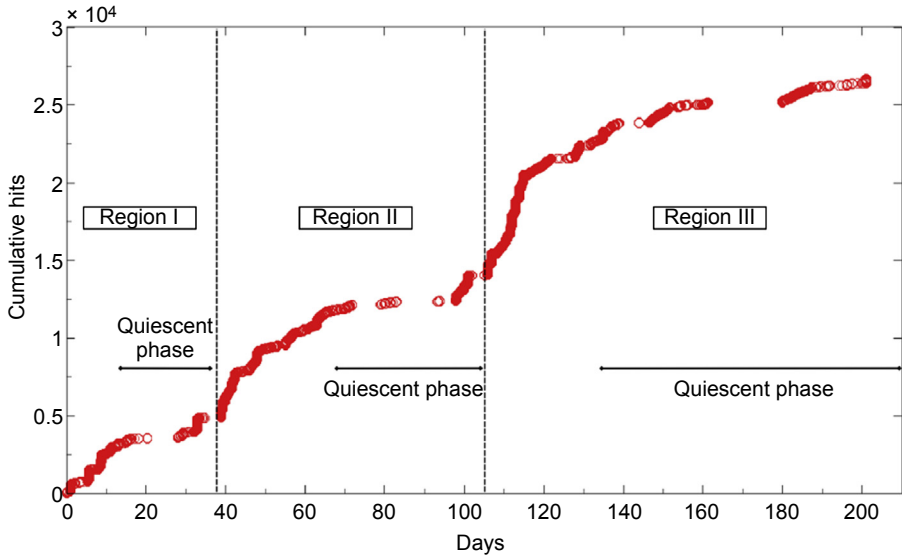

Figure 12.7 Cumulative hits plot versus time (denoised data).

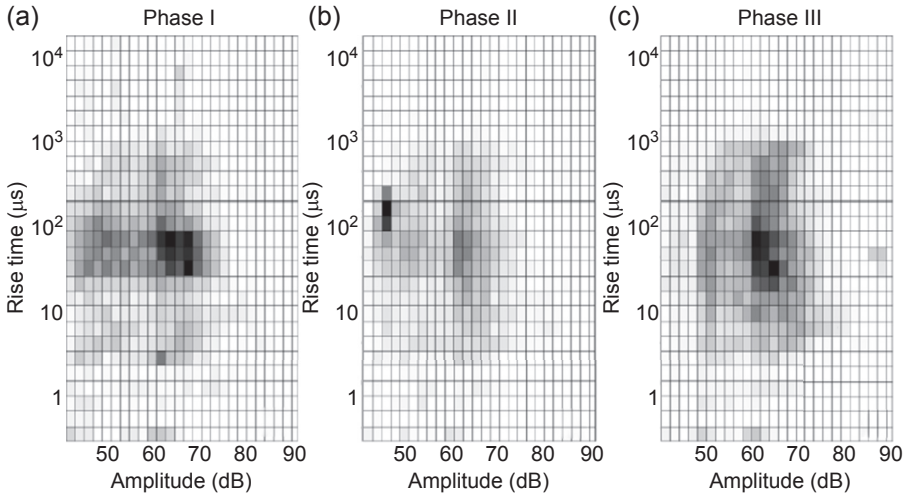

Figure 12.8 (a–c) Amplitude versus rise time grid maps.

the corrosive solution (Perrin, Gaillet, Tessier, & Idrissi, 2008b). Afterward, we observe a more relevant increase of AE hits (region II). As evidenced in Figure 12.8(a), region I is characterized by events having a wide range of amplitude (in the range 40–70 dB) and usually with a medium–high rise time (>30 µs). The low-amplitude events could be attributed mainly to hydrogen formation at the steel surface (Didier-Laurent, Idrissi, & Roue, 2008; Fregonese, Idrissi, Mazille, Cetre, & Renaud, 2001; Ramadan & Idrissi, 2008). As reported in the literature, AE with amplitudes in the range of 40–50 dB with high rise time can be induced by hydrogen evolution phenomena (West et al., 1999). Besides, the presence of hydrogen favours the breakdown mechanism of a pseudo-passive layer at the metal surface of the strand and the beginning of hydrogen diffusion inside the metal, inducing strong AE activity (Jomdecha, Prateepasen, & Kaewtrakulpong, 2007). During this incubation period, corrosion mechanisms are activated, such as random pit formation on the metal surface (Kovac, Leban, & Legat, 2007). However, the localized corrosion is not sufficiently energetic to be detected by AE, but it could also favour the energetically more relevant SCC (Ramadan, Gaillet, Tessier, & Idrissi, 2009). The SCC initiation phenomena induce events with low duration, counts and rise time and an amplitude in the same range of hydrogen evolution events (30–50 dB) (Kovac, Alaux, Marrow, Govekar, & Legat, 2010). The crack initiation is followed by short crack propagation, as identified in Figure 12.8(a), with the AE at higher amplitude (in the range 60–80 dB) (Kovac et al., 2010).

Region II: After 45 days, a new swarm of significant events occurred in a short period (in about 15 days over 5000 hits were observed) and the cumulative AE hit curve increased significantly. Afterward, the structure had a new quiescent phase where the increase of AE hits was very low. At this stage, at the strand surface, micro-cracks gradually initiate, increase and coalesce (Ramadan et al., 2008a; Budano, Giunta, & Lucci, 2011; Ramadan, Gaillet, Tessier, & Idrissi, 2008b).

This phase is the evolution stage concerning hydrogen embrittlement and propagation of cracks (Perrin et al., 2008b). This is confirmed by the relevant amount of events in the amplitude range of 40−50 dB (Figure 12.8(a)) with a rise time of about 100 μs. During the evolution stage, hydrogen diffusion through the metal lattice occurs. When the hydrogen uptake is sufficient for the steel to overcome its threshold stress intensity factor, a new acoustic activity will take place due to initiation and propagation of cracks (Perrin et al., 2008b). In region II, the time period between two AE events increases significantly. The reduction of event frequency, counts and energy could be related to the formation of a plastic zone at the crack tip during the crack propagation stages (Shaikh et al., 2007). With increasing crack length, an increase of stress concentration occurs, which induces a larger plastic zone ahead of the crack tips. This results in a larger blunting of the crack tip. A larger plastic zone implies that a longer time is needed for cracks to re-sharpen by dissolution for new further crack propagation. The time period between two subsequent AE events corresponds to the duration of material dissolution that induced the crack growth (Shaikh et al., 2007). This could explain the larger time gaps between two AE events during later stages of crack growth.

Region III: High-intensity AE events were recorded after 4 months of exposure. Some steel wires were approaching final rupture, and the post-tensioned concrete beam was undergoing a stabilization phase due to a new redistribution state of stress levels. This phase of reassessment was the prelude to new damaging phases progressively becoming much more destructive. After this period, we acquired about 25,000 AE events. In this phase, the AEs were mainly generated by crack propagation. However, corresponding to wire failure, the intense AE activity was probably generated by a rapid reduction of the cross-section during its rupture (Kovac et al., 2007). The large burst of activity, characterized by very high energy and amplitude up to 90 dB (Figure 12.8(c)), is symptomatic for final ductile fracture of a strand (Kovac et al., 2010).

Figure 12.9 shows the distribution of events as a function of some significant variables. Two families of events characterized by a linear relationship between energy and amplitude can be observed in Figure 12.9(a): a first, most populous group of events with low energy values and a second dispersed one characterized by high energy values.

Further information can be derived by observing Figure 12.9(b), where events are also distinguished according to the event frequency value. It may be noted that the data were classified into four clusters (as identified by using *k*-means algorithm). These four clusters were identified as cluster AE1 (characterized by low energy and high event frequency), cluster AE2 (a dense block of data characterized by low energy and low event frequency), cluster AE3 (characterized by high energy and low event frequency) and finally AE4 (characterized by high energy and high event frequency). This figure evidences the presence of energetically relevant AE, but, in this form, it is not possible to have temporal information about the occurrence and the emission conditions related to these AE clusters of AE events.

Univariate analysis allowed us to identify main damage steps of the strands. However, for better understanding the evolution of the corrosion phenomena and for a

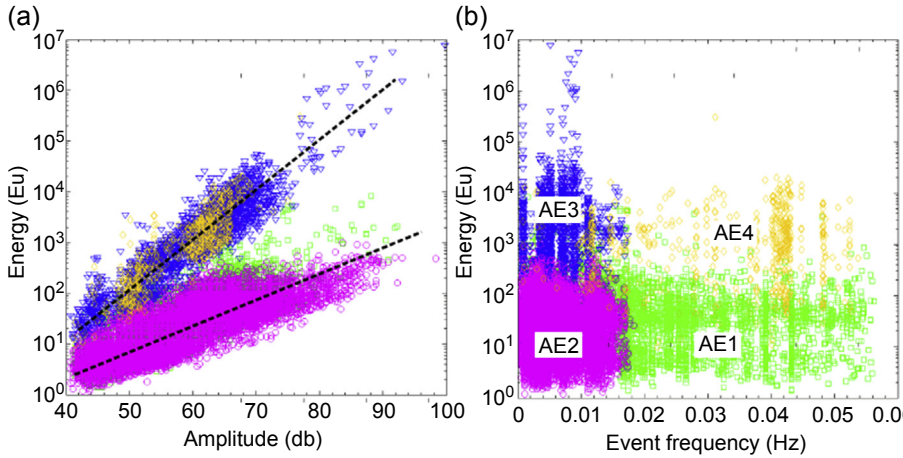

Figure 12.9 Clustered scatter plots of energy, amplitude (a) and event frequency (b) variables.

precise correlation of the identified damage phases with specific AE clusters, the multivariate technique is a suitable procedure, and it was then adopted. Although each fracture mechanism can be identified by specific AE parameters, clustered by means of statistical techniques, additional experimental techniques could be necessary to validate damage identification as obtained by this procedure.

12.5.4 Multivariate analysis

12.5.4.1 Principal component analysis

In Figure 12.10, bi-plots as obtained by PCA are shown. In the plots, the axes represent the first and second unrotated factors (principal components) and the second and third unrotated factors, respectively. The scale on the axes represents the so-called factor loading (Hardle & Simar, 2007); the 0 on the scale is set at the origin of rotated factors, and scales extend outward to about ± 0.75. In Figure 12.10, all the variables are labelled; furthermore, the clusters identified in Figure 12.9 are graphically evidenced.

Severity, time and event frequency (variables that we can generically define as time-dependent) are grouped together, and the second factor loading is fairly high (time axis in Figure 12.10(a)). On the other hand, variables strictly connected with AE wave features (rise time, duration, counts) generate an orthogonal second group characterized by a high first unrotated factor (wave axis in Figure 12.10(a)). This axis is orthogonal to the time axis.

Moreover, analysing the particular data distribution, we can confirm that the four AE clusters are strictly connected with time-dependent variables, thus indicating that these variables can be regarded as data discriminating factors (Figure 12.10(b)). The evolution of the damage over time could be evaluated by analysing the classification of these clusters with respect to the local axis identified by the time-dependent

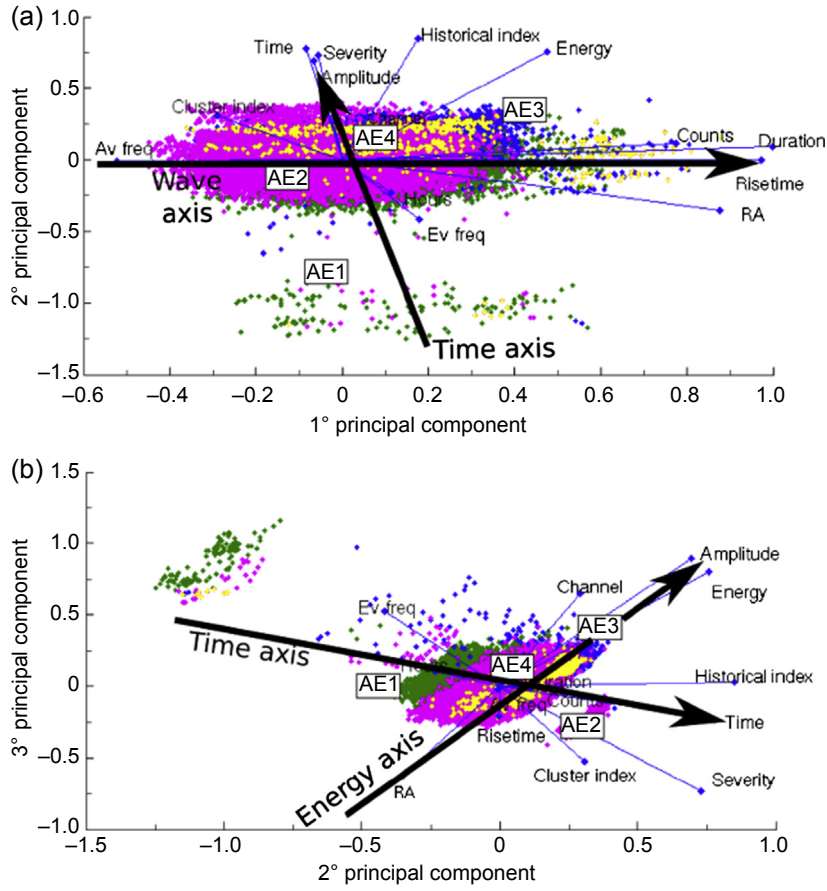

Figure 12.10 (a, b) Bi-plots of principal component analysis results (denoised data).

variables. In particular, cluster AE1 identifies mainly the first stage of the test, and it is characterized by high event frequency. It is located in the plot areas where the second unrotated factor is negative. Analogously, cluster AE3, identified by high energy events, is located on the right side of the plots, and it is related to the last stage of the test. This distribution confirms the results evidenced in Figure 12.9. Furthermore, cluster AE2 is characterized by high values of severity and HI variables. Cluster AE4 is less relevant in the PCA distribution.

For a better comprehension of PCA results, factor loadings greater than ± 0.2 are considered to meet the minimal level of significance; factor loadings greater than ± 0.3 are considered highly significant. With the purpose to avoid redundancy effects on the data distribution, only the uncorrelated variables, as identified in a correlation matrix, were selected for the SOM analysis. They are average frequency, amplitude, duration, energy, time and event frequency.

12.5.4.2 Self-organizing map

Kohonen's SOM algorithm was applied to the uncorrelated variables resulting from PCA. In Figure 12.11(a), the *U*-matrix map resulting from SOM analysis is reported. The *U*-matrix represents the cluster structure of the data by showing on a colour scale the distances between neighbouring units (a node of the two-dimensional array). The *U*-matrix visualization has much more cells than the component planes. This is because distances between map units are shown, not only the distance values at the map units. High values of *U*-matrix map (red and yellow pixels) mean large distances between neighbouring map units and, thus, indicate cluster borders. Elements belonging to the same cluster are, therefore, identified by uniform areas of low value (blue pixels). In this specific case, we identified many homogeneous areas associated with cluster areas. It is interesting to note that using the topological maps of the variables (reported in Figure 12.12) it should be possible, on the basis of variable magnitude distribution, to relate a data cluster to a local area of specific variables. In particular, according to the regions identified in Figure 12.7 and on the basis of a time variable map, we defined three regions on the *U*-matrix map.

Region I: The definition of the area associated with the first region is heavily influenced by the topological map of the variables (Figure 12.12). In fact, the events characterized by high event frequency (red and yellow pixels in the event frequency topological map) are grouped on the right side of the map. Furthermore, this group of data can be distinguished by specific energy and duration value. A lot of AE events, characterized by high energy and high duration, are grouped in area Ia (Figure 12.11(a)). Area Ib includes AE events of region I characterized by low energy, medium-low amplitude and high average frequency. Finally, region Ic is related to events with low energy and low amplitude.

Region II: The second region is located in the center and lower left of the *U*-matrix map. These events have a very low events frequency. The events that occur in the first stage of period II, grouped in area IIa, are characterized by high amplitude and medium energy. On the other hand, the events occurring during the quiescent phase of region II (IIb) showed a very low value for the wave parameters (amplitude, rise time, etc.).

Region III: The third region includes the top and right areas of the map. The AE events with very high energy are grouped in the top-right corner of the map (area IIIa). Instead, events with high duration and low average frequency are mainly grouped in area IIIb, while events with very high amplitude and low duration are predominantly in area IIIc.

Additional information can be obtained by plotting the so-called hits-*U*-matrix (Figures 12.11(b) and (c)). This graph shows the projection of data samples into the *U*-map. The projection is obtained by finding the BMU (best matching unit) of each data sample from the map and increasing a counter in the map unit each time it is the BMU. The colours are related to a specific cluster (Figure 12.11(b)) or magnitude of a variable (Figure 12.11(c)), whereas the size of the coloured hexagon is related to the number of AE hits related to that cluster point.

It may be noted that the IIIa area is associated mainly with clusters AE3 and AE4, grouping acoustic events with most critical energy values. Furthermore, region I is

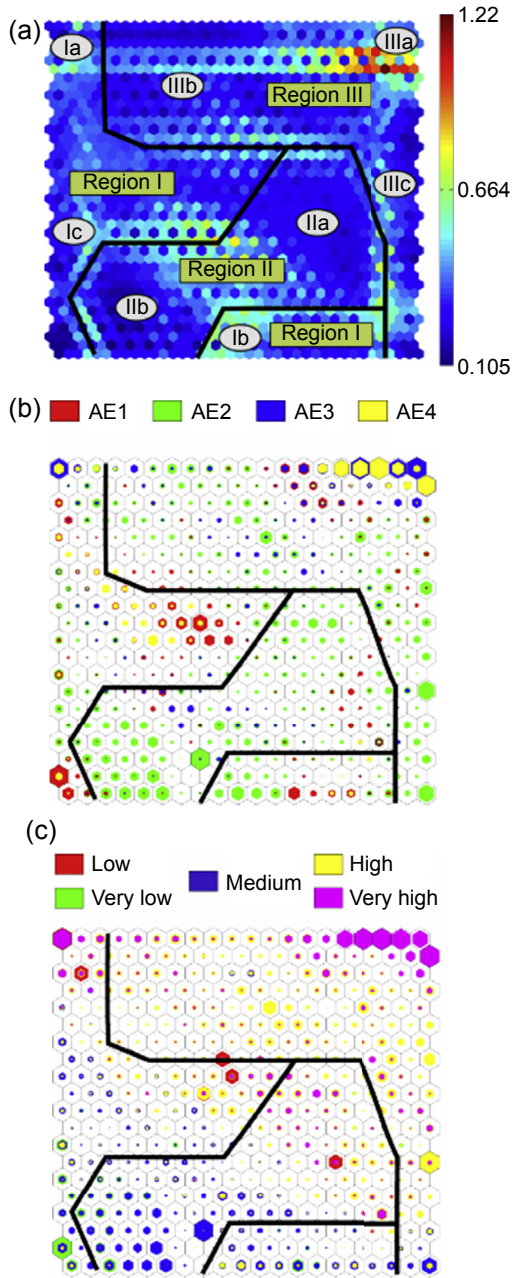

Figure 12.11 (a) *U*-matrix resulting from the application of the Kohonen self-organizing map algorithm; (b) hits *U*-matrix of clusters defined in Figure 12.9; and (c) hits *U*-matrix for the variable HI.

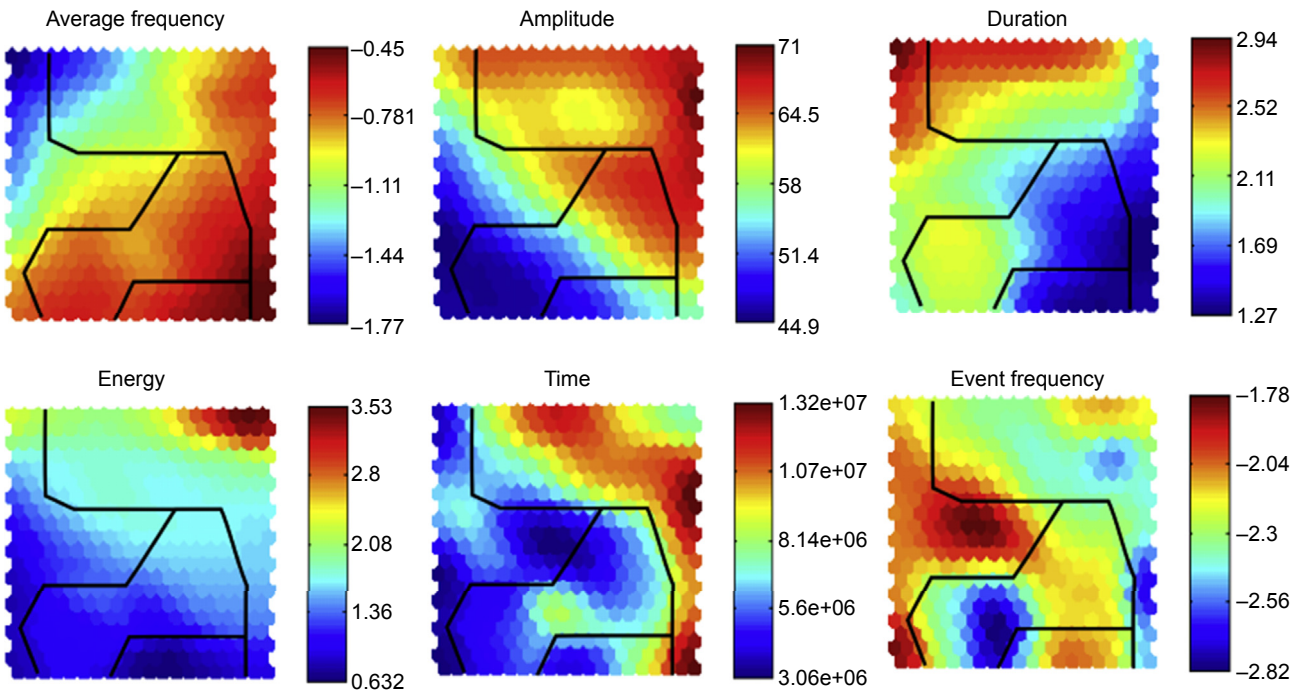

Figure 12.12 Topological maps of the variables as resulted from the application of Kohonen's self-organizing map algorithm.

related to cluster AE1 even if a certain amount of events from other clusters are also included, while region II and the peripheral areas of region III are dominated by events of cluster AE2. This distribution of hits indicates that the information obtained from the univariate analysis is in agreement with the results from the neural network analysis.

Interesting considerations can be done following the analysis of the distribution of the hits related to a specific variable, i.e. HI, taking into account that the most critical events, from the point of view of structural integrity, are characterized by very high HI value. Indeed, high HI hits are almost always grouped in region III (in particular in the IIIa area), while intermediate HI values are prevalent in region II of the *U*-matrix map. Finally, on the map we can distinguish two distinct regions: a medium critical region (related to data cluster AE2) and a high critical one (located in the top right of the map, grouping the data clusters AE3 and AE4).

Based on these considerations the *U*-matrix identified some clusters related with the damage evolution of the steel strand. But, further investigation is necessary to better clarify the discrimination of that damage phenomena and its time evolution. With this purpose, a hits-*U*-matrix (Figure 12.13), despite the data collected in the regions identified in Figure 12.7, was performed. The colours are related to a specific event group (activation or quiescence phase as defined in Figure 12.7), and coloured hexagon size is related to the number of AE hits related to that cluster point. Figure 12.13 shows that the interpretation of the *U*-matrix map is much more complex than the previous interpretation. The clusters associated with the regions I, II and III are characterized by several events that could create internal sub-clusters or interference regions where multiple families of events coexist.

Region I: About the data collected in region I, the activation AEs are located mainly in zone Ia (characterized by high energy and high duration) and Ib (characterized by low energy and low amplitude); instead, the quiescence data are not well identifiable in a specific area. Although, a group of hits of these events are identifiable in zones Ic and Id. Area Ic includes AE events of region I characterized by low energy, medium low amplitude and high average frequency. Instead, area Id is related mainly with quiescence AE with high amplitude and relatively high average and event frequency.

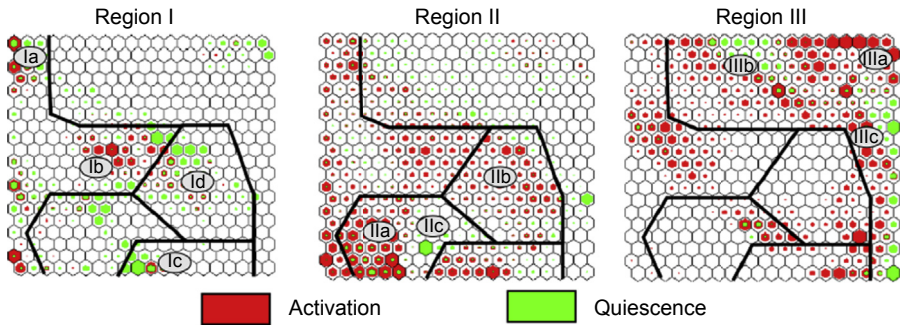

Figure 12.13 Hits *U*-matrix for the data regions identified in Figure 12.7.

Region II: Other considerations can be extrapolated for analysing the hits distribution for region II data. A large amount of activation AE is located in IIa and IIb region, with the former related with lower event frequency than the latter one. Zone IIc could be related with the quiescence phase of region II.

Region III: The analysis of the hits map for region III data confirms that the AEs of this region are located in the top of the map. In particular, a large amount of activation data are located in the top corner. The AEs with very high energy generated during the activation of region III are located in the top-right corner of the map (area IIIa). Instead, the quiescence phase is located in the peripheral region of this section of the map. In particular, in the quiescence phase, two sub-clusters can be identified. Events with high duration and low average frequency are mainly grouped in area IIIb, while events with very high amplitude and low duration are predominant in area IIIc.

With the purpose to verify the hits distribution and to better clarify the discriminating performances of the SOM analysis about the event evolution on SCC tests on post-tensioned strands, a hits validation map was analysed by using a fuzzy response parameter to show the relative goodness of each map unit in representing the data. The fuzzy response was calculated by summing a function of quantization error as follows (Himberg, Ahola, Alhoniemi, Vesanto, & Simula, 2001):

$$g(x, u_i) = \frac{1}{\left(1 + \left(q_i/a\right)^2\right)} \tag{12.4}$$

where $q_i = |x - u_i|$ is the quantization error (i.e. the distance between the sample x and map unit i). The scaling factor, a, is the average distance between each training data sample and its BMU. Consequently, a high value of the fuzzy response is related to a high affordability of the previsioned hits.

Figure 12.14 confirms that the SOM analysis well identified the damage phase of the SCC strand as evidenced in Figure 12.13. The activation and propagation data for each region are well clustered in local areas on the *U*-matrix map. All configurations evidenced a high fuzzy response index, related with high accuracy of the numerical analysis. A higher uncertainty was observed only for region II quiescence data, where we observe a low fuzzy response value (maximum value is only 480). Consequently, only for this dataset, we believe that not enough information was available to discriminate with good affordability clusters location on the *U*-matrix map. Furthermore, this investigation evidenced that in the middle of the *U*-matrix map an interference area generated by AE of regions I and II was clarified.

12.5.5 Damage analysis

On the basis of these reported considerations, it can be possible to divide the *U*-matrix map into specific damage mechanism areas (Figure 12.15), according to the schematic representation shown in Figure 12.11, in which we can distinguish the activation, propagation and critical damage areas, respectively related with areas Ia and Ib, IIa

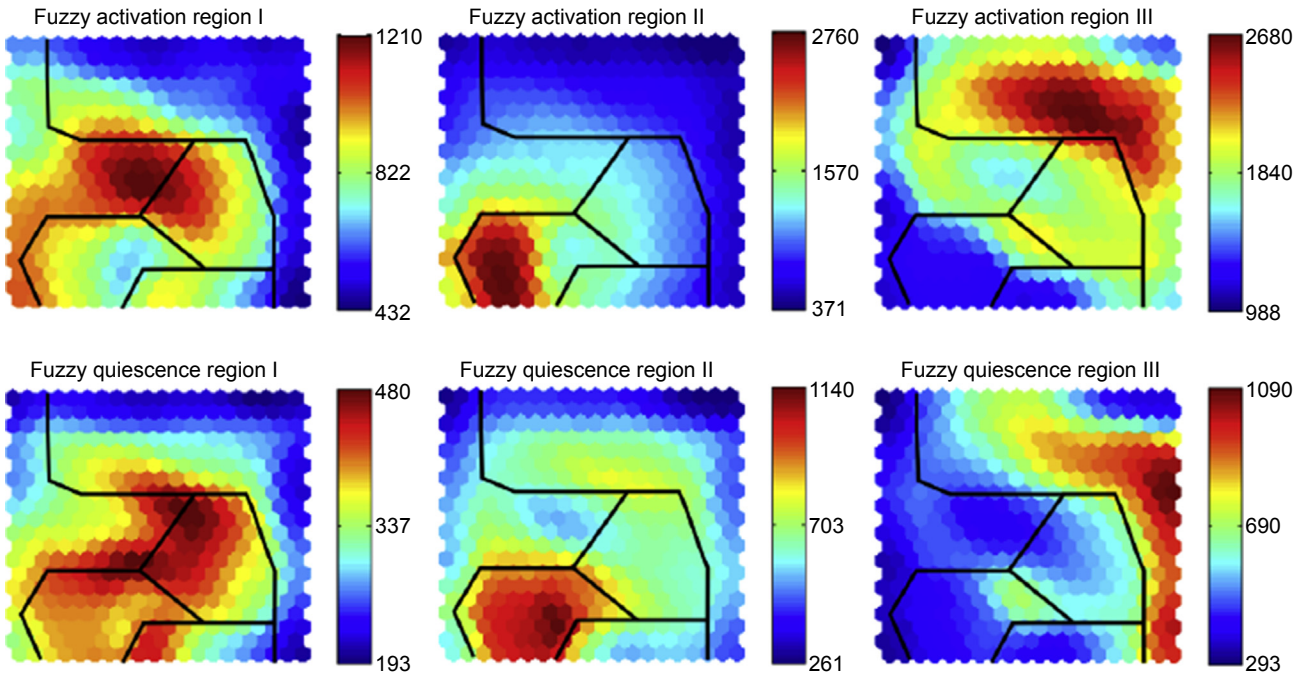

Figure 12.14 Fuzzy response index distribution for data regions identified in Figure 12.7.

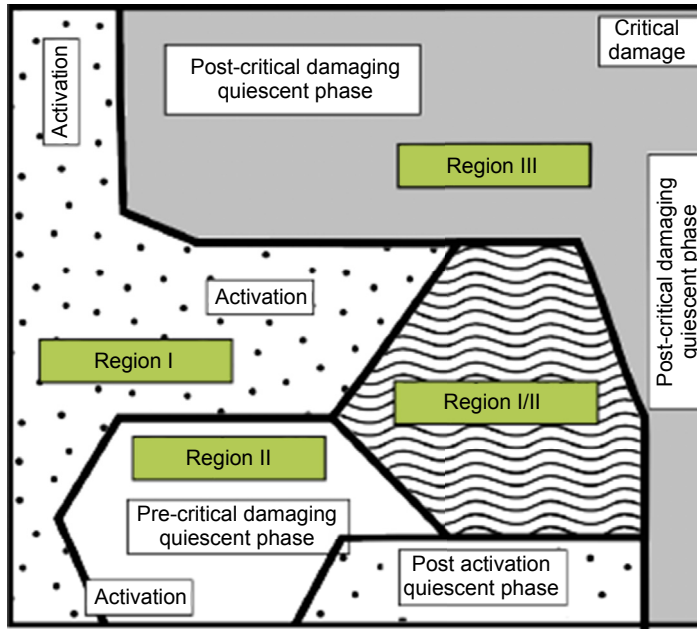

Figure 12.15 Damage mechanisms map.

and IIb and finally IIIa. The peripheral regions, not directly related with a specific variable (and characterized by multiple sub-clusters), represent the quiescence areas. In particular, the peripheral area Ic includes quiescent events that occurred after the electrochemical activation of steel surface characterized by high level of average frequency. The so-called pre-critical damaging quiescent area (IIc) was instead characterized by low event frequency and middle duration events. Consequently, the lower peripheral region in the map is related with the quiescent phase events before the critical damaging of the structure. Whereas, the peripheral regions at the top and right of the map (IIIb and IIIc) are related to the quiescent phase following the critical damaging and characterized mainly by high amplitude values.

Globally it is the opinion of the authors that the SOM algorithms and the related *U*-matrix maps are powerful instruments for analysing a multivariate dataset. In the specific cases, their application allowed not only the validation of preliminary hypotheses formulated on the basis of the interpretation of cumulative hits curve, but it also permitted discriminating between different damage mechanisms occurring during time on steel strands on the basis of the correlation between specific AE wave attributes.

Further information to evaluate and to validate the deterioration stages of a reinforced concrete structure could be provided by supplementary techniques (as electrochemical tests and failure analysis). A suitable procedure could be pointed out in coupling AE and electrochemical noise (Kovac et al., 2007).

12.6 Conclusions

Although the AE is widely used for monitoring of SCC phenomena, in post-tensioned concrete structures caution should be taken during analysis and interpretation of the results. Particular attention must be paid during the data denoising. An improper removal of spurious events may lead to a misleading interpretation of the degradation state of the structure. In this chapter, several denoising procedures were proposed to better support the researchers in this critical phase.

Afterward, even if it could be possible to distinguish the damage progression from the cumulative hit plot, a complete understanding of the damage mechanism occurring on steel wires was achieved by only adopting univariate and multivariate analysis methodology.

An affordable tool is the integration of traditional univariate and multivariate analysis in an effective and synergistic way by using PCA and SOM. This methodology has proven to be particularly effective in identifying the evolution and intensity of corrosion damage on steel wires in the monitored post-tensioned concrete beam. Initiation, propagation and critical rupture phases were clearly identified and associated with specific features of the AE events. Such results allow one, also on the basis of further refining of the methodology, to hypothesize the use of such a procedure for *in situ* recognition of damage processes.

12.7 Future trends

The AE technique is potentially ripe for its implementation as a technique for corrosion monitoring of structures in operating conditions. Many research activities allowed the AE user to provide many useful tools for its correct application and interpretation. In particular, in the field of civil engineering, different test configurations or data processing techniques have been proposed in order to make the discrimination of events representative of the degradation of the structures more reliable.

New hardware and more sophisticated software systems may allow the expansion of the acquired information as well as the development of more sophisticated analysis techniques.

The emission spectra have very complex acoustic characteristics influenced by energy, position and mechanisms of the acoustic source, which makes their identification difficult. In this concern the development of a differential approach (e.g. wavelet transform of AE signals) for the identification and recognition from different sources of acoustic signals is clearly prompted. The wavelet transform is a technique for signal analysis and finds a promising applicability in nondestructive testing. The method of AE can benefit greatly from adopting this technique to provide a better understanding and control of data flow in material testing and longterm structural monitoring.

Possible future objectives can be the application in pre-service inspection, periodic inspection, online monitoring and, finally, for forecasting the residual service life of the structure by this technique.

References

ACI. (2001). *ACI 222.2R-01. Corrosion of prestressing steels*. ACI Committee 222.

ACI. (2014). *ACI 423.4R-14 Report on Corrosion and Repair of Unbonded Single-Strand Tendons*, ACI Committee 423.

Aggelis, D. G., Shiotani, T., Philippidis, T. P., & Polyzos, D. (2008). Stress wave scattering: friend or enemy of non-destructive testing of concrete? *Journal of Solid Mechanics and Materials Engineering, 2*(3), 397−408.

Alvarez, M. G., Lapitz, P., & Ruzzante, J. (2012). Analysis of acoustic emission signals generated from SCC propagation. *Corrosion Science, 55*, 5−9.

Anastasopoulos, A. A. (2007). Signal processing and pattern recognition of AE signatures. In E. E. Gdoutos (Ed.), *Experimental analysis of nano and engineering materials and structures* (p. 929). Dordrecht, The Netherland: Springer.

Batagelj, V., Bock, H. H., Ferligoj, A., & Iberna, A. (2006). *Studies in classification, data analysis and knowledge organization*. Seraucus, NJ, USA: Springer-Verlag New York, Inc.

Benaim, R. (2008). *The design of prestressed concrete bridges: concepts and principles*. New York: Taylor & Francis.

Bindra J.S. (2006). *Variation-aware computer-aided design techniques for VLSI digital circuits* (Ph.D. thesis). Minnesota University.

Budano, S., Giunta, G., & Lucci, A. (2011). Acoustic emission data analysis to evaluate damage mechanisms in pipeline carbon steel. *NDT.net, 24*.

Calabrese, L., Campanella, G., & Proverbio, E. (2013). Identification of corrosion mechanisms by univariate and multivariate statistical analysis during long term acoustic emission monitoring on a pre-stressed concrete beam. *Corrosion Science, 73*, 161−171.

Calabrese, L., Campanella, G., & Proverbio, E. (2012). Noise removal by cluster analysis after long time AE corrosion monitoring of steel reinforcement in concrete. *Construction and Building Materials, 34*, 362−371.

Cardoso, M. G. M. S., & Carvalho, A. (2009). Quality indices for (practical) clustering evaluation. *Intelligent Data Analysis, 13*(5), 725−740.

Chatfield, C., & Collins, A. J. (1980). *Introduction to multivariate analysis*. London: Chapman & Hall.

Collins, M., Dasgupta, S., & Schapire, R. (2001). A generalisation of principal component analysis to the exponential family. In *Proceedings of advances in neural information processing systems (NIPS), AA27, Vancouver, British Columbia, Canada, December 3−8, 2001*.

Della Vedova, M., & Elsener, B. (2006). Enhanced Durability, quality control and monitoring of electrically isolated tendons. *Proceedings of 2nd International Fiber Congress, 5*(8).

Didier-Laurent, S., Idrissi, H., & Roue, L. (2008). In-situ study of the cracking of metal hydride electrodes by acoustic emission technique. *Journal of Power Sources, 179*, 412−416.

Enos, D. G., & Scully, J. R. (2002). A critical-strain criterion for hydrogen embrittlement of cold-drawn, ultrafine pearlitic steel. *Metallurgical and Materials Transactions A, 33A*.

Falasconi, M., Pardo, M., Vezzoli, M., & Sberveglieri, G. (2007). Cluster validation for electronic noise data. *Sensors and Actuators B, 125*, 596−606.

Fregonese, M., Idrissi, H., Mazille, H., Cetre, Y., & Renaud, L. (2001). Initiation and propagation steps in pitting corrosion of austenitic stainless steels: monitoring by acoustic emission. *Corrosion Science, 43*(4), 627−641.

Freyermuth, C. L. (1991). Durability of post-tensioned concrete structures. *Concrete International, 13*, 58−65.

Godin, N., Huguet, S., Gaertner, R., & Salmon, L. (2004). Clustering of acoustic emission signals collected during tensile tests on unidirectional glass/polyester composite using supervised and unsupervised classifiers. *NDT&E International, 37*, 253−264.

Golaski, L., Gebski, P., & Ono, K. J. (2002). Diagnostics of reinforced concrete bridges by acoustic emission. *Journal of Acoustic Emission, 20*, 83−98.

Haldiki, M., Batistakis, Y., & Vazirgiannis, M. (2001). On clustering validation techniques. *Journal of Intelligent Information Systems, 17*(2/3), 107−145.

Hardle, W., & Simar, L. (2007). *Applied multivariate statistical analysis*. Berlin: Springer.

Hay, D. R., Cavaco, J. A., & Mustafa, V. (2009). Monitoring the civil infrastructure with acoustic emission: bridge case studies. *Journal of Acoustic Emission, 27*, 1−10.

Hewson, N. R. (2003). *Prestressed concrete bridges: Design and construction*. London: Thomas Telford.

Himberg, J., Ahola, J., Alhoniemi, E., Vesanto, J., & Simula, O. (2001). The self-organizing map as a tool in knowledge engineering. In N. R. Pal (Ed.), *Pattern recognition in soft computing paradigm*. Singapore: World Scientific.

JCMS-IIIB5706. (2003). *Monitoring method for active cracks in concrete by acoustic emission*. Tokyo: Japan Construction Material Industries Federation.

Johnson, M. (2002). Waveform based clustering and classification of AE transients in composite laminates using principal component analysis. *NDT&E International, 35*, 367−376.

Jomdecha, C., Prateepasen, A., & Kaewtrakulpong, P. (2007). A study on source location using acoustic emission system on various types of corrosion in industry. *NDT&E International, 40*(2007), 584−593.

Kim, K. B., Kang, H. Y., Yoon, D. J., & Choi, M. Y. (2005). Pattern classification of acoustic emission signals during wood drying by principal component analysis and artificial neural network. *Key Engineering Materials*, 297−300, 1962−1967.

Kohonen, T. (1982). Self-organized formation of topologically correct feature maps. *Biological Cybernetics, 43*, 59−69.

Kovac, J., Alaux, C., Marrow, T. J., Govekar, E., & Legat, A. (2010). Correlations of electrochemical noise, acoustic emission and complementary monitoring techniques during intergranular stress-corrosion cracking of austenitic stainless steel. *Corrosion Science, 52*, 2015−2025.

Kovac, J., Leban, M., & Legat, A. (2007). Detection of SCC on prestressing steel wire by the simultaneous use of electrochemical noise and acoustic emission measurements. *Electrochimica Acta, 52*(2007), 7607−7616.

Laguerre, L., Bouhelier, J. M., & Grimauld, A. (2004). Application of ultrasonic guided waves to the evaluation of steel members integrity. In *2nd European conference on structural health monitoring (SHM), Munich, Germany, July 7−9, 2004*.

Manson, G., Worden, K., Holford, K., & Pullin, R. (2001). Visualisation and dimension reduction of acoustic emission data for damage detection. *Journal of Intelligent Material Systems and Structures, 12*, 529−536.

Nair, A., & Cai, C. S. (2010). Acoustic emission monitoring of bridges: review and case studies. *Engineering Structures, 32*(6), 1704−1714.

Newman, R. C., & Sieradzki, K. (1983). Correlation of acoustic and electrochemical noise in the stress-corrosion cracking of α-brass. *Scripta Metallurgica, 17*, 621−624.

Ohtsu, M., & Tomoda, Y. (2007). Acoustic emission techniques for rebar corrosion in reinforced concrete. In C. U. Grosse (Ed.), *Advances in construction materials* (pp. 615−621). Dordrecht, The Netherland: Springer.

Oja, E., & Kaski, S. (1999). *Kohonen maps*. Amsterdam: Elsevier.

Palakal, M. J., Pidaparti, M. V., Rebbapragada, S., & Jones, C. R. (2011). Intelligent computational methods for corrosion damage assessment. *AIAA Journal, 39*, 1936−1943.

Perrin, M., Gaillet, L., Tessier, C., & Idrissi, H. (2008a). Acoustic emission use for stress corrosion cracking detection in prestressing strands of bridge structures. In *International acoustic emission symposium (IAES-19), Kyoto, Japan December 9−12, 2008*.

Perrin, M., Gaillet, L., Tessier, C., & Idrissi, H. (2008b). Assessment of stress corrosion cracking in prestressing strands using AE technique. *Journal of Acoustic Emission, 26*, 32−39.

Proverbio, E. (2011). Evaluation of deterioration in reinforced concrete structures by AE technique. *Materials and Corrosion, 62*(2), 161−169.

Proverbio, E., & Longo, P. (2007). Sub critical crack growth in hydrogen assisted cracking of cold drawn eutectoid steel. *Corrosion Science, 49*, 2421−2437.

Ramadan, S., Gaillet, L., Tessier, C., & Idrissi, H. (2008a). Detection of stress corrosion cracking of high-strength steel used in prestressed concrete structures by acoustic emission technique. *Applied Surface Science, 254*, 2255−2261.

Ramadan, S., Gaillet, L., Tessier, C., & Idrissi, H. (2008b). Assessment of the stress corrosion cracking in a chloride medium of cables used in prestressed concrete structures by the acoustic emission technique. *Measurement Science and Technology, 19*, 115702−115710.

Ramadan, S., Gaillet, L., Tessier, C., & Idrissi, H. (2009). Contribution of acoustic emission to evaluate cable stress corrosion cracking in simulated concrete pore solution. *Journal of Acoustic Emission, 27*, 254−262.

Ramadan, S., & Idrissi, H. (2008). In situ monitoring of deposition and dissolution of calcium carbonate by acoustic emission techniques associated to electrochemical measurements. *Desalination, 219*, 358−366.

Salas, R. M., Schokker, A. J., West, J. S., Breen, J. E., & Kreger, M. E. (2005). Conclusions, recommendations and design guidelines for corrosion protection of post-tensioned bridges. In *Center for transportation research, the university of Texas at Austin, research Report 1405−9*.

Shaikh, H., Amirthalingam, R., Anita, T., Sivaibharasi, N., Jaykumar, T., Manohar, P., et al. (2007). Evaluation of stress corrosion cracking phenomenon in an AISI type 316LN stainless steel using acoustic emission technique. *Corrosion Science, 49*(2), 740−765.

Speidel, D. H., & Mattson, P. H. (1997). Problems for probabilistic seismic hazard analysis. *Natural Hazards, 16*, 165−179.

Thompson, N. G., Lankard, D. R., & Virmani, Y. P. (1992). Improved grouts for bonded tendons in post-tensioned bridge structures. *Transportation Research Record, 1347*, 56−65.

Toribio, J., & Lancha, A. M. (1998). Anisotropic stress corrosion cracking behaviour of pre-stressing steel. *Materials and Corrosion, 49*(1998), 34−38.

Vogel, T., & Koppel, S. (2003). Possibilities and limitations of acoustic emission analysis for reinforced concrete. In *International symposium on non-destructive testing in civil engineering (NDT-CE), Berlin, Germany, September 16-19, 2003*.

West, J. S., Larosche, C. J., Koester, B. D., Breen, J. E., & Kreger, M. E. (1999). State-of-the-art. Report about durability of post-tensioned bridge substructures. In *Centre for transportation research bureau of engineering research*. University of Texas at Austin. Research Report 1405−1.

Yuyama, S. (1986). Fundamental aspects of acoustic emission applications to the problems caused by corrosion. In G. C. Moran & P. Labine (Eds.), *Corrosion monitoring in industrial plants using nondestructive testing and electrochemical methods* (pp. 43−74). Philadelphia: American Society for Testing and Materials. ASTM STP 908.

Yuyama, S., Kishi, T., & Hisamatsu, Y. (1983). AE analysis during corrosion, stress corrosion cracking and corrosion fatigue processes. *Journal of Acoustic Emission, 2*, 71−93.

Acoustic monitoring for the evaluation of concrete structures and materials

13

D.G. Aggelis[1], *A.C. Mpalaskas*[2], *T.E. Matikas*[2]
[1]Vrije Universiteit Brussel, Pleinlaan, Brussels, Belgium; [2]University of Ioannina, Ioannina, Greece

13.1 Introduction

The safety and structural integrity of civil structures is of continuously increasing interest to the engineering community. Degradation due to operation loads and environment as well as unexpected events is within the natural process. Structural health monitoring (SHM) is the implementation of a damage characterization system in infrastructure aiming at the proper maintenance action. The final aim is the prevention of loss of lives and economic capital. SHM comprises different crucial issues: first the detection of damage, since this is the initial step toward eventual repair. A step up is the localization in order to know which part or point of the real size structure is the most sensitive and focus repair efforts there. Additionally, the extent of damage is another important piece of information that helps to prioritize the different indications from low to high risk. Finally, the procedure should result in the proper maintenance action based on the quantified results of the assessment in addition to the experience of the inspector.

SHM works closely with nondestructive testing (NDT) techniques. NDT is the tool to obtain crucial information and assist any SHM project (Achenbach, 2009). Taking into account that civil engineering structures possess a role of paramount importance in contemporary society (housing, transportation, storage, and energy production), safety and economic concerns obviously push toward implementation of SHM in infrastructure. Different NDT techniques have been used: visual inspection is the first that comes to mind. Additionally, radiography, infrared thermography, vibrations, and ultrasonics are also popular (Malhotra & Carino, 2004). These methods can be applied at predefined time intervals for a permanent record of the structure. The interval may be defined by fracture mechanics concepts if the load and material properties are well defined. This way, each assessment will take place before possible cracks reach a crucial size and cause instability to the structure. However, this is not always easy to accomplish due to material heterogeneity and the randomness of loading conditions, as well as the possibility of overloading moments that would strongly accelerate the propagation of damage. Therefore, in a number of cases, continuous monitoring takes place in order to record any transition that would signify an event worthy of study in relation to the integrity of the structure (Torres Arrendondo, 2013).

Acoustic Emission (AE) and Related Non-destructive Evaluation (NDE) Techniques in the Fracture Mechanics of Concrete
http://dx.doi.org/10.1016/B978-1-78242-327-0.00013-1
Copyright © 2015 Elsevier Ltd. All rights reserved.

The necessity of SHM is strengthened by the fact that most of the infrastructure that was built half a century ago or more has already reached or is approaching the service limit of the design operational life. Several catastrophic failures occurring in any part of the world remind the engineering community of the severity of this fact. Additionally, operating infrastructure of today was built based on design loads of previous decades, currently resulting in overloading, for example, bridges which have to bear trains of higher speed and excessive traffic loads due to the increased number of vehicles (Grosse, 2008). Apart from the obvious and serious safety issues, repair of existing infrastructure is continuously gaining engineering importance because the cost of repair is considerably lower than building new infrastructure (Aggelis & Ohtsu, 2012). In an SHM application, alarms and proactive interventions can be applied when measured indices deviate from the previous operational limits (Grosse, 2008).

Acoustic emission (AE) is a technique well suited for monitoring in the field as it has the ability to detect and localize cracks, measure their intensity, as well as characterize the type of damage (Grosse & Ohtsu, 2008).

13.2 Acoustic emission

The technique of AE includes detection and acquisition of elastic waves after irreversible changes in the material. The detection is conducted by piezoelectric sensors mounted on the surface of the material or structure. The sensors are triggered by any vibration of the surface, which is due to a transient wave emitted by a crack propagation event. Due to the piezoelectric element inside the sensor, the vibration is transformed into an electric waveform. This waveform is preamplified externally (sometimes preamps are included inside the transducer), and it is driven to the acquisition board, where it is digitized, stored, and main descriptors are measured in real time (Mindess, 2004). A typical AE setup is shown in Figure 13.1.

Descriptors are used because, apart from the number of incoming signals, the information of the waveform shape should be quantifiable. Figure 13.2 shows a typical waveform with its basic descriptors. Amplitude (A) is the voltage of the highest peak of the waveform and is normally correlated with the intensity of the cracking event. Duration (Dur) is defined as the time between the onset of the signal (first threshold crossing) and the end (last threshold crossing). Rise time (RT) is the time between the onset of the signal and the time of the maximum peak. Both these parameters are expressed in microseconds. A parameter that has successfully been used for characterization of the mode of fracture is called RA and is the ratio of RT over A, which is the inverse of the rise angle or "grade" (Ohtsu, 2010; Philippidis, Nikolaidis, & Anastassopoulos, 1998; Shiotani, 2006) of the waveform. Apart from the shape of the waveform, frequency features are also important. A good estimate of the frequency content is given by the average frequency (AF), which is defined as the ratio of the total number of threshold crossings over the duration of the waveform and is measured in kilohertz. If Fourier analysis on the whole waveform is conducted, the centroid of the spectrum and the frequency with the maximum

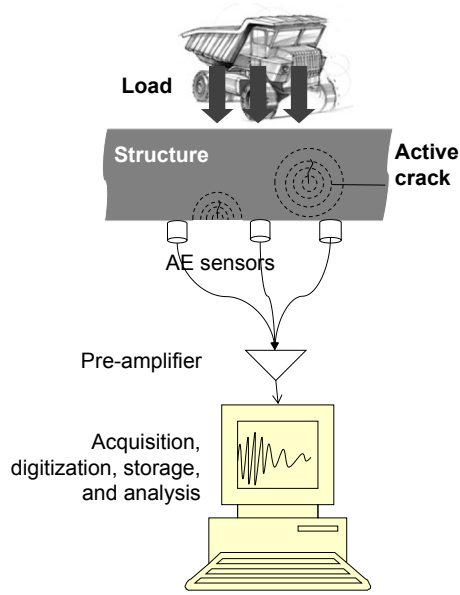

Figure 13.1 Typical setup of AE monitoring.

magnitude can be deduced (peak frequency). Finally, among other important parameters, AE energy (ENE) is the measured area under the rectified signal envelope (MARSE). This feature expresses the severity of cracking like the amplitude taking information from the whole waveform and not only its peak (Grosse & Linzer, 2008; Shiotani, 2008).

In several kinds of structures (e.g., pressure vessels, tanks, and aircraft components), recording of AE may be sufficient to categorize the damage status according to predefined criteria. However, in civil structures, the number of recordings is just

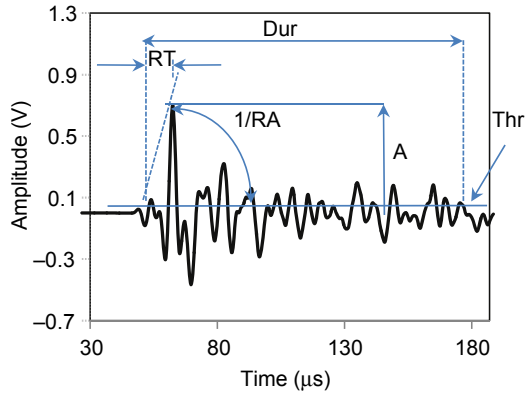

Figure 13.2 Typical AE waveform.

a small part of the received information. The qualitative features of the waveforms should also be evaluated in combination with the knowledge of the geometry of the structure (Ziehl & Pollock, 2012).

13.3 Continuous monitoring

Continuous acoustic monitoring is applied in many different types of civil structures, such as parking structures, bridges, pipelines, as well as rock for prediction of landslides. In the event of deterioration of pre-stressing cables, when some wires start to break, the monitoring system detects the released elastic waves, and the location of the failure can also be determined if multiple sensors are used. (Holley, 1998; Paulson, 2003; Shiotani, 2006; Shiotani, Oshima, Goto, & Momoki, 2013; Yuyama, Yokoyama, Niitani, Ohtsu, & Uomoto, 2007). Location of the source of an acoustic event uses the difference in the time of arrival of the acoustic wave as it encounters different sensors, the position of which is known. In any case, the effect of dispersion should be considered because different wave modes propagate on different velocities, and the reasons may be geometrical (cables, plate geometries) or scattering (Paulson, 1998; Polyzos, Papacharalampopoulos, Shiotani, & Aggelis, 2011; Scholey, Wilcox, Wisnom, & Friswell, 2010). In general, fractures of pre-stressing wires due to mainly corrosion are routinely detected. The challenge of the AE technique is to detect events of interest and filter out signals from noise and other irrelevant sources. The final outcome is that the actual data about possible failure of structural elements are available to owners and engineers based on which they can select the most appropriate and reasonable maintenance scheme in terms of cost and time (Tozser & Elliott, 2014).

AE also makes possible the monitoring of active corrosion in reinforcing bars and the cracking related to the excessive stresses due to the volume of corrosion products. The rate of incoming events signifies the different stages of corrosion, while additional information is taken from frequency and other features like RA (Kawasaki, Tomoda, & Ohtsu, 2010, 2013).

A characteristic of continuous acoustic monitoring of structures compared to normal acoustic emission studies is that the imposed load is not altered in a predefined way as part of the testing protocol of a finite duration. On the contrary, the detection of failure in members should be conducted for the entire structure and over a long time period. Therefore, it is impossible to avoid ambient noises as is the case in a quiet, controlled laboratory environment. Despite this difficulty, the energy and frequency emitted by real fracture incidents (like a fracture of a wire) are usually much higher than background noise. In any case, contemporary AE systems have the ability to apply filters in frequency and energy, as well as any other waveform parameter. Therefore, by monitoring reference intervals, the characteristics of the noise can be defined and excluded from the subsequent monitoring. Possible noise can be introduced by movement of supports and bearings, wind, or precipitation (Shiotani, Ohtsu, & Ikeda, 2001; Ziehl & Pollock, 2012). Special measurements as a simulation of the noise

source can be conducted in order to exclude AE signals not related to the actual cracking sources during monitoring, as in Shiotani (2006) where AE measurement of water drops of different diameters from different heights were conducted as a simulation of actual raindrops.

The transducers should be durable and reasonable in cost. The environmental exposure requires suitable wiring in difficult surroundings, and therefore, it must be kept as simple as possible. Additionally, fast analog to digital conversion in multichannel systems is required since the rate of incoming events may be high. The files should include information like the time, date, and location of the events. Cabling must be unaffected by environmental conditions and stay noise-free. With appropriate placement of the acquisition units, the length of cables can be optimized in order to allow large structures to be monitored efficiently. The files should be saved to hard disk for postprocessing, and therefore, another important parameter is the storage volume. Continuous monitoring produces a large amount of data, and therefore, reducing the information to what is necessary is desirable. In any case, storage can be done cheaply on removable media, while data transmission can nowadays be done through the internet, which is an inexpensive way to transfer data to a secure server (Paulson, 1998).

A serious issue that should always be kept in mind for large structure monitoring is attenuation. Propagation through a medium like concrete induces a serious loss of amplitude due to damping and scattering. Therefore, the spacing of the sensors should be such that successive sensors receive waveforms from the same event, especially if the source location is of interest. Figure 13.3 shows a graph of AE amplitude versus the propagation distance between the source and the sensors from a bridge monitoring in South Japan. Despite the large scatter of the amplitudes of the different events, all exhibit very strong attenuation of several dB/m. Therefore, a compromise should always be made between the smallest event that should be captured and the available number of sensors relative to the structure size. As a rule of thumb, in the specific case where the separation distance between sensors was 1.4 m, sensors of 60 kHz resonance were used (Shiotani, Aggelis, & Makishima, 2009).

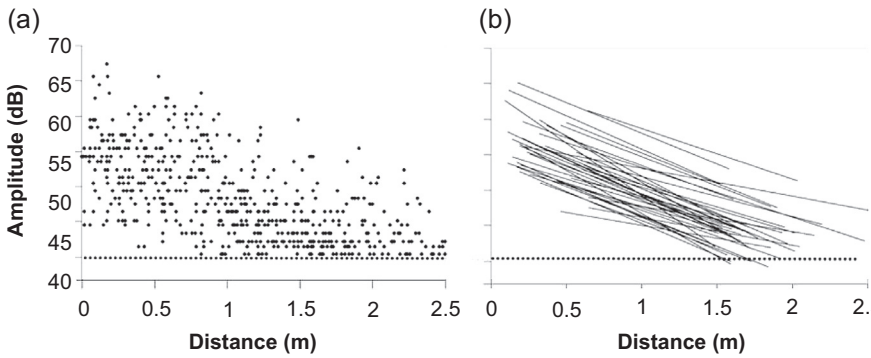

Figure 13.3 (a) Amplitude of AE signals versus distance and (b) corresponding fitted attenuation lines for each event (Shiotani et al., 2009).

13.4 Wireless systems

Until now, AE monitoring has been mainly based on wired transfer between sensor and acquisition board. This makes the monitoring complicated, especially when several tens of channels are used; it is also time-consuming, prone to damage or cable noise, and long cables increase the cost. Today, in order to facilitate continuous monitoring, there is a need to update the application of the AE system to wireless fashion (Grosse, 2008). In this case, the term "sensor" includes (apart from the piezoelectric transducer) signal processor and computational ability and wireless communication platforms (Glaser, Shoureshi, & Pescovitz, 2005; Grosse, Glaser, & Krüger, 2006; Krüger, Grosse, & Marrón, 2005). This node should also be supported by a battery supply. A typical wireless network consists of several nodes. They can be divided into clusters, where the data of all related nodes are shared. After a preprocess in the cluster level, transmission of the meaningful data to the sink takes place. There, information is extracted, and according to the established algorithm, alarms and deviations from the normal condition are noted. Consequently, the information can be sent to the engineer through the Internet. The AE data can be combined with other measurements since it is helpful to merge the information from various disciplines like temperature or strain for optimal structural health monitoring conclusions. Concerning localization, in most of the cases, it is limited to two dimensions, since three-dimensional localization requires more processing time and power consumption (Grosse, 2008).

Such wireless monitoring systems contribute toward the continuous SHM of structures allowing for proactive maintenance so that the actual macroscopic failure never occurs (Grosse, Glaser, & Krüger, 2010). Right now, the sampling rate of acquisition and data transfer is limited compared to the wire alternative. However, the advantages mentioned above push forward the study and use of wireless systems with the aim of casual application in civil structures.

13.5 Optimal performance and maintenance of highway bridges

Responding to the need for reliability in large structures monitoring, a national project was undertaken in the National Strategic Reference Framework (Regional Operational Program Thessaly-Mainland Greece-Epirus) by the Department of Materials Science and Engineering of the University of Ioannina, Greece. The project is called "Optimal performance and maintenance of highway bridges" and is occupied with different aspects of structures evaluation, mainly in the field of acoustic monitoring. The main aim is the development of a procedure based on a combination of techniques that would allow the investigation of the structural integrity as well as the "smart" maintenance that would ensure the continuation of the operation of the structure in an economic way. The investigated techniques were acoustic emission, ultrasound, impulse response, infrared thermography, and half-cell potential for corrosion. The fields for

investigation included the identification of different types of damage (fracture mode) in mortar and concrete, characterization of damage content in either concentrated or distributed form, as well as visualization of the interior. Also, the condition assessment of fire-damaged concrete using AE and ultrasonics was addressed. The project involved a pilot study in the field on the Aracthos Bridge in the Epirus region of Greece with all the aforementioned techniques. In the following, an overview of the acoustic results is presented.

13.5.1 Determination of fracture mode

Fracture of structural materials usually follows a sequence: initial micro-cracking is induced by tensile stresses, and shear phenomena appear later before final failure (Ohtsu, 2010). Detection of the dominant fracture mode provides information on the condition of the integrity of the structure and enables predictions on the operational life span. In order to check the sensitivity of AE in characterizing the fracture mode, controlled fracture experiments were performed. They targeted bending fracture of beams (due to tensile stresses at the bottom span) and shear, as seen in Figure 13.4(a) and (b). In the case of (b), only a narrow zone of the material was unsupported, which resulted in fracture by a diagonal shear crack. Finite element method (FEM) confirmed that the shear stress at that zone was higher than the normal stress, showing that this was a mixed-mode fracture with strong shear components (Aggelis et al., 2013a).

AE results showed considerable discrepancies for the different fracture tests. Figure 13.5 shows the correlation plot between AF and RA, as proposed by the relevant recommendation (Ohtsu, 2010). Each dot stands for the average value of the whole population of AE signals for one specimen. It is obvious that the specimens that were fractured under tensile stresses emitted signals of much lower RA value and higher AF.

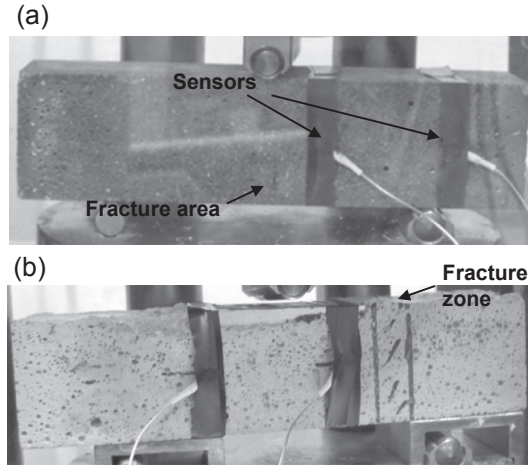

Figure 13.4 (a) Simple three-point bending, and (b) modification for promotion of shear stress.

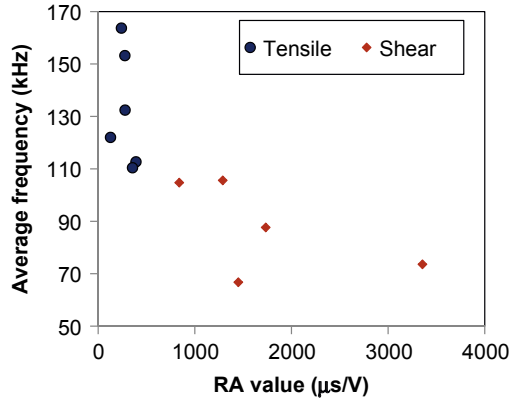

Figure 13.5 AF versus RA for bending and shear fracture in mortar.

The results have been extended to concrete beams showing similar results (Aggelis, Mpalaskas, Matikas, & Van Hemelrijck, 2014). Even if these results are obtained under controlled conditions, the trend clearly indicates the AE shifts that would signify a change in the modes. In a real monitoring condition, these relative shifts would be registered (lower frequency and higher RA for shear cracking) but more likely with different absolute values due to variable conditions (distances, material characteristics). An example is shown in Figure 13.6. There, the AF is monitored throughout bending loading of a real scale concrete beam (3.5 m), externally reinforced with a carbon fiber reinforced polymer (CFRP) patch (Aggelis et al., 2013b). As the concrete matrix is cracking, the average line of frequency is at approximately 80−100 kHz. At the moment of de-bonding of the CFRP strip (shear type of fracture, symbolized by

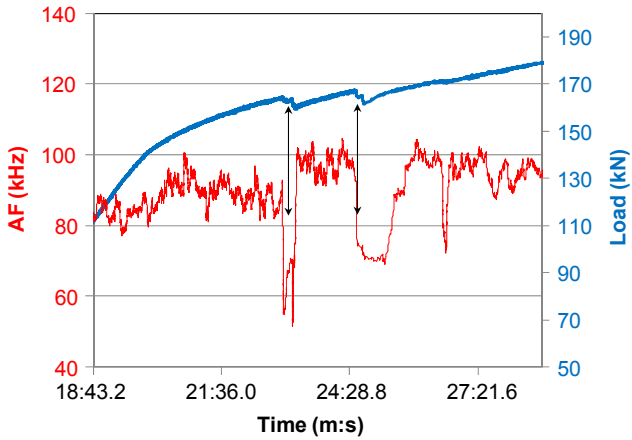

Figure 13.6 AF and load history of a large-scale concrete beam. The deviation of the AF line from the margin 80−100 kHz signifies CFRP de-bonding events, which were also accompanied by the load drops (see arrows).

arrows in Figure 13.6), the AF strongly decreased. This shows that in a continuous monitoring case, the fluctuations of AE descriptors throughout loading could be interpreted adequately to show the original source of damage (in this case de-bonding). Similarly, fluctuations of grade (inverse of RA) and I*b*-value have been used for monitoring the damage development in rock and real scale concrete beams (Kurz, Finck, Grosse, & Reinhardt, 2006; Shiotani et al., 2006).

13.5.2 Assessment of fire-damaged concrete

In the event of accidental fire, the temperature of concrete may increase to several 100 °C. Despite its relatively good behavior, which is due to low conductivity, it is essential to know the mechanical and physical behavior of the material after having sustained high temperatures in order to allow assessment of the residual strength and performance capacity in general (Rilem, 2007). Chemical decomposition, thermal micro-cracking, and spalling may well compromise the mechanical performance of concrete. Therefore, reliable assessment of the mechanical properties of concrete after exposure to high temperatures is a crucial issue in order to decide if the structure can be repaired and how (Poon, 2004; Royles & Morley, 1984). In this case, concrete specimens were subjected to direct fire action. After being exposed to temperatures of 850 °C, the concrete specimens were ultrasonically interrogated and mechanically tested in bending and compression with simultaneous AE monitoring. The concrete had a water to cement ratio of 0.7, total aggregates to cement 4 by mass, and the cement was a mixture of type I and II. The average compressive strength at 28 days was 33.8 MPa.

AE was monitored by two resonant piezoelectric sensors, namely the R15 (Mistras holdings) with resonance nominally at 150 kHz, see Figure 13.7(a) and (b). Both bending and compression specimens were examined. Herein, the overview of some indicative results is discussed.

The AE activity in terms of recorded hits for indicative specimens is shown in Figure 13.8 along with the load histories. Figure 13.8(a) shows the AE activity and load history of a fire-damaged specimen and (b) of a healthy one. It is seen that AE activity starts quite early in (a), while the rate of incoming signals increases

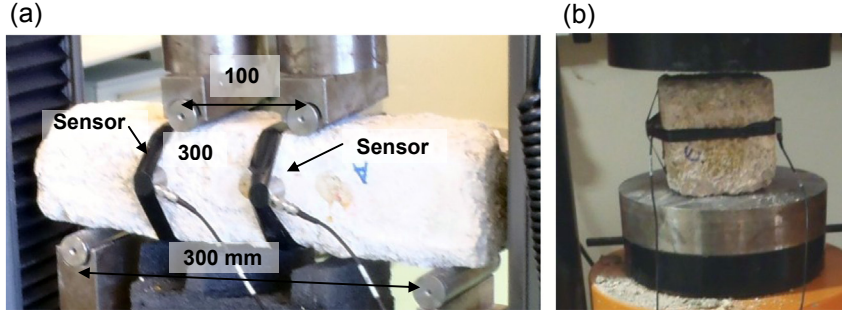

Figure 13.7 Fire-damaged concrete under four-point bending (a) and compression (b) with concurrent monitoring by AE.

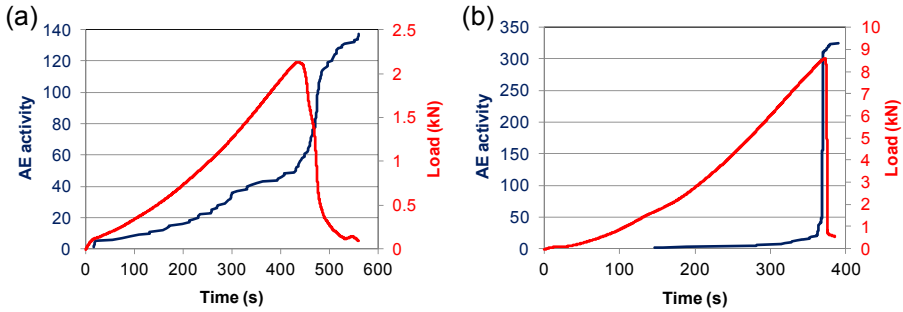

Figure 13.8 Load history and accumulated AE activity during bending of (a) a fire-damaged beam, (b) a healthy beam.

at the point of load drop. On the other hand, for healthy specimens (b), the load drop at the moment of main failure is much sharper (see Figure 13.8(b)), since the specimen fails catastrophically in two parts. The AE curve of these specimens reveals negligible activity at early stages of loading, whereas continuous emissions are recorded after 70% of the maximum load. At the moment of load drop, there is a vertical slope of the accumulated AE activity curve, which shows that almost all the energy is emitted at that time. Focusing again on the concrete directly exposed to fire action, the specimens did not split in two parts after the load drop, while the continuation of AE recording even after the maximum load confirms the more plastic nature of the material after fire (Rodrigues, Laím, & Correia, 2010). Concerning the moment of main failure, the maximum rate of acquisitions that was noticed at the load drop moment was approximately three hits/s for fire damaged, while it was 10 times higher for intact specimens.

Ultrasonic pulse velocity (UPV) was measured with a commercial device (PUNDIT), kindly offered by GEOTEST S.A., Ioannina, Greece, see Figure 13.9(a) and (b),

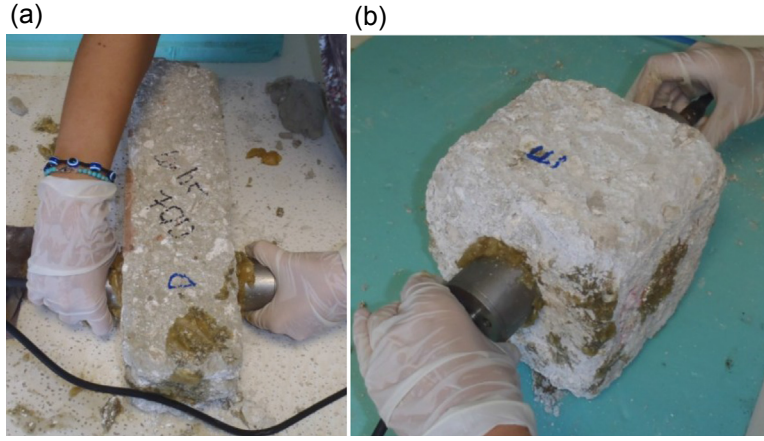

Figure 13.9 UPV measurements in (a) bending specimen, (b) compression specimen after fire damage.

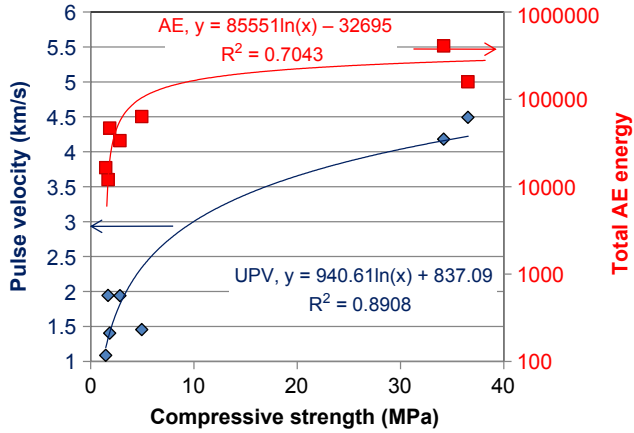

Figure 13.10 UPV and total AE energy versus compressive strength of fire-damaged specimens (specimens with strength higher than 30 MPa were reference at room temperature).

for testing of a prismatic and a cubic fire-damaged specimen, respectively. The frequency of excitation was 54 kHz while the transit time through the known thickness of the material was recorded. Figure 13.10 shows UPV results along with AE energy versus the compressive strength. The correlation between UPV and strength is quite high, while the average AE energy (among other parameters) emitted during fracture was also well correlated to the final strength.

Other AE parameters exhibit stronger correlation to the compressive strength. Specifically, the amplitude and counts register higher values for intact material, which also exhibited much higher strength than thermally degraded concrete, as shown in Figure 13.11. Correlation coefficients ρ^2 are between 0.8 and 0.9,

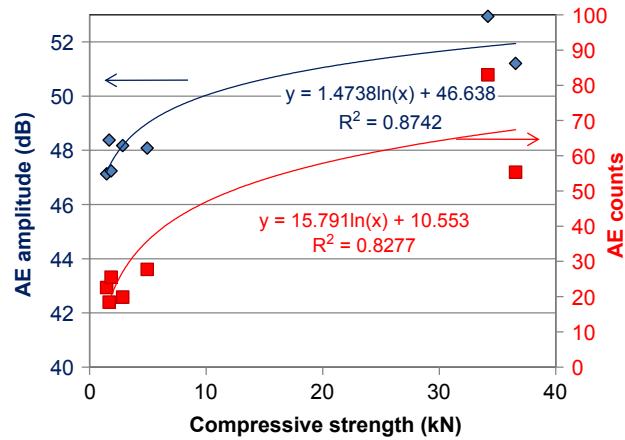

Figure 13.11 AE amplitude and counts versus compressive strength of fire-damaged specimens (specimens with strength higher than 30 MPa were reference at room temperature).

showing that AE can supply reliable predictions of strength in cases of post-damage assessment in combination with a slightly destructive technique such as the drilling resistance test or the pneumatic pin penetration test (Felicetti, 2006; Iwaki, Hirama, Mitani, Kaise, & Nakagawa, 2001).

13.5.3 Evaluation of distributed damage by ultrasonic examination and AE

Damage in a concrete structure can be in the form of distributed (micro-) cracks, as is the case of cracking from freezing−thawing cycles and alkali−silica reaction. To check the sensitivity of the NDT parameters to damage, prismatic mortar specimens of 160 × 40 × 40 mm were cast with different amounts of light inclusions (polystyrene, Figure 13.12(a)) (Mpalaskas, Thanasia, Matikas, & Aggelis, 2014). The simulated void content was from 0% (reference specimen) up to 12.5% by volume. The specimens were loaded in bending with concurrent monitoring of their AE. Earlier, they had been ultrasonically examined, as will be mentioned in the next paragraph. A schematic representation of the test is seen in Figure 13.12(b). In the case of AE monitoring, the sensors were broadband (pico type of Mistras Holdings) with central frequency of 450 kHz.

It is interesting to note that some AE parameters were well correlated to the ultimate load. Figure 13.13 shows an energy-related parameter (RMS, root mean square) of the waveforms versus the maximum load. The correlation is quite strong, showing that as the ultimate load of the different specimens increases, the RMS undertakes an increase by 100%.

On the other hand, different parameters of AE, like frequency indicators exhibit strong correlation to the simulated damage content. Specifically, the frequency centroid of the AE spectrum as average value of the whole population of AE hits is strongly correlated to the damage content in a negative way ($R^2 = 0.94$, see Figure 13.14).

The above investigation shows that some AE parameters are more sensitive to the strength and some others in damage content, something that can be utilized for *in situ* assessment of the quality of concrete.

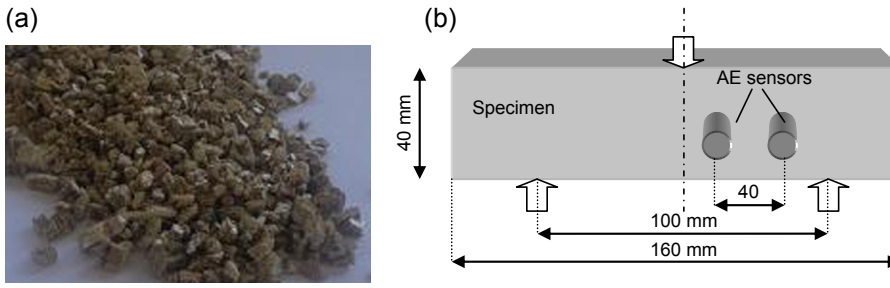

Figure 13.12 (a) Polystyrene particles acting as distributed damage, (b) schematic three-point bending setup with AE sensor positioning.

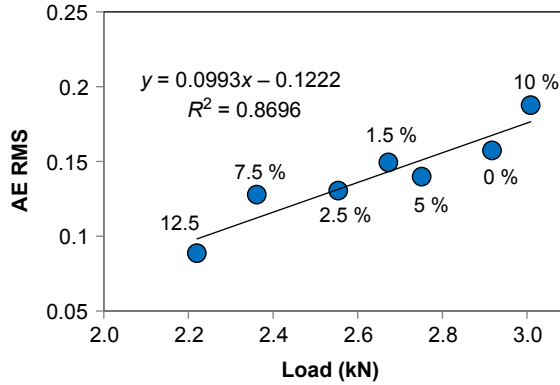

Figure 13.13 AE amplitude RMS versus ultimate load of bending test of mortar with light inclusions.

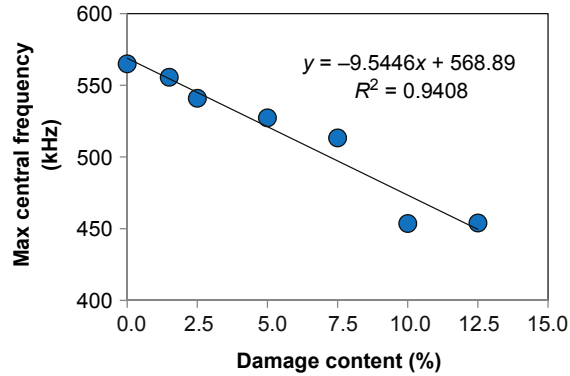

Figure 13.14 AE amplitude RMS versus inclusion content of bending test.

For the ultrasonic investigation prior to the bending test, resonant sensors of 150 kHz were used. The pulse velocity was measured according to the longitudinal axis of the specimen. An AE transducer acting as pulser was attached to one side of the specimen, and a similar transducer was used as receiver on the same point of the opposite surface (distance of 160 mm). The pulser was triggered by an electric signal of 150 kHz and duration of five cycles produced by a waveform generator. The delay between the excitation and the reception of the signal (after excluding sensor delay effects) is indicative of the material quality through the wave path. Because the length of the propagation path was constant (160 mm specimen length), the pulse velocity was calculated. Figure 13.15 shows the relation between the longitudinal wave velocity and the inclusion content. Reasonably, the velocity drops with the increase of polystyrene grains, a trend that agrees closely to the results of scattering theory on voids of similar diameter (Mpalaskas et al., 2014; Tsinopoulos, Verbis, & Polyzos, 2000). Indeed the severe mismatch between the acoustic impedance of the light inclusions and the heavier matrix enables one to solve the problem of scattering

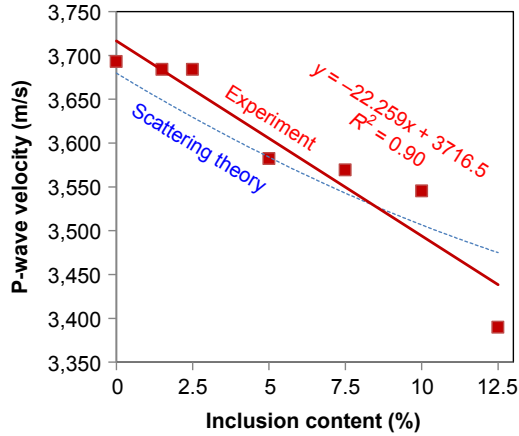

Figure 13.15 Longitudinal wave velocity versus inclusion content.

on cavities rather than on elastic scatterers (Pao & Mow, 1963). The sensitivity of the results confirms that pulse velocity occupies strong characterization power for the interior of the material, while its experimental simplicity enables application under a wide range of conditions (surface roughness, concrete thickness).

The aforementioned results open an interesting discussion on the nature and complementarity of the two elastic wave techniques. Indeed, ultrasonic waves physically propagate through the material, and therefore, they obtain information from its heterogeneity content. Each inclusion, pore, or grain having specific elastic properties and size results in scattering, which influences the propagation of ultrasound and can be depicted in the final pulse velocity or other more delicate parameters (attenuation, dispersion features, Aggelis & Shiotani, 2007). This is why a very good correlation between damage and ultrasonic velocity is reported. However, the maximum load (strength) of the material depends on all the fracture incidents from the early preliminary micro-cracking to the last large-scale events. AE captures information on each one of these events, and therefore, it is reasonable that correlations between strength and AE parameters emerge in addition to the well-known empirical correlations to UPV.

13.5.4 *Visualization of concentrated damage by ultrasonic examination*

In the context of the project, a part was also devoted to ultrasonic examination with the aim of visualization of damage. Actually, visualized techniques are in demand because this is the best way to indicate the existence and volume of damage within a structure, as the relevant technical committee prescribes (Rilem, 2014). For this purpose, different size heterogeneities were included in concrete specimens during casting. Ultrasonic investigation was conducted when the specimens were fully hydrated. Again resonant sensors at 150 kHz were used. The length of the propagation path

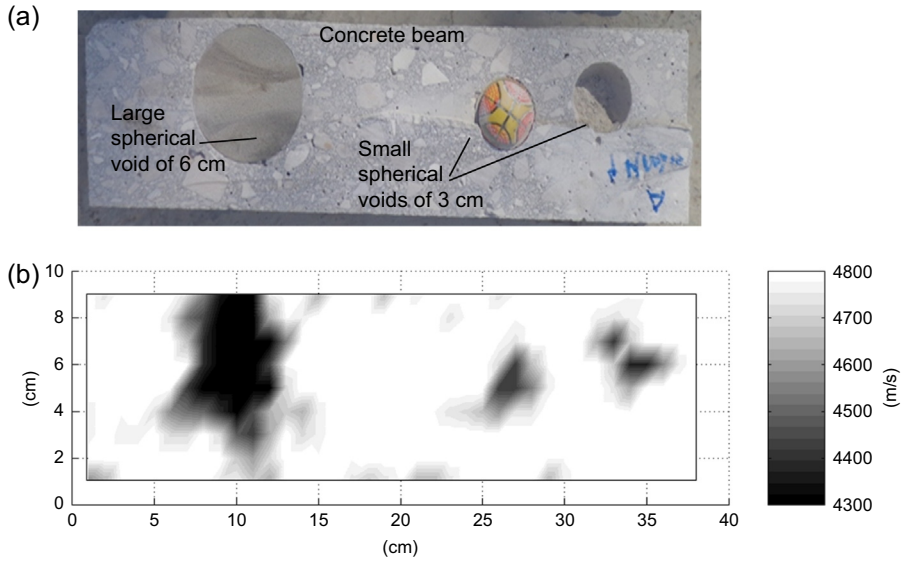

Figure 13.16 (a) Longitudinal cross-section of a concrete beam with different voids, and (b) ultrasonic velocity map of the same specimen.

was constant (in this case, 100-mm specimen thickness). The specimens were scanned in a through-thickness test with a distance between scanning points of 10 mm. In total, 400 points were examined. An example is shown in Figure 13.16(a) after cutting the specimen in two. Three voids can be seen in Figure 13.16(a) (one large void to the left and two smaller to the right). Figure 13.16(b) shows the visualized map of pulse velocity for the specimen with heterogeneities. The areas of low stiffness (voids) are clearly depicted by the lower pulse velocity relatively to the other parts of the specimen. UPV also manages to capture the difference in size of the voids. Though the result seems very satisfying, it should always be kept in mind that, in this case, the mesh of measurements was very dense (10 mm). In an actual case, this is not practical. Usually a mesh of 0.5 m is applied depending on the volume of the structure and the available resources (sensors, acquisition channels, time). Therefore, in order to adequately visualize the interior, elaborate tomography algorithms with ray tracing have been developed (Aggelis, Tsimpris, Chai, Shiotani, & Kobayashi, 2011; Kobayashi, 2013). This way, the number of necessary measurement points is decreased while maintaining sufficient detail of the heterogeneity characteristics.

13.6 Conclusion

Acoustic techniques have a great potential for the monitoring of concrete materials and structures. It has been demonstrated that quite accurate assessments can be conducted. These assessments concern the damage mode, the content and severity of

heterogeneity, and the projection of the ultimate strength. *In situ* acoustic monitoring provides substantial assistance to the structural health monitoring (SHM) of structures. Improving the reliability and the interpretation of data as well as applicability of these acoustic monitoring techniques will have a positive effect on SHM and will help to utilize the full potential of acoustic methods. The present chapter states the basic principles of acoustic monitoring and reviews recent developments in the field in the form of passive (AE) and ultrasonic techniques for assessment of concrete.

Acknowledgment

This research project has been co-financed by the European Union (European Regional Development Fund − ERDF) and Greek national funds through the Operational Program "THESSALY-MAINLAND GREECE AND EPIRUS-2007-2013" of the National Strategic Reference Framework (NSRF 2007-2013).

References

Achenbach, J. D. (2009). Structural health monitoring − what is the prescription? *Mechanics Research Communications, 36*, 137−142.

Aggelis, D. G., Mpalaskas, A., & Matikas, T. E. (2013a). Investigation of different fracture modes in cement-based materials by acoustic emission. *Cement and Concrete Research, 48*, 1−8.

Aggelis, D. G., Mpalaskas, A. C., Matikas, T. E., & Van Hemelrijck, D. (2014). Acoustic emission signatures of damage modes in concrete. In *Proc. SPIE 9062, smart sensor phenomena, technology, networks, and systems integration, 90620P (22 April 2014)*. ISBN 9780819499882. http://dx.doi.org/10.1117/12.2044750.

Aggelis, D. G., & Ohtsu, M. (2012). *Qualitative acoustic emission indices for characterization of concrete damage status (Book Chapter) theory and uses of acoustic emissions*. pp. 185−213.

Aggelis, D. G., & Shiotani, T. (2007). Experimental study of surface wave propagation in strongly heterogeneous media. *Journal of the Acoustical Society of America, 122*(5), EL 151−157.

Aggelis, D. G., Tsimpris, N., Chai, H. K., Shiotani, T., & Kobayashi, Y. (2011). Numerical simulation of elastic waves for visualization of defects. *Construction and Building Materials, 25*, 1503−1512.

Aggelis, D. G., Verbruggen, S., Tsangouri, E., Tysmans, T., & Van Hemelrijck, D. (2013b). Characterization of mechanical performance of concrete beams with external reinforcement by acoustic emission and digital image correlation. *Construction and Building Materials, 47*, 1037−1045.

Felicetti, R. (2006). The drilling resistance test for the assessment of fire damaged concrete. *Cement and Concrete Composites, 28*, 321−329.

Glaser, S. D., Shoureshi, R., & Pescovitz, D. (2005). Future sensing systems. *Smart Structures and Systems, 1*(1), 103−120.

Grosse, C. U. (2008). Wireless sensing and acoustic emission array techniques, Chapter 15. In C. U. Grosse & M. Ohtsu (Eds.), *Acoustic emission testing* (pp. 367−381). Springer.

Grosse, C. U., Glaser, S. D., & Krüger, M. (2006). Condition monitoring of concrete structures using wireless sensor networks and MEMS. In M. Tomizuka, C.-B. Yun, & V. Giurgiutiu (Eds.), *Proc. SPIE 6174, smart structures and materials 2006: Sensors and smart structures technologies for civil, mechanical, and aerospace systems* (pp. 407−418).

Grosse, C. U., Glaser, S. D., & Krüger, M. (2010). Initial development of wireless acoustic emission sensor motes for civil infrastructure state monitoring. *Smart Structures and Systems, 6*(3), 197−209.

Grosse, C. U., & Linzer, L. M. (2008). Signal-based AE analysis, Chapter 5. In C. U. Grosse & M. Ohtsu (Eds.), *Acoustic emission testing* (pp. 53−99). Springer.

Grosse, C. U., & Ohtsu, M. (2008). *Acoustic emission testing*. Springer.

Holley, M. (1998). *Continuous acoustic monitoring of infrastructure*. http://cigmat.cive.uh.edu/sites/cigmat/files/files/conference/presentation/2002/continuous-acoustic.pdf.

Iwaki, K., Hirama, A., Mitani, K., Kaise, S., & Nakagawa, K. (2001). A quality control method for shotcrete strength by pneumatic pin penetration test. *NDT&E International, 34*(6), 395−402.

Kawasaki, Y., Tomoda, Y., & Ohtsu, M. (2010). AE monitoring of corrosion process in cyclic wet−dry test. *Construction and Building Materials, 24*, 2353−2357.

Kawasaki, Y., Wakuda, T., Kobarai, T., & Ohtsu, M. (2013). Corrosion mechanisms in reinforced concrete by acoustic emission. *Construction and Building Materials, 48*, 1240−1247.

Kobayashi, Y. (2013). Mesh-independent ray-trace algorithm for concrete structure. *Construction and Building Materials, 48*, 1309−1317.

Krüger, M., Grosse, C. U., & Marrón, P. J. (2005). Wireless structural health monitoring using MEMS. *Key Engineering Materials, 293−294*, 625−634.

Kurz, J. H., Finck, F., Grosse, C. U., & Reinhardt, H.-W. (2006). Stress drop and stress redistribution in concrete quantified over time by the b-value analysis. *Structural Health Monitoring, 5*, 69−81.

Malhotra, V. M., & Carino, N. J. (Eds.). (2004). *CRC handbook of nondestructive testing of concrete*. Boca Raton (FL): CRC.

Mindess, S. (2004). Acoustic emission methods. In V. M. Malhotra, & N. J. Carino (Eds.), *CRC handbook of nondestructive testing of concrete*. Boca Raton (FL): CRC.

Mpalaskas, A. C., Thanasia, O. V., Matikas, T. E., & Aggelis, D. G. (2014). Mechanical and fracture behavior of cement based materials characterized by combined elastic wave techniques. *Construction and Building Materials, 50*, 649−656.

Ohtsu, M. (2010). Recommendation of RILEM TC 212-ACD: acoustic emissionxe "emission". *Materials and Structures, 43*(9), 1187−1189.

Pao, Y. H., & Mow, C. C. (1963). Scattering of plane compressional waves by a spherical obstacle. *Journal of Applied Physics, 34*, 493−499.

Paulson, P. O. (2003). The use of acoustic monitoring to manage concrete structures. In *International symposium (NDT-CE 2003) non-destructive testing in civil engineering 2003*. http://www.ndt.net/article/ndtce03/papers/v036/v036.htm.

Paulson, P. O. (March 31, 1998). Continuous acoustic monitoring of suspension bridges and cable stays. In *Proc. SPIE 3400, structural materials technology III: an NDT conference, 205*. http://dx.doi.org/10.1117/12.300092.

Philippidis, T. P., Nikolaidis, V. N., & Anastassopoulos, A. A. (1998). Damage characterization of carbonxe "carbon"/carbon laminates using neural networkxe "neural network" techniquesxe "techniques" on AE signalsxe "signals". *NDT&E International, 31*(5), 329−340.

Polyzos, D., Papacharalampopoulos, A., Shiotani, T., & Aggelis, D. G. (2011). Dependence of AE parameters on the propagation distance. *Journal of Acoustic Emission, 29*, 57−67.

Poon, C. S., Shui, Z. H., & Lam, L. (2004). Compressive behavior of fiber reinforced high-performance concrete subjected to elevated temperatures. *Cement and Concrete Research, 34*, 2215−2222.

Rilem. (2007). Recommendation of RILEM TC 200-HTC: mechanical concrete properties at high temperatures-modelling and applications. *Materials and Structures, 40*(9), 841−853.

Rilem. (2014). *On-site measurement of concrete and masonry structures by visualized NDT*. Technical Committee 239-MCM. http://rilem.net/gene/main.php?base=8750&gp_id=252

Rodrigues, J. P. C., Laím, L., & Correia, A. M. (2010). Behaviour of fiber reinforced concrete columns in fire. *Composite Structures, 92*, 1263−1268.

Royles, R., & Morley, P. D. (1984). Acoustic emission and bond degradation in reinforced concrete due to elevated temperatures. *Materials and Structures, 17*(3), 185−191.

Scholey, J. J., Wilcox, P. D., Wisnom, M. R., & Friswell, M. I. (2010). Quantitative experimental measurements of matrix cracking and delamination using acoustic emission. *Composites Part A, 41*, 612−623.

Shiotani, T. (2006). Evaluation of long-term "stability" for rock slope by means of acoustic "emission" technique. *NDT&E International, 39*(3), 217−228.

Shiotani, T. (2008). Parameter analysis, Chapter 4. In C. U. Grosse & M. Ohtsu (Eds.), *Acoustic emission testing* (pp. 41−52). Springer.

Shiotani, T., Aggelis, D. G., & Makishima, O. (2009). Global monitoring of large concrete structures using acoustic emission and ultrasonic techniques. *Journal of Bridge Engineering-ASCE, 14*(3), 188−192.

Shiotani, T., Ohtsu, M., & Ikeda, K. (2001). Detection and evaluation of AE waves due to rock deformation. *Construction and Building Materials, 15*(5−6), 235−246.

Shiotani, T., Oshima, Y., Goto, M., & Momoki, S. (2013). Temporal and spatial evaluation of grout failure process with PC cable breakage by means of acoustic emission. *Construction and Building Materials, 48*, 1286−1292.

Torres Arredondo, M-A. 2013. Acoustic emission testing and acousto-ultrasonics for structural health monitoring. PhD Thesis, ISSN 2191−5601 (Universitat Siegen).

Tozser, O., & Elliott, J. (2014 accessed). *Continuous acoustic monitoring of prestressed structures*. http://www.puretechltd.com/pdf/technical_papers/2000/PTL_Technical_Paper_20080212083309.pdf.

Tsinopoulos, S. V., Verbis, J. T., & Polyzos, D. (2000). An iterative medium approximation for wave dispersion and attenuation predictions in particulate composites. *Advanced Composite Letters, 9*(3), 193−200.

Yuyama, S., Yokoyama, K., Niitani, K., Ohtsu, M., & Uomoto, T. (2007). Detection and evaluation of failures in high-strength tendon of prestressed concrete bridges by acoustic emission. *Construction and Building Materials, 21*(3), 491−500.

Ziehl, P., & Pollock, A. (2012). Acoustic emission for civil structures. In W. Sikorski (Ed.), *Acoustic emission*. InTech, ISBN 978-953-51-0056-0. http://dx.doi.org/10.5772/32652. Available from http://www.intechopen.com/books/acoustic-emission/acoustic-emission-for-civil-structures.